Investigations on Cold Atmospheric Plasma Jets for Medical Applications

I n a u g u r a l d i s s e r t a t i o n

zur

Erlangung des akademischen Grades eines

Doktors der Naturwissenschaften (Dr. rer. nat.)

der

Mathematisch-Naturwissenschaftlichen Fakultät

der

Ernst-Moritz-Arndt-Universität Greifswald

vorgelegt von

Ansgar Schmidt-Bleker

geboren am 03.07.1986

in Hamburg

Greifswald, den 21. Januar 2016

Dekan: Prof. Dr. Werner Weitschies

1. Gutachter: Prof. Dr. Klaus-Dieter Weltmann

2. Gutachter: Prof. Dr. David B. Graves

Tag der Promotion: 18.07.2016

Contents

Abbreviations

CAP ...... cold atmospheric plasma

CCD ...... charge-coupled device

CFD ...... computational fluid dynamics

DBD ...... dielectric barrier discharge

FNS .... first negative system

FTIR ...... Fourier transform infrared

FWHM ..... full width at half maximum

ICCD ...... intensified CCD

LAAS ...... laser atom absorption spectroscopy

LIF .... laser induced fluorescence

MCP ...... multi channel plate

MPC ...... multi pass cell

NDPM ..... non-dispersive path mapping

PROES ..... phase resolved optical emission spectroscopy

RONS ...... reactive oxygen and nitrogen species

SPS .... second positive system

VUV ...... vacuum ultraviolet

Mathematical Symbols

C_p . . . . heat capacity at constant pressure

D . . . . diffusion coefficient

I . . . . light intensity

I_0 . . . . background intensity

L . . . . absorption length

Pe . . . . Péclet number

T . . . . gas temperature

T_0 . . . . ambient room temperature

$\eta(r)$ . . . . axisymmetric refractive index distribution of gaseous mixture

$\sigma_\mathbf{i}$ . . . . cross section of species i

$\mathbf{e}_\perp$ . . . . unit vector transverse to direction of flow field

$\mathbf{v}$ . . . . velocity field

ω_i . . . . mass fraction of species i

ρ . . . . mass density

τ . . . . natural lifetime of excited state

$\theta(x)$ . . . . Heaviside step function

c . . . . contrast obtained in Schlieren measurement

k . . . . heat conductivity

n . . . . density of ambient species

n_i . . . . density of species i

n_θ . . . . particular analytical solution to equation (2.3)

r_0 . . . . radius / half width of the axisymmetric / plane jet

v_0 . . . . average velocity at jet outlet

$v_\perp$ . . . . virtual velocity of particles transverse to flow field

Chemical Species

Ar^* . . . . metastable argon

Ar_2^+ . . . . molecular argon ion

Ar^+ . . . . argon ion

Ar_2^* . . . . argon excimer

Ar . . . . argon

CO_2 . . . . carbon dioxide

CO . . . . carbon monoxide

H_2O_2 . . . . . . hydrogen peroxide

H_2O . . . . water

HNO_2 . . . . . . nitrous acid

HNO_3 . . . . . . nitric acid

He . . . . helium

$N_2(A)$ . . . . . . metastable nitrogen

N_2O_5 . . . . . . dinitrogen pentoxide

N_2O . . . . nitrous oxide

N_2 . . . . nitrogen

NO_3 . . . . nitrate radical

NO_x . . . . nitrogen oxides (binary compounds of oxygen and nitrogen)

NO . . . . nitric oxide

$O_2(a)$ . . . . . . metastable singlet oxygen

O_2 . . . . oxygen

O_3 . . . . ozone

OH   . . . . hydroxyl radical

O   . . . . atomic oxygen

eN_2 . . . . a fictitious electronegative nitrogen species

Chapter 1

Introduction

Advances in technology are nowadays often achieved through highly interdisciplinary and translational approaches. Modern plasma medicine is a prime example: A diverse scientific community of engineers, physicists, chemists, biologists and medical doctors is engaged in developing suitable plasma sources, investigating the complex chemistry encountered in atmospheric pressure plasma and its action on biological tissue [1–9]. Plasma medicine comprises the application of plasma for modification of surfaces for further medical use [10–12], biological decontamination [4, 13–15], and its therapeutic application on living tissue. A brief introduction to the topic is given in section 1.1. The field of plasma medicine builds upon the development of novel cold atmospheric plasma (CAP) sources that generate various active components: Neutral reactive oxygen and nitrogen species (RONS) are generated in relevant amounts, but also electrons and ions, (vacuum) ultra violet radiation, visible light, thermal radiation and electromagnetic fields are delivered to the treated tissue. The first CAP sources approved as medical device in Germany are available only since 2013 - a breakthrough for the field. However, the medical CAP sources that are available today are based on a variety of different source concepts, each producing a different cocktail of RONS as presented in section 1.2. This raises a question of vital importance: *What is the optimum reactive species composition for a given medical application?* While this question is eventually to be answered by biologists and medical scientists in the years to come, the objective of the present work is to provide the tools required to tackle this problem. As outlined in section 1.3, this comprises

- a detailed analysis of the interaction of a CAP source with the ambient air,

- the identification and quantification of RONS produced by CAP,

- comprehension of the fundamental processes and control parameters for RONS generation and,

- based on the previous findings, the development of practical means to control the RONS composition that can be realized both in the lab and in the doctor's office.

1.1   Plasma Medicine as New Field of Research

The effect of cold atmospheric pressure plasma on living tissue strongly depends on the plasma properties. Already since the 1970s plasma has been employed for in therapeutic applications for cauterization and ablation [16–18]. Such applications primarily rely on a lethal effect of the plasma, causing necrosis in treated cells. In the 2000s it was discovered, that plasma can in fact also be applied in a non-lethal regime, leaving mammalian cells largely unharmed[1] while killing bacteria [22, 23]. This showed the potential for using plasma for the treatment of pathogen-based diseases. While CAP application in dermatology and dentistry were first targeted in plasma medical research, various further application sites ranging from lung to gastrointestinal tract are now studied [8]. Also the application of CAP in cancer treatment is under current investigation [24–26]. Until now neither resistance of pathogens against plasma treatment nor side effects or allergic reactions due to plasma treatment were observed if applied at appropriate treatment times e.g. as suggested by the company offering the device. [27–30]. In Germany, there are now three CAP sources that received a CE marking as medical device and were tested in clinical trials [31–35]. All three devices are based on different source concepts as discussed in the next section.

1.2   Plasma Sources for Medical Applications

In figure 1.1 a) - c) three different commercial CAP sources for medical applications are shown together with schemes of the respective source concepts (d-f). As the devices operate in ambient air (using rare gases or air as working gases), they generate a large variety of RONS, which are assumed to play the central role in plasma medical applications (besides further synergistic effects through electrons and ions, radiation and electric fields) [20, 21, 36, 37]. While the plasma chemistry in air is very complex, some crude estimations on general trends concerning the resulting gas phase chemistry can be made based on the time-of-flight of RONS from generation to reaching the target, the gas temperature in the core plasma and the working gas employed.

kinpen MED: DBD-Type Plasma Jet

The *kinpen MED* (neoplas tools GmbH, Germany) shown in figure 1.1 a) is based on the dielectric barrier discharge (DBD)-type plasma jet concept illustrated in figure 1.1 d). The electrodes are separated by a dielectric, preventing the formation of an arc between the electrodes. The device is operated with argon (Ar) as feed gas at a frequency of approximately 1 MHz. In contrast to its predecessor, the *kinpen 09* (neoplas tools GmbH) and the scientific version *kinpen Sci* (which allows for adjustment and measurement of the voltage applied at the inner electrode as well

---

[1]Depending on the treatment time, CAP can also have cytotoxic effects on mammalian cells. However, if applied in appropriate doses, it induces apoptosis, the programmed cell death, in a fraction of treated cells and does not lead to significant necrosis (as is e.g. caused in burn wounds) [19–21].

as feed gas control through external mass flow controllers; by INP Greifswald e.V.), it is operated in a burst mode at a frequency of 2.5 kHz with 50% duty cycle. The average gas temperature in these devices remains close to room temperature (see article [A3]) and the local temperature in the plasma does not exceed 430 K (based on measurements of the rotational temperature of nitric oxide, NO) [38]. In the visible plasma plume of approximately 1 cm length, e.g. atomic oxygen (O) and metastable singlet oxygen ($O_2(a)$) are abundant highly reactive species, whereas nitrogen oxides (NO_x), especially NO are generated in lower amounts. Average gas flow velocities of tens of m/s at the nozzle outlet and the low density of ambient air in the plasma plume diminishes the formation of slowly generated (on the timescale of ms), but long-living species like ozone (O_3) or dinitrogen pentoxide (N_2O_5) in large amounts in the plasma plume. However, these are found in considerable amounts in the far-field (at distances of some cm) of the jet. Note that the RONS concentrations resulting from therapeutic application are well below the maximum recommended concentration at the workplace for all RONS, as is evident from the discussion of the plasma chemistry of the *kinpen 09* in chapter 4. Similar RONS output is also observed in Ar CAP jets operated at higher frequencies [39, 40] and in helium (He) CAP jets [41, 42].
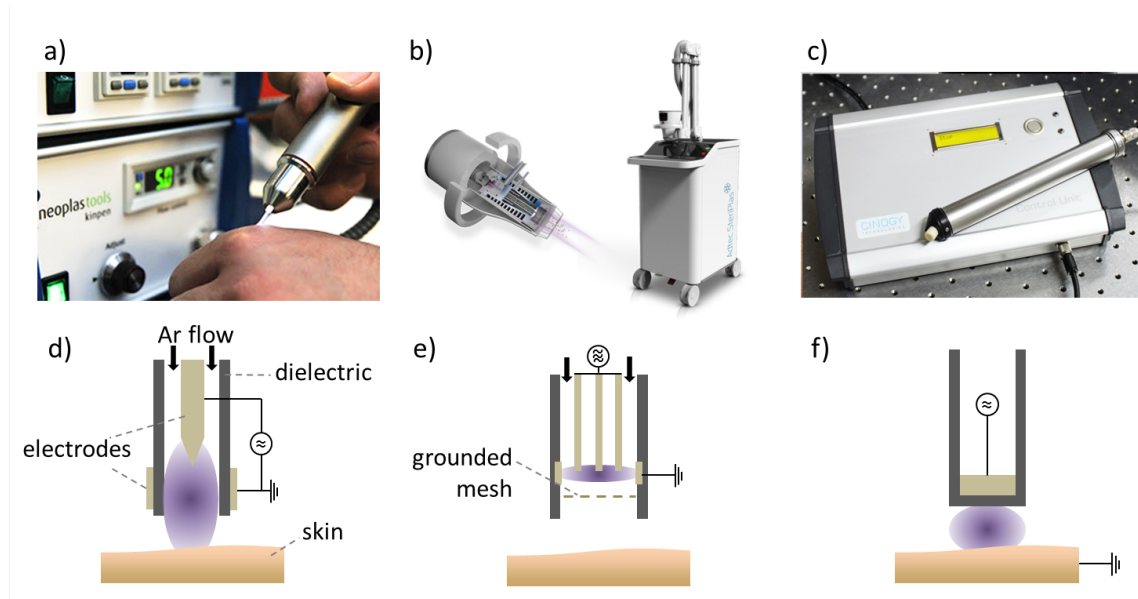

Figure 1.1: Images of the CAP sources *kinpen MED* (a), *SteriPlas* (b) and *PlasmaDerm* (c) and the corresponding design concepts DBD-plasma jet (d), plasma torch (e) and FE-DBD (f). Images (a,b) provided by courtesy of the respective manufacturers.

SteriPlas: Torch-Type Plasma Jet

The *SteriPlas* (Adtec Healthcare Ltd, United Kingdom) shown in figure 1.1 b) and its predecessors MicroPlaSter Alpha and MicroPlaSter Beta (ADTEC Plasma Technology Co. Ltd., Japan) are based on the plasma torch design. The devices are also operated with argon as feed gas, but are driven at microwave frequency (2.45 GHz) and the driving and grounded electrodes are not separated by a dielectric. Despite

the similarities in the applied feed gas and gas velocities, the higher gas temperatures in the core plasma (more than $800\,K$ were measured at the outlet of the device, the core plasma temperature can be expected to be significantly higher) result in a very different, NO_x-dominated chemistry [43, 44]. This is common for devices operated at higher temperatures due to the extended Zeldovich NO generation mechanism [45] and is also observed in air-operated plasma torches [46], the *Plason* electric arc plasma generator (Bauman Moscow State Technical University, Russia) [47] or plasma jets of the micro hollow cathode design operating at high gas temperatures [48]. A tissue-tolerable temperature at the suggested treatment distance is achieved through employing an additional cooling unit.

PlasmaDerm: Floating Electrode-DBD

In the floating electrode DBD concept of the *PlasmaDerm* (Cinogy GmbH, Germany) device shown in figure 1.1 c) and f), the skin acts as grounded electrode, separated from the driving electrode by a dielectric. In DBDs operated in air O_3 is typically the most abundant species, as O generated in large amounts is quickly converted to O_3 [49, 50]. As the mass transport is not forced by convection but occurs through much slower diffusion, significant densities of NO_x like nitrous oxide (N_2O), nitrate radical (NO_3) or N_2O_5 can build up on the timescale of minutes [49]. O_3 was measured in large quantities in a very similar device [51]. It is noted that DBD sources can also be operated in both an O_3-dominated and, by increasing the input power (and thereby the vibrational energies of nitrogen, N_2) an NO_x-dominated mode [52].

1.3   Scope of this Work

A major goal of current research in plasma medicine is the identification of plasma-generated RONS responsible for the biological response of bacteria and mammalian cells to plasma treatment [20, 36, 37, 53–56]. As discussed in the previous section, the RONS output of current CAP sources used in plasma medicine strongly differs and quantitative data on the RONS generated are rare for most CAP sources. Detailed knowledge of both the RONS output of plasma sources for plasma medicine and their biological effect on living tissue can help to optimize future CAP sources towards specific applications, avoid potential side effects of plasma treatment and elevates plasma medicine from a field based on heuristic approaches to one based on scientific rigor.

This work is concerned with the identification of the plasma-chemical mechanisms in the Ar-operated CAP jet kinpen shown in figure 1.2 that lead to the generation of RONS, their quantification and means to control their composition.
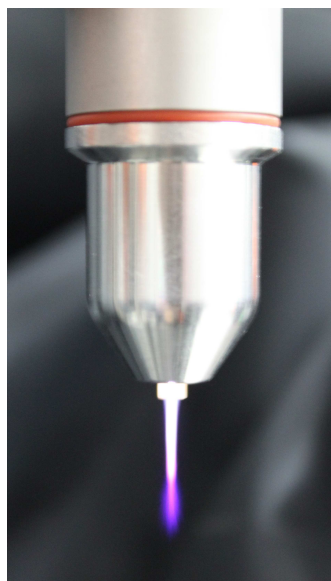

Figure 1.2: The argon-operated plasma jet kinpen. Reprint from [A3].

Non-Dispersive Path Mapping (NDPM) Approximation (articles A1 and A2)
- NDPM: An entirely new analytical approach to ambient species diffusion in jets.
- Combination of NDPM and LIF enables estimation of ambient species densities at the position of the guided streamer – not only in laminar, but also in turbulent jet flow.

Quantitative Schlieren Diagnostics (A3)
- Temporally averaged ambient species density and gas temperature measurements.
- Estimation of input power through combination with CFD simulations.

Shielding Gas Device (A4)
- Design of a device for efficiently controlling the ambient gas composition.

CHAPTER 2
mass & heat transport

Propagation Mechanisms of Guided Streamers (A5)
- Discovery of fundamental processes in guided streamer propagation related to the electronegativity of the gas surrounding the plasma jet.
- Information on the plasma dynamics on the ns scale.

CHAPTER 3
plasma dynamics

Combination of Quantitative RONS Measurements by FTIR Diagnostics and Zero-Dimensional Modelling (A6 and A7)
- The model uses input data obtained from the previous measurements:
  - Ambient species density
  - Gas temperature
  - Temporal dynamics
- Variation of the shielding gas composition is employed to control the RONS output and as additional parameter for benchmarking the model.

- Model yields information of reaction networks and near-field species.
- A parameter set of molecular feed gas admixtures and shielding gas composition is found, allowing for continuously switching from O-dominated to NO_X-dominated chemistry.
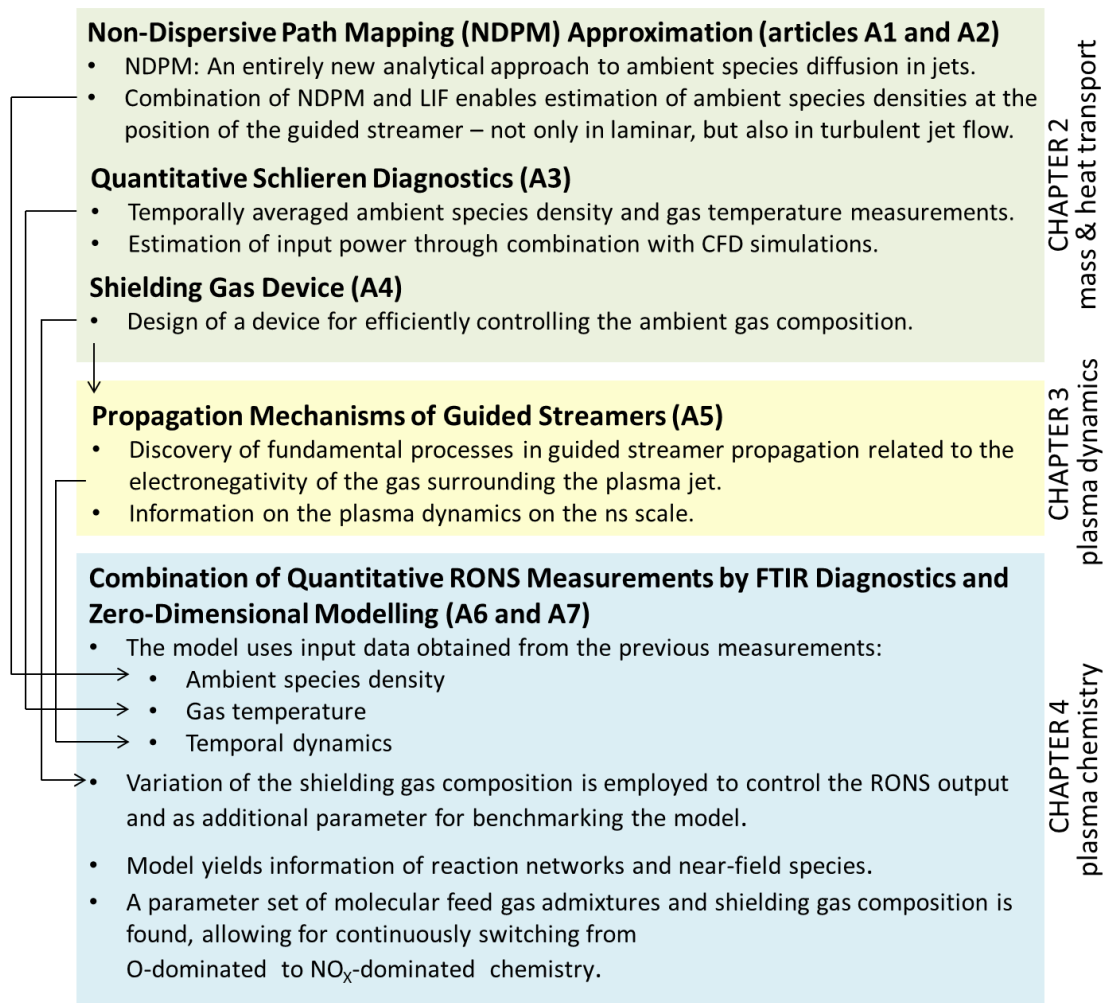
CHAPTER 4
plasma chemistry

Figure 1.3: Overview of topics covered in this work.

An overview on the here-presented investigations and their context is given in figure 1.3. In chapter 2, the transport of mass and heat through mixing of the jet with the ambient air is investigated, as both ambient air density in the plasma plume and temperature significantly affect the plasma chemistry. Therefore, a novel analytical approach to diffusion in jet flows is developed and quantitative Schlieren measurements are combined with computational fluid dynamics (CFD) simulations, yielding not only the ambient air density and gas temperature, but also an estimation of the calorimetric power deposited by the CAP jet. Furthermore a shielding gas device is introduced which allows to better control the gas the CAP jet is operating in. In chapter 3 the temporal dynamics and propagation mechanisms of guided streamers on the ns timescale are investigated using phase resolved optical emission spectroscopy (PROES). The findings yield new insights into fundamental processes in guided streamers, in particular on the role of the electronegativity of the surrounding gas. In chapter 4 the data obtained from the previous investigations are used as input values for zero-dimensional (volume averaged) modeling of the plasma-chemical processes. Such numerical simulations of the plasma chemistry are difficult due to the filamentary nature of the discharge, the turbulent flow

regime and relevant timescales ranging from the ns scale (propagation of guided streamers), through the μs (repetition rate) to the ms scale (convective and diffusive mass transport). In a novel approach, the fast electron impact reactions and the comparably slow RONS chemistry are treated in two separate models. The first electron impact reaction kinetics model is closely correlated to experimental data on fast Ar metastable dynamics. The second RONS chemistry model is verified by Fourier transform infrared (FTIR) spectroscopy measurements in the far-field. The shielding gas device is used with shielding gas mixtures ranging from pure N_2 to pure oxygen (O_2). This provides both a method to control the plasma chemistry and an additional parameter that can be used to benchmark the model. Through the insight obtained by the previous experimental and numerical studies, a parameter set of molecular feed gas admixtures and shielding gas composition is found that allows for continuously switching from an O-dominated to a NO_x-dominated plasma chemistry, changing the densities of the respective species by at least two orders of magnitude while being easy to implement (requiring no further changes to the plasma source itself).

Chapter 2

Investigations on Mass and Heat Transport (Articles [A1]-[A4])

As CAP jets for biomedical applications are operated in ambient air, the transport of mass and heat in the plasma plume strongly affects the plasma chemistry. If noble gases are used as feed gas, the RONS are almost entirely generated from ambient air diffusing into the active plasma plume (with a few RONS being generated from feed gas impurities). The gas temperature affects the reaction rates of gas phase reactions. Furthermore, knowledge of the local gas composition and temperature is also often required for evaluating measurements, for example when estimating quenching rates in laser induced fluorescence (LIF) experiments or fitting absorption profiles in spectroscopic measurements.

Both transport of mass and of heat can be described by convection-diffusion equations. For stationary flows, the transport of species i is described by

$$\rho \mathbf{v} \cdot \nabla \omega_i = \nabla \cdot (\rho D \nabla \omega_i) \tag{2.1}$$

with mass density ρ, velocity field $\mathbf{v}$, mass fraction ω_i and diffusion coefficient D. Similarly, the heat transport equation reads

$$\rho C_p \mathbf{v} \cdot \nabla T = \nabla \cdot (k \nabla T) \,, \tag{2.2}$$

where C_p is the heat capacity at constant pressure, T is the gas temperature and k the heat conductivity. Equations (2.1) and (2.2) are often solved numerically together with the Navier-Stokes equation of mass and momentum conservation.
While numerical solutions often yield highly accurate results for diffusion in jet flows [57], they give less information about the fundamental connections and scaling laws, as solutions are obtained for a specific set of parameters. In section 2.1 a novel analytical method, the so-termed non-dispersive path mapping (NDPM) approximation for describing diffusion of ambient species in both plane and axisymmetric laminar jet flows is introduced (first introduced in article [A1]). As an application example and prerequisite for further modeling studies, the NDPM approximation is used for the interpretation of planar LIF measurements on hydroxyl radicals (OH) (as presented in article [A2]). The combination of the experimental and analytical approach allows for an estimation of the density of ambient species at the position

of the guided streamer, even in turbulent jet flows. Diffusion in turbulent flows is further discussed in section 2.2, where Schlieren measurements are combined with CFD simulations of the jet flow in order to obtain temporally averaged density and temperature maps in the plasma plume (from article [A3]). The combination of Schlieren measurements and CFD simulations also yield the calorimetric power input of the CAP jet. Finally, in section 2.3 a gas shielding device is introduced, which allows for controlling the composition of the gas the CAP jet is operating in (from article [A4]).

2.1   Diffusion in Laminar Flows: The Non-Dispersive Path Mapping Approximation (Articles [A1] and [A2])

A common analytical approach for the investigation of jet flows is using boundary layer theory, first introduced by Prandtl in 1904, an approach that simplifies the Navier-Stokes equations by dividing the flow into two areas, one inside the boundary layer, where viscous drag dominates and one outside the boundary layer, where viscosity is negligible [58]. Schlichting presented boundary layer solutions for axisymmetric jet flows [59] and Bickley for plane jets [60], using a virtual origin of the jet (with infinitesimal width). Such boundary-layer solutions agree well with experimental results and CFD calculations in the far-field of the jet [61]. Based on the work of Schlichting and Pai, Crane investigated the mixing of jets with ambient species in both plane [62] and axisymmetric jets [63].
However, boundary layer theory cannot be applied for the investigation of ambient species diffusion in the near-field of the jet, since no actual nozzle of finite size is considered. For investigations on diffusion in the near-field, e.g. for the estimation of diffusion flame lengths, solutions can be derived assuming a uniform velocity field [64, 65]. Sanchez et al. gave the complete solution for the plane and axisymmetric jet, which is also employed in the NDPM approximation.

Random Walks and Path Mapping

Before NDPM can be applied as approximation to the convection-diffusion equation (2.1), an exact solution for a simpler case is required. A uniform velocity field with norm v (pointing in z-direction), a constant diffusion coefficient (e.g. negligible thermodiffusion) and an incompressible flow are assumed. Furthermore, it is assumed that diffusion can be neglected over convective transport in direction parallel to the flow, yielding

$$v \cdot \partial_z n = \Delta_r n. \tag{2.3}$$

Here, (r, z) denote the respective Cartesian or polar coordinates and n is the ambient species density and $\Delta_r = \partial_r^2$ or $\Delta_r = r^{-1}\partial_r(r\partial_r)$ for Cartesian or polar coordinates, respectively.

Assuming an initial condition $n(r, z = 0) = \theta(|r| - r_0)$, where r_0 is half of the width (plane jet) or the radius (axisymmetric jet) of the jet and $\theta(x) = 1$ for $x \geq 1$, $\theta(x) = 0$ for $x < 0$, the analytical solutions to (2.3) were found by Sánchez et al. [65] and are here denoted as n_θ.

The aim of the NDPM approach is to find a mapping

$$\tilde{n}_\theta(\tilde{r}, \tilde{z}) \approx n_\theta(r, z), \tag{2.4}$$

so that $\tilde{n}_\theta(\tilde{r}, \tilde{z})$ is an approximation for the ambient species density in a non-uniform velocity field $\mathbf{v} = (v_r, v_z)$ for jet flows with high Péclet number $Pe = r_0 v_0 / D$, where v_0 is the average velocity of the jet flow. In order to find a reasonable mapping, the paths on which particles diffuse from the ambient into a jet flow with uniform velocity field were investigated in [A1]. In figure 2.1 a) the trajectories of four particles that perform a random walk (with random movements in r-direction) starting at the side of the nozzle into the jet flow are illustrated. In article [A1] it was shown analytically that for $r \ll r_0$ and $z_0 \ll z/r_0 Pe$ all probable paths closely follow a straight line from $(1, 0)$ to the given position (r_1, z_1), illustrated as dashed line in figure 2.1 a).
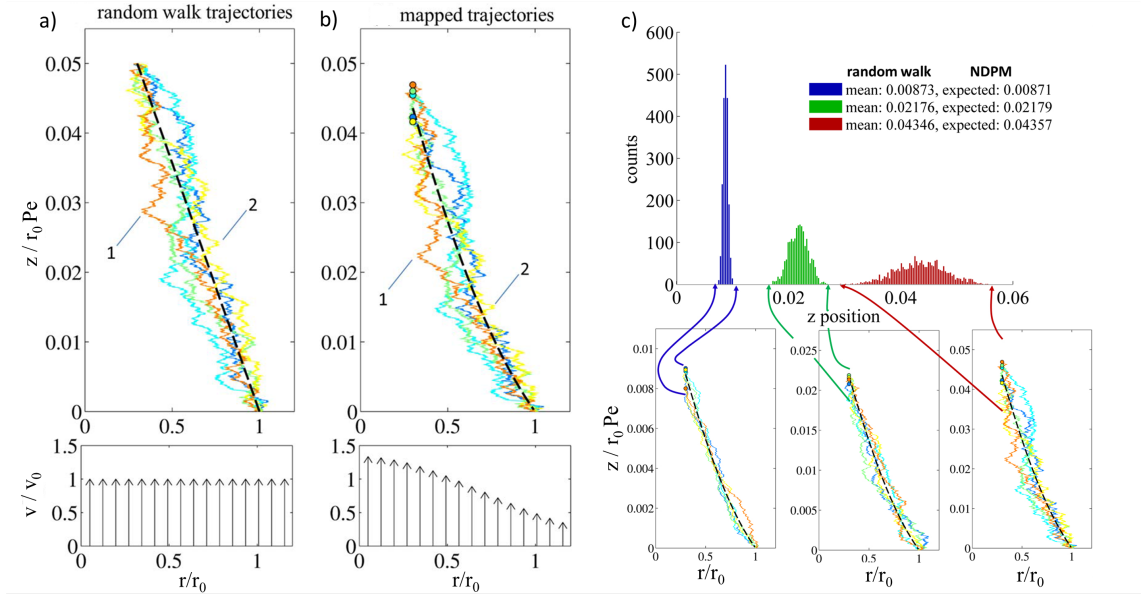
Figure 2.1: Random walk of particles with same origin and endpoint in a uniform velocity field (a). The trajectories shown in figure a) mapped according to the flow field $v_z(r)$, resulting in the mapped trajectories shown in b) and c). The dashed line is the path (2.5) according to NDPM approximation. Reprinted from [A1].

Each trajectory owns an inherent random walk history. In figure 2.1 b) paths with identical random walk history but subject to a non-uniform velocity field are shown. Accounting for the non-uniform velocity field, the most probable path is now mapped according to

$$\partial_t \tilde{\mathbf{x}} = \mathbf{v} + \mathbf{e}_\perp v_\perp, \tag{2.5}$$

where $v_\perp$ is defined as the transverse velocity in direction $\mathbf{e}_\perp$ associated to the unmapped path. Due to dispersion, the endpoints of the random walk trajectories

are distributed not exactly at the position of, but around the endpoint of the mapped path. For example a particle with the trajectory (1) spends a longer time in a region with higher velocity compared to one with trajectory (2). Hence, the endpoint of trajectory (1) is located further from the nozzle than that of (2). This was evaluated statistically for 2000 paths as shown in figure 2.1 c) for different axial distances of the endpoints. It is observed, that as the endpoint is located further from the nozzle, the distribution of endpoint positions becomes broader, while the mean values agree well with the mapped endpoint. In the NDPM approximation the dispersion and resulting scattering of endpoints is hence neglected and the mapping (2.5) of the most probable path is performed for every point $r < r_0$.

Results: NDPM vs. CFD Simulation

In figure 2.2 full CFD calculations (solving the Navier-Stokes equations and the convection-diffusion equation (2.1) numerically) are compared to two NDPM solutions for both the plane and the axisymmetric jet. The first NDPM approximation uses the velocity fields shown in figure 2.2 a) and b) from the CFD calculation for the NDPM approximation. The second uses a parabolic Poiseuille flow profile for the whole domain as approximation for the velocity field. This approach already gives a remarkably good agreement with the density distribution obtained from the full CFD simulation and has the advantage that mapping 2.5 can easily be solved analytically.

As can be expected, the NDPM approximation becomes less accurate at large distances where $z_0 \ll z/r_0 Pe$ is not fulfilled, e.g. the axisymmetric solution becomes discontinuous at $r = 0$. This is due to the fact that for the plane jet, the contributions to the density from the left ($r \leq r_0$) and the right side ($r \geq r_0$) of the slit were mapped separately. In the axisymmetric case this is not feasible and only the paths originating from $r \geq r_0$ are mapped, introducing an error which becomes relevant at larger distances from the nozzle.

In many applications the on-axis density of ambient species is of particular interest. The NDPM approximation yields especially simple, yet accurate expressions, e.g. for the Poiseuille flow the result for the axisymmetric jet is

$$\tilde{n}(r = 0, z) = \exp\left(-\frac{r_0^2 v_0}{3Dz}\right). \tag{2.6}$$

Application: Evaluation of LIF Experiments

The NDPM approximation has been applied in several applications: In [66] the on-axis solution (2.6) was used as a fitting function for the evaluation of experimental data on the ambient species density obtained from vacuum ultraviolet (VUV) absorption measurements, in [67] it was used for the estimation of quenching rates of metastable helium by ambient species in a helium-operated CAP jet and as estimation for the ambient species density in the plug-flow models presented in chapter 4. The NDPM approximation was especially useful for the interpretation of planar LIF experiments performed on OH presented in the following. In the plasma plume groundstate OH was excited to the $OH(A, X)(1, 0)$ state by a planar laser sheet at
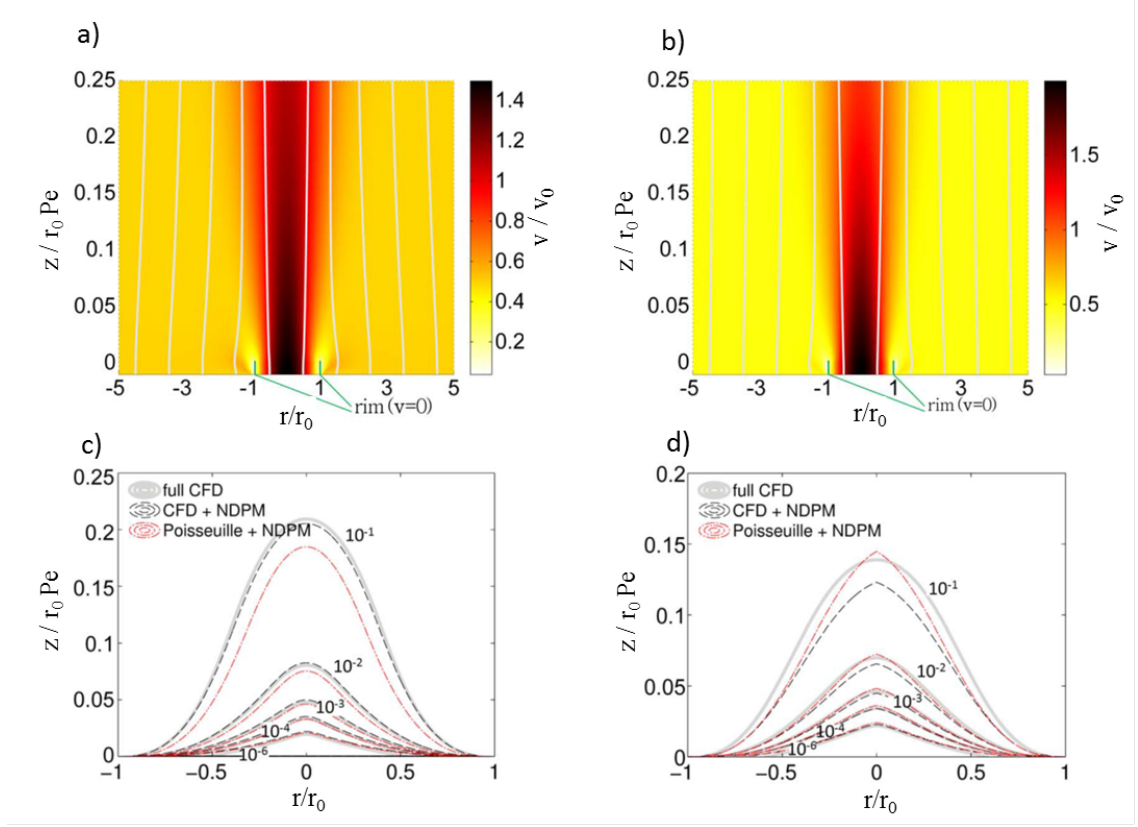
Figure 2.2: Velocity field (a,b) and densities computed by CFD simulation and NDPM approximation for the plane (a,c) and axisymmetric jet (b,d). Figure adapted from [A3].

a wavelength of 283.5 nm. Based on previous measurements on other CAP devices [68, 69] (and later also confirmed for this jet by reaction kinetics modeling, as shown in section 4.1), it was assumed that the OH density does not vary drastically in the visible plasma plume due to typical lifetimes in the ms-range and hence a rather cylindrical OH-distribution was expected as indicated by the dashed lines in figure 2.3 a). However, the observed fluorescence produced a pronounced triangular pattern if the jet was operated in the laminar regime at a flow rate of 0.5 slm while at a higher flow rate of 3 slm (figure 2.3 b) turbulent eddies occur.
The intensity of the LIF signal is proportional to

$$I_{\mathrm{LIF}} \sim \left(\tau^{-1} + \sum_i n_i k_i \right)^{-1}, \qquad (2.7)$$

where $\tau = 748\,\mathrm{ns}$ is the natural lifetime of the excited state $\mathrm{OH(A, X)(1,0)}$ and k_i are the quenching rates coefficients of $\mathrm{OH(A, X)(1,0)}$ by species i of density n_i, which are two orders of magnitude higher for the molecular species O_2, N_2 and water (H_2O) than for Ar.

The density of ambient species evaluated by NDPM approximation and the respective LIF intensity computed using this density are shown in figure 2.3 c) and d). The expected density pattern reveals the triangle shape as an effect of the strong quenching of $OH(A, X)(1, 0)$ by molecular species. The NDPM evaluation also shows, that a LIF signal cannot be expected in regions where the ambient species density exceeds 1%. Comparing the laminar and turbulent LIF signals, this implies that the ambient air density at distances of a few mm can be locally lower in the turbulent case than in the laminar case (while the average density

Figure 2.3: LIF signal at a flowrate of 0.5 slm (a, laminar case) 3 slm (b, turbulent case), ambient species mole fraction (c) and LIF signal estimation calculated by NDPM (d). Adapted from [A2].

is much higher due to turbulent diffusion as outlined in the following section 2.2). The local density is lower in the turbulent case due to the increased velocity (which is obvious from equation (2.6)). By simultaneously monitoring the LIF signal and argon emission, it was shown in [A2] that the guided streamer follows the argon-air boundary in the turbulent flow. Hence, the ambient species density that the guided streamer is exposed to on the ns timescale in the turbulent flow must be higher than expected from NDPM (due to the deformation of the flow field by turbulent eddies), but lower than the average value obtained by Schlieren measurements and Reynolds-averaged CFD simulations described in the next section.

2.2   Diffusion in Turbulent Flows: Quantitative Schlieren Diagnostics (Article [A3])

Schlieren imaging is a classic technique for the visualization of gradients of the refractive index in fluid flows introduced by Toepler in 1864. Several textbooks give good introductions to the topic [70–73] and also discuss methods for the quantitative evaluation of Schlieren images. Previously, Schlieren imaging had been used for qualitative investigations (e.g. in studies of the plasma-flow interaction) [74–78] or quantitative investigations in hot jets [79] but not for density and temperature measurements of CAP jets. Special care needs to be taken as the changes in the refractive index caused by temperature variations in the plasma plume are of the same order of magnitude as the changes caused by argon and the surrounding air. In article [A3] it was shown that the effect of refraction by Ar can not only be corrected for, but it can be used to accurately calibrate the Schlieren system.
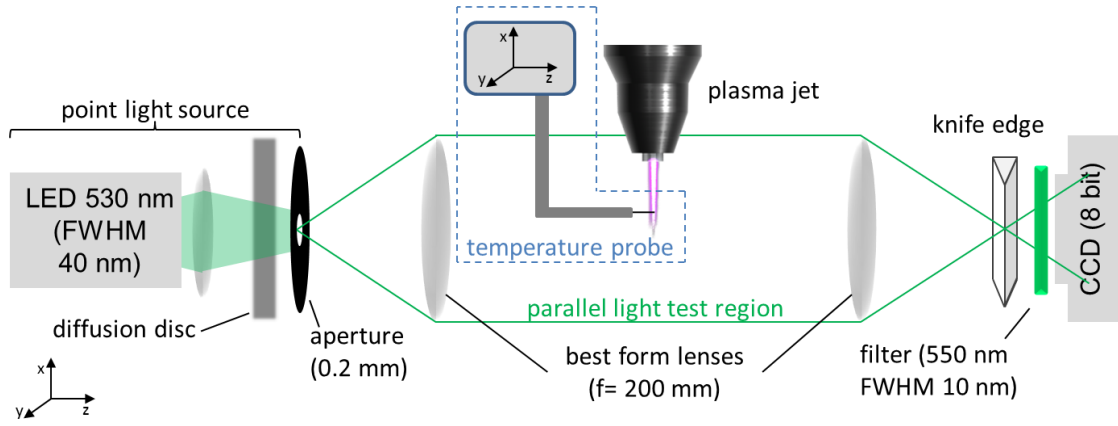
Figure 2.4: Experimental setup for Schlieren measurements. Reprinted from [A3].

In figure 2.4 the setup used in the measurements presented in [A3] is shown. A beam of parallel light is generated using an LED emitting at a wavelength of 530 nm (full width at half maximum, FWHM of 40 nm), diffusion disc and an aperture of 0.2 mm diameter which is placed in the focal point of a lens with 200 mm focal length. The beam of parallel light passes the test section and is subsequently collimated by a second lens. In the focal point of the second lens a knife edge is placed which reduces the total intensity on the behind charge-coupled device (CCD) detector by approximately 58%. A dielectric filter is placed in front of the CCD detector in order to prevent light emitted by the plasma jet itself from reaching the detector.

In order to determine an axisymmetric refractive index distribution $\eta(r)$ in the test region, two measurements need to be performed. Both the intensity I with Schlieren and second the intensity I_k without any Schlieren in the test region are measured and the resulting contrast $c = (I - I_k)/I_k$ is determined. Furthermore, the contrast $c_{\text{fl.}}$ measured with argon gas flow turned on and plasma turned off and $c_{\text{pl.}}$ need to be determined separately. Using the Gladstone-Dale relation and applying an inverse Abel transformation, it is shown in [A3] that the mole fractions of air and argon are linked to the contrast c by the relation

$$x_{\text{Ar}} = 1 - x_{\text{air}} = \frac{\hat{c}_{\text{fl.}}}{Sn(\eta_{\text{Ar}} - \eta_{\text{air}})} \text{ with } \hat{c}_{\text{j}} = \int_r^\infty \frac{c_j(y)dy}{\pi\sqrt{y^2 - r^2}}. \qquad (2.8)$$

Here S is the sensitivity of the Schlieren system and η_i are the indices of refraction of air and argon at the given pressure. Assuming that the mole fractions of air and argon are not significantly changed as the plasma is turned on, the temperature is determined as

$$T = T_0 \frac{\eta_{\text{air}} + \hat{c}_{\text{fl.}}/S - 1}{\eta_{\text{air}} + \hat{c}_{\text{pl.}}/S - 1}, \qquad (2.9)$$

where T_0 is the ambient room temperature.

A CFD simulation of the jet flow was performed using *Comsol Multiphysics* (Comsol AB, Sweden). The Navier-Stokes equations were solved with the convection-diffusion equation (2.1) and heat equation (2.2). In the heat equation (2.2) a heat

source was added, heating the gas inside of the capillary in order to mimic heating by the plasma. The thermal input power was varied until good agreement of CFD simulation and experimental results was obtained in the downstream region.

The results of both Schlieren measurements and CFD simulations are shown in figure 2.5. The evaluated argon mole fraction
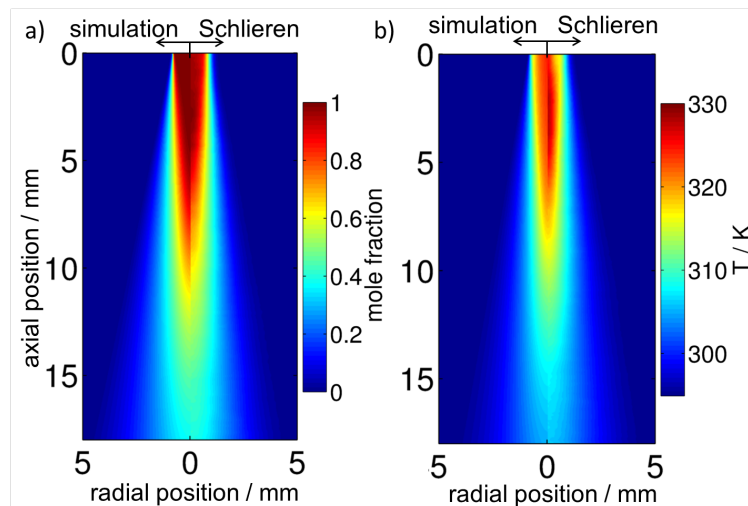

Figure 2.5: Argon mole fraction and temperature obtained from CFD simulation and Schlieren measurement. Reprinted from [A3].

agrees remarkably well with the CFD simulation result. In the direct vicinity of the nozzle the experimentally obtained density does not show an as sharp demarcation line as the CFD simulation, which presumably results from the limited resolution of the Schlieren system. The measured temperature also agrees well with the simulated values and additional probe measurements (which was unexpected as the probe was thought to influence the plasma through charging of the surface and/or polarization of the dielectric material). From the experiment it can be assumed, that while the majority of heat is deposited inside of the capillary, some heating in the plasma plume does occur. The good agreement in the far-field of the jet allows for an estimation of the calorimetric power of the plasma jet of 1.1 W.

2.3   Control of Ambient Species Diffusion: Shielding Gas Devices (Article [A4])

CAP jets for biomedical applications are commonly operated in open air. In jets operated with noble gases, most RONS are generated from ambient air that diffuses into the effluent of the plasma jet. However, the ambient air is subject to changes in the humidity level and may also change significantly if the jet is operated over surfaces, vessels or orifices of the body due to recirculation of Ar as shown in [A4]. While the effect of changes in the ambient humidity on RONS production is minor as shown in section 4.2 (contrary to the effect of humidity in the feed gas of CAP sources, which can strongly affect the RONS chemistry), it is still unknown what effect a recirculation has on the RONS production and the biological response, respectively. In order to achieve a better control over the reactive species output, a shielding gas device was designed using CFD simulations as shown in figure 2.6 a). The jet is placed inside of a shielding gas device made of glass. The shielding gas forms a gas curtain around the plasma plume, effectively shielding it from the environment. In figures 2.6 b) and c) the visible effect of using no shielding gas (b)

and oxygen as shielding gas (c) is shown. In the case of oxygen shielding gas the purple N_2 emission vanishes. The impact on the reactive species chemistry through using different shielding gas compositions is thoroughly investigated in chapter 4. Besides the viability studies on keratinocytes presented in [A4], the shielding gas device has been used in further biological studies on keratinocytes, immune cells and bacteria [20, 21, 56, 80]. Changing the composition of the shielding gas does not merely affect the local reactive species chemistry, but can also influence the fundamental processes leading of guided streamer propagation in the plasma plume, as investigated in the following chapter 3.
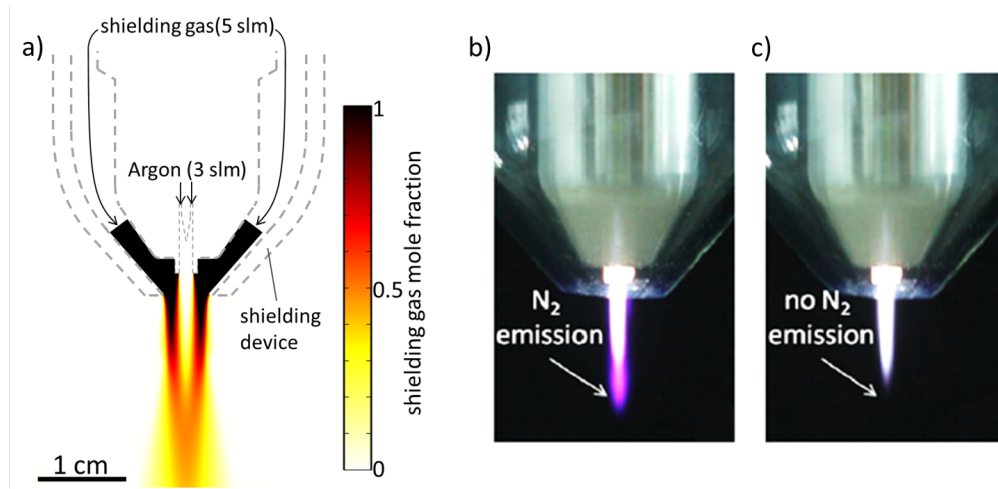
Figure 2.6: CFD simulation of the shielding gas flow (a) and photographs of the jet operating without shielding gas flow (b) and with oxygen shielding gas (c). CFD simulation result (a) adapted from [A6], images (b,c) reprinted from [A4].

2.4   Major Findings on Mass and Heat Transport

- NDPM is an entirely new analytical approach capable of estimating the diffusion of ambient species into laminar jet flows.

  - Comparison to CFD simulations of jet flows yielded good agreement, especially in the near-axis region close to the jet nozzle.

  - In case a simplified, e.g. a Poisseuille flow profile can be assumed, the NDPM approximation yields very simple expressions for the on-axis density.

- The NDPM approximation was applied for the evaluation of LIF measurements on OH. Through comparing measurements on laminar and turbulent jet flows, it was shown that along the path of the guided streamer the ambient species density is typically less than 1%.

- Quantitative Schlieren measurements can be used to determine the average ambient species density and temperature in argon-operated CAP jets.

  - As the gradient of the refractive index through mixing of argon and air is in the same order of magnitude as caused by the increase in temperature, the mixing needs to be accounted for in order to achieve accurate results with sub-Kelvin accuracy.

  - Through combining Schlieren measurement with CFD simulations including a virtual heating term accounting for the heating by the plasma, an estimation of the calorimetric power input by the plasma of 1.1 W was obtained.

- The lower bound of the ambient species density at the position of the streamer in the turbulent jet flow can be estimated by NDPM approximation, assuming molecular diffusion. The upper bound is given by the average density measured in Schlieren experiments.

- A shielding gas device was developed which can be used to control the gas the CAP jet is operating in.

Chapter 3

Influence of Ambient Gas Composition on Guided Streamer Propagation (Article [A5])

In [81] it was first reported that the kinpen features a strong temporal dynamics on the ns timescale. Similar emission phenomena had previously been observed in CAP jets operated with noble gases in the kHz regime and had been termed "plasma bullets" [82–86]: Localized emission phenomena, which propagate of speeds of tens to hundreds of km/s along the channel formed by the noble gas. These phenomena were investigated in several modeling studies and it was found, that the propagation mechanism is similar to that of streamers in air [87–91]. The fact that these streamers are guided by the noble gas channel was attributed to the lower electric fields that are required for the propagation in noble gases than in the surrounding air and memory effects such as preionization and accumulation of excited species from the preceding streamer.

For guided streamers propagating in dielectric tubes it has been found that surface charges that are generated in front of the streamer head promote the propagation of the ionization front by turning the electric field in propagation direction [92]. This especially leads to negative streamers propagating faster than positive streamers in tubes - a behavior that is adverse to what is observed for streamers in air, where diffusion of electrons significantly slows down the propagation of negative streamers [93].

Throughout all measurements presented in this and the following chapter, the kinpen has been used with the shielding gas device introduced in section 2.3 and a mixture of O_2 and N_2 was used at varying mixing ratios. Changing the ambient gas in which the CAP jet is working in can be expected not only to affect the local plasma chemistry, but also the propagation mechanisms of the guided steamers. In previous studies it was found that He operated CAP jets that produce a confined discharge when emanating into air produce rather broad and diffuse discharges when emanating into He [94, 95]. In article [A5] it was found that an important factor promoting the confinement and propagation of guided streamers within the channel of noble gas is the electronegativity of the surrounding gas.

3.1   Experimental Setup for Guided Streamer Investigation

Phase resolved optical emission spectroscopy is used in order to investigate the temporal dynamics of the plasma jet on the ns timescale. The experimental setup and gating sequence are shown in figure 3.1. A high-repetition rate gated intensified CCD (ICCD) camera (LaVision PicoStar HR12) was used for the imaging. The image intensifier consists of a photo cathode, multi channel plate (MCP) and phosphor screen. The *kinpen Sci* generates a trigger signal that is fed to the camera control unit. During each period of the plasma jet the control unit gates the MCP for 1 ns after a fixed phase locked delay with respect to the trigger signal. The gating signal and the voltage applied at the inner electrode of the jet are monitored on the oscilloscope allowing an assignment of the image with the phase of the jet. By varying the delay with respect to the trigger signal phase resolution is obtained. The exposure time of the CCD was adjusted for the light intensity and ranges from 20 ms to 800 ms. A 707 nm filter with a spectral FWHM of 9 nm was used for observing He emission (706.5 nm) or Ar emission (706.7 nm) and a 390 nm filter (FWHM 20 nm) was used for N_2 emission (first negative system, FNS and second positive system, SPS).
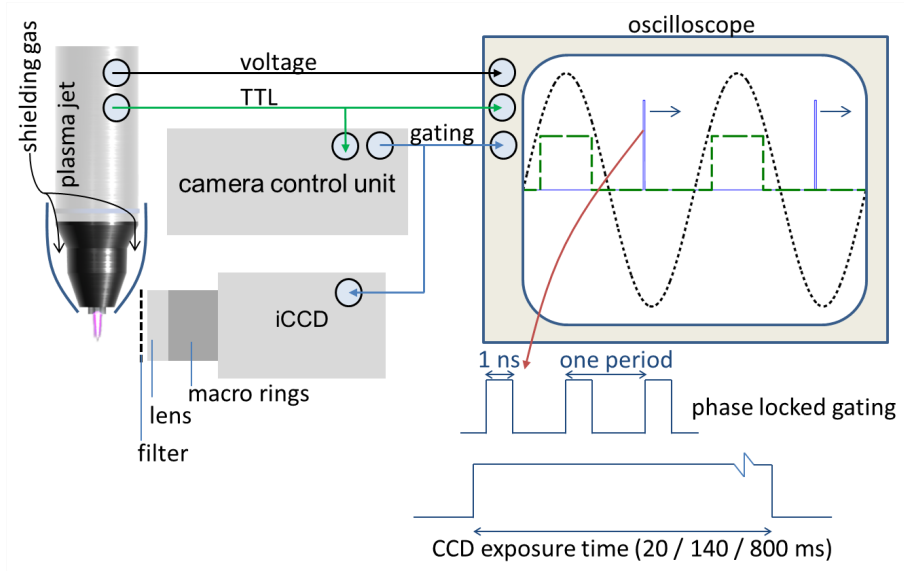
Figure 3.1: Schematics of the experimental setup and principle of the phase resolved optical emission measurements. In the sketch of the oscilloscope, the dotted black line represents the voltage signal, the dashed green line the trigger signal and the continuous blue line the gating signal for the MCP. Image and description of setup reprinted from [A5].

3.2 Electronegative Molecules Affect the Guided Streamer Propagation in a Helium-Operated Jet (Article [A5])

While for technical and biomedical applications operating the jet with Ar is more interesting due to its lower price and higher availability, performing optical diagnostics on the Ar-operated jet on the other hand is more challenging due to the statistical movement of the filament in the plasma plume. Therefore He was used as feed gas in the following fundamental investigations on guided streamer propagation.

In figure 3.2 the phase resolved emission of nitrogen and helium is shown using N_2, synthetic air (20%O_2, 80%N_2) and O_2 as shielding gas. A qualitative difference can be observed during the positive half-cycle (with positive voltage at the inner needle electrode) between the pure N_2 case and the cases with air or O_2 shielding gas. In the latter cases, an excitation wave travels against the flow direction from phase position 4 to 10 originating from the ambient towards the needle electrode, clearly visible in the short-lived He emission, while with N_2 shielding hardly any He emission occurs.

During the negative half-cycle shown in figure 3.2, also clear differences occur. With nitrogen shielding a strong N_2 emission occurs at the side of the nozzle between phase positions 20 and 24. This phenomena is not followed by significant increase of radiation in the downstream region, neither from N_2 nor from He. In case of air and O_2 shielding helium emission is observed between phase positions 18 and 24.
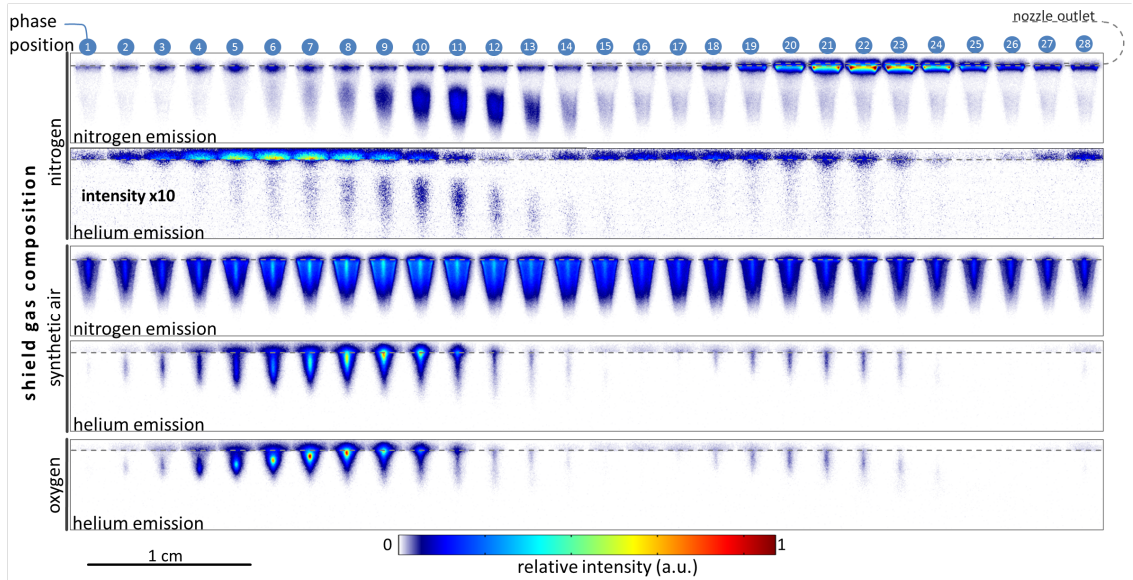
Figure 3.2: N_2 and He emission for different shielding gas compositions. Phase positions 1 to 14 show the emission during the positive, positions 15-28 during the negative half cycle. Note that the He emission intensity for the N_2 shielding case is multiplied by a factor ten compared to the He emission for the synthetic air and O_2 case. Adapted from [A5].

These observations led to the hypothesis, that in case of N_2 shielding, the ionization wave propagates radially outwards after leaving the nozzle during the negative half cycle, causing strong nitrogen emission at the side of the nozzle. This was further investigated by computer simulations by S. Norberg (University of Michigan at Ann Arbor, USA) using nonPDPsim, an electrohydrodynamics and fluid dynamics package developed by the group of Mark Kushner at University of Michigan at Ann Arbor [96, 97]. In order to obtain manageable computation times, a single negative pulse was simulated. Besides cases with O_2, air and N_2 shielding gas, a fourth case with a fictitious electronegative nitrogen eN_2 shiedling gas was studied. This eN_2 species inherited all reaction coefficients from N_2, but allowed for additional electron attachment reactions, inhereting the respective rate coefficients from O_2.

In figure 3.3 a snapshot of the simulation result is shown together with nitrogen emission at phase positions 22. If N_2 shielding gas is used, electrons tend to drift outwards towards the outer electrode. If O_2 shield gas is used, electrons that drift outwards attach, forming negative ions that have a low

Figure 3.3: Comparison of electron density obtained by simulation (left) and N_2 emission from PROES. Reprinted from [A5].

mobility compared to electrons. It was found that the electric field produced by these anions focuses electrons towards the axis of the jet.

In this sense, the negative ions produced by an electronegative shielding gas play a role similar to the charging of the dielectric by electrons for negative streamers propagating inside tubes. In these cases, the surface is charged in front of the streamer head and turns the electric field in parallel to the axis of the tube which reinforces the streamer propagation [92]. The second effect of the electronegative gas is the attachment process itself, which prevents ionization waves from propagating outwards in radial direction. In the N_2-shielded case these two confining mechanisms are absent. As O_2 and eN_2 shielding show the same behavior, it is clear that the observed dynamics is not an effect of other plasma chemistry, but of the electronegativity of the surrounding gas. This electrostatic focussing presumably also causes higher electron energies and hence effects the stronger He emission when O_2 is present in the shielding gas. The origin of the counter-propagating emission phenomena is not yet fully understood. One
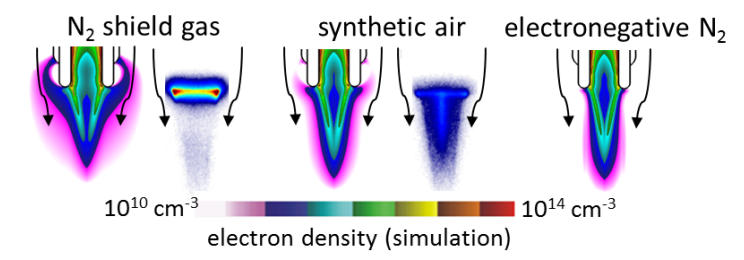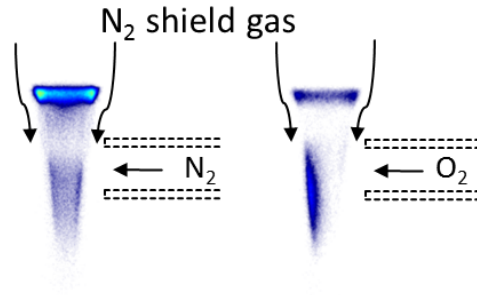

Figure 3.4: N_2 Emission (phase position 22) with additional crossflow. Note: Exposure time reduced by 85% in right image. Adapted from [A5].

hypothesis is, that the guided streamer during the negative half-cycle can deposit negative charge forming anions in the downstream region of the jet. This charge could then form a seed for a streamer propagating towards the anode during the consecutive positive half-cycle.

In a further experiment additional N_2 or O_2 was provided asymmetrically to the plasma plume using a pipet, while the jet is shielded with pure N_2. A low flux of 0.1 slm through the pipet was used. As shown in figure 3.4, the emission is not disturbed if N_2 is introduced through the pipet, but the discharge is pushed to the side opposing the pipet, if O_2 is introduced. This non-local effect strongly supports the hypothesis that anions formed from O_2 can guide and focus the guided streamer in the plasma plume.
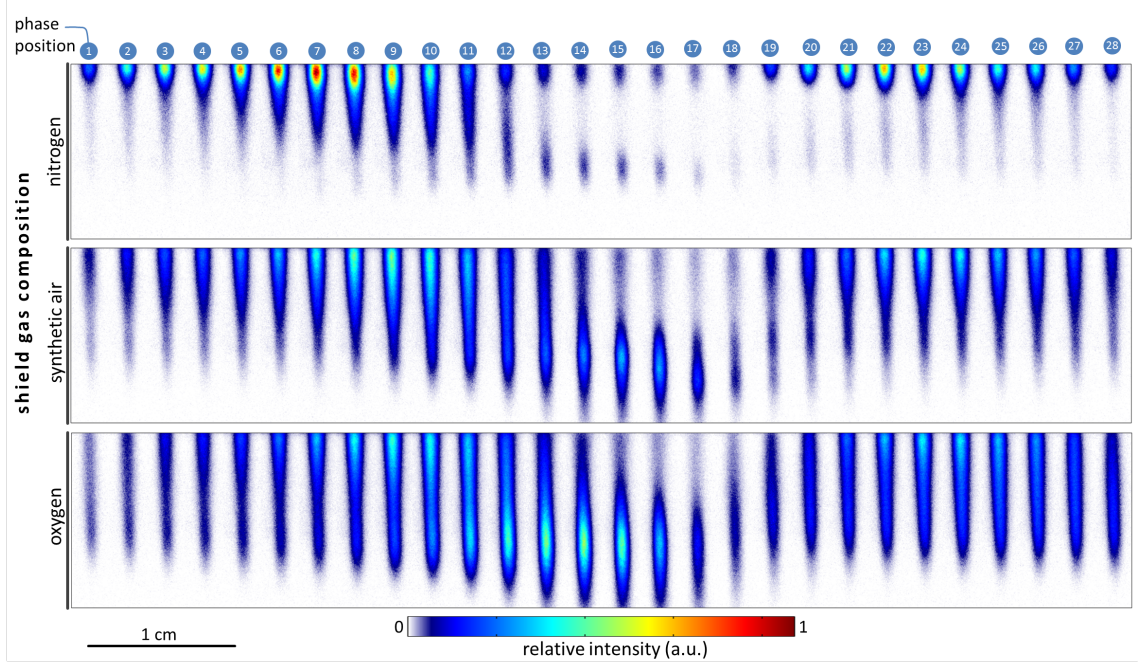
Figure 3.5: Ar emission for different shielding gas compositions. Phase positions 1 to 14 show the emission during the positive, positions 15-28 during the negative half-cycle.

3.3   Observations on an Argon-Operated Jet

Due to the turbulent flow and the filamented nature of the discharge when operating the jet with Ar, PROES measurements are smeared due to the averaging over many cycles. In figure 3.5 the phase resolved on-axis emission from Ar is shown using O_2, air and N_2 as shielding gas. As for the He-operated jet, the observed dynamics is hardly affected when oxygen is present in the shielding gas. A strong emission in the vicinity of the nozzle occurs during both the positive half-cycle at phase positions 3 to 10 and the negative half-cycle at phase positions 20 to 25 when pure N_2 is used as shielding gas, which is similar to the emission at the side of the nozzle observed in the He experiments. It is hence assumed that a similar electrostatic focusing effect as

observed in He also is responsible for the changes in the dynamics in the Ar-operated jet. However, further investigations are required to clarify these processes. The emission hardly changes when the O_2 content in the shielding gas is larger than 5%. Hence it is assumed that the excitation of Ar is largely independent of the shielding gas composition for these cases. Furthermore a temperature probe measurement was performed in the plasma plume at 8 mm axial distance. A constant gas temperature of 321.8 K was measured for O_2 content of 20% and higher. From 20% to 0% it dropped linearly to 320.3 K. Both PROES and temperature measurements hence imply that the energy deposited in the plasma plume is not significantly affected when O_2 is present in the shielding gas, and may drop mildly if no O_2 is present, which is an important result for plasma chemical modeling.

3.4   Major Findings on Guided Streamer Propagation

- An electrostatic focusing mechanism was discovered that affects the propagation of guided streamers in He-operated CAP jets operated in electronegative gases.

    - During the negative half-cycle of the jet, electrons tend to drift radially outwards in the plasma plume. In electronegative gases electrons attach in the He-air interface, forming a tube of comparably immobile anions.

    - This results in a negative space charge that contributes to confining the guided streamer in the He channel and promotes its propagation.

- During the positive half-cycle of the jet a counter-propagating emission phenomenon was observed which only occurs when the jet is shielded with O_2-containing gases. It is assumed, that this is caused by negative charge which is deposited in anions during the negative half-cycle and yields seed electrons for a cathode-directed streamer during the positive half-cycle.

- Measurements on the Ar-operated jet show similar trends, suggesting that the electrostatic focusing mechanism may also be responsible for the observed behavior in the Ar-operated jet. Due to the turbulent flow and filamented plasma the results are not as clear as is the case for the He-operated jet.

Chapter 4

Measurement, Modeling and Control of Plasma-Generated RONS (Articles [A6] and [A7])

A major goal of current research in plasma medicine is the identification and quantification of RONS that are generated by CAP sources. Naturally, a quantification of RONS directly in the plasma plume of the kinpen would be desirable. However, due to the filamentary nature of the discharge, the turbulent flow and the small absorption length in the plasma plume, this is difficult to achieve. Filamentation and turbulence also make numerical modeling difficult. While space resolved models of He CAP discharges can yield detailed information on the discharge development [87, 88, 90, 91, 98, 99], they are computationally demanding since the timescales of interest typically range from ns to ms and hence the number of species and reactions that can be taken into account is limited. An alternative approach is the reduction to zero-dimensional (volume averaged) models, which come with the advantage of fast computation times and the possibility of including thousands of reactions [39, 41, 49, 100]. However, such approaches are generally not self-consistent and hence need close correlation to experimental data. Recent approaches aim at reducing the computational cost for spatially resolved models by simulating only one cycle of a given CAP device, thereby obtaining the production rates of the RONS. These rates are then reused for the computation of the further development of the plasma chemistry [50, 101, 102]. However, even simplified space resolved models are out of reach for the turbulent and filamented CAP jet that has been investigated in this work.

Since the kinpen is commonly used with pure Ar feed gas, the quantification of RONS in this operation mode is the primary goal of the following studies. In articles [A6] and [A7] the RONS were quantified using FTIR spectroscopy in the far-field of the jet as described in section 4.1, where large absorption lengths can be realized by using a multi-pass cell. This naturally yields insufficient information on the RONS that can be expected within the plasma plume. In the present work, the plasma chemistry is therefore investigated by combining these measurements with zero-dimensional kinetic modeling approach. First, the local processes in the guided streamer are modeled using an electron impact reactions kinetic model, which is

closely correlated to densities of metastable argon (Ar^*, $Ar(1s^5)$ state) obtained by laser atom absorption spectroscopy (LAAS) measurements. A second plug-flow reaction kinetics model is then employed to investigate the formation of long-living RONS. The second model is validated by FTIR measurements in a parametric study, where the shielding gas composition is varied from pure N_2 to pure O_2.

4.1   Experimental Setup and Time-of-Flight Estimation

In figure 4.1 the setup used in the FTIR measurements is shown. The RONS density in the far field of the kinpen operated with Ar and with the shielding gas device was measured using an FTIR spectrometer (*Vertex 80v*, Bruker, USA). A multi pass cell (MPC) allowing for an absorption length of $L = 32\,\mathrm{m}$ was used in order to increase the sensitivity of the system. The CAP jet with the shielding gas device was mounted to a glass chamber with a volume of $0.5\,\mathrm{l}$.

The multi pass cell was either operated at a pressure of $100\,\mathrm{mbar}$ (measurements in article [A6]) or $600\,\mathrm{mbar}$ (article [A7]). While setting a low pressure in the MPC has the advantage that the reactions in the MPC are slowed down, the density of RONS and hence the sensitivity of the system decreases respectively.

As the RONS that are generated by the CAP jet continuously take part in further reactions while being transported from the glass chamber to the MPC and in the MPC itself, an estimation of the time-of-flight is essential. This was achieved by CFD simulations as shown in figure 4.1 b). At the inlet of the glass chamber where the CAP jet resides, a virtual tracer species was introduced with the flow for $10\,\mathrm{ms}$. At the glass chambers outlet to the MPC the mass flux of this tracer species was recorded, yielding the impulse response shown in figure 4.1 c). It was found, that while RONS can reach the MPC $0.1\,\mathrm{s}$ after they are generated by the CAP jet, many reside in the glass chamber for several seconds. In order to obtain quantitative results, cross sections σ_i of the respective species i at the given temperature and pressure are obtained from the HITRAN [103] and PNNL [104] databases. A fitting routine was developed, in which the densities n_i of all species i are used as fitting parameters so that the absorbance function

$$A(\{n_i\}) = -\ln\frac{I(\nu)}{I_0(\nu)} = \sum_i n_i\sigma_i(\nu)L \tag{4.1}$$

matches the experimental data. Here L is the absorption length, ν the wavenumber and I_0 the intensity measured when the plasma is turned off.

Electron Impact Plasma Reaction Kinetics Model

The plasma chemical processes that occur within the guided streamer are investigated with a zero-dimensional electron impact plasma reaction kinetics model. The rate balance equations are solved together with a local energy balance equation. In the model 51 electron impact, attachment and argon heavy particle reactions
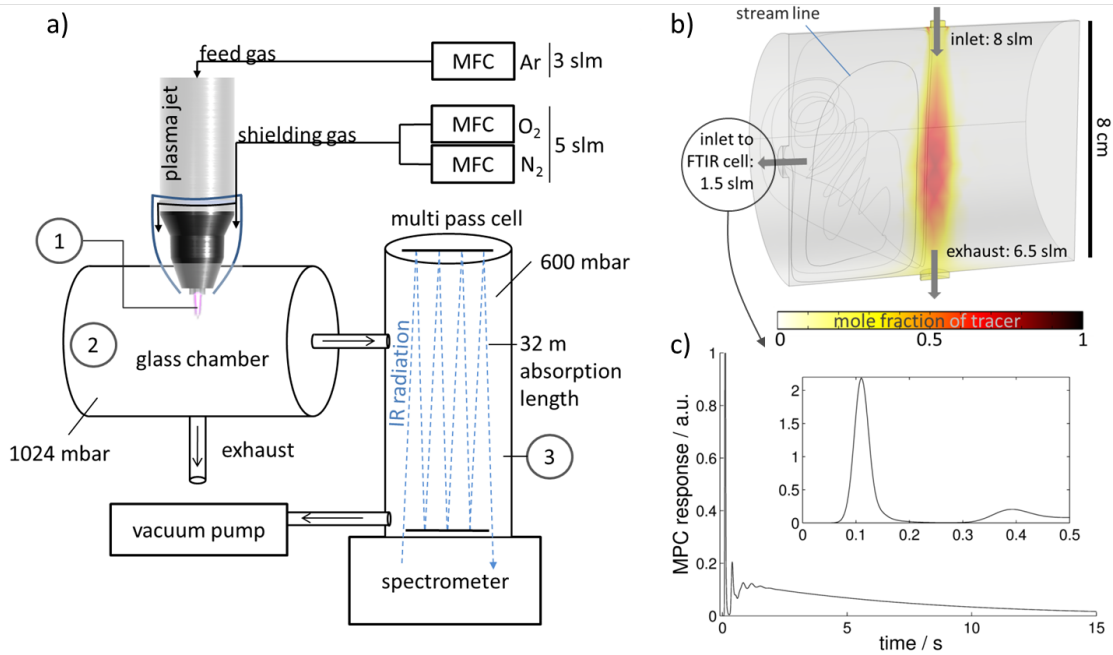
Figure 4.1: Schematics of the setup used in the FTIR measurements (a). The encircled labels 1 to 3 correspond to the simulation steps of the neutral species kinetic model. The residence time in the glass chamber was modeled by introducing a tracer species (b), yielding the impulse response shown in c). Adapted from [A6].

are considered. The density of $Ar(4s,^3P_2)$ in the guided streamer was measured by laser atom absorption spectroscopy by Dr. Jörn Winter (INP Greifswald) on the $Ar(1s_5-2p_9)$ optical transition at a wavelength of $811.53\,nm$ using an acousto-optic laser system (*EasyLAAS*, neoplas control GmbH, Germany). In the evaluation of these measurements the diameter of the filament was assumed to be $100\,\mu m$ based on single-shot ICCD measurements by Iseni et al. [105].

 The pulse width and input power P_{in} were used as free parameters used for fitting the modeled to the measured $Ar(4s,^3P_2)$ density as shown in figure 4.2. A maximum electron temperature of $T_e = 3.9\,eV$ and electron density of approximately $10^{12}cm^{-3}$ was obtained. As shown in figure 4.3 a), the measured $Ar(4s,^3P_2)$ state is the state with the highest abundance of all excited Ar states. The argon excimer Ar_2^* is formed at large quantities from excited Ar states and Ar_2^+ ions are generated from Ar^+ in three body collisions due to operation of the CAP jet at atmospheric pressure. In figure 4.3 b) the production rate of several primary RONS, defined as RONS that are generated directly from air species, are shown as computed from the electron impact model at different ambient air densities at the position of the streamer head. It is shown that most primary RONS are generated from reactions involving excited Ar species rather than through direct electron impact reactions. An exception are the $O_2(a)$ states, which carry a low energy of $0.98\,eV$ and hence have a minor effect on the generation of long-living RONS as studied in article [A6][1]. The dominant

---

[1] They are, however, important for the generation of O from O_3 in the downstream region of the jet [39]. As O largely reacts with O_2, again forming O_3, this hardly affects the far-field chemistry monitored in the FTIR experiments.
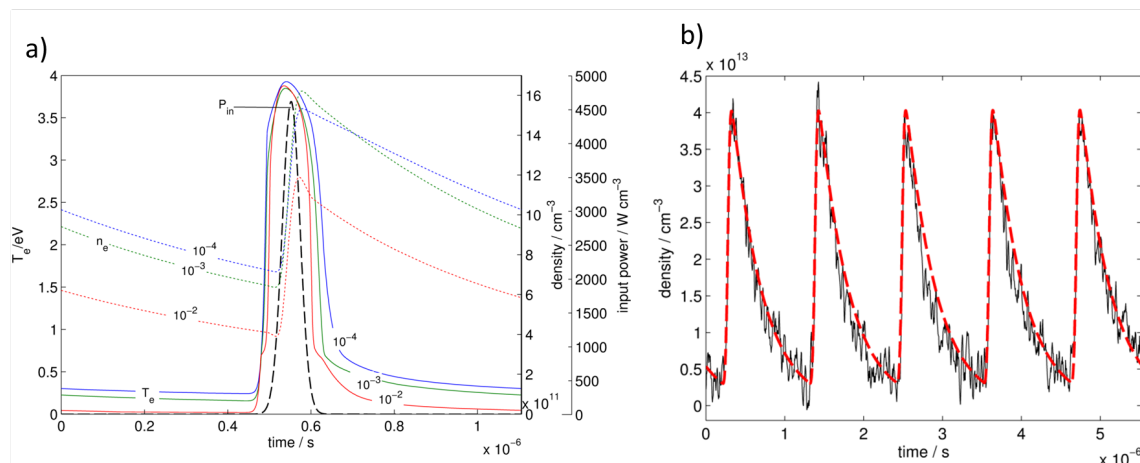
Figure 4.2: Input power and electron properties (a) at air mole fractions of 10^{-4} to 10^{-2} and fit of computed Ar* density to experimental data (b). Reprinted from [A7].

role of Ar* for the generation of primary RONS gives rise to the neutral reactive species reaction kinetics model presented in the following section.
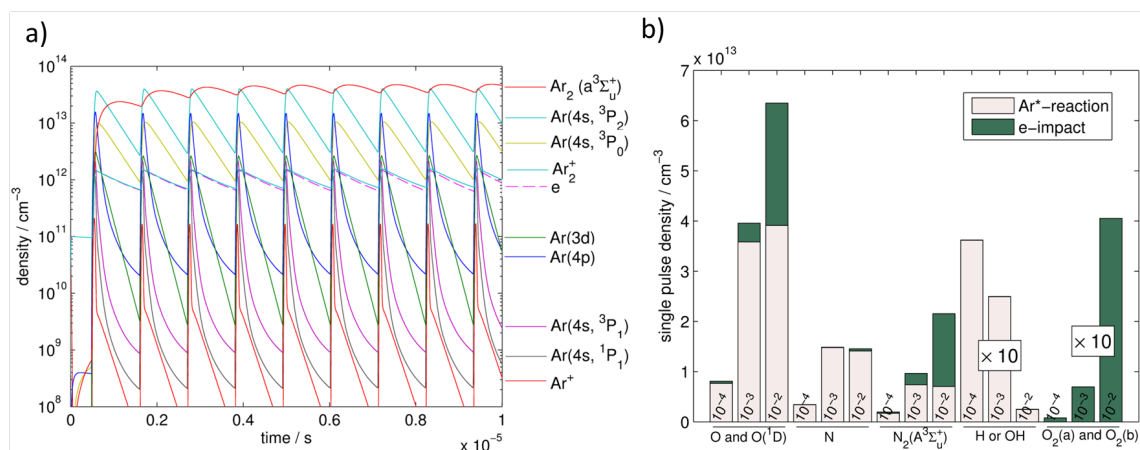

Figure 4.3: Densities of argon species computed by the model (a) and contributions to primary RONS production in reactions involving excited Ar species or electron impact reactions (b). Reprinted from [A7].

Neutral Reactive Species Reaction Kinetics Model

In the neutral reactive species kinetics model takes into account 22 species and 98 reactions listed in the appendix of article [A7]. In this zero-dimensional (volume averaged) plug flow approach, the local reaction kinetics is solved in a volume element co-moving with the flow. In this model no charged species are taken into account. Based on the findings from the electron impact model, an additional pulsed Ar* source term is used as sole energy input in this second model, as excited Ar species were found to be the dominant source of primary RONS. The magnitude of this

source term is a fitting parameter in the model, but the same magnitude is used regardless of the shielding gas composition (consistent with the PROES measurements presented in chapter 3). The simulation is subdivided into three steps corresponding to the conditions in the experimental setup. The simulation steps successively model the reaction kinetics in the effluent, the glass chamber and the MPC as illustrated in figure 4.4 a).
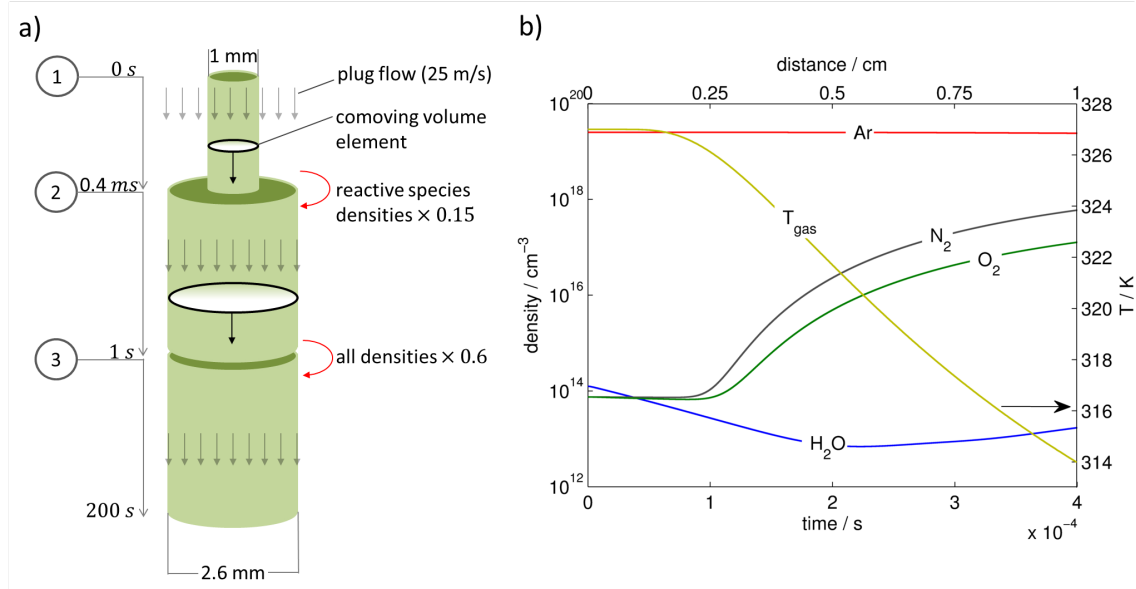
Figure 4.4: Scheme of the the simulation steps in the neutral species reactions kinetics model (a) and ambient air density and temperature assumed in the plasma plume (b). Figure and description of the model steps adapted from [A7].

Step 1: Plasma Plume (0 to $0.4\,\mathrm{ms}$)

The diameter of the co-moving volume element is chosen to be 1 mm in the plasma plume, which roughly corresponds to the diameter of the visible plume. This value is larger than the diameter of the guided streamer (estimated around 100 μm). The model can hence only yield densities averaged over the volume element, while the actual local densities may be higher or lower (due to diffusion). In the plasma plume region a periodic Ar^* source term was introduced. In figure 4.4 b) the assumed density of N_2 and O_2 diffusing into the effluent of the jet, the feed gas Ar and H_2O originating from impurities in the gas bottles and/or tubing is shown. The temperature profile was adapted to match the results obtained in the Schlieren measurements discussed in section 2.2. The density of ambient species was estimated using the NDPM approximation (equation 2.6). An intermediate diffusion coefficient based on literature values for laminar diffusion and computed turbulent diffusion coefficient (as obtained from the Schlieren measurements and respective CFD simulations) was chosen.

Step 2: Glass Chamber ($0.4\,\text{ms}$ **to** $1\,\text{s}$)

As the argon jet will rapidly mix with the shielding gas, an instant dilution of all reactive species in the glass chamber is assumed. This corresponds to an expansion of the volume element from 1 mm to 2.6 mm diameter (which at an average velocity of $25\,\text{m/s}$ yields a mass flow of $8\,\text{slm}$) and a dilution of the species by a factor 0.15. Based on CFD simulations shown in figure 4.1 an average residence time of $1\,\text{s}$ is assumed.

Step 3: Multi Pass Cell (1 **to** $120\,\text{s}$)

In the MPC the pressure is reduced to $600\,\text{mbar}$ and hence all species are diluted by a factor 0.6. As the reactive species are continuously measured while residing in the MPC, the densities computed by the model are averaged over the interval from $t = 1\,\text{s}$ to $t_{\max} = 120\,\text{s}$ corresponding to the estimated residence time.
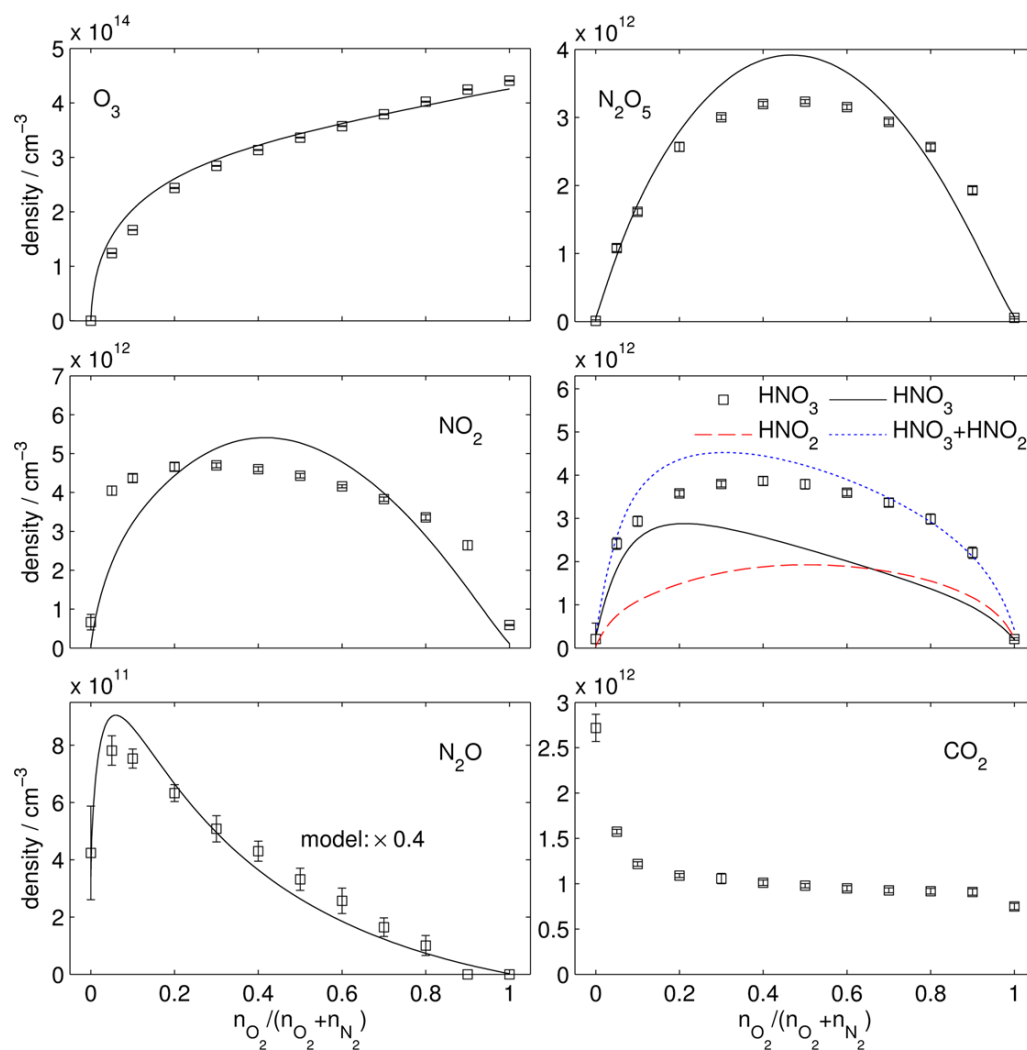
Figure 4.5: Density of RONS as obtained by FTIR measurements and the neutral reactive species reaction kinetics model. Reprinted from [A7].

4.2 The Influence of the Ambient on the Reactive Species Production

In figure 4.5 the densities of O_3, N_2O_5, NO_2, nitric acid (HNO_3), N_2O and carbon dioxide (CO_2) obtained from FTIR measurements and reaction kinetics model are shown when the shielding gas composition is varied from pure N_2 to pure O_2. In the model the O_3 density was fitted to the experimental data by varying the magnitude of the Ar^* source term (performed once for all simulation runs). The dynamics of O_3, N_2O_5, NO_2 and N_2O was predicted correctly by the model. The model also predicts nitrous acid (HNO_2) which was not detected. However, the predicted

Figure 4.6: Dynamics of O_3 and NO_2 densities upon variation of humidity in the shielding gas. Reprinted from [A6].

HNO_2 and HNO_3 values sum up to the measured value of HNO_3, possibly indicating that a conversion from HNO_2 to HNO_3 takes place that is not included in the model. The measured CO_2 presumably results from impurities (e.g. carbon monoxide, CO) in the feed gas. Based on this data, the RONS densities resulting from a therapeutic application can be assumed to be well below the maximum allowed workplace concentrations[2]. For the produced nitrogen oxides, the permissible exposure limits are of no concern due to the low densities of the respective species.

Figure 4.7: Simplified overview of reactions mechanisms leading to the formation of long-lived RONS.

---

[2]E.g. for the most abundant species O_3, the *kinpen 09* (with air as shielding gas) could be operated continuously for more than one hour in a $50\,\mathrm{m}^3$ room, assuming that all generated O_3 is accumulated (no ventilation and no destruction of O_3), before the permissible exposure limit of $0.1\,\mathrm{ppm}$ according to the *National Institute for Occupational Safety and Health* is reached [106]. Also note that the *kinpen Med* employed for therapeutic applications can be expected to produce significantly less O_3 due to its 50% duty cycle.
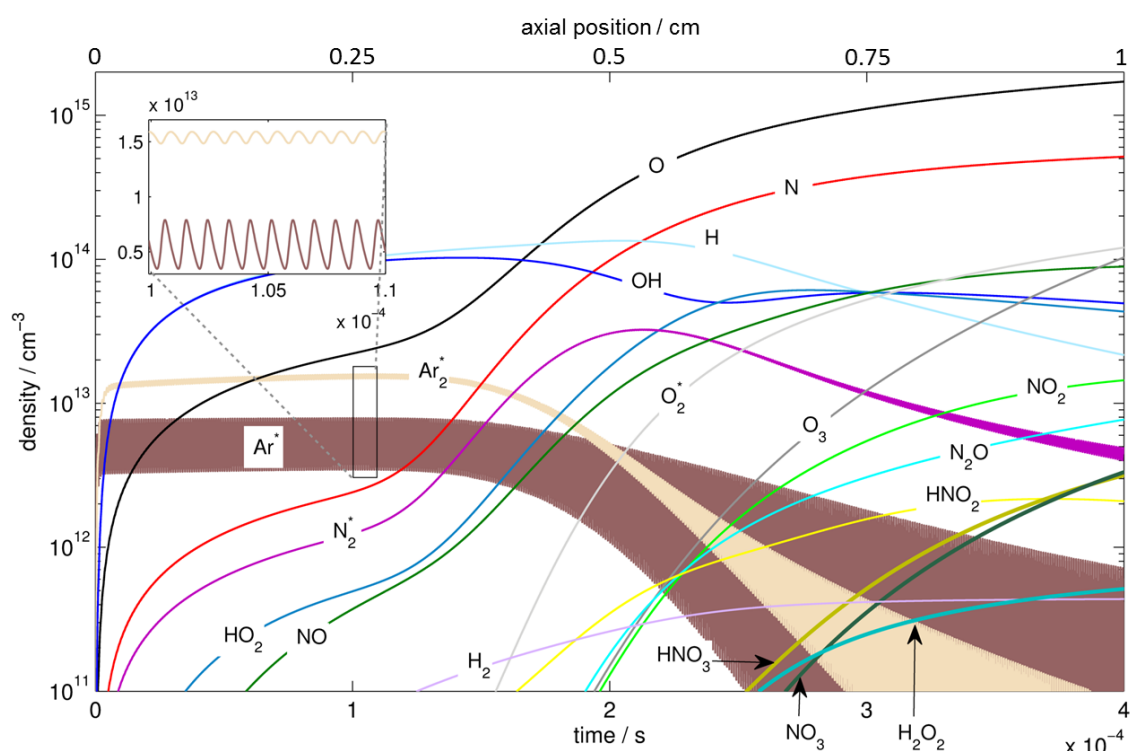
Figure 4.8: Temporal development of RONS densities in the plasma plume. Reprinted from [A7].

The model allows for a detailed analysis of the reaction pathways leading to the net production of these measured species. While a detailed analysis of the pathways can be found in article [A7], figure 4.7 gives a very simplified summary of relevant processes. The model also allows for an estimation of reactive species that can be expected in the plasma plume.

In figure 4.8 the species development in the plasma plume is shown as computed by the model for synthetic air shielding. Note, that most of the species detected in the FTIR can only be expected in comparably low quantities in the plasma plume (e.g. O_3 or N_2O_5), while their chemical predecessors (e.g. O, NO) reach high densities in the plasma plume but have too short lifetimes to be measurable in the MPC.

CAP devices that are operated in open air are exposed to varying atmospheric humidity. If the level of humidity is changed in the feed gas of CAP devices, this can heavily affect the reactive species output. In case of the argon-operated CAP jet, the influence of changes in the ambient humidity result from air diffusing into the jet. The effect on O_3 and NO_2 produced by the jet was investigated by varying the humidity of synthetic air used as shielding gas and is shown in figure 4.6.

While the net production of NO_2 is hardly affected, the amount of O_3 produced significantly drops with increasing humidity. The main reason for this is that the production of O from reactions of O_2 with Ar^*, Ar_2^* or metastable nitrogen ($N_2(A)$) is reduced as the rate coefficients for these species reacting with H_2O is significantly higher than for dissociating H_2O. However, as in Germany the relative atmospheric

humidity typically varies between 40% and 100%, its relevance for practical appli-
cations can be expected to be minor for argon-operated CAP jets, whereas a large
influence on RONS generation and biological response to plasma treatment was
found if the feed gas humidity is changed, e.g. the viability of human skin cells is
strongly affected by the feed gas humidity [107, 108].
Varying the shielding gas composition is useful for verifying the reaction kinetics
model and hence unraveling the complex reaction networks, but also for tailoring
the RONS output towards a specific application. This can be achieved most suc-
cessfully when both shielding gas and feed gas admixtures are employed as shown
in the following section.

4.3   Selective Reactive Species Generation

Adding molecular admixtures to the feed gas is an effective way to increase the
RONS output of CAP jets. In the previous measurements this option was not
chosen in order to work on a system that is as close as possible to the numerous
biological investigations performed with the CAP jet *kinpen 09* which were mostly
conducted without admixtures. However, based on the findings on reactive species
generation, a novel method is proposed that for the first time at all allows for a
continuous switching between an O/O_3 to an NO_x dominated plasma chemistry in a
CAP jet. Therefore, both the shielding gas composition and the feed gas admixture
are controlled. In figure 4.9 the dynamics of O_3 and NO densities are shown when
the composition of the feed gas admixture (amounting to 1% of the feed gas flux) is
varied from pure N_2 to pure O_2. The feed gas is either dry or humidified by bubbling
the molecular admixture through water (yielding a feed gas humidity of 320 ppm
measured with a chilled mirror dew point hygrometer DewMaster, EdgeTech, USA)
and as shielding gas N_2 is used. Humidifying the feed gas inhibits the production of
O/O_3 as the quenching of Ar^* by H_2O forming OH and H is faster than the reaction
of Ar^* with O_2 and at the same time the generation of NO through the reaction of
N with OH is increased. This means that the plasma jet can be operated in different
modes that reproduce a similar chemistry as the CAP devices presented in section
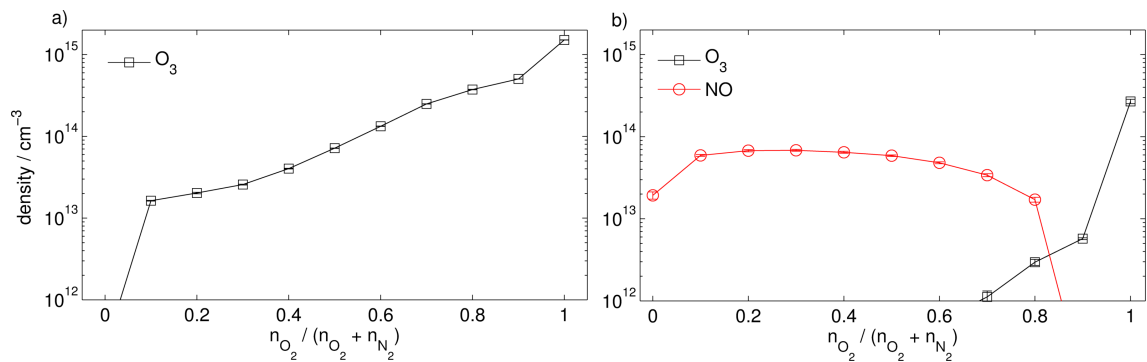1.2.

Figure 4.9: O_3 and NO densities measured via FTIR spectroscopy for with dry (a)
and humid (b) feed gas with varying admixture composition in 10% steps. The
shielding gas is N_2. Data points not shown are below detection limit.

O-Dominated Treatment

When operated without shielding gas device and with or without molecular feed gas admixture, the kinpen produces a plasma chemistry where short-lived species - dominantly O - are present at high densities at typical treatment distances of 1 cm (see figure 4.8).

O_3-Dominated Treatment

At larger treatment distances of a few cm but with previous device operating parameters, dominantly O_3 and further rather long-living RONS are present as observed in the FTIR far-field measurements (see figure 4.8). In this sense the chemistry is similar to what is typically observed in DBDs operating in air.

NO_x-Dominated Treatment

An NO_x dominated plasma chemistry typical for high power sources (e.g. observed in plasma torches or DBDs in high power mode) can be achieved by using N_2 as shielding gas and employing a lightly humidified molecular feed gas admixture as described above (see figure 4.3).

OH-Dominated Treatment

In order to achieve the previous NO_x dominated chemistry, the feed gas humidity must be kept at a significant (in the order of hundreds of ppm) but still low (e.g. lower than 2000 ppm), as otherwise almost exclusively water-related species (especially OH, HO_2 and hydrogen peroxide (H_2O_2) can be expected, while all densities of other RONS are diminished [108]. At high water concentrations, H_2O_2 is the only reactive species detectable in the far-field of the jet [107, 108].

The treatment options described above can easily be understood by retracing the pathways in the simplified reaction scheme shown in figure 4.7 considering Le Châtelier's principle of dynamic equilibrium[3]. It is noted that the proposed treatment options with lightly humidified feed gas (shown in figure 4.9 b) also have a practical advantage. Winter et al. [109] have shown that it can take a few minutes to some hours (depending on used tubing materials) until dry feed gas conditions can be reached due to diffusion of humidity through walls of the tubing of CAP sources. A feed gas humidity in the order of hundreds of ppm can be reached in a reproducible manner and presumably fast enough for practical applications in the doctor's office.

---

[3]This is of course a drastic simplification as the CAP jet chemistry is *not* an equilibrium system and in reality thousands of reactions are involved. In most cases it is not possible to make sound predictions concerning CAP chemistry on such oversimplified considerations due to the complex electron and ion dynamics involved.

4.4 Major Findings on RONS Measurement, Modeling and Control

- The production of O_3, NO_2, N_2O, N_2O_5 and HNO_3 by the argon-operated kinpen with shielding gas device can be controlled effectively by varying the shielding gas composition from pure N_2 to pure O_2.

- CFD simulations revealed that the time-of-flight of particles in the FTIR spectroscopy setup (before they reach the absorption measurement cell) varies from $\sim 0.1\,\text{s}$ to several seconds.

- An electron impact reaction kinetics model was established in order to simulate the local plasma chemical processes in the streamer. The input power assumed in the model was adjusted to obtain an agreement of the predicted $Ar(1s^5)$ densities with densities obtained from LAAS measurements.

  - The model showed that in the streamer most primary RONS are not generated directly by electron impact reactions, but via reactions of excited Ar species with air species.

  - The model yielded peak electron temperatures of $3.9\,\text{eV}$ and electron densities in the order of $10^{12}\,\text{cm}^{-3}$.

- Based on the findings from the electron impact model, a neutral reactive species reaction kinetics plug-flow model was implemented which uses an Ar^* source term as sole energy input.

  - The ambient species density and temperature in the plasma plume were estimated based on the previous Schlieren and NDPM investigations.

  - The PROES measurements suggest that the Ar^* source term can be assumed independent of shielding gas composition (at least for O_2 shielding gas content greater than 5%).

  - The model is subdivided into three steps, accounting for the plasma plume, the near-field and the multi-bass cell of the FTIR-spectrometer. It yields excellent agreement with the measured RONS densities.

  - Detailed information on reaction networks and RONS that can be expected in the plasma plume is provided by the model.

- Through varying the humidity level in the shielding gas of the jet, it was found that while variations in the atmospheric humidity do affect the generation of RONS by the CAP jet, the effect is small at typical relative humidity ranging from 40% to 100%.

- Choosing appropriate humidified feed-gas admixtures and shielding gas compositions, the plasma chemistry can be controlled from being O/O_3-dominated to being NO_x-dominated. Therefore, the humidity must be kept low, as otherwise water-related species (OH, HO_2, H_2O_2) dominate the chemistry.

Chapter 5

Summary

In this work the mechanisms leading to the generation of the various reactive oxygen and nitrogen species (RONS) in a cold atmospheric plasma (CAP) jet and means to control their composition were studied. The investigated CAP jet kinpen is typically operated with Ar feed gas (pure or with molecular admixtures), driven at a frequency of approximately $1\,\text{MHz}$ and features fast ionization waves or guided streamers, traveling at velocities of several km/s. The complex reaction networks were investigated by numerical and experimental techniques.

Detailed experimental, analytical and computational investigations on the mass and heat transport in the plasma plume were performed: A novel analytical approach to diffusion in jet flows, the non-dispersive path mapping approximation (NDPM) was developed. The method for the first time allows for an estimation of the ambient species density in the near-field of jets that feature a non-homogeneous flow-field. The NDPM approximation was employed for the evaluation of laser induced fluorescence measurements on OH. Through combining measurements and NDPM approximation, this approach yielded an estimation for the ambient species density at the position of the guided streamers, not only in the laminar, but also in the (standard) turbulent operating regime. Accurate measurements of the temporally averaged ambient species density and temperature in the plasma plume were obtained by quantitative Schlieren measurements. The method yields temperature values with sub-Kelvin accuracy and, through combination with CFD simulations, allowed for an estimation of the calorimetric power of the jet. In order to obtain a defined environment for the jet to operate in, a shielding gas device was designed in this work, which creates a gas curtain of defined composition around the plasma plume.

The plasma dynamics on the ns timescale was investigated by phase resolved optical measurements. The effect of different shielding compositions ranging from pure N_2 to pure O_2 on guided streamer propagation was investigated. An electrostatic focusing mechanisms was discovered, which promotes the propagation of guided streamers along the channels formed by a noble gas in the plume of plasma jets operating in electronegative gases (such as air or O_2).

Two zero-dimensional (volume averaged) models were developed: First, the local processes in the guided streamer were modeled using an electron impact reaction kinetic model, which is closely correlated to densities of metastable argon (Ar^*) ob-

tained by laser atom absorption measurements. This first model shows that Ar* is the species which dominantly drives the plasma chemistry in the plasma plume. This is exploited in the second plug-flow reaction kinetics model, which is employed to investigate the formation of long-living RONS and uses an Ar* source term as sole energy input. The model uses the previous experimental data on mass and heat transport and temporal dynamics as input and is in turn verified by quantitative FTIR absorption measurements on O_3, NO_2, N_2O, HNO_3 and N_2O_5 in the far-field of the jet, where large absorption lengths can be achieved using a multi pass cell. For the evaluation of the zero-dimensional model, the time-of-flight of RONS from their generation to reaching the multi pass cell was determined using CFD simulations.

The insight gained through this combined experimental-modeling approach on the reaction networks revealed relevant control parameters and enabled adjusting the plasma chemistry towards a desired RONS output. Through choosing appropriate feed-gas admixtures and shielding gas compositions, it is possible to generate an NO_x-dominated plasma chemistry, although the jet usually produces a strongly O/O_3-dominated chemistry.

Understanding and controlling the plasma chemistry of cold atmospheric plasma sources for medical applications is not only essential for research, but is also the key for designing future plasma sources for specific medical applications that yield an optimum efficacy and avoid potential side effects of plasma treatment.

Chapter 6

Outlook - The Findinigs in the Context of Plasma-Medical Research and its Potential for Clinical Application

The application of shielding gas devices for controlling the reactive species output of CAP jets is an effective method that can easily be integrated into existing experimental setups or medical CAP sources. In article [A5], the kinpen was employed with shielding gas device for the treatment of keratinocytes and a correlation of viability with O_2 content in the shiedling gas was observed. Barton (PhD dissertation, Ernst-Moritz-Arndt-Universität Greifswald, 2014) used the same setup and found that the cytotoxicity of keratinocytes correlated to the O_2 content in the shielding gas [20]. Furthermore the up-regulation of several cytokines

Figure 6.1: Densities of OH, HO_2 and H_2O_2 above the liquid surface obtained by modeling and measurements of H_2O_2 in the liquid phase. First presented at [110].

and growth factors was significantly affected by the shielding gas composition. Jablonowski and Hänsch et al. [56] employed the shielding gas variation for the inactivation of bacteria (Escherichia coli) and found that through choosing appropriate shielding gas composition an optimum can be found at which Escherichia coli can be inactivated effectively while the cytotoxicity for human keratinocytes is minimized .

While aforementioned studies employed the shielding gas device without further admixtures, the novel approach introduced in section 4.3 allows for entirely switching from an O / O_3 to an NO / NO_x dominated plasma chemistry, enlarging the available parameter space. This will be useful in further plasma medical research

and may eventually be employed in an optimized plasma treatment targeting the inactivation of harmful bacteria and at the same time preserving human cells.

For such optimization a detailed understanding of the plasma chemistry, but also of the transfer of RONS to liquids is necessary. The zero-dimensional plug-flow approach presented in this work provides some insight into the plasma-liquid interaction. In figure 6.1 the densities of OH, HO_2 and H_2O_2 as computed by the model in the gas phase above a liquid are compared to H_2O_2 measurements in $5\,ml$ sodium chloride solution from [111]. In the model an increase of humidity above the surface of the liquid was assumed. The species densities were evaluated after $4 \times 10^{-4}\,s$ corresponding to the time-of-flight to the liquid surface. A correlation between the computed OH density and the measured H_2O_2 density in the liquid was found. The significant increase of OH at 0% O_2 content in the shielding gas results from the absence of HO_2, which is only formed from H when O_2 is present and partly destroys OH in the plasma plume. Recent LAAS measurements on $Ar(4s,^3P_2)$ by Jörn Winter showed, that the $Ar(4s,^3P_2)$ density in the plasma plume does not change much if the jet is operated over liquids (data not published yet). Therefore, the here-presented gas phase reaction kinetics model could be extended to this case and a coupling to a further liquid reaction kinetics model could be achieved in future work. This would yield further insight into the processes that are relevant for biomedical applications of CAP sources.

Original Publications

This thesis is based on the following peer-reviewed articles published in international scientific journals. The authors' contributions to the publications are briefly summarized below.

Article A1

> A. Schmidt-Bleker, S. Reuter and K.-D. Weltmann. Non-dispersive path mapping approximation for the analysis of ambient species diffusion in laminar jets. *Physics of Fluids* 26(8): 083603, 2014.
> The method was developed by ASB. The analytical and numerical calculations were conducted by ASB. The manuscript was written by ASB and edited by all co-authors.

Article A2

> S. Iseni, A. Schmidt-Bleker, J. Winter, K.-D. Weltmann and S. Reuter. Atmospheric pressure streamer follows the turbulent argon air boundary in a MHz argon plasma jet investigated by OH-tracer PLIF spectroscopy. *Journal of Physics D: Applied Physics* 47(15): 152001, 2014.
> The experiment was designed and measurements were conducted by SI. The estimation of ambient species densities and respective LIF signal with NDPM approximation was done by ASB. The manuscript was written by SI with contributions by ASB and SR and edited by all co-authors.

Article A3

> A. Schmidt-Bleker, S. Reuter and K. D. Weltmann. Quantitative schlieren diagnostics for the determination of ambient species density, gas temperature and calorimetric power of cold atmospheric plasma jets. *Journal of Physics D: Applied Physics* 48(17): 175202, 2015.
> The measurements and the data evaluation was performed by ASB. The manuscript was written by ASB and edited by all co-authors.

Article A4

> S. Reuter, H. Tresp, K. Wende, M.U. Hammer, K. Masur, A. Schmidt-Bleker and K.-D. Weltmann. From RONS to ROS: tailoring plasma jet treatment of skin cells. *IEEE Transactions on Plasma Science* 40(11): 2986-2993, 2012.
> The design of shielding gas device and CFD simulations were conducted by ASB. The measurement of reactive species in liquids was performed by HT. OES measurements were carried out by JW. The cell viability measurements

were conducted by KW. The manuscript was written by SR with contributions from HT, KW, JW and ASB and edited by all co-authors.

Article A5

A. Schmidt-Bleker, S. A. Norberg, J. Winter, S. Reuter, K.-D. Weltmann and M. J. Kushner. Propagation mechanisms of guided streamers in plasma jets: the influence of electronegativity of the surrounding gas. *Plasma Sources Science and Technology* 24(3): 035022, 2015.

The PROES measurements were conducted by ASB, the OES measurements by JW. The numerical simulations were performed by SAN. The manuscript was written by ASB and SAN and edited by all co-authors.

Article A6

A. Schmidt-Bleker, J. Winter, S. Iseni, M. Dünnbier, K.-D. Weltmann and S. Reuter Reactive species output of a plasma jet with a shielding gas device - combination of FTIR absorption spectroscopy and gas phase modeling. *Journal of Physics D: Applied Physics* 47(14): 145201, 2014.

The FTIR measurements were conducted by JW and ASB. The reaction kinetics model was developed by ASB. The manuscript was written by ASB and JW and edited by all co-authors.

Article A7

A. Schmidt-Bleker, J. Winter, A. Bösel, S. Reuter, and K.-D. Weltmann. On the plasma chemistry of a cold atmospheric argon plasma jet with shielding gas device. *Plasma Sources Science and Technology* 25(1): 015005, 2016.

The FTIR measurements and reaction kinetics modeling was conducted ASB. The LAAS measurements were performed by JW. The LAAS system was set up by AB. The manuscript was written by ASB with contributions from JW and edited by all co-authors.

Approved:

_____   _____
Date   Ansgar Schmidt-Bleker

_____   _____
Date   Prof. Dr. Klaus-Dieter Weltmann

Article A1

50

Non-dispersive path mapping approximation for the analysis of ambient species diffusion in laminar jets

Ansgar Schmidt-Bleker,[a] Stephan Reuter, and Klaus-Dieter Weltmann
INP Greifswald e.V. / ZIK Plasmatis, Felix-Hausdorff-Str. 2, 17489 Greifswald, Germany

The present work for the first time presents an analytical approximation capable of describing the diffusion of surrounding species into laminar fluid jets in the near-field with a known (but arbitrary) velocity field. The diffusive transport of ambient air into fluid jets is studied analytically and numerically on the basis of a convection-diffusion equation with a predefined velocity field and diffusion coefficient. It is shown that the majority of particles entering a jet flow in an artificial uniform velocity field can only reach the axis in the near-field following narrow straight paths. This is exploited in the here-proposed non-dispersive path mapping approximation, where these paths and the underlying solution for the uniform velocity field are mapped according to the flow field. Dispersion is assumed to be negligible for every single path if the velocity profile does not vary significantly over the width of the path. The resulting formula for the on-axis density can easily be evaluated using a pocket calculator. The analytical model is compared to numerical studies of diffusion in jet flows with different geometries and shows good agreement. © *2014 AIP Publishing LLC*. [http://dx.doi.org/10.1063/1.4893573]

I. INTRODUCTION

Mixing in laminar jets is relevant in various technical applications, including diffusion flames and atmospheric pressure plasma jets.[1–3] Many approaches for studying these processes analytically use uniform flow fields or focus on far field solutions and will be presented briefly in the next paragraph. The present work for the first time proposes an analytical approximation capable of describing the diffusion of surrounding species into laminar fluid jets in the near-field with a known and non-uniform flow field. The approach allows considering diffusion in shear flows by mapping the exact solution for the density for a uniform flow field case to account for a non-uniform flow field. This so-termed non-dispersive path mapping (NDPM) method gives an approximation for the diffusion of ambient species near the jet nozzle. The advantage of the NDPM method is that it yields a simple-to-use formula for every day lab work, allowing an estimation of the effect of changes in experimental parameters such as the average velocity or nozzle diameter for a given setup on the ambient species densities. In this work, plane and axisymmetric jets are studied and the NDPM solutions are compared to computational fluid dynamics (CFD) calculations for different nozzle geometries.

In the following, preceding studies on the topic will be described briefly. The basic fluid dynamics of laminar jets has been studied in the early works by Schlichting[4] for axisymmetric jets and by Bickley[5] for plane jets. Their boundary layer solutions agree well with the exact solutions of the Navier-Stokes equations in the far-field of jets if the virtual origin of the jets are placed correctly.[6] Based on the boundary layer equations, Crane and Pack have investigated the diffusion of ambient particles into both plane[7] and axisymmetric jets.[8] The method has been extended for different applications, e.g., Pai studied the influence of radiative energy losses in jet mixing relevant for hot jets[9] and Sánchez-Sanz *et al.* recently derived an asymptotic solution for the diffusion of ambient species into a jet with vanishing density in the far-field.[10] Apart from approaches based on

---

[a] ansgar.schmidt-bleker@inp-greifswald.de

26, 083603-1

boundary layer theory, diffusion of ambient species into laminar jets has been studied in the context of laminar diffusion flames in order to estimate flame lengths,[1] assuming uniform velocity fields and considering only on-axis solutions. Sánchez *et al.* gave the complete solutions for the plane and axisymmetric jet for this case,[11] which also form the starting point for the method discussed in the present article.

Diffusion in shear flows has been studied extensively for several flow geometries: Taylor and Aris relate the dispersion of particles in a longitudinal laminar tube flow to the molecular diffusion coefficient,[12,13] thus giving a tool for measuring the diffusion coefficient in the downstream region of a longitudinal tube flow. The Taylor-Aris dispersion is commonly applied in various dispersion processes ranging from drug delivery,[14] transport in porous media to dispersion in turbulent flows, such as coastal basins and rivers.[15] A solution for the convection-diffusion equation with linear shear characterized by a constant velocity gradient is given in Ref. 16. The solution can be expressed in closed form for simple flow fields. For potential flows, the convection-diffusion equation can be solved for complicated geometries using conformal mappings.[17]

To the best of the authors' knowledge, an analytical study of the diffusion of ambient particles in the near-field of fluid jets accounting for non-uniform velocity profiles is still missing. In the present work, the diffusion of ambient species into a 2D-planar or axisymmetric fluid jet, described by the stationary convection-diffusion equation

$$\mathbf{v}^* \cdot \nabla^* n^* = \nabla^* \cdot \left(D^* \nabla^* n^* \right) \tag{1}$$

is studied, where $\mathbf{v}^*$ denotes a known velocity field of an incompressible flow, n^* is the density, and D^* is the diffusion coefficient, whereas the asterisk indicates the use of standard units. In the following, dimensionless units $n = n^*/n_0$, $r = r^*/r_0$, $z = z^*/r_0 Pe$, $t = t^* v_0/r_0$ are used, where r_0 is half of the width (plane jet) or the radius (axisymmetric jet) of the jet, $v_0 = v^*/v$ an average velocity and n_0 the equilibrium ambient species density. Here $Pe = r_0 v_0/D^*$ is the Péclet number, which is a measure for the relevance of convective transport compared to diffusive transport. Assuming that the diffusion coefficient is a constant and diffusive transport can be neglected over convective transport in direction parallel to the flow, Eq. (1) can be simplified to

$$\mathbf{v} \cdot \nabla n = \nabla \cdot \left(\mathbf{e}_\perp (\mathbf{e}_\perp \cdot \nabla) n \right), \tag{2}$$

where $\mathbf{e}_\perp = (v_z, -v_r)/|\mathbf{v}|$ is the unit vector in transverse direction. The aim of the present work is an approximate solution for Eq. (2) for high Péclet number jet flows.

In Sec. II, diffusion of ambient species into a fluid jet with uniform velocity field is studied. It is shown that in high Péclet number jet flows ambient particles that reach the axis in the near-field can only do so following narrow straight paths. This gives rise to the so-termed NDPM approximation proposed in Sec. III: The solution obtained for uniform velocity fields is mapped by a coordinate transformation, yielding an approximation for the ambient particle density in the shear flow. Dispersion is assumed to be negligible for every single path, if the velocity profile does not vary significantly over the width of the path. The applicability of the obtained NDPM approximation for realistic free jet flows is studied in Sec. IV, where the results of CFD simulations are compared to the NDPM approximation. The resulting on-axis solution has already been applied in Refs. 18 and 19 for the interpretation of VUV-absorption measurements for the detection of molecular oxygen in an atmospheric pressure plasma jet. However, the formula for the on-axis densities of ambient species has merely been introduced as a fitting function. Furthermore, the NDPM approximation has been applied to explain triangular laser induced OH-emission patterns observed in the effluent of a plasma jet.[20] In the present work, the underlying theory is described in detail.

II. DIFFUSION IN UNIFORM VELOCITY FIELDS

A. Solution of the diffusion equation

In this section, it is assumed that the velocity field points in axial direction $\mathbf{v} = \mathbf{e}_z$. Hence (2) simplifies to
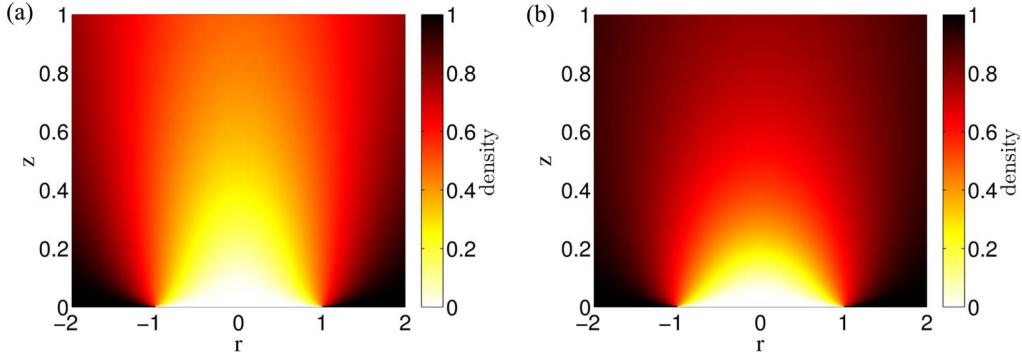
$$\partial_z n = \partial_r^2 n, \tag{3a}$$

FIG. 1. Density of ambient species in a uniform velocity field pointing in axial direction in (a) planar and (b) axisymmetric geometry.

$$\partial_z n = r^{-1} \partial_r \left(r \partial_r \right) n. \tag{3b}$$

Here and in the following the label (a) denotes the planar, (b) the axisymmetric case, and (r, z) denote the respective Cartesian or polar coordinates. With the initial condition $n(r, z = 0) = \theta(|r| - 1)$, where $\theta(x) = 1$ for $x \geq 1$, $\theta(x) = 0$ for $x < 0$, the analytic solutions to (3), found by Sánchez *et al.*,[11]

$$n_\theta^P = \underbrace{\frac{1}{2} \left(1 + \mathrm{erf} \left(\sqrt{\frac{1}{4z}} (r - 1) \right) \right)}_{n_\theta^{\mathrm{right}}} + \underbrace{\frac{1}{2} \left(1 - \mathrm{erf} \left(\sqrt{\frac{1}{4z}} (r + 1) \right) \right)}_{n_\theta^{\mathrm{left}}}, \tag{4a}$$

$$n_\theta^R = \frac{1}{2z} e^{-r^2 1/4z} \int_1^\infty dr' r' e^{-r'^2/4z} I_0 \left(\frac{rr'}{2z} \right), \tag{4b}$$

can be obtained by Fourier transformation in r and are plotted in Figure 1. Here $I_0(x)$ is the zeroth order modified Bessel function of the first kind and the lower index θ indicates the initial condition, the upper indices P and R indicate the planar and rotational symmetry. Note that the planar solution n_θ^P is subdivided into the contribution from the right ($r \geq 1$) and left ($r \leq 1$) side of the boundary condition at $z = 0$. Expanding $I_0(\frac{1}{2}rr')$ for small arguments, the series

$$n_\theta^R = e^{-r^2/4z} \sum_{j=0}^{} \frac{1}{j!^2} \left(\frac{r^2}{4z} \right)^j \Gamma \left(j + 1, \frac{1}{4z} \right) \tag{5}$$

is received for the axisymmetric case which yields the correct on-axis solution for the density

$$n_\theta^R(r = 0, z) = e^{-1/4z} \tag{6}$$

in zeroth order and converges rapidly with higher orders in the near-axis region. Here $\Gamma(a, x) = \int_x^\infty t^{a-1} e^{-t} dt$ denotes the upper incomplete gamma function.

B. Paths in uniform velocity fields

In the following, the paths are studied that particles take which enter the domain at $z = 0$, $r > 1$ and reach a certain point $z = z_0$ on the axis $r = 0$. First the solution of (3) is determined assuming a point source $n(r, z = 0) = \delta(r - a)/(2\pi)^k$ at a given position $r = a$ as initial condition, where here and in the following $k = 0$ for the planar and $k = 1$ for the axisymmetric case. This yields the density

$$n_{\delta,a}^P(r, z) = \sqrt{\frac{1}{4\pi z}} e^{-(r-a)^2 1/4z}, \tag{7a}$$

Original Publications

083603-4   Schmidt-Bleker, Reuter, and Weltmann   Phys. Fluids **26**, 083603 (2014)

$$n_{\delta,a}^R(r, z) = \frac{1}{4\pi z} e^{-(r^2 + a^2)1/4z} I_0\left(\frac{ra}{2z}\right). \tag{7b}$$

The probability that particles at a position (r, z) originate from $z = 0$, $r > 1$, given that they are transported to a point $(0, z_0)$ on the axis can be calculated using Bayes theorem: The probability of event A given B is $P(A|B) = P(B|A) P(A)/P(B)$. Here the event A is: A particle from the ambient is located at the position (r, z). The event B is: The particle will reach the position $(0, z_0)$. The probability $P(B|A)$ can be obtained by reversing the time and tracing back the particles originating from $(0, z_0)$ in a reversed flow field. The resulting probability density is

$$P_{\theta,z_0} = \frac{(2\pi r)^k n_\theta(r, z) n_{\delta,0}(r, z_0 - z)}{n_\theta(0, z_0)}. \tag{8}$$

Here the function $n_{\delta, a}(r, z_0 - z)$ describes the density due to a point source at the position (a, z_0) subject to reversed time $t \to -t$ (leading to a reversed flow field). The factor $2\pi r$ in Eq. (8) accounts for the rotational symmetry, normalizing $\int_0^\infty P_{\theta,z_0} dr = 1$ if $z \in [0, z_0]$. The probability density is plotted in Figures 2 (i) for $z_0 = 0.5$ and (ii) for $z_0 = 0.05$. It can be stated that particles reaching $z_0 = 0.5$ originate from a broad area at $z = 0$, $|r| > 1$. The possible paths on which these particles can reach z_0 cover almost the whole domain $0 < |r| < 2$. Furthermore, particles reaching the nearer point $z_0 = 0.05$ do so following narrow straight paths originating close to the edge of the jet at $z = 0$, $|r| = 1$. To investigate the latter case in greater detail, we focus on particles originating from a point source at $z = 0$, $r = 1$ only, and obtain the corresponding probability density

$$P_{\delta,z_0} = \frac{(2\pi r)^k n_{\delta,1}(r, z) n_{\delta,0}(r, z_0 - z)}{n_{\delta,1}(0, z_0)}, \tag{9}$$

which is plotted in Figure 2 (iii). Approximating $I_0(x) \approx \exp(x)\sqrt{1/2\pi x}$ in Eq. (7b) and for values $z \ll 1$, the density profiles of the observed paths have a Gaussian profile

$$P_{\delta,z_0} \sim \exp\left[\frac{(r - (1 - z/z_0))^2}{4z(1 - z/z_0)}\right] \tag{10}$$

following straight lines with the width $w = 2\sqrt{z/(1 - z/z_0)}$ for both the planar and the axisymmetric case. Above condition $z \ll 1$ thus ensures that the paths are both sufficiently narrow, follow straight lines and originate from a small domain near the edge of the jet. If the point $(r, z) = (0, z_0)$ is not located on the axis, but slightly off-axis, e.g., at $(0.05, 0.05)$, as shown in Figure 2(a) (iv), it is observed that only the nearest source on the right side significantly contributes to the density at the destined point. Naturally, the same is true for the axisymmetric case (b) (iv). However the effect is not visible as the axial symmetry was exploited in the previous calculations and hence all results are integrated over the angular coordinate. If the endpoint is moved further away from the axis to $(0.75, 0.05)$ as shown in Figure 2 (v), the paths broaden and the area at $z = 0$, $r \geq 1$ from which particles can reach the given point increases. The NDPM approximation presented in Sec. III is thus best suitable for near-axis solutions and at short axial distances to the jet nozzle.

III. NON-DISPERSIVE PATH MAPPING APPROXIMATION

Diffusion processes can be described by random walk models. From this perspective, the paths presented in Figure 2 depict the sum of all possible trajectories of particles performing random walks that start and end at the respectively defined points (or domains). In this section, the influence of arbitrary velocity profiles on these trajectories is investigated and the non-dispersive path mapping approximation is introduced using the illustrative example of the statistical analysis of particle random walks.

A. Random walk and path mapping

We now consider the one-dimensional random walk of particles performing a step Δr in random direction in each time interval Δt. Defining the diffusion coefficient for the random walk $D_{RW} = 1/2 (\Delta r)^2/\Delta t$, the evolution of the particle distribution can be described by the diffusion
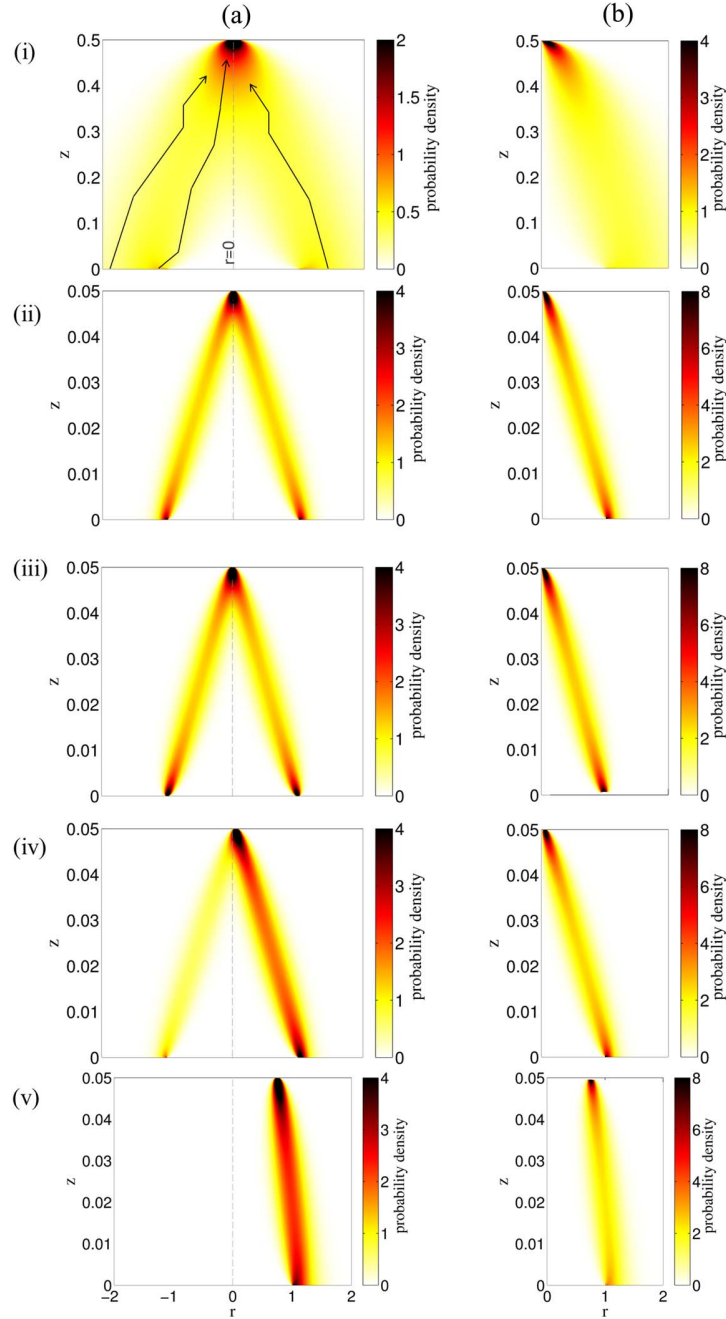
FIG. 2. Study of the paths that ambient particles can follow from the side of the nozzle to a given endpoint in (a) planar and (b) axisymmetric jets. (i) From $|\mathbf{r}| > \mathbf{l}, \mathbf{z} = \mathbf{0}$ (origin) to $\mathbf{r} = \mathbf{0}, \mathbf{z} = \mathbf{0.5}$ (endpoint). The black lines illustrate possible particle trajectories. The possible trajectories cover a large part of the domain $0 < r < 2$ (ii) From $|\mathbf{r}| > \mathbf{l}, \mathbf{z} = \mathbf{0}$ to $\mathbf{r} = \mathbf{0}, \mathbf{z} = \mathbf{0.05}$. If $z \ll 1$, possible paths form straight lines from origin to destination. (iii) From $|\mathbf{r}| = \mathbf{l}, \mathbf{z} = \mathbf{0}$ to $\mathbf{r} = \mathbf{0}, \mathbf{z} = \mathbf{0.05}$. If the finite source in case (ii) is replaced by a δ-source, the possible paths are hardly changed. (iv) From $|\mathbf{r}| > \mathbf{l}, \mathbf{z} = \mathbf{0}$ to $\mathbf{r} = \mathbf{0.05}, \mathbf{z} = \mathbf{0.05}$. Only the shortest paths significantly contribute to the density at the destination. (v) From $\mathbf{r}| > \mathbf{l}, \mathbf{z} = \mathbf{0}$ to $\mathbf{r} = \mathbf{0.75}, \mathbf{z} = \mathbf{0.05}$. As the destination is placed further from the axis, the width of the contributing source increases.

equation (3a) in the limit $\Delta r \to 0$, $\Delta t \to 0$ when the limiting process is performed so that D_{RW} remains finite.[21] In order to study individual particle trajectories in a plane jet flow that form paths of finite width as previously shown in Figure 2, Monte Carlo simulations were performed with a step-size $\Delta r = 5 \times 10^{-3}$ and $\Delta t = 1.25 \times 10^{-5}$. While the particles perform the random walk in

Original Publications

083603-6   Schmidt-Bleker, Reuter, and Weltmann   Phys. Fluids **26**, 083603 (2014)
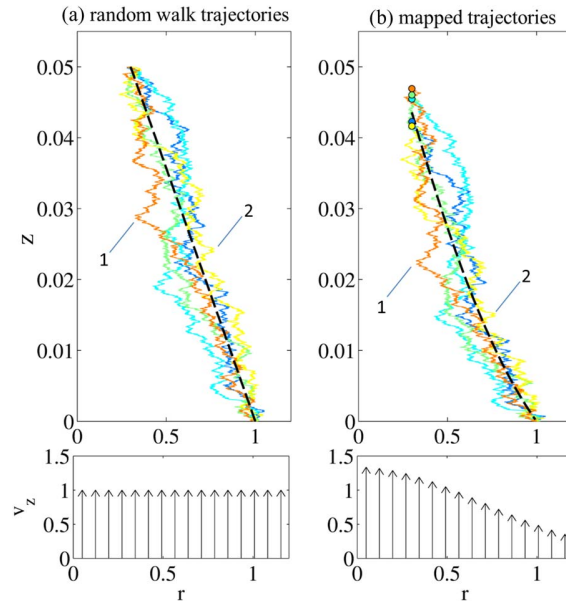
FIG. 3. Random walk of particles with same origin and endpoint in a uniform velocity field (a). The trajectories shown in Figure (a) mapped according to the flow field $v_z(r)$, resulting in the mapped trajectories shown in Figure (b). The dashed line is the path (13) according to NDPM approximation.

r-direction, they are moved in z-direction with the uniform velocity $v_z = 1$. Figure 3(a) shows five random walks of particles that start at the position (r, z) = (1,0) and end at the position (0.3,0.05) together with the uniform velocity field (bottom). The dashed line indicates a straight path from source to origin which marks the highest probability of presence for particles for $z \ll 1$ according to (10).

Now, the influence of shear flow on particles performing a random walk is studied. In order to simplify computations and data evaluation, a velocity field without radial component is assumed as shown in Figure 3(b) (bottom). The trajectories shown in Figure 3 own an inherent random walk history, which determines their movement in r-direction. The particle trajectories shown in Figure 3(b) are produced with the same random walk history as the respective trajectories in Figure 3(a), however they are moved in z-direction with the hydrodynamic velocity $\mathbf{v}(r) = \exp(-r^2)\mathbf{e}_z$. Due to dispersion in the shear flow, the mapped trajectories do not end in a single point anymore, but are spread in z-direction. For example, the trajectory labeled "1" spends a longer time in a region with a higher velocity and therefore reaches a farther z-position, while the trajectory "2" spends more time in a region with lower velocity and hence ends at a closer z-position.

The idea behind the non-dispersive path mapping approximation is, that if the velocity field $v(r, z)$ does not significantly vary over the width w of the path, thus fulfilling

$$w(\mathbf{e}_\perp \cdot \nabla)\mathbf{v} \ll 1, \tag{11}$$

the effect of dispersion on the particle density may be negligible as mapped trajectories will end up in a small interval around the expected endpoint. Instead of mapping all individual particle trajectories which form paths with finite width as shown in Figure 2, only the most probable trajectories are mapped, which, as is evident from Eq. (10), converge to infinitely narrow straight paths as $Pe \to \infty$. A given straight path as shown in Figure 3(a) can be mapped as follows: For a particle following an infinitely narrow straight path originating at the position $(r_0, z_0) = (1, 0)$ and ending at the endpoint (r_1, z_1) in the constant axial velocity field $\mathbf{v} = \mathbf{e}_z$, it takes the time $T = z_1$. In order to describe the transverse motion of the particle, its transverse velocity

$$v_\perp = \frac{r_1 - r_0}{T} \tag{12}$$
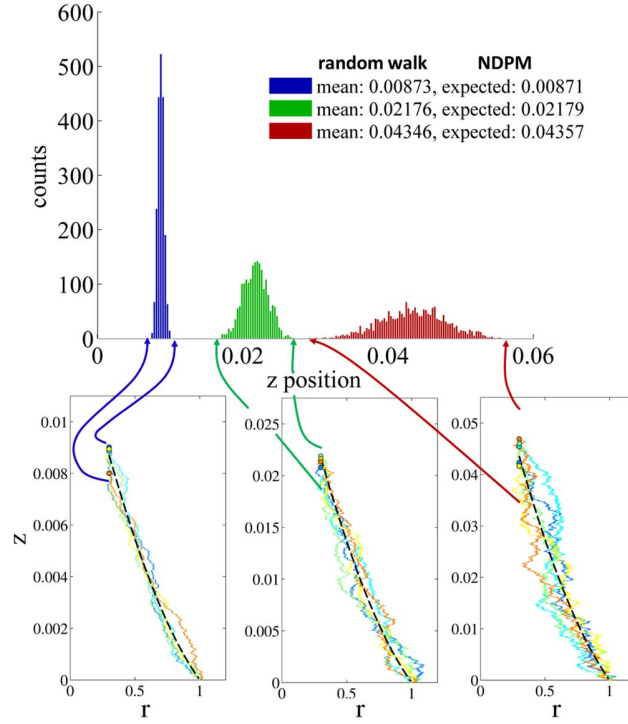
FIG. 4. Random walk statistics: The paths are mapped analytically according to the NDPM approximation and by mapping 2000 random walk trajectories numerically.

is defined. In an arbitrary velocity field $\mathbf{v} = (v_r, v_z)$ the mapped path $\tilde{\mathbf{x}} = (\tilde{r}(t), \tilde{z}(t))$ is thus defined by

$$\partial_t \tilde{\mathbf{x}} = \mathbf{v} + \mathbf{e}_\perp v_\perp. \tag{13}$$

The mapping of the straight path and individual particle trajectories has been applied for three different endpoints $((0.3, 0.01), (0.3, 0.025),$ and $(0.3, 0.05))$ as shown in Figure 4. For each endpoint 2000 random walks have been acquired that start at $(1,0)$ and end at the respective endpoint (only five are plotted for better visibility). The positions of the mapped endpoints are depicted in the histogram and compared to the endpoint according to NDPM approximation. It is observed that while at larger distances the statistical spread of the mapped endpoint positions increases, the mean value still agrees very well with the endpoint position expected from NDPM approximation. It is noted that the distribution of the endpoints around the mean z-position will in general depend on the velocity field. Mathematically, the exact solution in this case hence differs from the NDPM approximation by a convolution in z-direction of the NDPM solution with the space-dependent distributions shown in Figure 4. Also, in real jet flows, where the radial component of the velocity field is nonzero, a small spread of endpoints in radial direction will occur.

B. Evaluation of the density

1. 2D planar geometry

As discussed in Sec. III A, in 2D planar geometry the density caused by a point source at $(r_0, z_0) = (1, 0)$ and subject to the arbitrary velocity field $\mathbf{v}$ is mapped according to

$$\tilde{n}_{\delta,1}(\tilde{r}, \tilde{z}) \approx n_{\delta,1}(r, z), \tag{14}$$

where $\tilde{n}$ is the desired density after NDPM and the mapped coordinates $\tilde{r}, \tilde{z}$ are defined by Eq. (13). If particles do not only originate from the point $(r_0, z_0) = (1, 0)$ but from the whole domain

$r \geq 1$ (or $r \leq -1$), one would need to perform this mapping for every source point $r \geq 1$, $z = 0$ (or $r \leq -1$, $z = 0$). However, as discussed in Sec. II B, all paths contributing to the density in the region $z \ll 1$, $|r| < 1$ originate from a region close to the jet nozzle $|r| \gtrsim 1$. We therefore merely map the contributions from right and left side to the standard solution n_θ making the approximation

$$\tilde{n}_\theta^{\text{right/left}}(\tilde{r}, \tilde{z}) \approx n_\theta^{\text{right/left}}(r, z). \tag{15}$$

Note that the paths originating from the right side $r \geq 1$, $z = 0$ and the left side $r \leq 1$, $z = 0$ are mapped separately.

2. Axisymmetric geometry

For the axisymmetric case, the mapping would have to be performed for the infinite number of sources located at $r = 1$ and every value of the angular coordinate $\phi \in [0, 2\pi)$, which does not lead to a convenient expression. However, as observed in Figure 2(a) (iv), the path with the shortest distance from (r_0, z_0) to (r, z) yields the major contribution to the density at (r, z). The mapping of the standard solution (4b) (which is integrated over ϕ) therefore still is a reasonable approximation for the axisymmetric case, yielding

$$\tilde{n}_\theta^{\text{R}}(\tilde{r}, \tilde{z}) \approx n_\theta^{\text{R}}(r, z). \tag{16}$$

Note, that on the axis $r = 0$, all paths are mapped correctly due to their symmetry.

3. Axial velocity field with axial dependence

It is noted that in an artificial velocity field $\mathbf{v} = v_z(z)\mathbf{e}_z$ with an axial dependence only (and hence no dispersive mass transport), the mapping of the standard solution is obtained by performing the substitution

$$z \to \int_0^z dz' v_z(z')^{-1}, \tag{17}$$

which is the exact solution to the convection-diffusion equation.

C. Expansion/compression of the density

In order to study the expansion and compression of the standard solution due to the mapping, a simplified velocity field without radial component $\mathbf{v} = v_z(r)\mathbf{e}_r$ is investigated. In this case, Eq. (13) can be integrated directly, yielding

$$\tilde{z}(r) = z \frac{\int_1^r v_z(r')dr'}{r - 1} \tag{18}$$

for the start point $(r_0, z_0) = (1, 0)$, while the radial coordinate is unaffected. Consequently, volume elements are resized according to

$$(2\pi r)^k dr d\tilde{z} = (2\pi r)^k dr dz \frac{\int_1^r v_z(r')dr'}{r - 1}. \tag{19}$$

However, this effect is compensated by the fact that due to the applied mapping, the amount of particles that can reach a given point (r_1, z_1) also changes: Consider the three paths depicted in Figure 5 starting at (r_1, z_1) with reversed flow field, following the curves

$$z(r) = z_1 - s_i \int_{r_1}^r v_z(r)dr \tag{20}$$

with $s_1 = s$ and $s_{2/3} = s \pm \epsilon$, where ϵ is an arbitrary small constant and $s \leq z_1 \left(\int_{r_1}^1 v_z(r)dr \right)^{-1}$. It is observed that the interval Δz from which particles at $r = 1$ originate is resized according to

$$\Delta\tilde{z} = \Delta z \frac{\int_1^{r_1} v_z(r')dr'}{r_1 - 1}, \tag{21}$$

which compensates the effect of the volume deformation (19).
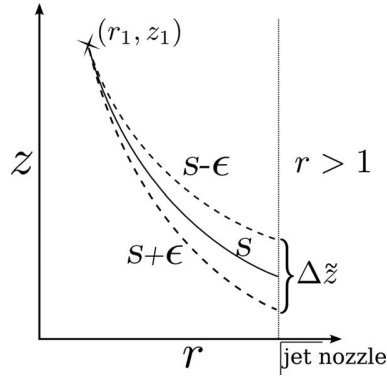
FIG. 5. The collecting area $\Delta\tilde{z}$ of the point (r_1, z_1) depends on the integral over the velocity profile $v_z(r)$.

The NDPM approximation for jet flows (15) does not take the velocity field in the region $r > 1$ into account, implicitly assuming that the velocity field in this region is not changed compared to the standard case $\mathbf{v} = \mathbf{e}_z$. However, Figure 5 illustrates that the density at any point (r_1, z_1) must be affected by the density at $r = 1$, which in real jet flows is influenced by the detailed nozzle geometry. The applicability of the NDPM approximation for realistic jet flows is therefore compared to computational fluid dynamics simulations in Sec. IV.

IV. NUMERICAL CASE STUDIES

In this section, the NDPM approximation is compared to full numerical simulations for different jet geometries. In a first step, the velocity field is obtained either by using boundary layer solutions for free jet flows or by solving the incompressible Navier-Stokes equations numerically using COMSOL 4.3 with the CFD Module. Second, the convection-diffusion equation (1) is solved numerically using the respective velocity field. This numerical solution is then compared to the results obtained by the NDPM approximation. Therefore, the ordinary differential equations (13) for the path mapping are integrated with Matlab using a built-in Runge-Kutta algorithm with automatic step size control. For every study 250 000 (500 · 500) points are mapped. All studies presented in this section are evaluated for $Re = Pe = 100$.

A. Boundary layer solutions

The self-similar solutions to the boundary layer equations for the free jet were given by Bickley for the plane jet[5] and earlier by Schlichting for the axisymmetric jet.[4] For the plane jet the solution reads

$$\eta = 0.2751(2Re^2)^{1/3}rz' - 2/3, \tag{22a}$$

$$v_r = 0.5503 \left(\frac{2}{z'^2 Re}\right)^{1/3} \left(2\eta(1 - \tanh^2\eta) - \tanh\eta\right), \tag{22b}$$

$$v_z = 0.4543 \left(\frac{4Re}{z'}\right)^{1/3} \left(1 - \tanh^2(\eta)\right), \tag{22c}$$

with $z' = z Pe + z_0$, where $z_0 = 0.192 Re$ is the virtual origin of the jet, defined so that the kinetic energy flux at the nozzle matches the energy flux of a jet with $v_z = 1$ at the outlet.[22] The Reynolds number is defined as $Re = v_0 r_0/\nu$ with kinematic viscosity ν and v_0 defined as the average velocity over the nozzle outlet at $z = 0$, $r \leq 1$. In the axisymmetric case the velocity field is given by

$$\xi = Re\sqrt{3/16}r/z', \tag{23a}$$
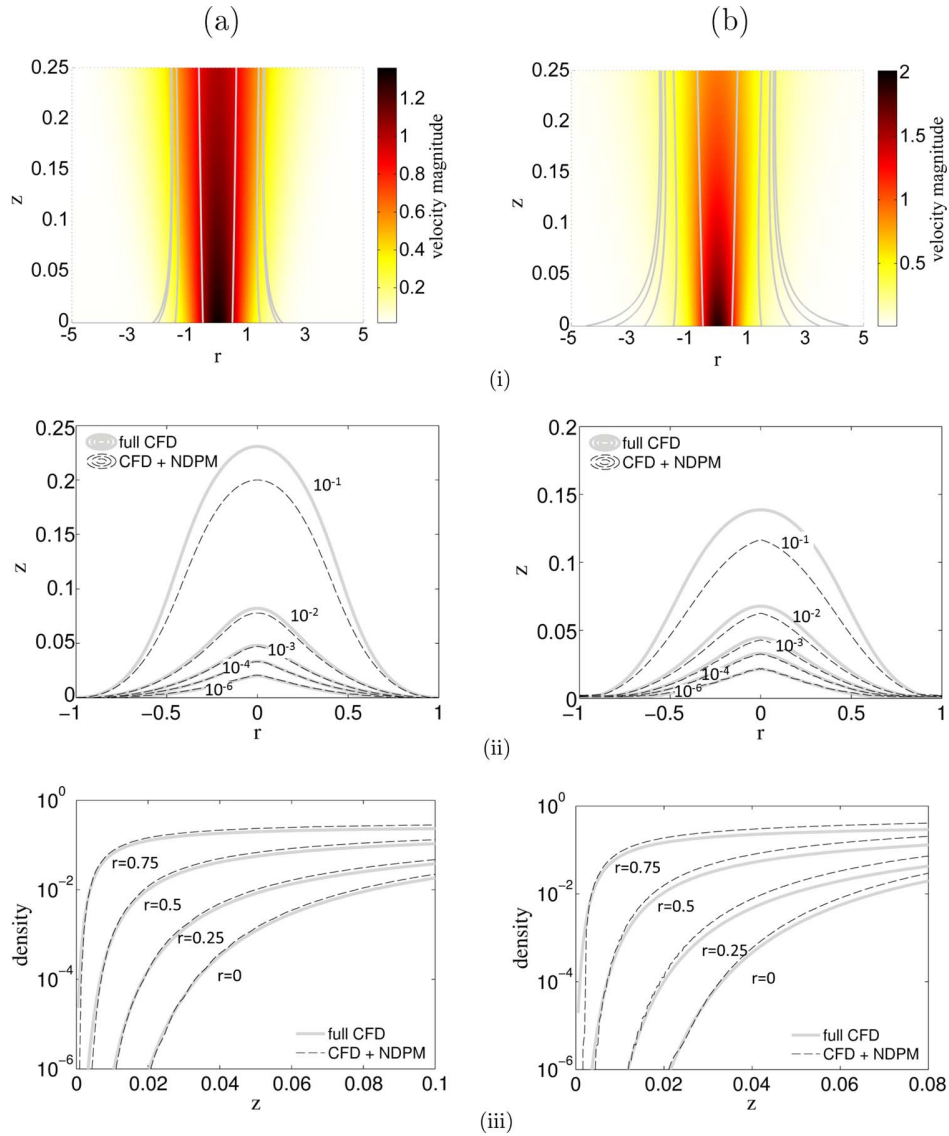
FIG. 6. Study of NDPM approximation using self-similar velocity fields for (a) planar and (b) axisymmetric jets. (i) Velocity magnitude v and streamlines according to self-similar solutions (22) and (23). (ii) Contour plot of the density obtained by full numerical solution and obtained by NDPM approximation using the velocity field (i). (iii) Density evaluated along paraxial lines at the indicated radial positions.

$$v_r = \sqrt{3/16}\frac{1}{x}\frac{\xi - \xi^3/4}{1 + \xi^2/4}, \tag{23b}$$

$$v_z = \frac{3}{8}\frac{Re}{z'}\left(1 + \xi^2/4\right)^{-2}, \tag{23c}$$

and the respective virtual origin is $z_0 = 0.225\,Re$.[23] The solution for both the plane (a) and the axisymmetric (b) jet are plotted in Figure 6 (i) for $Re = 100$. It is noted, that these self-similar solutions are not suitable for the description of real flow fields of jets in the vicinity of the nozzle outlet, but make good approximations for the far-field of the jet, if the virtual origin is placed correctly.[6] However, they make good basic test cases for the NDPM approximation, as they are independent of any real nozzle geometry. The solution obtained by solving the convection-diffusion equations (1) numerically with the boundary condition $n(r, z = 0) = \theta(|r| - 1)$ and $Pe = 100$ (labeled

full CFD) is compared to the density obtained by NDPM approximation (labeled CFD + NDPM) in Figures 6 (ii) and (iii). Especially for short distances, the agreement between the solutions is very good, but still better for the plane jet, as n_θ^{right} and n_θ^{left} were mapped separately, while in the axisymmetric case only n_θ^R is mapped (see Sec. III B). In the contour plot in Figure 6(b) (ii) it can be seen, that high density contours $n = 10^{-1}$ and $n = 10^{-2}$ do not appear continuously differentiable at $r = 0$. This occurs, as the approximation (16) for the axisymmetric case, mapping only the paths with the largest contribution correctly, becomes insufficient at large distances for $r \neq 0$ (see discussion in Sec. III B 2).

B. CFD simulation of jet with thin rim

In this study, a jet flow from a nozzle with vanishing thickness of the rim is studied. The velocity profile at $z = -0.01$ is initialized as a Poisseuille flow

$$v_z = \frac{3}{2} \left(\frac{4}{3}\right)^k \left(1 - r^2\right), \tag{24}$$

for $|r| \leq 1$ with a coflowing stream $v_z = 0.5$ for $|r| > 1$. As illustrated in Figure 7 (i), the most important difference compared to the previous case is, that the velocity drops down to zero at the nozzle outlet $|r| = 1$, $z = 0$. Additional to the full CFD and CFD + NDPM studies shown in Figure 7 (ii) and (iii), another study, labeled Poisseuille + CFD, is given. In this study, the NDPM mapping is applied, assuming the Poisseuille flow profile (24) in the whole domain. In this case, the mapping can be performed analytically using Eq. (18) and no CFD simulation is needed to obtain the velocity profile. This especially yields the simple expressions

$$\tilde{n}_P(r = 0, z) = 1 - \text{erf}\left(\sqrt{\frac{1}{4z}}\right), \tag{25a}$$

$$\tilde{n}_R(r = 0, z) = \exp\left(-\frac{1}{3z}\right) \tag{25b}$$

for the on-axis density. As expected, the agreement between this analytical NDPM approximation and the full CFD and CFD + NDPM cases is good in the vicinity of the nozzle, where the flow field is very similar to the Poisseuille flow in the region $|r| < 1$ and gets worse in the far field. Another important point is, that diffusion against the flow direction cannot be accounted for in the NDPM approximation, as diffusion in axial direction is neglected in the basic study. While at high Péclet numbers, diffusion against the flow direction is usually negligible, it may still occur in the vicinity of the wall, where the velocity approaches zero. For the full CFD solution in Figure 7 (iii) we therefore observe that the ambient particle density at $r = 0.75$, $z = 0$ reaches much higher values than predicted by the NDPM approximation.

C. CFD simulation of jet with broad rim

Finally, the diffusion in a jet with broad rim (thickness much larger than jet radius) is studied. The velocity field obtained by CFD simulation is illustrated in Figure 8 (i). Compared to the previous studies, the flow is not mainly directed in paraxial direction in the region $r > 1$. The comparison of the density obtained by full CFD simulation and CFD + NDPM and Poisseuille + NDPM is shown in Figures 8 (ii) and (iii). The density obtained by the NDPM approximations is always a bit higher compared to the full CFD solution. This occurs, as the wall at $z = 0$ hinders the ambient particle flow and thus fewer particles can be collected from the region $|r| = 1$ (see Figure 5).

D. Far field

In Figure 9, the far field density of ambient particles is evaluated for two cases. As illustrated, the best agreement of full CFD simulations and NDPM approximation is achieved for the plane
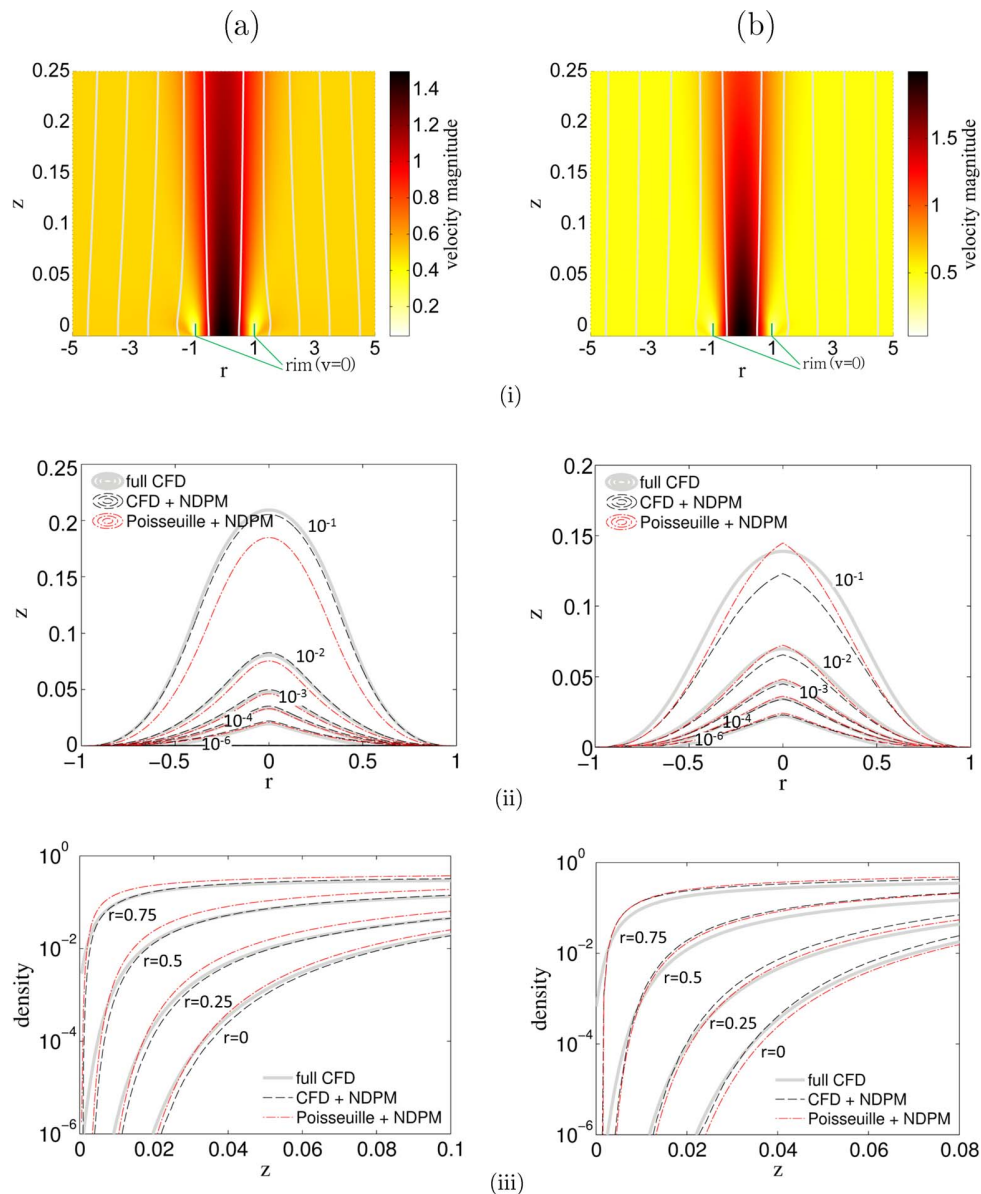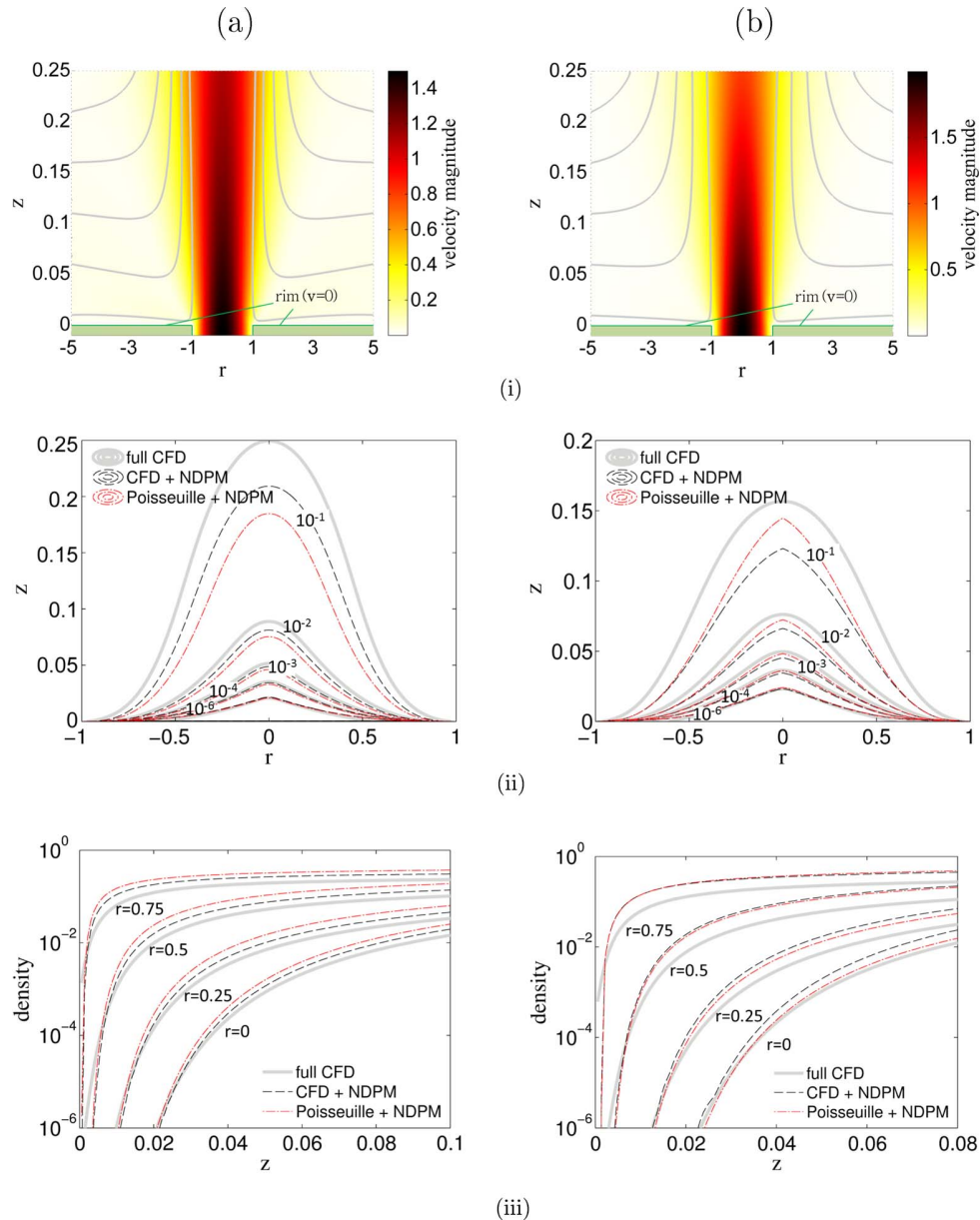
FIG. 7. Study of the NDPM approximation using a jet with vanishing rim thickness for (a) planar and (b) axisymmetric geometry. (i) Velocity magnitude v and streamlines according to CFD simulation. (ii) Contour plot of the density obtained by full numerical solution, obtained by NDPM approximation combined with the velocity field (i) and NDPM approximation assuming a Poisseuille flow profile (24). (iii) Density evaluated along paraxial lines at the indicated radial positions.

jet (Figure 9(a)) with coflowing stream (which is the case already shown in Figure 7(a)). Here, the combination of NDPM approximation and the velocity field from CFD simulation yields acceptable agreement for densities up to 20% of the equilibrium density. However, when combining NDPM with a Poisseuille flow the ambient particle density is significantly overestimated. The worst agreement in the far field is observed in case of the axisymmetric jet with broad rim shown in Figure 9(b) (previously presented in Figure 8(b)). As in the CFD simulations, the flow of ambient particles is hindered due to the wall at $z = 0$, the ambient particle densities are significantly overestimated in the NDPM approximation. Note, that for $r = 0$ the combination of the NDPM approximation with the Poisseuille field actually yields better results than the NDPM + CFD study. Apparently, errors

FIG. 8. Study of the NDPM approximation using a jet with broad rim for (a) planar and (b) axisymmetric geometry. (i) Velocity magnitude v and streamlines according to CFD simulation. (ii) Contour plot of the density obtained by full numerical solution, obtained by NDPM approximation combined with the velocity field (i) and NDPM approximation assuming a Poisseuille flow profile (24). Density evaluated along paraxial lines at the indicated radial positions.

due to the NDPM and the simplified flow field cancel each other to some extent. The agreement in the far field seems rather poor in this case. For evaluation and interpretation of spectroscopic measurements however, knowledge about the order of magnitude of the ambient species density as depicted in Figures 6–8 (iii) is often already valuable.[18,20,24] Note, that completely neglecting the flow profile (e.g., by assuming $\mathbf{v} = \mathbf{e}_z$), the density obtained in the near-field may easily be off by two orders of magnitude.

As a rule of thumb, the NDPM approximation yields acceptable agreement for densities up to about 1% (depending on the accuracy required and geometry studied). As the z-coordinate in the diffusion equation (2) scales with the Péclet number, this density is reached either farther
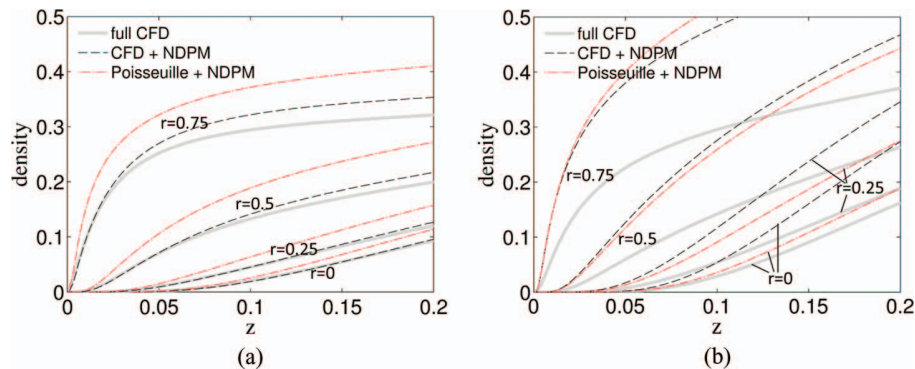
FIG. 9. Density evaluated along paraxial lines for the far field at the indicated radial positions. (a) Plane jet with coflowing stream (same as shown in figure 7(a)) and (b) axisymmetric jet with coflowing stream (same as shown in figure 8(b)).

away ($Pe > 100$) or closer ($Pe < 100$) to the jet nozzle than presented in the current study at $Pe = 100$.

V. CONCLUSION

An analytical model has been presented capable of describing the diffusion of ambient air into laminar fluid jets in the near-field with a known velocity field. It is shown that the majority of particles diffusing into the near-field of the jet reach the near-axis region following narrow straight paths that originate from the side of the jet nozzle. The shear flow is accounted for by the coordinate transformation (13) of the exact solution (4) for ambient particle diffusion in jets with uniform velocity field, which can be evaluated using the series expansion (5). The method proves to be most accurate in the near-field region or for high Péclet numbers, where $z \ll 1$ is fulfilled and for the near-axis region, as paths broaden for the far off-axis region as depicted in Figure 2 (v). For the practical application of the NDPM approximation, a velocity field will usually not be available. However, as studied in Secs. IV B and IV C, it may often be sufficient to assume a velocity field of the form $\mathbf{v} = v(r)\mathbf{e}_z$, e.g., a Poisseuille flow profile (24). In this case, the NDPM mapping can be performed analytically using Eq. (18). The resulting formula for the density becomes especially simple if only the on-axis solution (25) is considered: In this case, the influence of a radial velocity profile can simply be accounted for by multiplying the z-coordinate with the integral over the normalized radial velocity profile. The applicability of the NDPM approximation for realistic flow geometries has been studied by comparison to a CFD simulation of simple jet flows. Although complete CFD simulations as presented in Sec. IV of course yield higher accuracy in the off-axis and downstream region, the advantage of the NDPM approximation lies in its simplicity and applicability in every day lab work: When changing experimental parameters like the average velocity or nozzle diameter for a given setup, the resulting effect on ambient species densities can easily be estimated.

[1] R. Günther and H. Wilhelmi, *Verbrennung Und Feuerungen* (Springer, Berlin, 1984).
[2] A. Revuelta, A. L. Sánchez, and A. Liñán, "Laminar mixing in diluted and undiluted fuel jets upstream from lifted flames," Combust. Flame **128**(3), 199–210 (2002).
[3] S. Reuter, H. Tresp, K. Wende, M. U. Hammer, J. Winter, K. Masur, A. Schmidt-Bleker, and K.-D. Weltmann, "From rons to ros: Tailoring plasma jet treatment of skin cells," IEEE Trans. Plasma Sci. **40**(11), 2986–2993 (2012).
[4] H. Schlichting, "Laminare strahlenausbreitung," Z. Angew. Math. Mech. **13**, 260–263 (1933).
[5] W. Bickley, "The plane jet," Philos. Mag. **23**, 727–731 (1937).

[6] A. Revuelta, A. L. Sánchez, and A. Linán, "The virtual origin as a first-order correction for the far-field description of laminar jets," Phys. Fluids **14**(6), 1821–1824 (2002).

[7] L. J. Crane and D. C. Pack, "The mixing of a jet of gas with an atmosphere of a different gas at large distances from the orifice: Part I. The plane jet," Q. J. Math. **14**(4), 385–391 (1961).

[8] L. J. Crane, "The mixing of a jet of gas with an atmosphere of a different gas at large distances from the orifice: Part II. The round jet," Q. J. Math. **14**(4), 393–402 (1961).

[9] S. I. Pai, "Laminar jet mixing in radiation gasdynamics," Phys. Fluids **6**(10), 1440–1445 (1963).

[10] M. Sánchez-Sanz, M. Rosales, and A. L. Sánchez, "The hydrogen laminar jet," Int. J. Hydrogen Energ. **35**(8), 3919–3927 (2010).

[11] A. L. Sánchez, M. Vera, and A. Liñán, "Exact solutions for transient mixing of two gases of different densities," Phys. Fluids **18**(7), 078102 (2006).

[12] G. Taylor, "Dispersion of soluble matter in solvent flowing slowly through a tube," Proc. R. Soc. London A **219**(1137), 186–203 (1953).

[13] R. Aris, "On the dispersion of a solute in a fluid flowing through a tube," Proc. R. Soc. London A **235**(1200), 67–77 (1956).

[14] W. Hulse and R. Forbes, "A Taylor dispersion analysis method for the sizing of therapeutic proteins and their aggregates using nanolitre sample quantities," Int. J. Pharm. **416**(1), 394–397 (2011).

[15] O. G. Bakunin, *Turbulence and Diffusion: Scaling Versus Equations*, Springer Series in Synergetics Vol. 101 (Springer, Berlin, 2008).

[16] R. T. Foister and T. G. M. Van de Ven, "Diffusion of Brownian particles in shear flows," J. Fluid Mech. **96**(01), 105–132 (1980).

[17] M. Z. Bazant, "Conformal mapping of some non-harmonic functions in transport theory," Proc. Roy. Soc. London A **460**(2045), 1433–1452 (2004).

[18] S. Reuter, J. Winter, A. Schmidt-Bleker, D. Schroeder, H. Lange, N. Knake, V. Schulz-von der Gathen, and K.-D. Weltmann, "Atomic oxygen in a cold argon plasma jet: Talif spectroscopy in ambient air with modelling and measurements of ambient species diffusion," Plasma Sourc. Sci. Technol. **21**(2), 024005 (2012).

[19] S. Reuter, J. Winter, A. Schmidt-Bleker, H. Tresp, M. U. Hammer, and K.-D. Weltmann, "Controlling the ambient air affected reactive species composition in the effluent of an argon plasma jet," Plasma Sourc. Sci. Technol. **40**(11), 2788–2794 (2012).

[20] S. Iseni, A. Schmidt-Bleker, J. Winter, K.-D. Weltmann, and S. Reuter, "Atmospheric pressure streamer follows the turbulent argon air boundary in a mhz argon plasma jet investigated by oh-tracer plif spectroscopy," J. Phys. D **47**(15), 152001 (2014).

[21] J. L. Plawsky, *Transport Phenomena Fundamentals* (CRC Press, Boca Raton, 2001).

[22] E. N. Andrade, "The velocity distribution in a liquid-into-liquid jet. Part 2: The plane jet," Proc. Phys. Soc. **51**(5), 784 (1939).

[23] E. N. Andrade and L. C. Tsien, "The velocity-distribution in a liquid-into-liquid jet," Proc. Phys. Soc. **49**(4), 381 (1937).

[24] D. Dudek, N. Bibinov, J. Enge'mann, and P. Awakowicz, "Direct current plasma jet needle source," J. Phys. D **40**(23), 7367–7371 (2007).

Article A2

Fast Track Communication

Atmospheric pressure streamer follows the turbulent argon air boundary in a MHz argon plasma jet investigated by OH-tracer PLIF spectroscopy

S Iseni[1,2]**, A Schmidt-Bleker**[1,2]**, J Winter**[1,2]**, K-D Weltmann**[2] **and S Reuter**[1,2]

[1] Centre for Innovation Competence plasmatis, Felix-Hausdorff-Str. 2, 17489 Greifswald, Germany
[2] Leibniz Institute for Plasma Science and Technology INP Greifswald e.V., Felix-Hausdorff-Str. 2, 17489 Greifswald, Germany

E-mail: sylvain.iseni@inp-greifswald.de

Abstract

An open question in the research of the dynamics of non-equilibrium cold atmospheric pressure plasma jets is the influence of ambient species on streamer propagation pathways. In the present work, by means of planar laser-induced fluorescence (PLIF), an atmospheric pressure argon plasma jet is investigated in a laminar and turbulent gas flow regime. The flow pattern is investigated with plasma on and plasma off. It is shown that in turbulent mode, the streamer path changes according to the flow pattern changes and the resulting changes in air abundance. From a comparison of an analytical diffusion calculation and LIF measurements, the air impurity boundary is determined. Most importantly, the origin of the streamer pathway is investigated in detail, by recording the flow pattern from OH-PLIF measurements and simultaneously measuring the streamer path by an overlay technique through emission measurements. It is shown that the streamer path is correlated to the turbulent flow pattern.

(Some figures may appear in colour only in the online journal)

1. Introduction

Only a few years ago, so-called plasma bullet [1, 2] and guided-streamer [3] jets came to be known. Recently, researchers have identified the fundamental processes behind these dynamics (see e.g. [4, 5]). However, their propagation in air has continued to raise questions. In this work, the connection of gas flux regime, ambient species and streamer head propagation in a MHz atmospheric pressure argon plasma jet is investigated by laser spectroscopic methods. The diagnostic technique is based on planar laser-induced fluorescence (PLIF) on hydroxide molecules (OH) generated by the plasma jet itself due to water impurities. With stereoscopic imaging, both flow structure and streamer propagation are investigated simultaneously for a single discharge event. The study reveals that the flux field with plasma differs strongly from the flux field without plasma. Furthermore, it is most prominently and for the first time shown that the streamer propagates in the noble gas channel of a turbulent plasma jet effluent itself and follows the boundaries of ambient species impurities. Especially

revealing are the differences observed for the laminar and turbulent case.

2. Experimental setup

In this work, the flux and streamer propagation of a MHz atmospheric pressure plasma jet (kINPen, neoplas tools GmbH, Germany) [6, 7] have been investigated. The feed gas is argon (Ar purity 99.999%), which may contain water impurities of up to 20 ppm originating from the gas pipe as reported in [8]. The OH PLIF measurements are performed with a frequency doubled dye laser (Cobra Stretch, Sirah Laser und Plasmatechnik GmbH, Germany) pumped with a 10 Hz pulsed Nd : Yag laser (Spectra-Physics, Inc.). The pulse duration is measured to be 8.1 ns after frequency doubling at 283 nm. The laser linewidth has been recently measured on a similar dye laser from the same company to be 1.4 pm [9]. Although this parameter remains crucial for the determination of absolute density [10], it does not influence qualitative measurements. The P1(4) transition of the OH(A, X)(1,0) at 283.5 nm is chosen as the energy transition due to its good absorption efficiency. Additionally, it is well separated from other lines. The linearity of the OH fluorescence signal versus the laser energy has been checked. The laser beam is expanded to a sheet via a cylindrical quartz lens and guided through the plasma jet effluent. The laser energy integrated along the 12 mm high sheet is measured to be 13 mJ. An aperture is mounted in front of the jet in order to illuminate only the area of interest. A CCD camera Imager Pro X (LaVision GmbH, Germany), combined with an external gated image intensifier and a 100 mm f/2.8 UV lens, is used as detection system. The fluorescence emission is observed at a 90° angle to the p-polarized laser beam in order to reduce unwanted signals due to Rayleigh scattering. Additionally, a stereoscopic optical imaging system is coupled to the lens in order to record two images with each laser shot. By installing different filters for the two images respectively, different information can be gathered simultaneously. Here, on the first optical input, a BK7 neutral density filter is mounted, which allows observation from 350 to 1100 nm, where most of the plasma emission is found due to argon lines [8, 11]. On the second optical input, a 10 nm FWHM band-pass filter centered at 313 nm is used to collect the fluorescence only of OH. Both signals are recorded on a vertical split CCD chip, so that the exposure time is identical for both signals.

The plasma jet frequency is phase locked with the laser pulse as well as the detection system, which allows phase-resolved optical emission spectroscopy (PR-OES). The exposure time is set to 200 ns, which is sufficient to obtain enough intensity for single shot acquisition. The optical aberrations such as distortion produced by the stereoscopic imaging system are corrected by Davis software [12] after the calibration procedure described in the manual [13]. The inhomogeneity of the laser sheet is measured by Rayleigh scattering and corrected by intensity normalization.

The observation of the flow pattern with plasma off is performed by PLIF using acetone as a tracer. As described in [14], acetone fluorescence is a suitable tracer to image
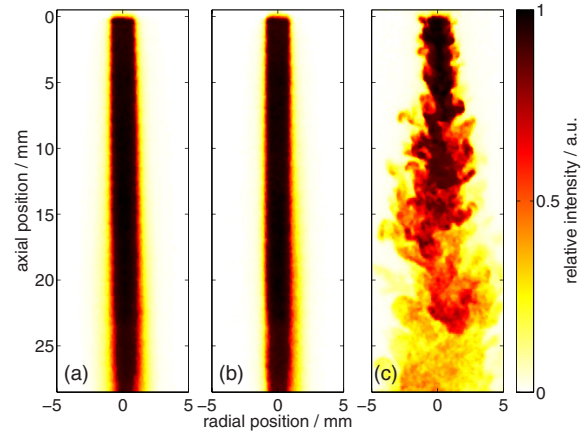

Figure 1. Space resolved single shot fluorescence signal of acetone for different argon gas flow rates of (*a*) 0.5 slm/Re= 465, (*b*)1.0 slm/Re= 930 and (*c*) 3.0 slm/Re= 2790. The jet nozzle is located at an axial distance of zero. The plasma was switched off.

turbulent flows. During the measurements, the feed gas is bubbled through acetone into the plasma device. The acetone molecules are excited by the laser beam at 283.5 nm, and the fluorescence from 350 to 800 nm is collected by an intensified CCD camera and recorded. Observing the flow pattern with plasma-on requires the use of a different tracer, since acetone would be destroyed by the reactive species in the plasma. In the past, hydroxyl fluorescence was already used in combustion with good success on turbulence studies [15]. Moreover, one report stated that the hydroxyl molecule lifetime is 1 ms to a few milliseconds at atmospheric conditions [16, 17]. The hydroxyl radical is produced by the plasma itself from water impurities within the feed gas [8], meaning that the plasma generates the tracer itself and no external species need to be admixed for the flow measurements. Recently, hydroxyl molecule densities on-axis were measured by UV absorption on the same discharge [18]. The results show that the density remains constant up to a 7 mm distance from the nozzle. It can thus be assumed that the hydroxyl density does not decay significantly along the first 10 mm from the nozzle [18]. For these reasons, the hydroxyl radical, for the present studies, can be used as a fluorescent tracer.

3. LIF on acetone—plasma off measurements

Figure 1 shows the fluorescence of acetone for three different feed gas flow rates. As can be seen, at both 0.5 and 1 standard liter per minute (slm) the flow is laminar, while at 3 slm the flow is turbulent. The indicated Reynolds numbers $Re = 2r_0 v_{av}/\nu$ are defined via the capillary radius r_0 and the kinematic viscosity ν. The critical Reynolds number (Re) for the transition from the laminar to turbulent regime in pipe flows is $Re_C = 2300$, which is consistent with the observed flow regimes.
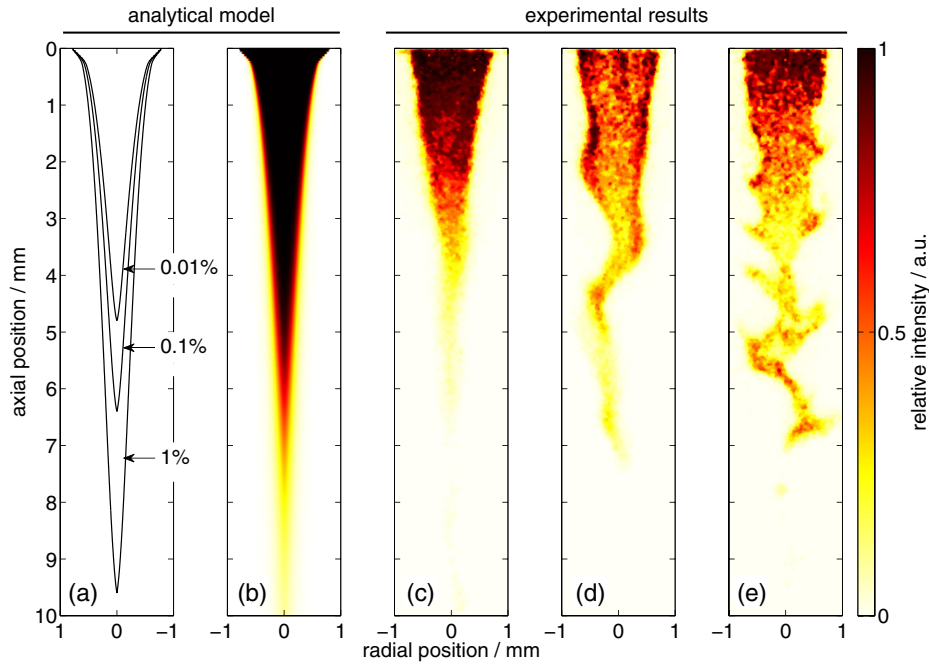
68

J. Phys. D: Appl. Phys. **47** (2014) 152001

Fast Track Communications

Fast Track Communication

Figure 2. Analytical estimation of the ambient species density (*a*) and the resulting analytical OH emission pattern (*b*). Space resolved fluorescence signal of hydroxyl for different argon gas flow rates of (*c*) 0.5 slm, (*d*) 1.0 slm and (*e*) 3.0 slm. The jet nozzle is located at an axial distance of zero. The plasma was switched on. Single shot acquisition.

4. OH fluorescence and quenching by ambient air—plasma on measurements

The radiative lifetime of the OH(A, X)(1,0) is known to be around $\tau = A^{-1} = 748$ ns, where A is the Einstein coefficient for spontaneous emission. The emission is strongly quenched by atmospheric species [18]: the combined quenching rate (Q) and vibrational energy transfer (VET) coefficient of OH(A, X)(1,0) by argon (0.27×10^{-11} cm^3 s^{-1} [19]) is two orders of magnitude lower than for nitrogen ($k_Q^{N_2} = 23.3 \times 10^{-11}$ cm^3 s^{-1} [20]), oxygen ($k_Q^{O_2} = 20.6 \times 10^{-11}$ cm^3 s^{-1} [20]) and water ($k_Q^{H_2O} = 66 \times 10^{-11}$ cm^3 s^{-1} [20]). Despite that, the quenching rate of OH fluorescence by water is in the same order of magnitude as dry air, and ambient humidity has a negligible effect on the OH fluorescence quenching due to a much lower density compared to air. In consequence, OH(A, X)(1,0) has a longer lifetime when it is mixed with argon than in presence of air. The OH originates dominantly from the dissociation of water impurities in the feed gas. Even at what is considered to be dry feed gas conditions, the quantity of water molecules lies in the order of some 10 ppm. When the gas leaves the jet, the OH concentration is distributed relatively homogeneously along the diameter of the nozzle (see figure 2(*c*)). Similar observations have been reported earlier. Here the main hydroxyl production is localized near the powered electrode in case of water impurities in the feed gas [21]. Additionally, the hydroxyl density remains presumably constant until several mm distance [18]. The spatial distribution can be expected to resemble the acetone distribution as shown above (see figure 1). From these as well

as the quencher considerations, it can be safely assumed that the LIF signal reveals rather the influence of the quenching by the ambient species than the ground state OH molecule distribution. The measured data therefore reflects the argon flow pattern and the argon air boundary shape, as will be described in the following.

The diffusion of ambient species into the effluent of the plasma jet can be estimated by solving the convection diffusion equation

$$v(r)\partial_z n_A + D\Delta_r n_A = 0$$

with the boundary condition $n_A = \theta(r - r0)n_A^0$ for the ambient species density, where $\theta(x)$ is the Heaviside step function $\theta(x) = 0$ for $x < 0$, $\theta(x) = 1$ for $x \geqslant 0$. Here, D is the diffusion coefficient and $v(r)$ a velocity field with a radial dependence and Δ_r the radial part of the Laplace operator. The solution in the case of a constant velocity profile is given in [22] and can be evaluated using an infinite series. For a laminar jet flow, the velocity field in the near field of the jet can be approximated by a Poiseuille flow profile $v(r) = 2v_{av}(1 - r^2/r_0^2)$. In order to account for this flow profile, non-dispersive path mapping [23] can be applied, mapping the constant velocity solution according to the flow field. The contour lines of the resulting ambient air density n_A/n_A^0 for an average velocity of $v_{av} = 4.1$ m s^{-1} and diffusion coefficient $D = 0.2$ cm^2 s^{-1} are shown in figure 2(*a*). Assuming a constant OH-density in the jet's effluent, the fluorescence intensity of OH(A, X)(1,0) can be estimated to be proportional to

$$I_{\mathrm{LIF}} \sim A/(A + n_{O_2}k_Q^{O_2} + n_{N_2}k_Q^{N_2} + n_{H_2O}k_Q^{H_2O})$$

as depicted in figure 2(*b*). In figures 2(*c*)–(*e*), the single shot LIF signal at flow rates of 0.5, 1 and 1.5 slm are displayed. The signal is a pure LIF signal, as spontaneous emission from excited hydroxyl OH(A, X)(1,0) is negligible. The analytically obtained triangular emission pattern (figure 2(*b*)) agrees very well with the experimentally observed OH emission at a gas flux of 0.5 slm (figure 2(*c*)). A sharp edge in the emission pattern occurs at an ambient air density of approximately 0.01–1%. This shows that due to the strong hydroxyl fluorescence quenching by air, the contour of the argon–air boundary can be determined and reflects the relative space-resolved argon density. The plasma does not change the flow regime at this flow rate.

For a flow rate of 1 slm, the occurrence of Kelvin–Helmholtz (KH) instabilities is observed, leading to a breaking of the laminar jet downstream. KH instabilities are likely to appear at the mixing layer of two fluids with different densities and/or in a shear flow [24]. Both mechanisms may be triggered when heating of the gas by the plasma occurs: its density is decreased, while its expansion leads to an increased shear.

Electro hydrodynamic forces can also trigger flow regime transitions. In [25] it is observed that the flow regime of a helium jet is significantly affected by the plasma while the temperature remains at around room temperature. It is noted that helium jets may be affected more strongly by equal electro hydrodynamic forces, as their momentum is ten times less compared to argon jets at identical flow conditions. It was recently observed that the air mixing in an argon plasma jet similar to the one used in the present study is significantly increased when the plasma is turned on, which agrees with our findings [26]. Their gas temperature is around 480 K. They also attribute this effect to the occurrence of KH instabilities and/or electro hydrodynamic forces.

At 3 slm, the flux seems to remain fully turbulent as in the plasma-off case.

5. Turbulent flow and streamer propagation

The observation of the turbulent behavior of the effluent flow is possible only if the acquisition time is much faster than the turbulence time scale. At 200 ns exposure time, the flow dynamics is static, but the discharge propagation is fast enough to grow and develop itself. Therefore looking at the effluent turbulence pattern as well as the streamer path within the same single time shot leads to fundamental information about the discharge propagation. Figure 3 shows a superimposed image of the streamer and the hydroxyl fluorescence. The hydroxyl fluorescence resembles the argon flow pattern. Both are following the same path and—especially at greater distances to the nozzle, where the argon abundance has the same dimension as the streamer thickness—the patterns are identical. On figure 3(*b*) and (*c*), which corresponds to 1 slm and 3 slm flow rates respectively, the flow patterns are not laminar and result in density gradients of argon which form a non-rectilinear argon channel. Also the streamer propagation does not follow a straight path. For the 3 slm case, it is clear that the turbulent flow has an impact on the streamer morphology (see figure 1(*c*)). This argon channel is about
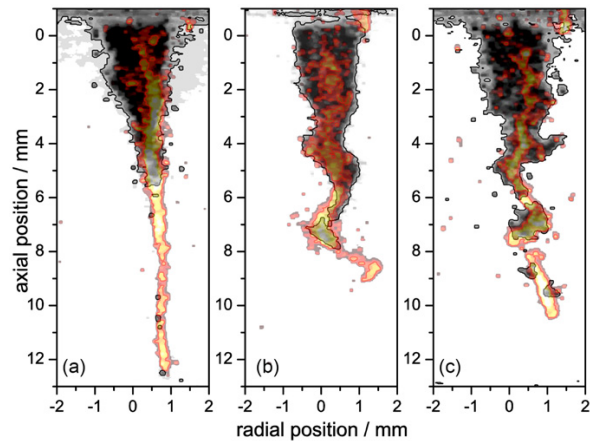

Figure 3. Overlay of the spatial OH fluorescence signal and of the spatial plasma emission (visible and near-infrared) for different argon gas flow rates of (*a*) 0.5 slm, (*b*) 1.0 slm and (*c*) 3.0 slm. Both signals were obtained simultaneously on the same detector.

2 mm in size at the nozzle and thins down as it propagates along the jet-axis. The experimental results show that the streamer propagates into the argon channel from the wider side and ends its propagation within the very thin argon channel surrounded by air impurities from diffusion, at the space where the argon density remains the highest. This means that the streamer is always bound by argon abundance, as shown in figure 3. In the case of 0.5 slm (figure 3(*a*)), the argon flow is laminar, inducing a rectilinear argon channel where the streamer propagates linearly. The argon flow is only clearly visible along the first 5 mm because of the induced fluorescence, which is quenched by the diffusion of ambient species as described previously. Moreover, we observe that the streamer position is well aligned on the axis of a right circular cone resulting from the gradient of the air diffusion into the argon channel. It is especially true towards greater distances from the nozzle. These observations are in perfect agreement with the fact that the streamer propagation follows the highest argon density which obviously is located on the axis of the channel. However, those measurements have been made over a 200 ns gate which means that the flow dynamics remains static with respect to the streamer head propagation. In order to confirm the results observed from single shot acquisitions, successive acquisitions of streamer propagations are recorded with the same gating time with an interval of 100 ms between two shots. At this acquisition frequency, the flow dynamics has time to develop from one shot to the other. Thus, it is ensured that between two consecutive acquisitions, the flow pattern must differ from one to the other in the case of turbulence or non-stationary flow.

Accumulation of 50 streamers is recorded for 0.5 slm and 3 slm flow rates, which correspond to a laminar and a turbulent flow, respectively. The results are presented in figure 4. In the turbulent case at 3 slm, the streamers' spatial distribution is spread over a wider area compared to the laminar case at 0.5 slm. This observation is even more pronounced after a 6 mm distance from the nozzle, where the structure
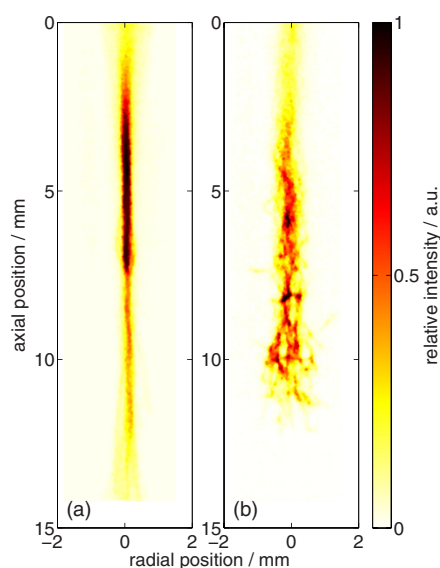
Figure 4. Spatial streamer distribution in the jet effluent for an argon gas flow rate of (*a*) 0.5 slm and (*b*) 3.0 slm. The number of accumulations was 50. (The slight vertical tilt is due to the alignment of the plasma jet.)

of the turbulence is developing, as shown in figure 2(*c*). For the laminar case, (figure 4(*a*)), the position of the streamers remains constant. This is in agreement with the laminar flow pattern measured for the same conditions and presented in figure 2(*a*) . It thus becomes evident that the atmospheric streamers are bound by argon and propagate through this argon channel. A previous study on streamer propagation in argon flow surrounded by air has been published [27]. The authors report that the reason for the propagation of a guided streamer in argon in the ambient air is due to the interface between these two gases. They observe the brightest emission on the edge on the plasma effluent and identify it as an emission from the second positive system of nitrogen, $N_2(C)$, mainly resulting from the efficient energy transfer of the near-resonant transition between the argon metastables of the ($^3P_{0,2}$) states and $N_2(X)$ to produce $N_2(C)$ [28]. In this work, N2(*C*) emission position differs from the referred study and is located in the center of the effluent. Moreover, the highest emission intensity was detected in the range from 4 mm up to 7 mm from the nozzle. This is in excellent agreement with figure 2(*c*)), where one sees that OH quenching by ambient molecules reaches the on-axis. Therefore it can be assumed that metastables of argon are, in the present case, located within the argon channel where the streamer develops. One reliable reason for the difference observed to [27] is attributed to the presence of a grounded ring electrode in the plasma source which must induce a different electric field and thus different ionization mechanisms. Due to the high frequency in the present case, streamer events will benefit from previous ionization and excitation phenomena. The memory effect of metastables and ions contributes largely to the development of the discharge within the argon dominating channel. This is also valid for the turbulent cases as the vortexes remain

constant on the time scale of streamers. A simulation of discharge development in the case of a pure helium laminar flow surrounded by air *without diffusion* explains that so-called streamer bullet propagation is more favourable within the helium tube than in air because of the ionization coefficient differences of each gas [29].

The similarity in streamer path and gas flow path was also found by [30] in pulsed atmospheric pressure plasma streams operated in helium and neon. Interestingly, they found clear evidence that under their experimental conditions, the plasma determines the gas channel behavior and not, as commonly thought, vice versa [25, 30, 31]. Since the mass density of argon is ten times higher than for helium, this plasma-induced gas channel forming is not directly transferable to the argon plasma jet investigated in this work. Hence, for the laminar-to-turbulent transition in the 1.0 slm case when the plasma is switched on, it is not clear whether the streamers are responsible for inducing the turbulence of the argon flow or whether the argon flow becomes turbulent itself by pure fluid dynamics. Experiments with the focus on this effect need to be performed in future. The studies presented in the present work clearly show that the path of highest argon density, lowest air impurity density and streamer propagation are identical.

6. Conclusion

In this study, it was shown by means of PLIF on an atmospheric pressure argon plasma jet that in turbulent mode, the streamer path changes according to the flow pattern changes and the resulting changes in air abundance. Furthermore, with known OH quenching coefficients from a comparison of analytical diffusion calculation and LIF measurements, the air impurity boundary can be determined. Comparing the plasma-on and plasma-off case, it was shown that in the laminar case, the development of KH instabilities is promoted, while in the turbulent flow, the flow patterns remain comparable. Most importantly, it was shown that the streamer pathway is defined by the ambient air diffusing into the effluent. From a convection diffusion model, a steep increase of ambient air particle density in radial direction was revealed. This gradient forms a boundary which leads to the observed streamer enclosure within the argon channel.

Acknowledgments

References

[1] Laroussi M, Hynes W, Akan T, Xinpei L and Tendero C 2008 The plasma pencil: a source of hypersonic cold plasma bullets for biomedical applications *IEEE Trans. Plasma Sci.* **36** 1298–9

[2] Teschke M, Kedzierski J, Finantu-Dinu E G, Korzec D and Engemann J 2005 High-speed photographs of a dielectric barrier atmospheric pressure plasma jet *IEEE Trans. Plasma Sci.* **33** 310–1

[3] Robert E, Sarron V, Ries D, Dozias S, Vandamme M and Pouvesle J M 2012 Characterization of pulsed atmospheric-pressure plasma streams (PAPS) generated by a plasma gun *Plasma Sources Sci. Technol.* **21** 034017

[4] Xiong Z M and Kushner M J 2012 Atmospheric pressure ionization waves propagating through a flexible high aspect ratio capillary channel and impinging upon a target *Plasma Sources Sci. Technol.* **21** 034001

[5] Niemeyer L 2001 *Wiley Encyclopedia of Electrical and Electronics Engineering* (New York: Wiley)

[6] Weltmann K D, Kindel E, Brandenburg R, Meyer C, Bussiahn R, Wilke C and von Woedtke T 2009 Atmospheric pressure plasma jet for medical therapy: plasma parameters and risk estimation *Contrib. Plasma Phys.* **49** 631–40

[7] Reuter S, Winter J, Iseni S, Peters S, Schmidt-Bleker A, Dünnbier M, Schäfer J, Foest R and Weltmann K-D 2012 Detection of ozone in a MHz argon plasma bullet jet *Plasma Sources Sci. Technol.* **21** 034015

[8] Winter J, Wende K, Masur K, Iseni S, Dünnbier M, Hammer M, Tresp H, Weltmann K-D and Reuter S 2013 Feed gas humidity: a vital parameter affecting a cold atmospheric-pressure plasma jet and plasma-treated human skin cells *J. Phys. D: Appl. Phys.* **46** 295401

[9] Verreycken T, van der Horst R M, Sadeghi N and Bruggeman P J 2013 Absolute calibration of OH density in a nanosecond pulsed plasma filament in atmospheric pressure He–H$_2$O: comparison of independent calibration methods *J. Phys. D: Appl. Phys.* **46** 464004

[10] Verreycken T, Mensink R, van der Horst R, Sadeghi N and Bruggeman P J 2013 Absolute OH density measurements in the effluent of a cold atmospheric-pressure Ar–H$_2$O RF plasma jet in air *Plasma Sources Sci. Technol.* **22** 055014

[11] Reuter S, Tresp H, Wende K, Hammer M U, Winter J, Masur K, Schmidt-Bleker A and Weltmann K D 2012 From RONS to ROS: tailoring plasma jet treatment of skin cells *IEEE Trans. Plasma Sci.* **40** 2986–93

[12] LaVision GmbH, DaVis, 8.1.1, 2012, www.lavision.de

[13] LaVision GmbH 2011 *1004067 Image Doubler D80* (Göttingen: LaVision GmbH) p 46

[14] Lozano A, Yip B and Hanson R K 1992 Acetone: a tracer for concentration measurements in gaseous flows by planar laser-induced fluorescence *Exp. Fluids* **13** 369–76

[15] Tanahashi M, Murakami S, Choi G-M, Fukuchi Y and Miyauchi T 2005 Simultaneous CH–OH PLIF and stereoscopic PIV measurements of turbulent premixed flames *Proc. Combust. Inst.* **30** 1665–72

[16] Kanazawa S, Tanaka H, Kajiwara A, Ohkubo T, Nomoto Y, Kocik M, Mizeraczyk J and Chang J S 2007 LIF imaging of OH radicals in DC positive streamer coronas *Thin Solid Films* **515** 4266–71

[17] Pei X, Lu Y, Wu S, Xiong Q and Lu X 2013 A study on the temporally and spatially resolved OH radical distribution of a room-temperature atmospheric-pressure plasma jet by laser-induced fluorescence imaging *Plasma Sources Sci. Technol.* **22** 025023

[18] Verreycken T, Mensink R, Horst R v d, Sadeghi N and Bruggeman P J 2013 Absolute OH density measurements in the effluent of a cold atmospheric-pressure Ar–H2O RF plasma jet in air *Plasma Sources Sci. Technol.* **22** 055014

[19] Dilecce G and De Benedictis S 2011 Laser diagnostics of high-pressure discharges: laser induced fluorescence detection of OH in He/Ar–H$_2$O dielectric barrier discharges *Plasma Phys. Control. Fusion* **53** 124006

[20] Williams L R and Crosley D R 1996 Collisional vibrational energy transfer of OH ($A\,^2\Sigma^+$, $v' = 1$) *J. Chem. Phys.* **104** 6507

[21] Yonemori S, Nakagawa Y, Ono R and Oda T 2012 Measurement of OH density and air–helium mixture ratio in an atmospheric-pressure helium plasma jet *J. Phys. D: Appl. Phys.* **45** 225202

[22] Saìnchez A L, Vera M and Liñán A 2006 Exact solutions for transient mixing of two gases of different densities *Phys. Fluids* **18** 078102

[23] Schmidt-Bleker A, Reuter S and Weltmann K-D 2013 Non-dispersive path mapping approximation for the analysis of ambient species diffusion in the near-field, near-axis region of laminar jets in preparation, for details see www.plasmatis.de/NDPM.html

[24] Kull H J 1991 Theory of the Rayleigh–Taylor instability *Phys. Rep.* **206** 197–325

[25] Sarron V, Robert E, Fontane J, Darny T, Riès D, Dozias S, Joly L and Pouvesle J M 2013 Plasma plume length characterization *21st Int. Symp. on Plasma Chemistry (ISPC 21) (Cairns Convention Centre, Australia)*

[26] van Gessel B, Brandenburg R and Bruggeman P 2013 Electron properties and air mixing in radio frequency driven argon plasma jets at atmospheric pressure *Appl. Phys. Lett.* **103** 064103

[27] Hofmann S, Sobota A and Bruggeman P 2012 Transitions between and control of guided and branching streamers in dc nanosecond pulsed excited plasma jets *IEEE Trans. Plasma Sci.* **40** 2888–99

[28] Nguyen T D and Sadeghi N 1983 Rotational and vibrational distributions of N$_2$($C\,3\Pi u$) excited by state-selected Ar(3P2) and Ar(3P0) metastable atoms *Chem. Phys.* **79** 41–55

[29] Boeuf J P, Yang L L and Pitchford L C 2013 Dynamics of a guided streamer ('plasma bullet') in a helium jet in air at atmospheric pressure *J. Phys. D: Appl. Phys.* **46** 015201

[30] Robert E, Sarron V, Darny T, Riès D, Dozias S, Fontane J, Joly L and Pouvesle J M 2013 Rare gas flow structuration in plasma jet experiments *Plasma Sources Sci. Technol.* submitted

[31] Pouvesle J-M, Sarron V, Robert E, Fontane J, Darny T, Ries D, Dozias S and Joly L 2013 Plasma jets for biomedical applications: PAPS control of the rare gas jets *66th Gaseous Electronics Conf. (Princeton, NJ)* vol 58 (American Physical Society) http://meetings.aps.org/link/BAPS.2013.GEC.MR1.61

Article A3

Quantitative schlieren diagnostics for the determination of ambient species density, gas temperature and calorimetric power of cold atmospheric plasma jets

A Schmidt-Bleker, S Reuter and K-D Weltmann

INP Greifswald / ZIK plasmatis, Felix-Hausdorff-Str. 2, 17489 Greifswald, Germany

E-mail: ansgar.schmidt-bleker@inp-greifswald.de and stephan.reuter@inp-greifswald.de

CrossMark

Abstract

A measurement and evaluation technique for performing quantitative Schlieren diagnostics on an argon-operated cold atmospheric plasma jet is presented. Combined with computational fluid dynamics simulations, the method not only yields the temporally averaged ambient air density and temperature in the effluent of the fully turbulent jet, but also allows for an estimation of the calorimetric power deposited by the plasma.

The change of the refractive index due to mixing of argon and air is in the same range as caused by the temperature increase of less than 35 K in the effluent of the plasma jet. The Schlieren contrast therefore needs to be corrected for the contribution from ambient air diffusion. The Schlieren system can be calibrated accurately using the signal obtained from the argon flow when the plasma is turned off. The temperature measured in this way is compared to the value obtained using a fibre-optics temperature probe and shows excellent agreement. By fitting a heat source in a fluid dynamics simulation to match the measured temperature field, the calorimetric power deposited by the plasma jet can be estimated as 1.1 W.

(Some figures may appear in colour only in the online journal)

1. Introduction

Knowledge about ambient air diffusion and temperature is a vital information for atmospheric pressure plasma sources. Schlieren imaging is a common technique for the visualization of fluid flows and several textbooks give good introductions to the topic [1–4]. Cold atmospheric plasma (CAP) jets are employed as tools in the novel field of plasma medicine [5–8]. For both the biomedical application and for understanding basic chemical mechanisms in low temperature plasmas, a detailed knowledge about the gas temperature and ambient air diffusion into the active plasma zone is crucial. Schlieren imaging has been used to qualitatively study the interaction of the plasma and gas flow in such devices for various geometries and feed gases [9–13]. For plasma sources operated at higher

temperatures also quantitative Schlieren [14] or similar techniques including laser Schlieren deflectometry [15] and quantitative shadowgraphy [16] have been used to determine the gas temperature in the respective plasma devices. However, to the best of the authors knowledge quantitative Schlieren diagnostics have not yet been used for the determination of air densities and gas temperature in CAP jets operating close to room temperature.

With the quantitative Schlieren measurement and evaluation technique presented in this work the temporally averaged argon and accordingly air density as well as the averaged temperature of the fully turbulent CAP jet kinpen Sci is measured by Schlieren imaging. Additionally the calorimetric power deposition is estimated by combining the Schlieren measurements with computational fluid dynamics (CFD) simulations. This

A Schmidt-Bleker *et al*

is challenging as the gas temperature rises by less than 35 K when the plasma is turned on and consequently the change in refractive index due to gas heating lies in the same range as the change due to gas mixing of argon and air. Obtaining both the ambient air density and the gas temperature requires two subsequent measurements with plasma turned off and turned on. In order to be accurate, the method requires that the diffusion process is not significantly affected when the plasma is turned on. Previously the ambient species diffusion was studied using a VUV absorption method combined with an analytical model [17, 18] and molecular beam mass spectrometry [19] and it was found, that the ambient species diffusion into the effluent of the CAP jet is not significantly changed when the plasma is turned on at an argon flux of 3 slm. However, both measurements were performed with the jet not operating in open air, but impinging upon a plate. Several groups have shown, that the plasma can significantly influence the fluid dynamics and a transition of flow regime from laminar to turbulent (or vice versa) can occur when the plasma is switched on [10, 12, 20–22]. This is attributed to electrohydrodynamic forces or temperature effects. In a previous study on the kinpen using planar laser induced fluorescence (PLIF) spectroscopy on OH as tracer molecule (with plasma turned on) as well as PLIF on acetone (with plasma turned off) it was found that while a laminar to turbulent transition does occur at lower feed gas flow rates (1 slm) when the jet is turned on, the flow remains turbulent at a flow rate of 3 slm [23]. The CAP jet is operated in the turbulent regime at an argon flow rate of 3 slm (standard liter per minute) corresponding to a Reynolds number of Re = 2980. Besides quantitative Schlieren diagnostics, the temperature is also measured using a non-metallic fiber-optics probe. Although probe measurements are likely to disturb the plasma and the temperature measurement, very good agreement between both techniques was found. Computational fluid dynamics (CFD) simulations are performed and compared to the Schlieren results. While in the simulation the plasma is merely considered as a heat source, the agreement between the measured and simulated flow fields and temperature distributions in the far-field is very good. The heat source employed in the simulation is consequently used to estimate the calorimetric power in the downstream region of the jet.

2. Methods

2.1. Plasma jet

The plasma jet kinpen Sci previously introduced in [19] is used. As feed gas dry argon at a mass flow rate of 3 slm is used. The jet features a powered inner needle electrode that is mounted in the center of a capillary with radius $r_0 = 0.8$ mm and a grounded outer electrode that can be seen in the image of the jet in figure 1. The inner electrode is driven at a frequency of ~0.9 MHz and a peak-to-peak Voltage of 2.1 kV. The visible plasma effluent measures about 12 mm in length.

2.2. Schlieren diagnostics

2.2.1. Setup.
In figure 2 the experimental setup for the Schlieren and probe measurements is shown. The point light

Figure 1. Image of the argon-operated plasma jet kinpen Sci.

source is constructed by focusing the light from a green LED lamp (HighLED-G, Linos Photonics GmbH, Germany) on an aperture with a diameter of $d = 0.2$ mm. Between the focusing lens and and the aperture a diffusion disc is placed in order to achieve an homogeneous lighting in the test region. The aperture is placed in the focal point of a best-form lens (focal length $f = 200$ mm), which creates the parallel light test region of the Schlieren system. Best form lenses are used in order to minimize spherical aberration. After passing through the test region in which the plasma jet is placed, the parallel light is again focused by another lens ($f = 200$ mm) on the knife edge. The knife edge is adjusted so that the detected intensity signal is reduced to approximately 42% of the signal without knife edge. The Schlieren signal is imaged using a simple 8 bit USB camera (DCC1545M, Thorlabs, USA). In front of the camera a dielectric filter with a transmission wavelength of 550 nm at a full width at half maximum of 10 nm is used. The combination of a green light source and this filter is chosen as the jet does not emit any light in this wavelength region. As the light intensity from the point source is not very high due to the small aperture, any light emitted by the jet makes the measurement impossible. It is noted, that a subsequent subtraction of the light emitted by the plasma jet is difficult, as the emission is not perfectly constant in time. For probe measurements of the gas temperature, a non-metallic fiber-optics probe mounted on a three-axis linear table is used. The device determines the temperature by spectroscopically measuring the band gap of a GaAs crystal which is deposited at the tip of the optical fiber (FOTEMP1-OEM and TS3, Optocon AG, Germany).

2.2.2. Theory.
The refractive index of a gaseous medium depends on the molecular composition, its density or pressure and the wavelength. The well-known Lorenz–Lorentz (also termed Clausius–Mossotti) equation

$$\frac{n^2 - 1}{n^2 + 2} = \frac{4\pi}{3} N \sum_i x_i \alpha_i \qquad (1)$$
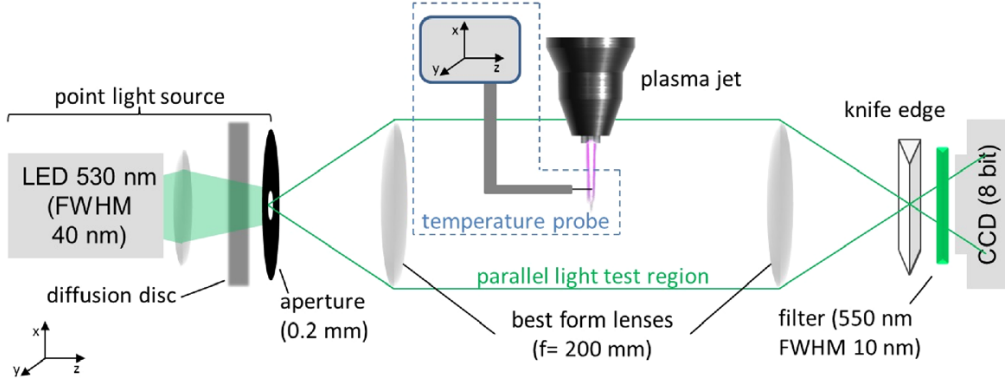
Original Publications

J. Phys. D: Appl. Phys. **48** (2015) 175202   A Schmidt-Bleker *et al*

Figure 2. Experimental setup.

relates the refractive index n of a medium at a given wavelength to the mean polarizability α_i of species i at the molar fraction x_i and particle density N. For gases the deviation from the refractive index in vacuum $n - 1 = \varepsilon \ll 1$ is very small. Expanding (1) to first order in ε yields the Gladstone–Dale relation

$$\varepsilon = N/N_r \sum_i \epsilon_{r,i} x_i = \frac{pT_r}{Tp_r} \sum_i \epsilon_{r,i} x_i,, \qquad (2)$$

where $1 + \epsilon_{r_i}$ denotes a reference index of refraction for species i at density N_r. In equation (2) the density can be replaced by the pressure p and temperature T using the ideal gas law. Note that in the literature equation (2) is often formulated using mass fractions instead of molar fractions. A Schlieren measurement of the temperature hence requires knowledge of the local gas composition, pressure and reference values $n_{r,i}$ for the refractive indices which can be found in the literature. The Schlieren system measures the derivative of the refractive index in y-direction (determined by the orientation of the knife edge). As the parallel light beam passes the test region in z-direction, the signal is integrated in z-direction. It can be shown (see e.g. [1]), that the intensity I measured on the detector relates to the refractive index in the test region for $\varepsilon \ll 1$ via the measured contrast

$$c = \frac{I - I_k}{I_k} = S \int_{-\infty}^{\infty} \frac{\partial n}{\partial y}\, \mathrm{d}z = S \frac{\partial}{\partial y}\left(2 \int \frac{n(r)r}{\sqrt{y^2 - r^2}}\, \mathrm{d}r \right). \quad (3)$$

Here I_k is the signal measured without any Schlieren in the test region and an axisymmetric distribution of the gas causing the Schlieren signal is assumed, where the axis points in x-direction. S is the sensitivity of the Schlieren system and is determined by the geometry of the setup and can either be calculated as discussed in the appendix A or obtained from the experimental data as described in section 3. Equation (3) is the y-derivative of the Abel transform of $n(r)S$. Using Abels inversion formula, $n(r)$ can be calculated from

$$n(r) - n_0 = \underbrace{\frac{1}{S} \int_r^{\infty} \frac{c(y)\, \mathrm{d}y}{\pi\sqrt{y^2 - r^2}}}_{\hat{c}(n)}. \qquad (4)$$

Note, that compared to the standard Abel inversion formula, $c(y)$ is not derived in y-direction in $\hat{c}$, as the Schlieren system already gives the y-derived quantity. In the following, we will term $\hat{c}$ as modified Abel inversion of c. Together with (2) this yields

$$n_0 + \hat{c}/S - 1 = \frac{N}{N_r} \sum_i \epsilon_{r,i} x_i. \qquad (5)$$

The determination of the temperature now requires two measurements: First, the mole fraction of argon and air need to be determined. This can be achieved by measuring the contrast $c_{\mathrm{fl.}}$ when only the gas flow is turned on, but the plasma is not ignited. In a second measurement, the plasma is turned on and the respective contrast $c_{\mathrm{pl.}}$ is measured. The gas temperature in the effluent can be determined using equation (5) together with the ideal gas law:

$$T = T_0 \frac{n_0 + \hat{c}_{\mathrm{fl.}}/S - 1}{n_0 + \hat{c}_{\mathrm{pl.}}/S - 1} F \qquad (6)$$

with factor

$$F = \frac{\epsilon_{\mathrm{r,air}} + x_{\mathrm{Ar,pl.}}(n_{\mathrm{Ar}} - n_{\mathrm{air}})}{\epsilon_{\mathrm{r,air}} + x_{\mathrm{Ar,fl.}}(n_{\mathrm{Ar}} - n_{\mathrm{air}})}, \qquad (7)$$

where T_0 denotes the ambient gas temperature.

2.2.3. Data processing. In order to determine the contrast, the intensity I is measured for the plasma on and plasma off case and is then divided by I_0 as evident from equation (3). The relative intensities are obtained by averaging a 1280×1024 pixel, 1000-frame video sequence with an exposure time of 89 ms per frame. Figure 3 shows the contrast $c_{\mathrm{fl.}}$ and $c_{\mathrm{pl.}}$ obtained for both measurements.

Before a modified Abel inversion can be performed, the axis of symmetry needs to be determined. As shown in figure 4, the centerline can accurately be found by displaying only data that is close to zero. Before further processing, it is essential to turn the image so that the axis of symmetry points in vertical direction. In figure 5 the contrast along the two lateral cuts indicated in figure 3 is shown. The lateral cut at 1.5 mm shown in figure 5(*a*) demonstrates that the signal in the plasma on case is not completely symmetric in the near field. However, already at a distance of 5 mm the asymmetry vanishes. Although the data is already very smooth due to the averaging procedure,
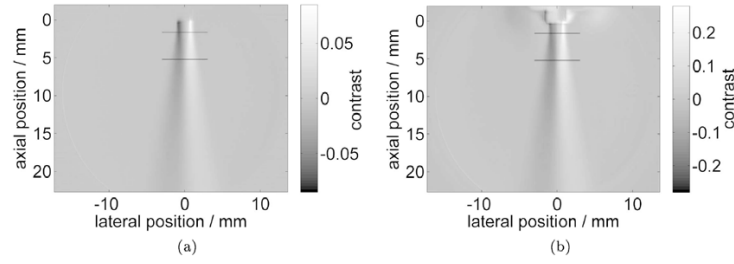
Figure 3. Schlieren contrast obtained (*a*) for an argon gas flow of 3 slm and (*b*) when plasma is turned on.

a smoothing algorithm [24] is employed to speed-up the modified Abel inversion. The data is then interpolated using piecewise cubic Hermite polynomials. The expression for $\hat{c}$ in equation (4) assumes that the data is point symmetric and hence only takes values of $c(y)$ for $y > 0$ into account. In order to use the complete measured data the values for $y < 0$ inverted in the point of origin and the contributions from $y < 0$ and $y > 0$ are then averaged, as illustrated by the dashed line in figure 5. Now the Integral $\hat{c}$ is calculated for each line in the region of interest. As noise should not be integrated in the modified Abel-Inversion, an upper integration limit is set for each row of the image, as indicated by the dashed line in figure 4.

2.2.4. Refractive indices. An acurate determination of the refractive indices is crucial for the correct evaluation of the Schlieren measurements. Apart from the wavelength and temperature, the refractive index of air depends on the humidity and the CO_2 content. The relative humidity in the lab was measured to be 43% using a hygrometer (DewMaster, EdgeTech, USA), the CO_2 concentration was assumed to be 450 ppm and the central transmission wavelength of the filter is 550 nm. The room temperature was measured to be 294.7 K. For the calculation of the refractive index the web application provided by the National Institute for Standards and Technology was used, which is based on the Ciddor equation and yields $n_{air} - 1 = 2.713 \times 10^{-4}$ [25, 26]. For argon a refractive index $n_{Ar} - 1 = 2.619 \times 10^{-4}$ for a wavelength of 546 nm was used from [27].

2.3. Computational fluid dynamics simulations

The CFD simulation was performed using COMSOL 4.2 with the CFD module as described in the previous publication [28]. The compressible Reynolds-averaged Navier–Stokes equations are solved and a standard $k - \varepsilon$-model is employed to account for the turbulence. Rotational symmetry is assumed in the model. Additionally to the simulations presented in [28], the heat transport equation

$$\rho C_p \mathbf{u} \cdot \nabla T = \nabla \cdot (k \nabla T) + Q \tag{8}$$

is coupled to the Navier–Stokes equations. Here C_p is the heat capacity at constant pressure, $\mathbf{u}$ the velocity field, k the thermal conductivity and Q is the heat source term. For the thermal conductivity the Kays–Crawford model was employed to account for the turbulent heat transport [29]. The heat capacity of the gas is weighted according to the mole fractions of argon and air as $C_p = \sum_i x_i C_{p,i}$.
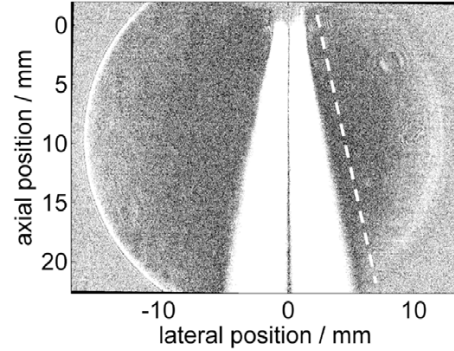
Figure 4. Displaying only contrast values close to zero makes finding the axis of symmetry easy. The dashed line indicates the upper bound that is used for the modified Abel inversion integral at the respective axial position after averaging the values from the left and right side of the axis.

The geometry used in the CFD simulation is shown in figure 6. The right hand side of figure 6 illustrates the boundary conditions used. At boundary *A* an inflow of 3 slm argon is defined corresponding to an average velocity $v_{av} = 25$ m s^{-1} at the jet nozzle, at boundary *B* a normal inflow velocity of $v_B = 0.1$ m s^{-1} is defined to obtain faster convergence (further decreasing v_B does not influence the densities obtained in the effluent), at *C* an outlet is defined. The temperature of the inflowing gas at boundaries *A* and *B* is set to $T_0 = 294.7$ K which is the ambient room temperature measured when the Schlieren experiment was performed. All other boundaries were assumed to be thermally insulating.

Two studies corresponding to the two Schlieren experiments performed: In the first study, the heat term was set to $Q = 0$, which consequently yields an isothermal result. In the second study the heat source term was set to

$$Q = 2.36(1 - r^4/r_0^4)\ 10^8 \text{Wm}^{-3} \tag{9}$$

in the domain between the pin-type electrode and the nozzle exit as shown in the left part of figure 6. The total power deposited hence amounts to $P = 1.12$ W.

3. Results and discussion

3.1. Density

Figure 7 shows the mole fraction of argon obtained by the isothermal CFD simulation and the Schlieren measurement.
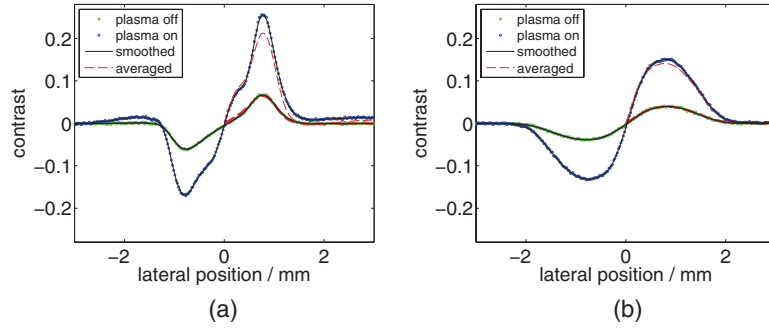
Figure 5. Lateral cuts through the data along the lines shown in figure 3 located at axial positions of (*a*) 1.5 mm and (*b*) 5 mm.
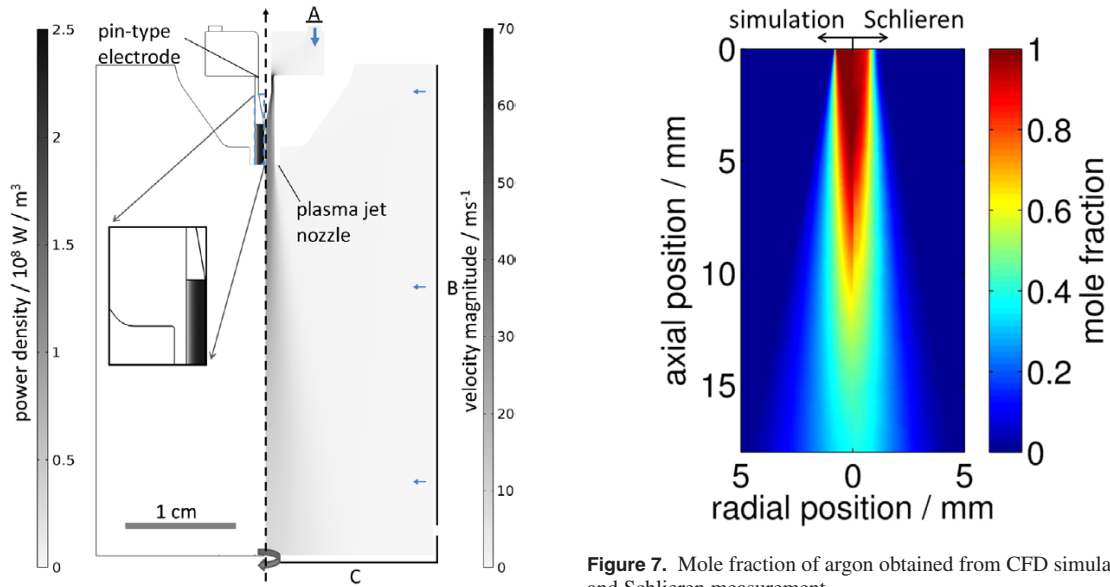

Figure 6. Geometry used in the CFD simulation. The left side illustrates the heat source term used for the thermal case, while the right side depicts the velocity magnitude and the influx of argon and air applied in the model.

The agreement between the measurement and the simulation is very good. However, some deviations can be observed in the axial and lateral cuts of this data shown in figure 8: the on-axis density values drop a bit earlier in the measured values compared to the simulation. It is unclear however, if this is due to uncertainties in the simulations, or due to systematic errors of the measurement. The good agreement between experiment and simulation for larger radial distances ($r > 0.8$ mm) observed in figure 8(*b*) may indicate that the deviations for the on-axis values result from errors linked to the evaluation procedure: In the modified Abel inversion of the contrast values obtained for a specific radial position $r = r_1$ depend on all the data obtained in the domain $r > r_1$. Small deviations may therefore add up towards the axis. Previous CFD simulations of the jet impinging on a plate yielded very good agreement with quantitative molecular beam mass spectroscopy measurements of the on-axis densities. Another kind of deviation can be seen for the lateral cut at $z = 0.5$ mm. Here the simulated profile drops steeper than the measured profile
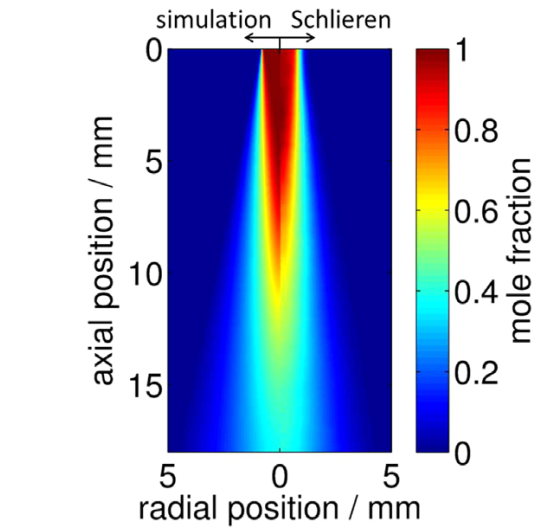
Figure 7. Mole fraction of argon obtained from CFD simulation and Schlieren measurement.

at the rim of the nozzle. This probably results from the finite spatial resolution of the Schlieren system due to the aperture with 0.2 mm diameter. The agreement at an axial distance of 15 mm is excellent. Note that the parameter S describing the sensitivity of the Schlieren system was fitted so that we obtain an argon mole fraction of $x_{Ar} = 1$ at the jet nozzle. This calibration method proved to be more accurate than the direct calculation of the sensitivity as discussed in the appendix A and also yields correct temperature values as presented in the following section.

3.2. Temperature and power

Figure 9 shows the temperature obtained by the CFD simulation with heat source and the measured temperature assuming no change in air mole fraction, hence $F = 1$ in equation (7). Compared to the mole fraction profile in figure 7 the measured temperature distribution looks very similar, which indicates that no flow regime transition occurred and, since the diffusion is dominated by the turbulent diffusive transport (the computed turbulent diffusion coefficient is 10 to 50 times larger than the molecular diffusion coefficient in the effluent region), no
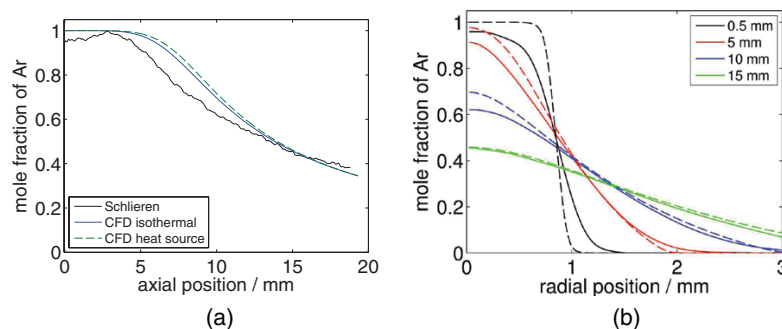
Figure 8. (*a*) Axial and (*b*) lateral cut through the density profile shown in figure 7. In (*a*) the measurement is compared to data obtained from the isothermal and thermal CFD simulation. In (*b*) the dashed lines indicate the simulation results.
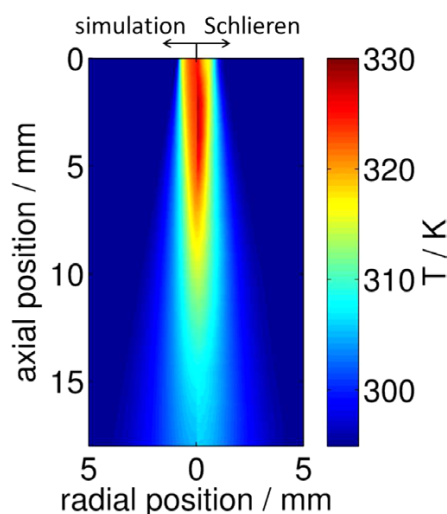

Figure 9. Temperature obtained from CFD simulation and Schlieren measurement.

drastic change in average mole fractions is expected. An absolute difference of 10% in the average mole fractions $x_{Ar,pl./fl.}$ would result in a maximum error of 1.2 K according to equation (7). The experimental results are in agreement with the CFD simulations: figure 8(*a*) shows the mole fraction of argon obtained from the CFD simulations both with and without heat source and both yield almost identical mole fractions. The input power for the CFD simulation was adjusted to yield the same far-field temperature as obtained from experimental data. From experimental temperature data in figure 7 it is clear that in the near effluent some heating still occurs. In the CFD simulations this additional heat source is compensated by a broader temperature profile at the nozzle exit. This can be seen in the axial and lateral cuts presented in figure 10. Figure 10(*a*) also shows the temperature obtained from the probe measurement. Both experimental results agree very well, which was not expected a priori in the region of the visible effluent, as the probe was thought to possibly influence the plasma. However, the Schlieren measurement yields slightly higher temperature values in the region between 2 mm and 6 mm axial distance. This could result from the finite size of the temperature probe, which may lead to some slight smoothing of the temperature

or from the asymmetry of the temperature field in the vicinity of the jet nozzle (see figure 5). The probe measurements also yield information about the temperature inside of the device, where the temperature appears to rise linearly from the tip of the needle electrode towards the nozzle exit. The good agreement between the experimental data and the CFD simulations in this region indicate that a quite homogeneous average volume heating inside of the device can be expected.

In figure 10(*a*) the effect of neglecting the difference between the refractive indices of argon and air also becomes clear: The uncorrected evaluation (for which $n_{air} = n_{Ar}$ was assumed) yields too high temperature values.

Obtaining the correct calorimetric power from the measurements requires, that not only the temperature, but also the mole fractions of argon and air are known in the far-field, as $C_{p,air} \approx 2C_{p,Ar}$. As evident from the far-field values shown in figures 8(*b*) and 10(*b*), both mole fractions and temperature of the CFD simulation and Schlieren measurement agree very well. As for axial distances larger than 8 mm no significant heating takes place, it can be assumed that the thermal input power of $P = 1.1$ W gives a good estimation of the thermal power deposited by the plasma jet, whereas a systematic error in the order of 5% is assumed.

The jet used in this study is very similar to the plasma jet investigated in [17], for which an ozone production rate of 2.5×10^{16} particles/s was measured. As ozone is the dominant reactive species in the far-field of the jet (the production rate of the second most abundant species NO_2 is 40 times less), this value can be used to estimate the chemical energy stored in the far-field of the jet. According to the kinetic model presented by van Gaens and Bogaerts for a similar argon CAP jet, only a small amount of atomic oxygen can be expected in the far-field (at 15 mm distance) of the jet, which is quickly converted to ozone as it reacts with molecular oxygen [30]. As ozone is almost exclusively generated from this reaction, half of the bond-dissociation energy of oxygen (497 kJ mol^{-1}) multiplied with the ozone production rate is used as an upper limit estimate for the chemical far-field power. The respective power stored in chemical energy in the far-field thus amounts to approximately 0.01 W and hence is much smaller than the thermal far-field energy. Another energy loss channel is the radiation emitted by the jet which is not quantified here but can also contain a significant part of the input power [31].
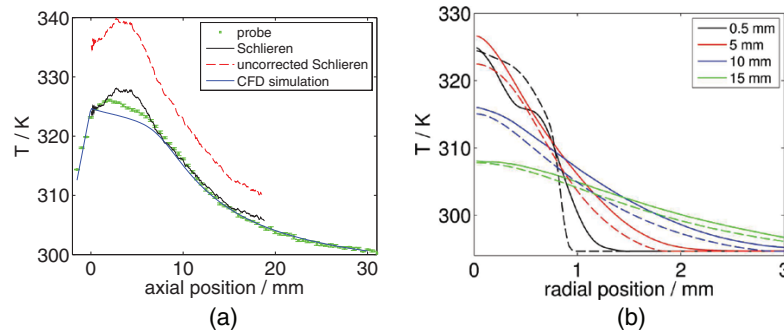
Figure 10. Axial and (*b*) lateral cut through the temperature profile shown in figure 9. In (*a*) the measurement is compared to data obtained from the CFD simulation and probe measurements. Additionally, the temperature that is obtained when the refraction of argon is not corrected for is shown. In (*b*) the dashed lines indicate the simulation results.

The thermal power value stated here is therefore a good estimate for the power that is transfered to the plasma minus the radiation losses that do not contribute to reactive species generation in the far-field. For the very similar plasma jet kinpen 09 (neoplas GmbH, Germany) a power of 1.4 W to 1.8 W was recently measured for molecular admixtures of up to 1% [32] by performing an electrical measurement following the method presented in [33]. As this method determines the total plasma input power, the slightly higher value is consistent with the value obtained in the present work.

4. Conclusion

Quantitative Schlieren measurements are a simple and precise technique for the determination of both the ambient air density and the temperature in CAP jets. The maximum temperature measured in the effluent of the CAP jet is 328 K. For obtaining precise temperature measurements it is necessary to verify that the flow regime does not change from laminar to turbulent (or vice versa) when the plasma is turned on. The fact that for low gas temperatures the change of the index of refraction due to the mixing of argon and air is in the same order of magnitude as the change due to the gas temperature is not problematic. In the contrary, the pure argon flux (with plasma turned off) can be used to calibrate the system in the sensitivity region of interest. Note, that since the jet studied operates in the turbulent flow regime and the exposure time is in the order of several seconds, the measured densities and temperatures are temporally averaged values, which on a shorter timescale undergo significant fluctuations.

The temperature obtained from the Schlieren images have been compared to measurements with an fiber-optics probe. While a deviation between both techniques was expected as the probe was thought to influence the plasma, the measured deviation was not more than 3 K. The probe was also used to measure the temperature inside of the capillary where a Schlieren measurement cannot be performed. Here a linear increase of the temperature towards the nozzle exit was found. Additionally to the measurements, CFD simulations of the jet with plasma turned off and turned on were performed. In order to mimic the heating of the gas by the exothermic reactions and thermalization of fast particles in the plasma, a heat source term was added to
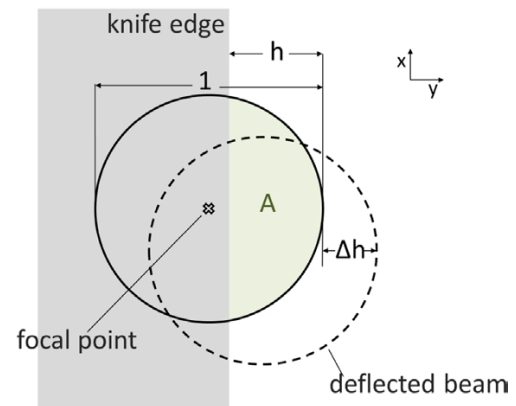
Figure A1. The aperture is imaged on the knife edge. The circle segment *A* of height is not blocked and contributes to the illumination on the CCD. A beam deflected in *y*-direction by a distance Δ is detected as it produces a higher or lower intensity on the CCD.

the heat transport equation located inside of the capillary. The simulation also yields a linear temperature increase in the capillary and produces the correct far-field air density (and hence heat capacity) and temperature. Therefore the power of 1.1 W applied in the CFD simulation gives a good calorimetric power estimation for the CAP jet. The comparison of the temperature distribution obtained from simulation and Schlieren measurement clearly shows that while most of the heat is deposited inside of the device, some heating also takes place in the effluent up to a distance of about 5 mm from the nozzle exit.

Appendix A.   Linear contrast region for circular apertures

Slits are more commonly used for Schlieren systems and most textbooks focus on such rectangular apertures. However,
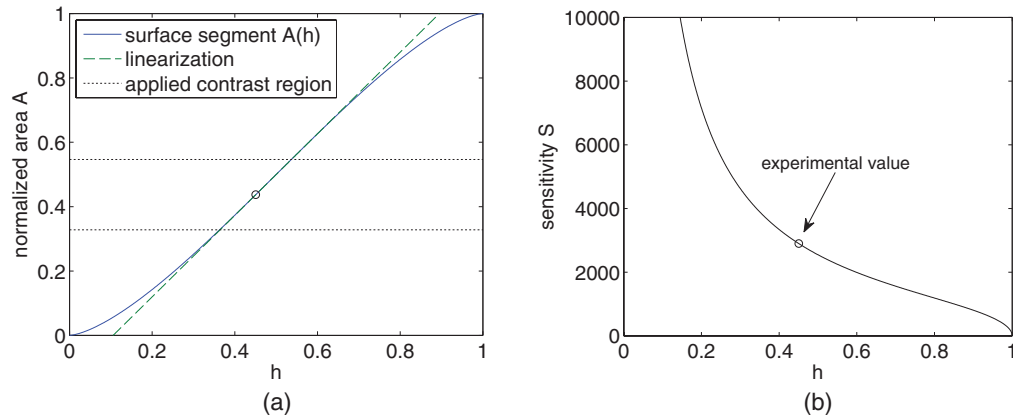
Figure A2. The circular aperture used in the Schlieren system is imaged onto the knife edge. A fraction corresponding to the normalized surface area of height h shown in (a) passes the knife edge, yielding the sensitivity as shown in (b).

circular apertures are attractive if a high spatial resolution is required. While circular apertures are covered in [4], the nonlinear behavior that can arise is neglected. In the following the issue should therefore be discussed briefly.

The Schlieren system images the aperture onto the knife edge. Let I_0 be the intensity measured on the detector without any Schlieren in the test region and without knife edge installed. When the knife edge is inserted, the intensity is homogeneously reduced to

$$I_k = I_0 A(h), \tag{A.1}$$

where

$$A(h) = (\arccos{(1 - 2h)} - 2\sqrt{h(1 - h)}(1 - 2h))/\pi \tag{A.2}$$

is the normalized area of the segment of a circle with diameter d of height h/d as shown in figure A1(a). A beam of light that is deflected at an angle α in y-direction in the test region is hence displaced by $\Delta h = \pm \alpha f/d$ at the knife edge (for $\alpha \ll 1$), whereas the sign depends on the orientation of the knife edge. This locally leads to a change in intensity of

$$I = I_k S(h + \Delta h) \approx I_k(A(h) + \Delta h A'(h)) \tag{A.3}$$

on the detector. The contrast can now be expressed as

$$c = \frac{I - I_k}{I_k} = \frac{\Delta h A'(h)}{A(h)} = \underbrace{\pm \frac{fA'(h)}{dA(h)}}_{S} \alpha \tag{A.4}$$

Together with the expression for the deviation angle (see e.g. [1] for derivation)

$$\alpha = \int \frac{\partial n}{\partial y} \, \mathrm{d}z \tag{A.5}$$

this yields equation (3) which is the basis for the quantitative evaluation of the Schlieren contrast.

The linearization in equation (A.3) is only valid if h is not too close to 0 or 1 and Δh is small. Although a higher contrast may always be achieved by choosing a lower value for h and hence increasing the factor $A'(h)/A(h)$ in (A.4), as can be seen in figure A2(a), this may result in a nonlinearity which must then be taken into account.

The sensitivity of the Schlieren system can be determined by measuring the ratio of the intensities $I_k/I_0 = A(h)$ and calculating S for the respective value of h. However, due to the strong dependence of the sensitivity on h, small errors significantly affect the densities and temperatures evaluated. For the present setup case the intensity ratio was measured to be $I_k/I_0 = 42\%$, which would yield a mole fraction of argon at the nozzle of $x_{Ar} = 0.94$, which is obviously too low. The deviation is not drastic, but as the mole fraction of argon at the nozzle is known to be $x_{Ar} = 1$, the system was calibrated using the argon Schlieren signal as described in section 3.1. Alternatively, the system could also be calibrated using the probe measurements for the temperature in the far-field which, as evident from figure 10, would yield the same results.

The sensitivity obtained in this way yields a value $h = 0.45$ as shown in figure A2(b), while the respective value for the circle segment is $A(h) = I_k/I_0 = 0.437$. Since the contrast in all experiments $c < 0.25$ (see figure 3) is small enough, the linearization in (A.3) can be applied.

References

[1] Goldstein R 1996 *Fluid Mechanics Measurements* (Boca Raton, FL: CRC Press)
[2] Merzkirch W 1987 *Flow Visualization* (Amsterdam: Elsevier)
[3] Settles G S 2001 *Schlieren and Shadowgraph Techniques* (Berlin: Springer)
[4] Panigrahi P K and Muralidhar K 2012 *Schlieren and Shadowgraph Methods in Heat and Mass Transfer* **2** (Berlin: Springer)
[5] Fridman G, Friedman G, Gutsol A, Shekhter A B, Vasilets V N and Fridman A 2008 Applied plasma medicine *Plasma Proc. Polym.* **5** 503–33
[6] Weltmann K D, Kindel E, von Woedtke T, Hähnel M, Stieber M and Brandenburg R 2010 Atmospheric-pressure plasma sources: prospective tools for plasma medicine *Pure Appl. Chem.* **82** 1223–37
[7] Laroussi M, Kong M G and Morfill G 2012 *Plasma Medicine: Applications of Low-Temperature Gas Plasmas in Medicine and Biology* (Cambridge: Cambridge University Press)
[8] von Woedtke T, Reuter S, Masur K and K-D Weltmann 2013 Plasmas for medicine *Phys. Rep.* **530** 291–320

[9] Jiang N, Yang J, He F and Cao Z 2011 Interplay of discharge and gas flow in atmospheric pressure plasma jets *J. Appl. Phys.* **109** 093305

[10] Oh J-S, Olabanji O T, Hale C, Mariani R, Kontis K and Bradley J W 2011 Imaging gas and plasma interactions in the surface-chemical modification of polymers using micro-plasma jets *J. Phys.* D*: Appl. Phys.* **44** 155206

[11] Ghasemi M, Olszewski P, Bradley J W and Walsh J L 2013 Interaction of multiple plasma plumes in an atmospheric pressure plasma jet array *J. Phys.* D*: Appl. Phys.* **46** 052001

[12] Robert E, Sarron V, Darny T, Riès D , Dozias S, Fontane J, Joly L and Pouvesle J-M 2014 Rare gas flow structuration in plasma jet experiments *Plasma Sources Sci. Technol.* **23** 012003

[13] Boselli M, Colombo V, Ghedini E, Gherardi M, Laurita R, Liguori A, Sanibondi P and Stancampiano A 2014 Schlieren high-speed imaging of a nanosecond pulsed atmospheric pressure non-equilibrium plasma jet *Plasma Chem. Plasma Proc.* **34** 853–69

[14] Sutton Y, Moorev J, Sharp D and Braithwaite N S J 2011 Looking into a plasma loudspeaker *IEEE Trans. Plasma Sci.* **39** 2146–7

[15] Schäfer J, Foest R, Reuter S, Kewitz T, Šperka J and K-D Weltmann 2012 Laser schlieren deflectometry for temperature analysis of filamentary non-thermal atmospheric pressure plasma *Rev. Sci. Instrum.* **83** 103506

[16] De Izarra G, Cerqueira N and De Izarra C 2011 Quantitative shadowgraphy on a laminar argon plasma jet at atmospheric pressure *J. Phys. D: Appl. Phys.* **44** 485202

[17] Schmidt-Bleker A, Winter J, Iseni S, Dünnbier M, Weltmann K D and Reuter S 2014 Reactive species output of a plasma jet with a shielding gas device: combination of ftir absorption spectroscopy and gas phase modelling *J. Phys. D: Appl. Phys.* **47** 145201

[18] Reuter S *et al* 2012 Atomic oxygen in a cold argon plasma jet: talif spectroscopy in ambient air with modelling and measurements of ambient species diffusion *Plasma Sources Sc. Technol.* **21** 24005–11

[19] Dünnbier M, Schmidt-Bleker A, Winter J, Wolfram M, Hippler R, Weltmann K D and Reuter S 2013 Ambient air particle transport into the effluent of a cold atmospheric-pressure argon plasma jet investigated by molecular beam mass spectrometry *J. Phys.* D*: Appl. Phys.* **46** 435203

[20] Foletto M, Puech V, Fontane J, Joly L and Pitchford L C 2014 Evidence of the influence of plasma jets on a helium flow into open air *IEEE Trans. Plasma Sci.* **42** 2436–7

[21] Papadopoulos P K, Vafeas P, Svarnas P, Gazeli K, Hatzikonstantinou P M, Gkelios A and Clement F 2014 Interpretation of the gas flow field modification induced by guided streamer ('plasma bullet') propagation *J. Phys. D: Appl. Phys.* **47** 425203

[22] Zhang S, Sobota A, van Veldhuizen E M and Bruggeman P J 2015 Gas flow characteristics of a time modulated appj: the effect of gas heating on flow dynamics *J. Phys. D: Appl. Phys.* **48** 015203

[23] Iseni S, Schmidt-Bleker A, Winter J, Weltmann K D and Reuter S 2014 Atmospheric pressure streamer follows the turbulent argon air boundary in a mhz argon plasma jet investigated by oh-tracer plif spectroscopy *J. Phys. D: Appl. Phys.* **47** 152001

[24] Garcia D 2010 Robust smoothing of gridded data in one and higher dimensions with missing values *Comput. Stat. Data Anal.* **54** 1167–78

[25] National Institute of Standards and Technology. Engineering metrology toolbox http://emtoolbox.nist.gov/Wavelength/Ciddor.asp (Last updated November 2004)

[26] Ciddor P E 1996 Refractive index of air: new equations for the visible and near infrared *Appl. Opt.* **35** 1566–73

[27] Weber M J 2002 *Handbook of Optical Materials* **19** (Boca Raton, FL: CRC press)

[28] Reuter S, Tresp H, Wende K, Hammer M U, Winter J, Masur K, Schmidt-Bleker A and Weltmann K 2012 From rons to ros: tailoring plasma jet treatment of skin cells *IEEE Trans. Plasma Sci.* **40** 2986–93

[29] Kays W M, Crawford M E and Weigand B 1980 *Convective Heat Transfer* (New York: McGraw-Hill) pp 45–57

[30] van Gaens W and Bogaerts A 2013 Kinetic modelling for an atmospheric pressure argon plasma jet in humid air *J. Phys. D: Appl. Phys.* **46** 275201

[31] Despax B, Pascal O, Gherardi N, Naude N, Belinger A and Pitchford L C 2012 Influence of electromagnetic radiation on the power balance in a radiofrequency microdischarge with a hollow needle electrode *Appl. Phys. Lett.* **101** 144104

[32] van Gaens W, Iseni S, Schmidt-Bleker A, Weltmann K-D, Reuter S and Bogaerts A 2014 Numerical analysis of the effect of nitrogen and oxygen admixtures on the chemistry of an argon plasma jet operating at atmospheric pressure *New J. Phys.* **17** 033003

[33] Hofmann S, Van Gessel A, Verreycken T and Bruggeman P 2011 Power dissipation, gas temperatures and electron densities of cold atmospheric pressure helium and argon rf plasma jets *Plasma Sources Sci. Technol.* **20** 065010

Article A4

From RONS to ROS: Tailoring Plasma Jet Treatment of Skin Cells

Stephan Reuter, *Member, IEEE*, Helena Tresp, Kristian Wende, Malte U. Hammer, Jörn Winter,
Kai Masur, Ansgar Schmidt-Bleker, and Klaus-Dieter Weltmann, *Member, IEEE*

Abstract—Finding a solution for air species contamination of atmospheric pressure plasmas in plasma medical treatment is a major task for the new field of plasma medicine. Several approaches use complex climate chambers to control the surrounding atmosphere. In this paper, ambient species are excluded in plasma–human-skin-cell treatment by ensheathing the plasma jet effluent with a shielding gas. Not only does this gas curtain protect the plasma jet effluent from inflow of air species but it also, more importantly, allows controlling the effluent reactive species composition by adjusting the mixture of the shielding gas. In the present investigations, the mixture of nitrogen to oxygen within the gas curtain around an argon atmospheric pressure plasma jet (kinpen) is varied. The resulting reactive plasma components produced in the jet effluent are thus either oxygen or nitrogen dominated. With this gas curtain, the effect of reactive oxygen species (ROS) and reactive nitrogen species (RNS) on the cell viability of indirectly plasma-treated HaCaT skin cells is studied. This human keratinocyte cell line is an established standard for a skin model system. The cell viability is determined by a fluorometric assay, where metabolically active cells transform nonfluorescent resazurin to the highly fluorescent resorufin. Plasma jet and gas curtain are characterized by numerical flow simulation as well as by optical emission spectroscopy. The generation of nitrite within the used standard cell culture medium serves as a measure for generated RNS. Measurements with the leukodye dichlorodihydrofluorescein diacetate show that, despite a variation of the shielding gas mixture, the total amount of generated reactive oxygen plus nitrogen species is constant. It is shown that a plasma dominated by RNS disrupts cellular growth less than a ROS-dominated plasma.

Index Terms—Atmospheric pressure plasma jet, gas curtain, plasma liquid interaction, plasma medicine, reactive nitrogen species (RNS), reactive oxygen plus nitrogen species (RONS), reactive oxygen species (ROS), skin cells.

I. INTRODUCTION

FUNDAMENTAL understanding of processes in plasma medical research can hardly be reached unless treatment effects of plasma jets with biological matter can be investigated separately. Particularly in this field of research, however, plasma sources are—and need to be—operated in ambient atmosphere [1]–[3], which results in hard-to-define conditions. These plasma sources generate a high density of reactive oxygen or nitrogen species [4], [5]. A significant factor in plasma-generated reactive species composition is the inflow of atmospheric species introducing a mixture of nitrogen, oxygen, or water impurities in significant quantities [6]. This uncontrolled influence makes it impossible to separate effects of, e.g., reactive nitrogen or oxygen species.

One approach frequently used is to perform investigations in large or complex climate chambers, which poses a drastic interference with the experimental conditions. In this paper, on the treatment effects of an atmospheric pressure argon plasma jet (kinpen) [7] on human-skin cells, ambient species are excluded by ensheathing the plasma jet with a gas curtain. This curtain serves two purposes: 1) It protects the jet effluent from inflow of air species, and 2) it allows controlling the type of species diffusing from the shielding gas into the jet effluent. By a variation of oxygen-to-nitrogen ratio in the gas curtain, the ratio of plasma-generated reactive oxygen to nitrogen species is investigated, and their respective effect on the cell viability—a combined factor of cell vitality and cell division rate—of so-called human adult low-calcium high-temperature keratinocyte (*HaCaT*) skin cells is studied. The human keratinocyte cell line of HaCaT cells is an established standard for a skin model system. This cell line represents an *in vitro* spontaneously transformed type of keratinocytes from histologically normal skin and was the first epithelial cell line from adult human skin that exhibits normal differentiation [8]. It therefore provides a promising tool for studying skin-cell-related regulatory and metabolic pathways. Since almost all eukaryotic cells depend on the oxygen-consummating respiratory chain, they all possess a set of reactive oxygen species (ROS) defense mechanism as certain percentage (2%–3%) of oxygen ends up as ROS [9]. Efficiency and composition of these systems vary between the different eukaryotic cell types on a wide scale. Concerning the HaCaT cells, research already revealed some of the mechanisms present or involved [10]. These reactive oxygen or nitrogen species are known to be major components of nonthermal plasmas interfering with cell viability or cell performance. Several groups have shown that, depending on

the chosen plasma source and the corresponding experimental setup and procedure, reactive oxygen plus nitrogen species (RONS) are responsible for either inhibiting cellular proliferation via cell cycle blockage or even triggering apoptosis in some cell lines. However, using other plasma conditions/cell lines, stimulating effects on cell performance had also been observed [11]–[15]. To gain an understanding of the relevant processes, a detailed diagnostic and designed tuning of the plasma reactive component composition is essential to identify the responsible mechanisms or involved reactive species.

The cell viability is determined by a fluorometric assay, where metabolically active cells transform nonfluorescent resazurin to the highly fluorescent resorufin.

The plasma jet and the gas curtain are characterized by numerical flow simulation showing the gas flux field as well as by optical emission spectroscopy (OES) demonstrating the gas curtain's ability to exclude ambient species and to tailor the reactive species composition in the effluent to be either oxygen or nitrogen dominated. Liquid cell environment serves as the interface of physical plasma and cells. To study the tailored plasma jet–skin-cell treatment, first, the plasma-treated liquid which is applied to the cells is investigated regarding the reactive species composition. The concentration of nitrite and nitrate within the cell medium serves as a measure for plasma-induced nitrogen species. Investigations with the leukodye dichlorodihydrofluorescein diacetate (H_2DCFDA)—a frequently used dye for both ROS and reactive nitrogen species (RNS) detection [16]—determine the total amount of generated oxygen and nitrogen species (RONS) within the cell medium in general (for screening purposes). Compared to more specific probes, it offers the possibility to estimate the sum RONS reactivity. After plasma treatment, the liquid is applied to the HaCaT cells, whose viability is investigated.

It is shown that treatment with plasma dominated by oxygen reactive species affects cellular growth stronger compared to treatment with plasma dominated by nitrogen reactive species.

II. Plasma Jet and Gas Curtain

Plasma treatment was performed by a cold atmospheric pressure plasma jet, the kinpen (neoplas GmbH, Greifswald, Germany), which consists of a centered rod electrode inside a ceramic capillary and a grounded ring electrode [17]. To the powered central electrode, a voltage of 2–6 kV_{pp} at high frequency (1.1 MHz) is applied. The working gas was argon (Ar purity 99.999%) with a gas flow rate of 5 standard liters per minute (slm).

For the generation of the gas curtain, a glass hull was used [18]. As shielding gas, nitrogen (N_2 purity 99.999%) or oxygen (O_2 purity 99.995%) with a total shielding gas flow rate of 5 slm was used. This shielding gas creates a protective curtain around the effluent and, in consequence, shields it from ambient air species. The function of the gas curtain is demonstrated in the two plasma jet photographs of Fig. 1. In the left picture [Fig. 1(a)], no shielding gas is applied, and a considerable emission of excited molecular nitrogen (violet color impression) is observed at the tip and around the effluent. Since no additional nitrogen is admixed to the working gas, this nitrogen emission
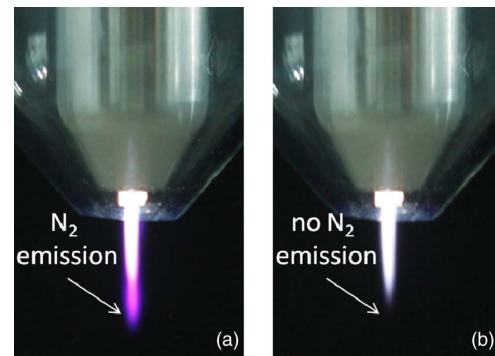

Fig. 1. Photograph of the modified plasma jet with two different shielding gas conditions. (a) No shielding gas; (b) 5-slm oxygen shielding gas.

results from excited ambient nitrogen diffused from ambient air into the effluent. In contrast to that, neither on the tip nor around the effluent can any nitrogen emission be observed visually when 5 slm of oxygen is applied as shielding gas [Fig. 1(b)]. This indicates that the oxygen shielding gas ensheathes the effluent, which impedes ambient air nitrogen diffusion into the effluent.

As standard cell culture medium for this study, Roswell Park Memorial Institute (RPMI) 1640 medium with and without phenol red, supplemented with 8% fetal calf serum, 1% penicillin, and streptomycin, was used. For plasma treatment, 5 mL of this standard cell culture medium was placed in a polystyrene petri dish with an outer diameter of 60 mm. The distance between the plasma jet nozzle and the liquid surface was set to 9 mm, and the distance between plasma jet nozzle and glass cover outlet was 1.9 mm. Samples were treated for 90, 180, and 360 s and moved with the same velocity for each treatment time continuously, by using a computer-controlled xy table, during the treatment to ensure a homogeneous treatment of the medium.

For the cell vitality assay, an indirect treatment procedure was used: Immediately after plasma treatment, cells were brought in contact to either undiluted plasma-treated medium or serial dilutions thereof. Our investigation shows that, in indirect plasma treatment, dilution of cell medium has the same effect as reduction of treatment time (data not shown). From the serial dilution, a treatment time equivalent is calculated.

The indirect treatment was chosen to focus only on the effects of RONS and ROS and to exclude effects resulting from radiation, electric fields, and excited plasma species.

III. Simulation and Diagnostic Setups

A. Fluid Dynamics Simulation

Transport of ambient air into the effluent of the plasma jet operated above a petri dish is investigated by numerical simulations. Simulations were carried out both with and without applied gas curtain. The isothermal Navier–Stokes equations are coupled to the standard $k - \varepsilon$ turbulence model [19] and solved using COMSOL Multiphysics 4.2.

Convective and diffusive mass transport of argon, air, and shielding gas is implemented as described in [18]. A working gas inflow of pure argon and an inflow rate of pure shielding

Original Publications

This article has been accepted for inclusion in a future issue of this journal. Content is final as presented, with the exception of pagination.

REUTER *et al.*: FROM RONS TO ROS: TAILORING PLASMA JET TREATMENT OF SKIN CELLS 3

gas are fixed at 5 slm each. Equal molar masses of shielding gas and air are assumed. From the side, a gas flow of pure air is allowed with a normal velocity of 0.1–0.5 m/s.

B. OES

In order to investigate the effect of an oxygen and a nitrogen gas shielding on the effluent emission signal, space-resolved OES was performed. This furthermore yields information about the excited species distribution. For the measurements, the plasma jet was positioned side on to a focusing lens. The lens images a spot with a diameter of 0.25 mm of the effluent region into an optical fiber. This UV transparent quartz fiber was connected to a two-channel spectrometer (AvaSpec-ULS2048x64-USB2-2, Avantes) with a 25-μm slit width. The first channel is UV sensitive in the spectral range from 200 to 450 nm and has a spectral resolution of 0.33 nm. The second channel covers the visible and near-infrared spectral range (450–960 nm) with a spectral resolution of 0.7 nm. In order to obtain spatial information of the emission signal, the lens and the optical fiber holder are mounted on a two-direction stepping motor stage. The step sizes in axial (z) and radial (r) directions were set to 0.5 and 0.15 mm, respectively. The number of collected spectra in each direction was 21 covering a range of -1.5–1.5 mm from the effluent center in the radial direction. Due to the glass cover, the axial measurement started not immediately at the jet nozzle but from a distance of 1.9 mm and ended at 11.9 mm. Three different shielding gas conditions were investigated by the OES measurements: no shielding gas, 5-slm nitrogen shielding gas, and 5-slm oxygen shielding gas.

C. Nitrite and Nitrate Concentration Measurements

The concentration of nitrite and nitrate in plasma-treated liquid was measured via a colorimetric assay (nitrate/nitrite colorimetric assay kit, Cayman Chemical Company, Ann Arbor, MI). This assay is a simple-to-use method for the measurement of the total nitrite/nitrate concentration. The standard curve was diluted eightfold to 4.375 μM from original maximal standard concentration of 35 μM. The nitrite concentration was determined by adding two different Griess reagents (1 + 2) to the sample, which react with nitrite into a deep purple azo compound. The absorbance at 540 nm in comparison with the standard curve gives the total concentration of nitrite. The light absorbance was measured by a microplate reader (Tecan Infinite M200 Pro, Tecan Group Ltd., Männedorf, Switzerland).

For the determination of the nitrate concentration, it is necessary to use an additional step. Due to the fact that only nitrite reacts with Griess reagents to form the purple azo compound, nitrate has first to be reduced to nitrite by a nitrate reductase enzyme and a related cofactor. After this step, the difference between the total concentration of nitrate plus nitrite and the total concentration of nitrite yields the initial nitrate concentration.

The test was performed in four 96-well plates, two for nitrate and two for nitrite. For each sample, a standard curve was measured by mixing a defined standard concentration into our standard cell culture medium (as described in Section II). For each data point, three independent samples were investigated.

Each sample was prepared and analyzed in triplicate. For the detection of nitrite, 80 μL of every sample was used, and 20 μL of our standard cell culture medium (described in Section II) was added. For the determination of the nitrate concentration, 20 μL of our standard cell culture medium was replaced by 10-μL nitrate reductase and 10-μL nitrate cofactor. This activation of the samples and the corresponding standard curve measurements were performed immediately after the plasma treatment. After 1-h incubation time at room temperature, 50-μL Griess reagent 1 and 50-μL Griess reagent 2 were added. After further 10 min, the concentration was determined by measuring the light absorbance at 540 nm, from which the background light absorbance of the untreated liquid and of the well plate was subtracted.

D. ROS/RNS Detection in Standard Cell Culture Media

ROS/RNS concentration was estimated utilizing the conversion of the nonfluorescent leukodye $2',7'$-(H_2DCFDA) into the highly fluorescent oxidation product dichlorofluorescein.

Plasma treatment was done according to Section II: Kinpen with different shield gas compositions was applied (0%/20%/40%/60%/80% O_2 in N_2, pure O_2) was used to treat 5-mL standard cell culture medium. Two hundred microliters of the medium or its dilutions were immediately pipetted into a black flat bottom 96-well plate (Nunc, Roskilde, Denmark) using eight replicates each. An eight-channel pipettor was used to add 25 μL of 4.5-μM H_2DCFDA (Sigma, Deisenhofen, Germany) in phosphate-buffered saline (PBS) as quickly as possible. Plates were kept in dark and humid conditions at 37 °C. Fluorescence intensity was measured after 6 h to allow spontaneous deacetylation of H_2DCFDA (Tecan F200 with 485/535-nm filter set, Tecan Group Ltd., Männedorf, Switzerland). Under these conditions, H_2DCFDA showed a dose-dependent response to H_2O_2 without a specific deacetylation. A de-esterification, e.g., by adding esterases, was avoided to reduce interference with plasma-generated RONS. Nontreated medium served as background control.

E. Cell Viability Assay

Cell viability was determined using the conversion of 7-hydroxy-3H-phenoxazin-3-one 10-oxide (resazurin) by metabolically active cells into the highly fluorescent 7-hydroxy-3H-phenoxazin-3-one (resorufin) [20]. Adherent HaCaT cells were used for the assay. Only cells with less than 75 cell population doublings (30 passages) were used and subcultured twice a week using standard cell culture procedures. RPMI 1640 medium with 8% fetal calf serum, penicillin, and streptomycin (1%) served as standard cell culture medium, and the cells were maintained at 37 °C, 95% humidity, and 5% CO_2 level.

For the assay, 35 000 cells/mL were seeded in standard medium in 96-well plates and were allowed to rest in an incubator for 24 h.

Plasma treatment was accomplished according to Section II: The plasma treated medium was immediately transferred into one row of wells of the cell culture plate and serially diluted
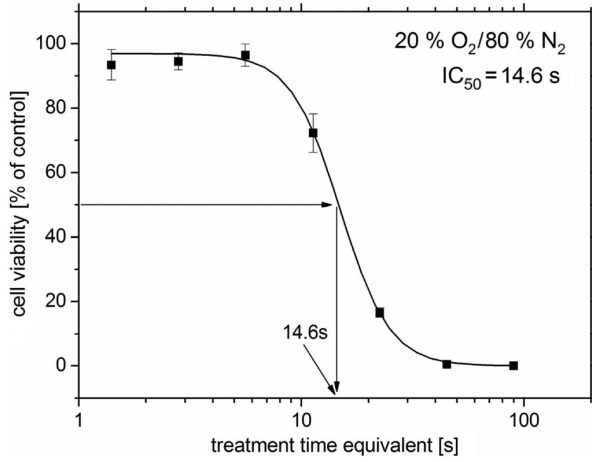
Fig. 2. Cell viability over treatment time equivalent. Example indicates IC_{50} value determination via sigmoidal regression (here, 14.6-s treatment time equivalent).

with complete medium immediately (six parallel wells per treatment time) to obtain different treatment time equivalents. Etoposide (0.5 μM) was used as negative control and interplate standardization, and argon-gas-treated medium (5 slm, kinpen with plasma off) served as background control. Seventy-one hours after treatment, plates were washed using Hanks buffered saline with Ca^{2+}/Mg^{2+} and cultivated with 100-μM resazurin in standard medium for 1 h. Finally, fluorescence intensity of the produced resorufin was read using the Tecan M200 multiplate reader described in Section III-C (530-nm excitation and 590-nm emission). Cell viability was calculated as percentage of background control. Fifty percent inhibition of cell viability (IC_{50}) was estimated of relative resorufin fluorescence data as a function of treatment time equivalent (see Fig. 2). Each IC_{50} value was determined for serial dilutions of 90- and 180-s plasma treatment, respectively.

IV. Results and Discussion

A. Fluid Dynamics Simulation Results

In Fig. 3, the mole fractions $x_i = \omega_i M/M_i$ of ambient air and shielding gas are shown. It can be observed that vortices driven by the argon flux from the plasma jet occur due to the geometry of the petri dish. During operation in ambient air, pure air diffuses into the effluent of the plasma jet, while the petri dish leads to an argon-enriched atmosphere above the dish, consisting of 63% air only. With applied gas curtain [Fig. 3(b)], the shielding gas forms a protective cover or curtain around the argon-enriched atmosphere, making the production of reactive species in the effluent independent from the geometry of the experimental (or clinical) setup and from environmental influences such as humidity. This enables well-definable conditions for the chemistry in the plasma jet effluent. Furthermore, the shielding gas mixture can be adjusted in order to produce a tailored composition of reactive oxygen and nitrogen species for biomedical applications of low temperature plasma jets.
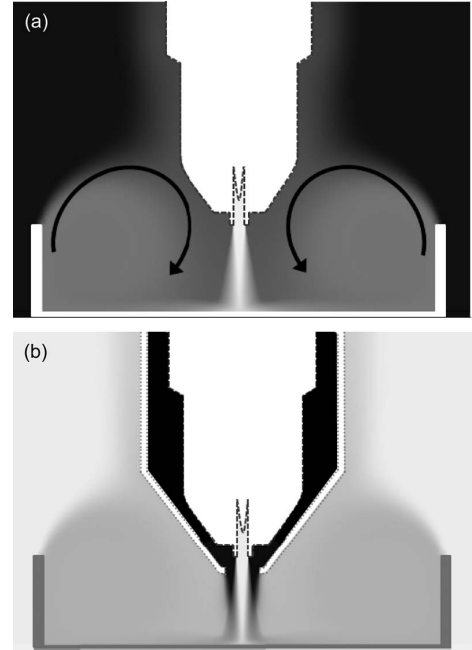
Fig. 3. Mole fractions of (a) ambient air and (b) shielding gas (a) without and (b) with gas curtain. The values for the mole fractions are displayed on a linear gray scale with black marking one and white representing zero.

B. OES Results

The OES reveals the existence of different excited species in the radiating effluent of the investigated plasma jet, namely, hydroxyl (OH), nitrogen (N_2), atomic oxygen (O), and argon (Ar). Since neither oxygen nor nitrogen is admixed directly to the working gas, the appearance of both species in the spectrum is due to ambient air diffusion or working gas impurities. The influence of the latter is very small since argon gas with a high purity was used. Furthermore, the plasma jet was operated 30 min prior to the measurement to provide steady-state conditions. Despite both precautions, OH emission was detected. This indicates that remaining water vapor, originating from the tube wall, is dissociated in the plasma zone. Water-vapor dissociation not only produces OH but also generates (atomic) oxygen. Hence, atomic oxygen detected in the effluent has two origins: the tube-induced water vapor and the influx of ambient air. This is in contrast to nitrogen molecules, which only originate from ambient air. In order to visualize the change of emission intensity of excited nitrogen and excited atomic oxygen due to different shielding gas configurations, two defined spectral ranges are evaluated. These spectral regions include the nitrogen emission $N_2(C^3\Pi_u - B^3\Pi_g)$ in the range of 330–338 nm and the atomic oxygen emission $O(^5P - ^5S)$ in the range of 775–778 nm. The normalized integrated intensities of both emission signals are shown for the three applied shielding gas configurations in Fig. 4. The N_2 and O emission signals are normalized separately to the highest obtained intensity value that was measured for the three shielding gas configurations. This provides comparability between different shielding gas settings but not between N_2 and O emission intensities. In
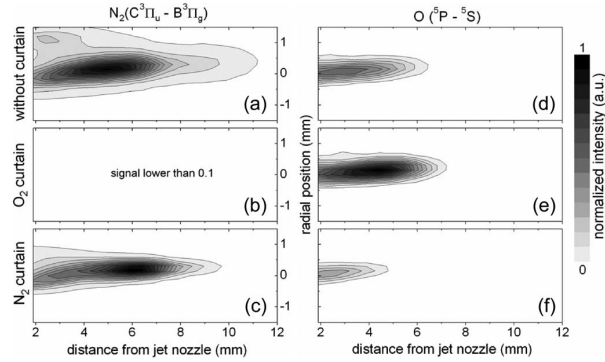
Fig. 4. Optical emission map of the second positive system of nitrogen and of atomic oxygen of the plasma jet effluent for three different shielding gas conditions (100% nitrogen, 100% oxygen, and without shielding gas).
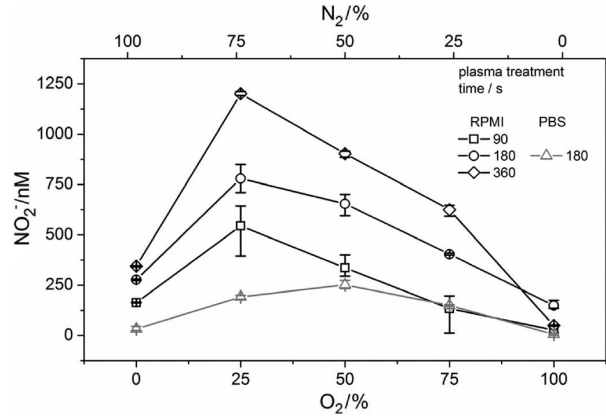

Fig. 5. Nitrite concentration after 90-, 180-, and 360-s plasma treatment of 5-mL cell culture medium in dependence of different oxygen-to-nitrogen ratios of the shielding gas.

Fig. 4(a)–(c), emission signal of N_2 is shown for no shielding gas (a), 5-slm oxygen shielding gas (b), and 5-slm nitrogen shielding gas (c). When no shielding gas is applied, the highest N_2 emission is detected at about 5 mm from the jet nozzle in the center of the effluent. A comparable intensity distribution is obtained when a nitrogen shielding gas is applied. However, two major differences can be observed. First, the maximum of the N_2 emission is shifted from $z = 5$ mm to $z = 6.1$ mm, and second, the radial profile is much smaller. Both differences are due to the additional nitrogen shielding gas flux that produces less turbulence directly behind the glass nozzle. In consequence, nitrogen-exciting particles like metastable argon atoms are not dragged into the radial outer regions in the same amount as they are when no shielding gas is applied. This leads to a thinner radial profile and prolongs the effect range of energetic species. Hence, the excitation maximum of nitrogen is shifted. With oxygen as shielding gas, no nitrogen emission can be detected, which shows the efficiency with which the gas curtain shields from ambient nitrogen influx.

The measurement results for the O emission signal are shown in Fig. 4(d)–(f) for the same shielding gas variations as for the presented N_2 emission signals. The highest emission intensity of the evaluated atomic oxygen line is found in the oxygen shielding condition [Fig. 4(e)]. This maximum is positioned in the center of the effluent at $z = 4.5$ mm. The profile shape is similar to the shape in the case of no shielding gas [Fig. 4(d)]. Compared to the results of N_2 emission, this indicates that changes in turbulence do not much affect the formation and excitation of atomic oxygen. Since no ambient oxygen is expected in the effluent when applying a nitrogen shielding gas, no emission signal should be detected [compare situation in Fig. 4(b)]. However, Fig. 4(f) still shows a small emission signal located near the glass nozzle. This remaining signal is assumed to be not due to the ambient oxygen influx but due to the already discussed production of atomic oxygen from the dissociation of water vapor.

To summarize the OES findings, the reactive species composition in the effluent is adjustable toward a ROS-determined plasma (oxygen shielding gas) or toward an RNS-determined plasma (nitrogen shielding gas).

C. Nitrite and Nitrate Assay

Plasma treatment of liquids with a designed effluent reactive species composition can tailor the reactive nitrogen and oxygen species concentrations within the treated liquid [18]. In this paper, plasma-induced nitrite concentration in our standard cell culture medium (described in Section II) is investigated. Nitrite concentration is used as a measure for nitrogen-based reactive species within the liquid. The plasma-generated nitrite concentration is shown in Fig. 5.

The data show that the trend is the same for all treatment times, and the maximum amount of nitrite can be expected between 0% and 25% oxygen shielding gas. The highest measured concentration of nitrite (for example, after 360 s, there were 1200 nM produced) was at 25% oxygen and 75% nitrogen shielding gas mixture. With higher oxygen concentration in the shielding gas, the nitrite concentration decreases to a minimum of 50 nM (after 360 s) at 100% oxygen, so that plasma treatment with a pure oxygen gas shielding leads to almost no nitrite in the liquid.

The nitride concentration can be finely tuned: With only oxygen as shielding gas, the lowest nitrite concentration is achieved because no RNS is generated in the jet effluent. With only nitrogen as shielding gas, the nitrite concentration is low as well because there are almost no oxygen species from which nitrite can be produced. From 20% of oxygen toward higher oxygen concentrations, the nitrite concentration in the cell medium continuously decreases to the lowest concentration at 100% oxygen.

Due to the high concentration of nitrate in the cell culture medium (840 μM) and due to the comparatively small amount of nitrate generation (around a few nanomoles), no significant change of nitrate concentration could be measured. For the total concentration of nitrate and nitrite, the test was also performed in a nitrate-free solution, in PBS. The trend for the nitrite concentration as a function of shielding gas mixture is comparable to plasma-treated cell culture medium shown in Fig. 5. In untreated PBS, almost no nitrate could be found.
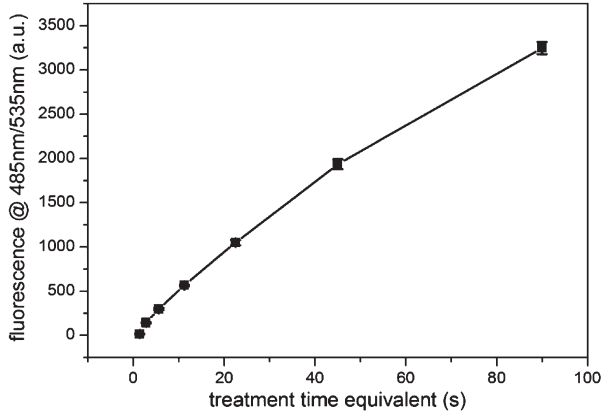
Fig. 6. H$_2$DCFDA fluorescent assay for determination of reactive oxygen and nitrogen species generated. Dependence of fluorescent intensity and treatment time in complete medium.
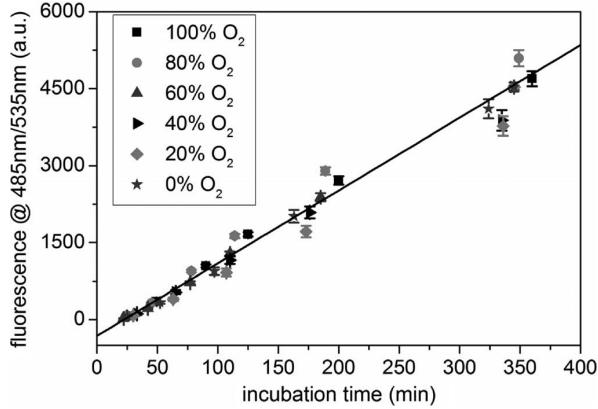

Fig. 7. H$_2$DCFDA fluorescent assay for determination of reactive oxygen and nitrogen species generated within the plasma-treated cell culture medium.

D. ROS/RNS Concentration

The leukodye H$_2$DCFDA is a frequently used dye for both ROS and RNS detection. However, it is described that H$_2$DCFDA lacks sensitivity regarding RNS and ROS [14], but other literature mention the different reactivities toward different kinds of ROS or RNS species. Even if the total amount of RONS cannot be determined exactly, the potential of a solution to convert H$_2$DCFDA is measured. As a first approximation, this conversion potential can be used as a quick measure for the total amount of RONS in liquids.

The conversion of H$_2$DCFDA is clearly dependent on treatment time equivalent of complete medium using the kinpen and the incubation time of the leukodye with the plasma-treated medium (see Fig. 6 example for 90-min incubation time). The data show a tendency toward lower conversion efficacy for long (45 s) and very long treatment times (90 s) as indicated by the decrease linearity. This observation is typical for rate-limited chemical reactions and might be due to a beginning H$_2$DCFDA depletion during reaction.

On the other hand, no influence of shielding gas composition in total H$_2$DCFDA conversion rate could be observed (see Fig. 7). With respect to the discussed sensitivity of this
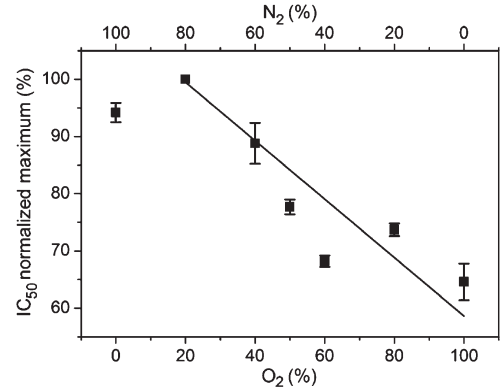
Fig. 8. Cell viability/cell division assay. Shielding gas composition significantly influences HaCaT cell response. One hundred percent IC_{50} value corresponds to 14.6-s treatment time equivalent.

assay against RNS and ROS species, this can be interpreted as follows: The total conversion potential of reactive species generation by the argon plasma is independent from the composition of the shielding gas but remains constant all the time. However, the composition of the reactive species generated is changing with the composition of the shielding gas ranging from rather oxygen-dominated species to nitrogen-dominated species with increasing N$_2$ proportion in the shielding gas (see Fig. 7). This can be interpreted that the total amount of reactive species remains constant, but the mixture of species can be controlled by the shielding gas composition; however, further investigations—focusing on specific reactive species—need to be carried out to confirm this assumption.

E. Cell Viability

The used resazurin conversion assay depends on the cell viability, a combined parameter of cell vitality and cell division rate. The reported data reflect mainly a disruption in cell division, as this would lead to a decreased cell number at the end of the incubation time and, hence, a lower overall metabolic activity. The cell division is a tightly regulated cellular process and a very sensitive parameter to reveal changes in the cellular environment or the effect of extracellular noxes [21], [22].

As reported in Section IV-D, the shielding gas composition does not affect the total reactive species flux (Fig. 7). However, both the NO$_2^-$ production rate and the reaction of HaCaTs show a change in reactive species quality with altering the gas curtain composition. With increasing oxygen fraction in the shielding gas, NO$_2^-$ production drops, and cell viability decreases (see Fig. 8). For low to intermediate O$_2$ concentrations (0%–40%) in the shielding gas, cell viability is high. A further increase of O$_2$ partial pressure decreases cell viability significantly in a proportion-dependent manner.

V. Conclusion

In this paper, the effect of atmospheric pressure plasma-generated reactive oxygen and RNS has been investigated. For the investigations, a gas curtain was set up around a plasma jet effluent. Optical emission spectra and numerical flow

Original Publications

This article has been accepted for inclusion in a future issue of this journal. Content is final as presented, with the exception of pagination.

REUTER *et al.*: FROM RONS TO ROS: TAILORING PLASMA JET TREATMENT OF SKIN CELLS 7

simulation showed that the shielding gas ensheathes the plasma jet effluent and protects the effluent from ambient species diffusion. By adjusting the shielding gas composition, the gas curtain allows for a reduction of RNS yielding a ROS-dominated plasma. For the investigation of the plasma-generated reactive species, human-skin cells were treated indirectly by the modified plasma jet. Our standard cell culture medium (described in Section II) was plasma treated and subsequently applied to the cell culture. Liquid diagnostics indicate the following: A variation of shielding gas composition does not affect the total number of reactive oxygen and nitrogen species produced. Only the fraction of RNS is reduced down to the level of impurities. Within the cell culture medium, nitrite, as an indicator for RNS, decreases with decreasing nitrogen fraction in the shielding gas. With decreasing RNS in the cell culture medium, the cell viability of the treated cells is reduced. From this, it can be concluded that treatment with a ROS-dominated plasma has a higher impact on cell viability than a plasma dominated by RNS.

REFERENCES

[1] O. Lademann, H. Richter, A. Patzelt, A. Alborova, D. Humme, K. D. Weltmann, B. Hartmann, P. Hinz, A. Kramer, and S. Koch, "Application of a plasma-jet for skin antisepsis: Analysis of the thermal action of the plasma by laser scanning microscopy," *Laser Phys. Lett.*, vol. 7, no. 6, pp. 458–462, Jun. 2010.

[2] M. Laroussi, "Low-temperature plasmas for medicine?" *IEEE Trans. Plasma Sci.*, vol. 37, no. 6, pp. 714–725, Jun. 2009.

[3] K. D. Weltmann and T. von Woedtke, "Basic requirements for plasma sources in medicine," *Eur. Phys. J. Appl. Phys.*, vol. 55, no. 1, pp. 13 807-1–13 807-10, Jul. 2011.

[4] S. Reuter, K. Niemi, V. Schulz-von der Gathen, and H. F. Döbele, "Generation of atomic oxygen in the effluent of an atmospheric pressure plasma jet," *Plasma Sources Sci. Technol.*, vol. 18, no. 1, pp. 015006-1–015006-9, Feb. 2009.

[5] A. V. Pipa, S. Reuter, R. Foest, and K. D. Weltmann, "Controlling the NO production of an atmospheric pressure plasma jet," *J. Phys. D, Appl. Phys.*, vol. 45, no. 8, pp. 085201-1–085201-7, Feb. 2012.

[6] S. Reuter, J. Winter, A. Schmidt-Bleker, D. Schroeder, H. Lange, N. Knake, V. Schulz-v.d.Gathen, and K.-D. Weltmann, "Atomic oxygen in a cold argon plasma jet: TALIF spectroscopy in ambient air with modelling and measurements of ambient species diffusion," *Plasma Sources Sci. Technol.*, vol. 21, no. 2, p. 024005, Apr. 2012.

[7] K. D. Weltmann, E. Kindel, R. Brandenburg, C. Meyer, R. Bussiahn, C. Wilke, and T. von Woedtke, "Atmospheric pressure plasma jet for medical therapy: Plasma parameters and risk estimation," *Contrib. Plasma Phys.*, vol. 49, no. 9, pp. 631–640, Oct. 2009.

[8] P. Boukamp, R. T. Petrussevska, D. Breitkreutz, J. Hornung, A. Markham, and N. E. Fusenig, "Normal keratinization in a spontaneously immortalized aneuploid human keratinocyte cell-line," *J. Cell Biol.*, vol. 106, no. 3, pp. 761–771, Mar. 1988.

[9] V. G. Arciuch, M. E. Elguero, J. J. Poderoso, and M. C. Carreras, "Mitochondrial regulation of cell cycle and proliferation," *Antioxid Redox Signal*, to be published.

[10] W. Chamulitrat, W. Stremmel, T. Kawahara, K. Rokutan, H. Fujii, K. Wingler, H. H. H. W. Schmidt, and R. Schmidt, "A constitutive NADPH oxidase-like system containing gp91phox homologs in human keratinocytes," *J. Invest. Dermatol.*, vol. 122, no. 4, pp. 1000–1009, Apr. 2004.

[11] K. P. Arjunan, G. Friedman, A. Fridman, and A. M. Clyne, "Non-thermal dielectric barrier discharge plasma induces angiogenesis through reactive oxygen species," *J. Roy. Soc. Interface*, vol. 9, no. 66, pp. 147–157, Jan. 2012.

[12] S. Kalghatgi, C. M. Kelly, E. Cerchar, B. Torabi, O. Alekseev, A. Fridman, G. Friedman, and J. Azizkhan-Clifford, "Effects of non-thermal plasma on mammalian cells," *Plos One*, vol. 6, no. 1, p. e16 270, Jan. 2011.

[13] R. Sensenig, S. Kalghatgi, E. Cerchar, G. Fridman, A. Shereshevsky, B. Torabi, K. P. Arjunan, E. Podolsky, A. Fridman, G. Friedman, J. Azizkhan-Clifford, and A. D. Brooks, "Non-thermal plasma induces apoptosis in melanoma cells via production of intracellular reactive oxygen species," *Ann. Biomed. Eng.*, vol. 39, no. 2, pp. 674–687, Feb. 2011.

[14] M. Vandamme, E. Robert, S. Lerondel, V. Sarron, D. Ries, S. Dozias, J. Sobilo, D. Gosset, C. Kieda, B. Legrain, J. M. Pouvesle, and A. Le Pape, "ROS implication in a new antitumor strategy based on non-thermal plasma," *Int. J. Cancer*, vol. 130, no. 9, pp. 2185–2194, May 2012.

[15] E. Stoffels, A. J. M. Roks, and L. E. Deelmm, "Delayed effects of cold atmospheric plasma on vascular cells," *Plasma Process. Polym.*, vol. 5, no. 6, pp. 599–605, Aug. 15, 2008.

[16] A. Gomes, E. Fernandes, and J. L. F. C. Lima, "Fluorescence probes used for detection of reactive oxygen species," *J. Biochem. Biophys. Methods*, vol. 65, no. 2/3, pp. 45–80, Dec. 31, 2005.

[17] K. D. Weltmann, E. Kindel, T. von Woedtke, M. Hahnel, M. Stieber, and R. Brandenburg, "Atmospheric-pressure plasma sources: Prospective tools for plasma medicine," *Pure Appl. Chem.*, vol. 82, no. 6, pp. 1223–1237, Jun. 2010.

[18] S. Reuter, J. Winter, A. Schmidt-Bleker, H. Tresp, M. Hammer, and K.-D. Weltmann, "Controlling the ambient air affected reactive species composition in the effluent of an argon plasma jet," *IEEE Trans. Plasma Sci.*, 2012. DOI: 10.1109/TPS.2012.2204280, to be published.

[19] D. C. Wilcox, *Turbulence Modeling for CFD*. La Cañada, CA: DCW Industries, 1998.

[20] J. O'Brien, I. Wilson, T. Orton, and F. Pognan, "Investigation of the Alamar Blue (resazurin) fluorescent dye for the assessment of mammalian cell cytotoxicity," *Eur. J. Biochem.*, vol. 267, no. 17, pp. 5421–5426, Sep. 2000.

[21] A. J. Levine, "p53, the cellular gatekeeper for growth and division," *Cell*, vol. 88, no. 3, pp. 323–331, Feb. 7, 1997.

[22] J. Lukas, C. Lukas, and J. Bartek, "Mammalian cell cycle checkpoints: Signalling pathways and their organization in space and time," *DNA Repair*, vol. 3, no. 8–9, pp. 997–1007, Aug.–Sep. 2004.

Stephan Reuter (M'12) received the M.Eng. (Dipl. Phys.-Ing.) and M.Sc. (Dipl. Phys.) degrees in plasma physics from the University of Duisburg-Essen, Essen, Germany, and the Ph.D. (Dr. rer. nat.) degree in 2007 for the investigation of oxygen formation mechanisms in atmospheric pressure plasma jets.

In 2008, he became a Research Fellow with the Centre for Plasma Physics, Queen's University Belfast, Belfast, U.K. He is currently the Head of the junior research group "Extracellular Effects" with the BMBF-funded Center for Innovation Competence *plasmatis*, Leibniz Institute for Plasma Science and Technology (INP Greifswald e.V.), Greifswald, Germany, where he performs research on controlling the interaction of atmospheric pressure plasmas with biological liquids in the field of plasma medicine. The focus of his research group lies on optical diagnostics and modeling of atmospheric pressure plasma jets interacting with liquids.

Dr. Reuter is a member of the German Physical Society (DPG), the International Society for Plasma Medicine, and the International Society for Plasma Chemistry.

Helena Tresp received the Diploma degree in physics from the Ernst-Moritz-Arndt University of Greifswald, Greifswald, Germany, in 2011. She is currently working toward the Ph.D. degree in the BMBF-funded Center for Innovation Competence *plasmatis*, Leibniz Institute for Plasma Science and Technology (INP Greifswald e.V.), Greifswald, investigating plasma-cell interactions with the focus on plasma liquid interactions.

Since 2011, she has been a Member of the scientific staff with the Leibniz Institute for Plasma Science and Technology (INP Greifswald e.V.).

Ms. Tresp is a member of the German Physical Society (DPG).

Kristian Wende received the Diploma and Ph.D. ("Dr. rer. nat.") degrees from the Ernst-Moritz-Arndt University of Greifswald, Greifswald, Germany, in 1998 and 2003, respectively, where he worked on the phytochemical composition of plants and different analytical techniques.

Between 2004 and 2009, he was a Cell Biology Group Leader with the Institute of Pharmacy, Ernst-Moritz-Arndt University of Greifswald, investigating the interaction of marine/terrestrial natural products, UV light, and nonthermal plasmas with different cellular models. Since 2010, he has been a Member with the BMBF-funded Center for Innovation Competence *plasmatis*, Leibniz Institute for Plasma Science and Technology (INP Greifswald e.V.), Greifswald. His research interest concentrates mainly on eukaryotic cell responses after exogenic stimuli.

Dr. Wende is a member of the International Society of Plasma Medicine and the German Pharmaceutical Society (DPhG).

Malte U. Hammer was born in Germany in 1978. He received the Diploma and "Dr. rer. nat."–the German equivalent of the Ph.D. degree–degrees in biophysics from Christian-Albrechts-Universitat zu Kiel, Kiel, Germany, in 2004 and 2007, respectively.

From 2003 to 2008, he was with the Research Center Borstel, Borstel, Germany, where he worked on peptide membrane interactions. From 2008 to 2010, he was with the University of California, Santa Barbara, where he worked for Prof. J. Israelachvili's group. Since 2010, he has been with the BMBF-funded project Center for Innovation Competence *plasmatis*, Leibniz Institute for Plasma Science and Technology (INP Greifswald e.V.), Greifswald, Germany. His research interests include but are not limited to plasma liquid interaction as well as membrane interaction.

Dr. Hammer is a member of the International Society for Plasma Medicine and the Biophysical Society as well as the German Society for Biophysics (DGfB) section "Membranes, Cells, Networks."

Jörn Winter received the Diploma degree in physics and the Ph.D. (Dr. rer. nat.) degree in experimental physics from the Ernst-Moritz-Arndt University of Greifswald, Greifswald, Germany, in 2005 and 2009, respectively.

Since 2006, he has been a Member of the scientific staff with the Leibniz Institute for Plasma Science and Technology (INP Greifswald e.V.), Greifswald, where he worked on mercury-free low-pressure gas discharges for lighting and on plasma diagnostics and where he has been a Postdoctoral Researcher with the BMBF-funded Center for Innovation Competence *plasmatis* since 2010, investigating plasma-cell interactions with the focus on plasma diagnostic. In 2008, he joined the R&D department of Webeco GmbH & Co. KG, Selmsdorf, Germany, working on plasma generation for the sterilization of endoscopes.

Kai Masur was born in Germany in 1974. He received the Diploma degree in biochemistry at the University Leipzig, Leipzig, Germany, in 1998 and the Ph.D. (Dr. rer. nat.) degree for his studies on the signal transduction of metastasizing tumor cells from the University of Witten/Herdecke, Witten, Germany, in 2001.

From 2001 to 2003, he was with New England Medical Center/TUFTs University, Boston, MA, where he worked on signal transduction of pancreatic beta cells. From 2003 to 2009, he was a PI with the University of Witten/Herdecke—establishing his own work group by combining diabetes research and oncology. Since December 2009, he has been the Head of the junior research group "Cellular Effects" with the BMBF-funded Center for Innovation Competence "*plasmatis*," Leibniz Institute for Plasma Science and Technology (INP Greifswald e.V.), Greifswald, Germany, where his group is investigating the interplay of nonthermal plasma with living cells and tissues—focusing on the alterations of the genome and proteome—in order to stimulate cellular activities. His focus lies on cellular signal transduction cascades and how to manipulate those signals.

Dr. Masur is a member of the German Society for Biochemistry and Molecular Biology (GBM), the International Society for Plasma Medicine, and the Signal Transduction Society.

Ansgar Schmidt-Bleker received the Diploma degree in physics from the RWTH Aachen University, Aachen, Germany, in 2010. He is currently working toward the Ph.D. degree in the BMBF-funded Center for Innovation Competence *plasmatis*, Leibniz Institute for Plasma Science and Technology (INP Greifswald e.V.), Greifswald, Germany, where he works on simulations for biomedical applications of plasmas.

Until 2011, he was a Scientific Employee with the Institute for Theory of Statistical Physics, RWTH Aachen University, where he subsequently investigated nonlinear effects in quantum plasmas.

Klaus-Dieter Weltmann (M'95) received the Diploma degree in electronics and the Ph.D. (Dr. rer. nat) degree in applied physics from the Ernst-Moritz-Arndt University of Greifswald, Greifswald, Germany, in 1989 and 1993, respectively, where he worked on nonlinear dynamics in low-temperature plasmas and plasma diagnostics.

In 1994, he was a Visiting Scientist with the Plasma Physics Laboratory, West Virginia University, Morgantown. In 1995, he joined ABB Corporate Research Ltd., Baden-Dättwil, Switzerland, working on the research and development of HV and MV switchgears, where he became the head of High Voltage Systems Group in 1998. In 2000, he was appointed to lead R&D of gas-insulated switchgear [(GIS), e.g., PASS] with ABB High Voltage Technologies Ltd., Zurich, Switzerland, where he became a Business Unit R&D Manager of GIS in 2002. Since 2003, he has been the Director and Chairman of the Board of the Leibniz Institute for Plasma Science and Technology (INP Greifswald e.V.), Greifswald, and a Professor for experimental physics with the Ernst-Moritz-Arndt University of Greifswald. His current research interests include switchgears, arc physics, atmospheric plasmas, modeling and simulation, plasma medicine, and plasma decontamination.

Dr. Weltmann is the President of the International Society for Plasma Medicine, a member of the German Physical Society, and a member of several consulting committees in industry and research. He is the initiator of three spin-off companies.

Article A5

Propagation mechanisms of guided streamers in plasma jets: the influence of electronegativity of the surrounding gas

Ansgar Schmidt-Bleker[1], Seth A Norberg[2], Jörn Winter[1], Eric Johnsen[2], S Reuter[1], K D Weltmann[1] and Mark J Kushner[3]

[1] Leibniz Institute for Plasma Science and Technology e.V. (INP Greifswald) and ZIK plasmatis, Felix-Hausdorff Straße 2, 17489 Greifswald, Germany
[2] Department of Mechanical Engineering, University of Michigan, 2350 Hayward Street, Ann Arbor, MI 48109-2125 USA
[3] Department of Electrical Engineering and Computer Science, University of Michigan, 1301 Beal Avenue, Ann Arbor, MI 48109-2122, USA

E-mail: stephan.reuter@inp-greifswald.de and mjkush@umich.edu

Abstract

Atmospheric pressure plasma jets for biomedical applications are often sustained in He with small amounts of, for example, O_2 impurities and typically propagate into ambient air. The resulting poorly controlled generation of reactive species has motivated the use of gas shields to control the interaction of the plasma plume with the ambient gas. The use of different gases in the shield yields different behavior in the plasma plume. In this paper, we discuss results from experimental and computational investigations of He plasma jets having attaching and non-attaching gas shields. We found that negative ion formation in the He-air mixing region significantly affects the ionization wave dynamics and promotes the propagation of negative guided streamers through an electrostatic focusing mechanism. Results from standard and phase resolved optical emission spectroscopy ratios of emission from states of N_2 and He imply different electric fields in the plasma plume depending on the composition of the shielding gas. These effects are attributed to the conductivity in the transition region between the plasma plume and the shield gas, and the immobile charge represented by negative ions. The lower conductivity in the attaching mixtures enables more extended penetration of the electric field whereas the negative ions aid in focusing the electrons towards the axis.

Keywords: Atmospheric pressure plasma jets, guided ionization waves, phase resolved optical emission spectroscopy, modeling

(Some figures may appear in colour only in the online journal)

1. Introduction

Cold atmospheric plasma jets (CAPJ) emanating into ambient air are being investigated for a wide range of biomedical and biotechnological applications [1–3]. The typical CAPJ consists of a rare gas seeded with a small fraction of reactive gas, usually less than a few percent, flowed through a tube of up to a few mm in diameter [4, 5]. Pulse periodic electric discharges in the tube produce an ionized, radical and excited state laden plume, which subsequently mixes with and reacts with the ambient air. The plasma component of the plume takes the form of periodic ionization waves through the more easily ionized rare-gas dominated channel that is bounded by the less easily ionized ambient gas. The plasma plume is therefore often referred to as a guided streamer. The reactive oxygen and nitrogen species (RONS) produced by CAPJ having guided streamers can be influenced by gas curtains of defined composition surrounding the plume of the plasma jet [6, 7]. Such

control has enabled making correlations of plasma-generated reactive species with biological effects [8, 9].

The effect of the surrounding gas on the plasma propagation and formation of RONS has previously been investigated using helium (He) jets emanating into ambient air and in He atmospheres. Plasma jets using sinusoidally excited needle-shaped electrodes [10] and positive pulses [11] emanating into He atmospheres produce a diffuse discharge due to the ability of the discharge to freely propagate into the ambient gas. When emanating into an air atmosphere, the confining effects of the electronegative and low ionization rate molecular gas surrounding the plume produce a guided streamer. Simulations of a He plasma jet produced similar trends [12].

Several modelling studies have investigated the mechanisms leading to the formation of guided streamers in He-operated plasma jets. Sakiyama and Graves simulated a He plasma jet flowing into nitrogen (N_2) impinging on a glass plate with a grounded metal plate underneath [13]. They were able to explain the ring shaped emission patterns and bacteria killing patterns experimentally observed [14] by mixing of excited and ionized He with the surrounding N_2. Naidis also found annular emission patterns in a simulation including both N_2 and oxygen (O_2) as the surrounding gas [15]. He found that in regions where the mole fraction of air exceeded 0.1%, attachment to O_2 prevented further radial expansion of the streamer. Detachment from O_2^- formed in a previous pulse can provide seed electrons for the propagation of the subsequent streamer. The numerical investigation of Breden *et al* showed that while photoionization in front of the streamer head does increase the propagation speed of guided streamers, it is not a necessary requirement for streamer propagation [12]. They also found that molecular impurities (N_2, O_2, air) of up to 1% can enhance the development of the streamer within the discharge tube while possibly quenching the streamer outside the tube. Several numerical studies have suggested that a finite mixing layer between He and air is not a necessary requirement for the development of a guided streamer [12, 16, 17]. The guiding of streamers by the He gas flow is usually explained by the lower electric fields required for the streamer propagation in He than in the surrounding gas, as well as memory effects such as preionization and accumulation of excited species from the preceding streamer [11, 18].

Naidis [19] investigated the differences between guided streamers created by positive and negative voltage pulses of the same magnitude and found that positive streamers lead to a stronger electric field in the streamer head and tend to propagate faster and further than negative ones. The emission patterns found in that work agreed well with experiments [20]. A comparison of positive and negative streamers was also made by Xiong and Kushner for ionization waves propagating inside dielectric tubes [21]. Unlike guided streamers into ambient gas, it was found that negative streamers propagate faster than positive streamers, an effect attributed to the focusing effect of the tube walls. While in a free jet, electron diffusion leads to a broadening of the streamer head, and consequently to lower electric fields and a slower propagation as found for streamers in air [22], the walls of the tube can rapidly charge and produce an electric field pointing in the direction of streamer propagation.

Winter *et al* [23] measured metastable He (He(2^3S_1), He_m) concentrations using laser absorption spectroscopy on a CAPJ while incorporating shielding gases consisting of mixtures of N_2 and O_2. It was found that the He_m concentration in the plume strongly depends on the composition of the shielding gas: The He_m density in the vicinity of the jet nozzle amounts to $10^{13} cm^{-3}$ if the O_2 concentration in the shielding is between 15% and 100%. As the O_2 content in the shielding gas is decreased below 10% the He_m density drops by at least two orders of magnitude (below the detection limit of the system). Similar densities and trends were observed when a mixture of O_2 and Ar was used as the shielding gas. These findings indicate that the decrease in He_m density with decreasing O_2 content in the shielding gas is not due to the presence of N_2, but due to the absence of O_2.

In this paper, we report on the consequences of ambient O_2—and especially its electronegative properties—on dynamic processes in the plume of a He CAPJ. Several previous investigations have been performed on the particular CAPJ used in this study, the kinpen Sci [24]. For example, the previously mentioned measurements of He_m densities were made using this device [23]. As a result, the baseline operating characteristics of the CAPJ are well known and can be extrapolated to the broader class of CAPJ [4–6]. The consequences of O_2 content in the ambient and shield were investigated by using optical emission spectroscopy (OES) and numerical modelling. The OES measurements include low-resolution observations of the emission of atomic and molecular lines, high spectral and spatial resolution of N_2 emission bands and time resolved images of the plume of the jet jets using a fast-gating iCCD camera. We found that if the jet is shielded with N_2, an intense N_2 emission occurs at the side of the jet nozzle and a dark space occurs at a distance of 0.5 to 1 mm from the nozzle. These features do not occur if the jet is shielded by synthetic air. We also observed a backwards directed emission (travelling along the jet axis against the flow direction) during the positive half-cycle if the shielding gas contains O_2.

Two dimensional numerical modeling of the discharge was also performed. A correlation between the observed emission patterns and the computed electron densities and electric fields was obtained. This leads to the central hypothesis that anions formed from O_2 contribute to a focusing of the electrons in the plume of the jet during the negative half-cycle.

2. Description of the experiment and model

2.1. Experiment

In this investigation, the plasma jet kinpen Sci was operated with a shielding gas device. The jet is identical to that diagnosed by Winter *et al* [23]. The device features an inner needle electrode which is mounted in the center of a ceramic capillary of 1.6 mm inner diameter with a grounded outer electrode. The inner electrode is driven at a frequency of 940 kHz with a peak-to-peak voltage of 1.7 kV [23]. The jet and shielding gas device are schematically shown in figure 1. The feed gas is He at 2.5 standard liters per minute (slm) (Alphagaz 1, Air
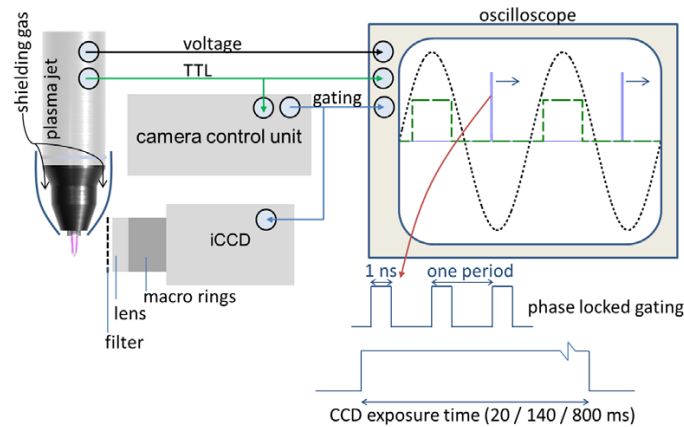
Figure 1. Schematics of the experimental setup and principle of the phase resolved optical emission measurements. In the sketch of the oscilloscope, the dotted black line represents the voltage signal, the dashed green line the TTL signal and the continuous blue line the gating signal for the MCP.

Liquide, France). The employed shielding gas mixtures were 5 slm of N_2 and O_2 (Alphagaz 1, Air Liquide, France) in different mixing ratios ranging from pure N_2 to pure O_2.

Low resolution spectra of the jet emission in the region of 250–970 nm were obtained using the AvaSpec ULS2048X64-2-USB2 (Avantes, Netherlands) spectrometer with a slit width of $25 \mu m$. The end-on spectrum was obtained by placing an optical fiber in front of the plume. The spectral sensitivity was calibrated using the light source DH-2000-CAL (Ocean Optics, USA).

Side-on spatially resolved spectra were made with the imaging spectrograph Shamrock 750 (Andor, Northern Ireland) with the EMCCD Newton 971 (Andor) with an entrance slit width of $20 \mu m$ and a grating with 600 lines mm^{-1}. Using two lenses, the jet was imaged onto the entrance slit of the spectrometer.

The experimental setup and gating sequence for the PROES measurements are shown in figure 1. A high-repetition rate gated iCCD camera (LaVision PicoStar HR12) was used for the imaging. The image intensifier consists of a photo cathode, micro channel plate (MCP) and phosphor screen. The kinpen Sci generates a TTL signal that is fed to the camera control unit. During each period of the plasma jet the control unit gates the MCP for 1 ns after a fixed phase locked delay with respect to the TTL signal. The gating signal and the voltage applied at the inner electrode of the jet are monitored on the oscilloscope allowing an assignment of the image with the phase of the jet. By varying the delay with respect to the TTL signal phase resolution is obtained. The exposure time of the CCD was adjusted for the light intensity and ranges from 20 ms to 800 ms. A 707 nm filter with a spectral FWHM of 9 nm was used for observing He emission (He 3^3S-2^3P) and a 390 nm filter (FWHM 20 nm) was used for N_2 emission (first negative system, FNS and second positive system, SPS). The field of view of the camera for the PROES measurements with the plasma turned off is shown in figure 2. An additional gas flow of 0.1 slm can be introduced in the plume of the plasma jet using a glass pipet.
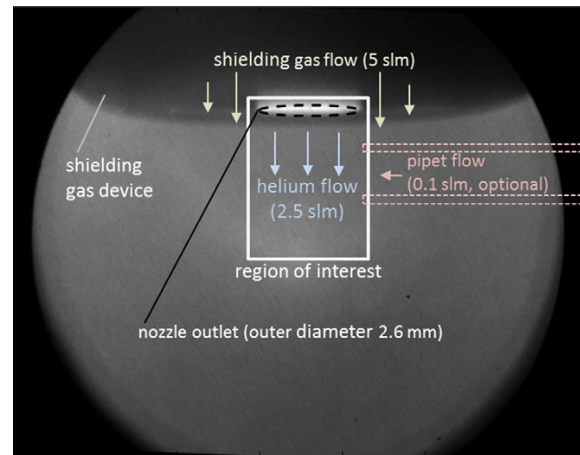
Figure 2. Field of view of camera and geometry used in the PROES setup.

2.2. Model

Using the 2-D cylindrically symmetric, plasma hydrodynamics model, *non-PDPSIM* [25, 26], a single jet with a shielding gas curtain with dimensions similar to that of the kinpen Sci was simulated using an unstructured triangular mesh as shown in figure 3. The computational domain is 24 mm by 8.8 mm and contains nearly 16 000 nodes with 13 000 being plasma nodes. The mesh has refinement zones that, as shown in the left panel of figure 3, allow for finer resolution in the discharge region (from $30 \mu m$ at the tip of the pin electrode) to coarser resolution (0.2 mm) far from the plasma. The primary goal of this computational investigation was to analyze the effects of the shielding gas on the propagation of the ionization wave and the production of reactive species from the interaction of the plasma produced charged and reactive species and the gas in the curtain. A secondary aspect was to validate the model through comparison of trends with the experiment using this
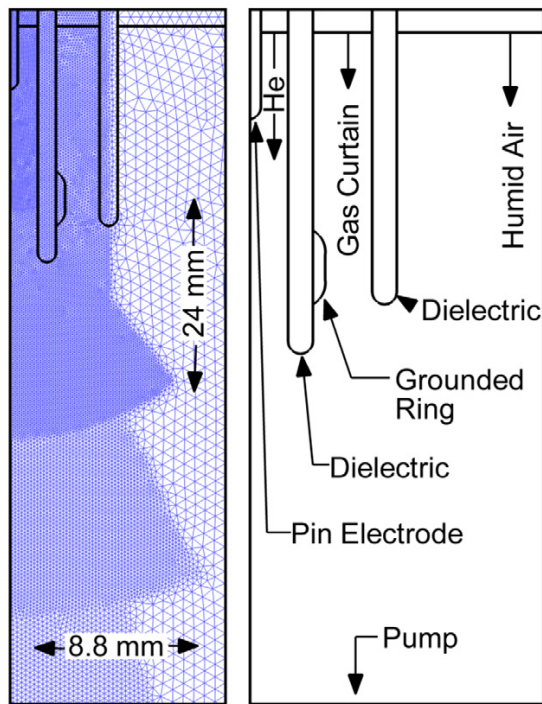
Figure 3. Geometry and mesh applied in the numerical model.

unique scenario of gases shrouding the helium plasma jet to optimize production of RONS.

In this study, the plasma transport module, the radiation transport module and the fluid transport modules of *non-PDPSIM* were used. The neutral flow field was modeled by integrating modified versions of the compressible Navier–Stokes equations which account for large gradients in average molecular weight. The flow field is allowed to develop for 5 ms prior to applying voltage to the electrode. At this point, the plasma transport module is used to solve Poisson's and charged and neutral species continuity equations with picosecond time-steps using a fully implicit Newton-iteration technique with a maximum allowed error of 3×10^{-6} for convergence for each timestep. Poisson's equation is solved throughout the entire computational domain, including both dielectric tubes ($\varepsilon/\varepsilon_o$ = 4 without conductivity) and electrodes (treated as metal). Using a time-slicing technique, the electron energy equation is updated for electron temperature which is then used to provide transport coefficients and rate coefficients. These coefficients are obtained from tabular stationary solutions of Boltzmann's equation for the electron energy distributions. These tables are updated every 5×10^{-11} seconds to reflect instantaneous changes in gas composition. Photoionization of O_2 is addressed in the radiation transport module. During the discharge pulse the fluid module is called every 5×10^{-11} seconds to provide close coupling to the plasma transport. The description of the model of an atmospheric pressure plasma jet into humid air is described in depth in [27].

In the numerical investigation, impure He (containing 2 ppm O_2 and 3 ppm H_2O) flows through the central tube at

2.5 slm. The shielding gas flows at 5 slm into humid air (N_2/O_2/H_2O = 79.5/20/0.5). Four shielding gas compositions were analyzed: N_2/O_2 = 99/1, 1/99, 80/20 (synthetic air), and an artificial electronegative N_2 (eN_2). In order to isolate the consequences of an electronegative shield, an N_2 shield was modelled while allowing the N_2 to additionally attach to form a fictitious N_2^- using the same rate of attachment and ion–ion neutralization as would occur for O_2^-. This is referred to as electronegative N_2 (eN_2).

The voltage profile used in the model is a 5 ns rise time to −15 kV and 75 ns duration at that voltage. The ring electrode on the inner tube is grounded. Compared to the experiments, a higher voltage is applied in the model in order to produce a guided streamer on the first discharge pulse. The propagation of a single negative streamer during an 80 ns interval is simulated.

3. Results and discussion

3.1. Optical emission spectroscopy

An example of the low resolution optical emission spectrum is shown in figure 4 when using N_2 or synthetic air as the shielding gas. The emission originates from atomic He, the He excimer, atomic oxygen (O), molecular N_2 and molecular N_2 ions, as well as from hydroxyl and atomic hydrogen [28–30]. The end-on spectra obtained with N_2 and synthetic air as shielding gases are similar, which is expected as the emission in this case mainly originates from inside the capillary. Only a slight increase of the intensity of the O lines and a small decrease of the N_2 emission were observed when synthetic air was used compared to N_2. Note that emission from O, hydroxyl (OH) and atomic hydrogen (H) is observed which originates from impurities in the He. The feed gas contains up to 3 ppm of water vapor and up to 2 ppm of O_2. Further impurities may result from desorption from the interior surfaces of the feed gas tube, back diffusion from the ambient or diffusion through PTFE tubes [31].

Differences in the spectra for different shielding gases were found when observing the plume from the side, as shown in figure 5. Emission originating from the FNS (N_2^+ (B) → N_2^+(X)) and SPS (N_2(C) → N_2(B)) of N_2 is shown spatially resolved along the axis of the jet for N_2 and synthetic air shielding gases. In both cases the emission is strongest in the vicinity of the jet nozzle. However, in the N_2-shielded case, the FNS emission first drops to near zero at around 1 mm and then rises again up to 4.5 mm. Switching from N_2 to synthetic air shielding produces a 50% increase in FNS emission while the SPS emission is nearly totally quenched.

3.2. Effect of shielding gas on ionization wave propagation

The voltage applied at the electrode of the jet is shown in figure 6 together with the total phase resolved emission of the jet along the axis for shielding gas compositions of N_2/O_2 = 100/0, 90/10, 80/20 and 0/100. While operating at a carrier frequency of 940 kHz, the voltage signal is additionally modulated at 470 kHz: During a 2.1 μs period, the voltage
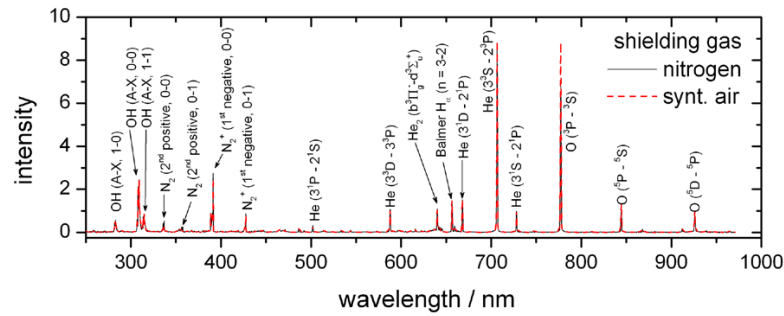
Figure 4. End-on spectra when using N_2 or synthetic air as the shielding gas. These spectra do not significantly differ with varying shielding gas composition since the emission dominantly originates in the tube (in contrast to side-on measurements).
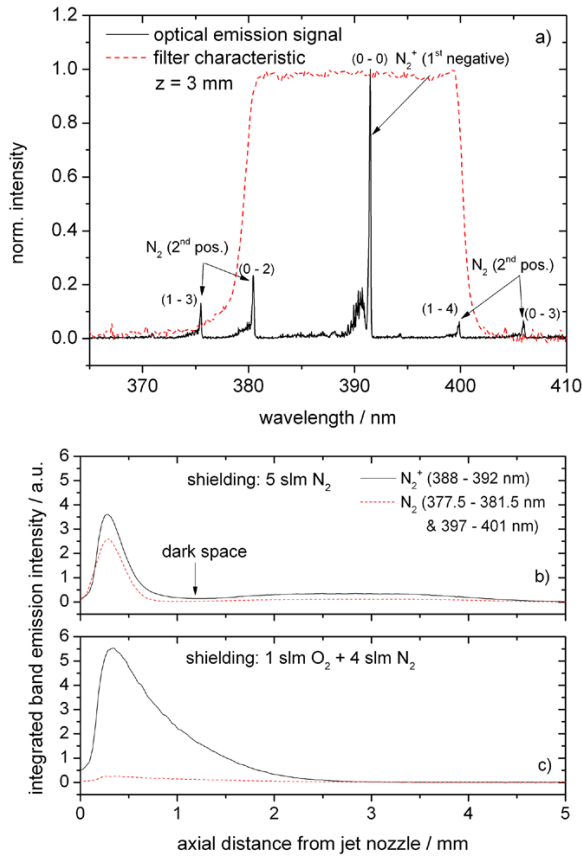

Figure 5. (a) Side-on measurement N_2 and N_2^+ emission from the jet operated with N_2 shielding gas. The dashed line shows the transmission curve of the filter used for monitoring the N_2 emission in the PROES measurements. (b) Integrated N_2 and N_2^+ band emission intensity along the axis of the jet for N_2 as the shielding gas. (c) Integrated emission for synthetic air as the shielding gas.

Figure 6. Applied voltage (a) and phase resolved on-axis emission without a filter and shielding gases having N_2/O_2 mixtures of (a) 100/0, (c) 90/10, (d) 80/20 and (e) 0/100. The angles of the emission patterns yield the speed of the excitation fronts. Images in figures 7–10 were taken at phase positions 1–28 shown in (b).

signal has a strong positive half-cycle, followed by a strong negative, a weak positive and a weak negative half-cycle. This pattern is regular with a 2.1 μs period and is reflected in the axial PROES measurements shown in figures 6(b)–(e). The excitation dynamics strongly depend on the O_2 content of the shielding gas. With an N_2 shield, the excitation front

propagates from the nozzle in the direction of the gas flow with a speed of 1800 m s^{-1} during the positive half-cycle. The emission features a dark space at a distance of about 0.5 to 1 mm, which is visible to the naked eye. The excitation front
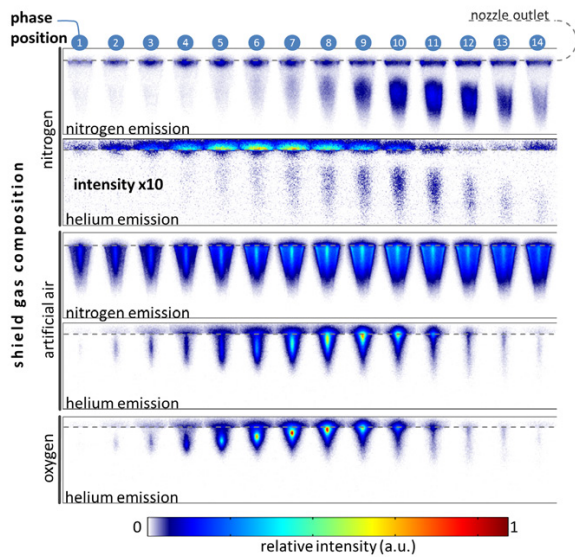
Figure 7. N_2 and He emission during the strong positive half-cycle for different shielding gas compositions. The phase positions are chosen as defined in figure 6. Note that the He emission intensity for the N_2 shielding case is multiplied by a factor ten compared to the He emission for the synthetic air and O_2 case.

Figure 8. Same as figure 7 for the strong negative half-cycle (continued).

propagates in the opposite direction with a speed of about $4200\,m\,s^{-1}$ if the shielding gas contains O_2. The speeds of the forward and the backwards directed excitation waves were obtained from the angle of spatial position versus time in figures 6(b) and (e). The backwards directed excitation wave originates from the plume region and propagates towards the inner needle electrode. It only appears if the shielding gas contains O_2 and is most pronounced if the shielding gas is pure O_2 (see figure 6(e)). Such backwards directed excitation waves have been observed in needle-to-plane discharges [32].

Phase resolved optical emission from He and N_2 is shown in shown in in figure 7 for the strong positive half-cycle and in figure 8 for the strong negative half-cycle. The timings of the images are indicated by the phase number using the scale shown in figure 6(b). The exposure time of the CCD is 140 ms for N_2 emission and 800 ms for He emission. The bandwidth of the filter for the He 706.7 nm line is small enough to dominantly capture this line. The filter used for N_2 emission captures both SPS and FNS radiation (see figure 5(a)).

With N_2 shielding gas, the N_2 emission during the positive half-cycle is low in the plume region. Emission from N_2 is strong from phases 9–13 after which it decays (phase positions 14–28). During the negative half-cycle (phase positions 19–25), strong emission from N_2 occurs at the side of the nozzle outlet. This emission is not followed by an increase in emission at distances further from the nozzle. The ionization wave here appears to spread radially outward rather than being focused in the axial direction.

As O_2 is introduced in the shielding gas, the emission dynamics change. A low but broad N_2 emission occurs throughout the entire period. This emission follows the contours of the ambient air density. A similar fluorescence pattern
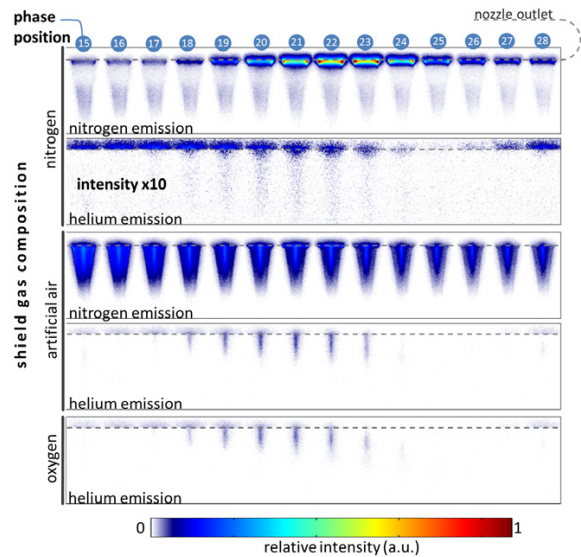
was observed in laser induced fluorescence measurements of OH and was explained by diffusion of air into the active plume of the jet [33, 34]. Strong N_2 emission also occurs on-axis during phase 7–12 and at the He-air boundary. Emission maxima at the He-air boundary may result from the higher N_2 densities at this position. The strong on-axis emission directly correlates with the emission from He at these phases. The maximum in He emission propagates from a distance of 2.5 mm towards the nozzle. This behavior occurs at low O_2 concentrations (10%) in the shielding gas and becomes more pronounced as the O_2 content increases. Qualitatively the He emission dynamics are the same for 10–100% O_2 in the shielding gas. The emission dynamics suggest that a backwards directed excitation wave occurs from the plume region towards the anode.

The emission during the negative half-cycle (figure 8) is also qualitatively different when O_2 is present in the shielding gas. The strong N_2 emission at the side of the nozzle with pure N_2 shielding gas does not occur. Instead, He emission is observed on-axis at phase positions 18 to 23 with O_2 in the shield. One explanation is that without O_2 in the shielding gas, high energy electrons propagate in the radial direction where they excite N_2 at the side of the jet nozzle. With O_2 in the shielding gas, these electrons are focused towards the axis and are able to excite the high energy He states.

Both the N_2 FNS ($N_2^+(B) \rightarrow N_2^+(X)$) and the He 706.7 nm emission are more intense if O_2 is in the shielding gas while the FNS emission is stronger without O_2 present (see figures 5, 7 and 8). These trends indicate that the N_2 shielded jet produces lower electric fields (and lower electron energies) than the synthetic air or O_2-shielded jet. The energy levels involved in the emission of FNS and SPS radiation and He 706.7 nm emission and the rate coefficients for the direct excitation from the ground states are shown in figure 9. The rate coefficients were computed with BOLSIG+ [35] using the cross sections from
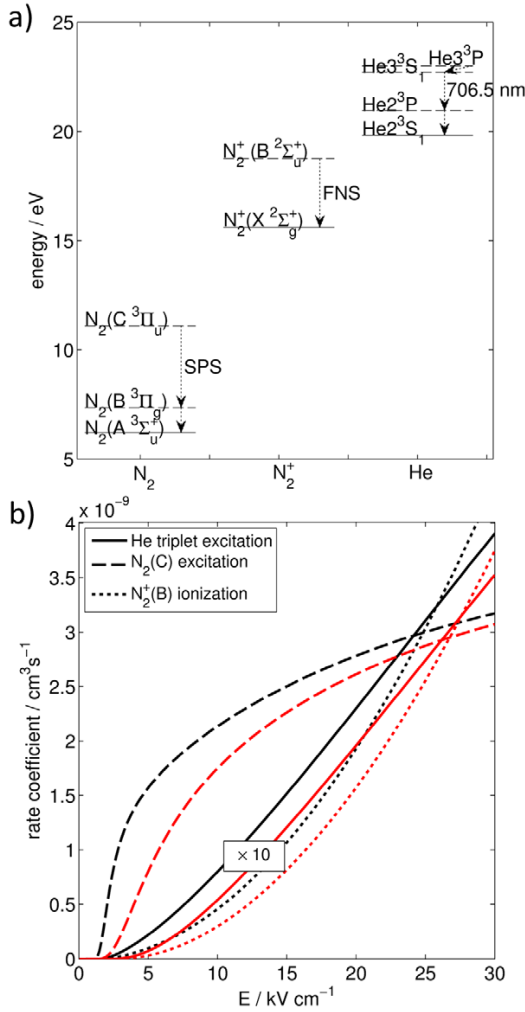
Figure 9. (a) Energy levels involved in the FNS and SPS emission from N_2 and He 706.7 nm emission. (b) Electric field-dependent rate coefficients for the excitation of the levels for FNS, SPS and 706.7 nm emission. Rate coefficients are shown for pure He (black lines) and 99% He with 1% dry air (red lines).
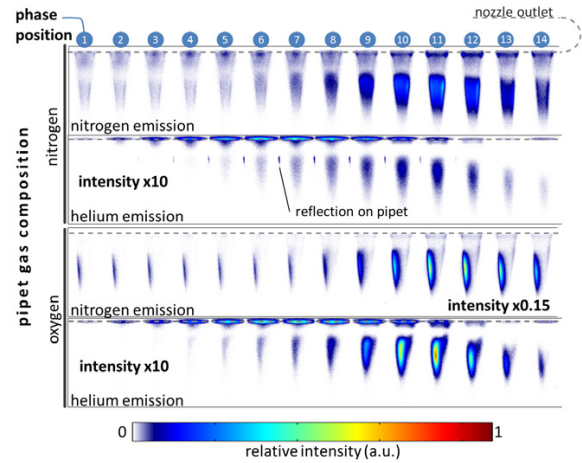

Figure 10. N_2 and He emission during the strong positive half-cycle of the N_2-shielded jet doped with either N_2 or O_2 from a pipette. The phase positions are chosen as defined in figure 6.
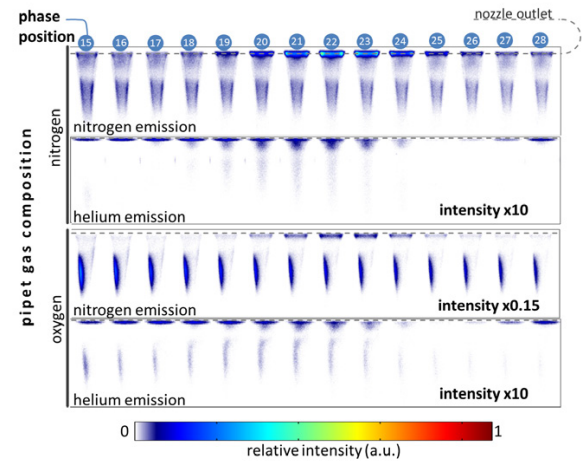
Figure 11. Same as figure 10 for the strong negative half-cycle (continued).

[36, 37]. At lower electric fields, more SPS radiation can be expected, while at high electric fields the FNS radiation and He 706.7 nm emission should increase on a relative basis.

3.3. Effect of asymmetric O_2 distribution in the plasma plume on ionization wave propagation

To investigate the effect of an electronegative gas in the ambient gas surrounding the jet, gas was injected asymmetrically into the jet using the pipet (see figure 2). A flow of 0.1 slm of either O_2 or N_2 was injected. The average lateral speed of the injected gas was $2 \, ms^{-1}$ compared to the average speed of the gas through the capillary of $21 \, ms^{-1}$ and of the shield gas of $3 \, ms^{-1}$. He and N_2 emission are shown in figure 10 for the positive half-cycle and figure 11 for the negative half-cycle. When N_2 is flowed through the pipette, there is little change in the emission from either He or N_2. The additional

gas flow through the pipette does not significantly influence the flow field as the flow remains laminar. However, when O_2 is flowed through the pipette from the right side, a stronger emission from both He and N_2 occurs on the left side of the plume. The overall dynamics are not as significantly changed as when O_2 is in the shielding gas, especially no backwards directed excitation wave is observed during the positive half-cycle. As without the pipet, the emission in the positive half-cycle is stronger than in the negative half-cycle. Qualitatively the results do not depend on the exact position of, or the mass flow through the pipet. The exception is when the flow through the pipet is in the slm range, which resulted in bending of the visible plasma plume due to the crossflow.

From these results, two conclusions may be drawn. First, the differences in the guided streamer dynamics observed when O_2 is present in the shielding gas likely do not result
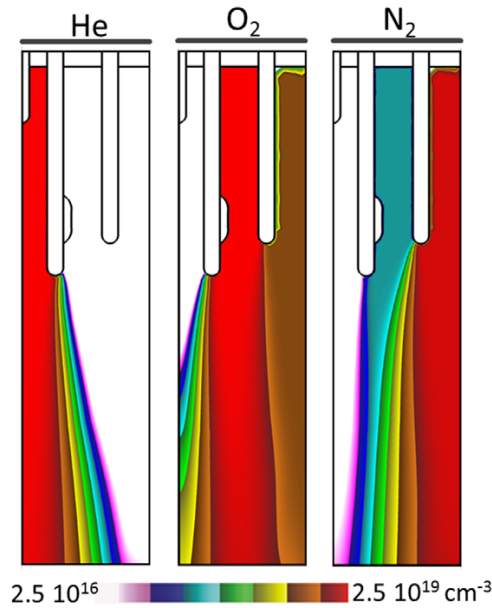
Figure 12. Gas composition resulting from the jet flow with O_2 shield gas obtained from the model.

from local chemical processes. The distortion of the discharge indicates a long-range effect. Second, providing O_2 in the downstream region is not sufficient to initiate the backwards directed excitation wave during the positive half-cycle. The backwards directed excitation wave requires that O_2 be present in the vicinity of the jet nozzle.

3.4. Modelling of plasma jets with gas shields

The computed densities of He, O_2 and N_2 at 5 ms corresponding to the steady state flow profile for the helium plasma jet with a shielding gas of 99% oxygen and 1% nitrogen are shown in figure 12 prior to the application of a negative voltage at the inner electrode. The sharp demarcation of the central He flow occurs as convective transport strongly dominates diffusive transport into the oxygen shielding gas for the given jet configuration.

Results from the model for the densities of electrons, anions (total of negatively charged ions) and cations (total of positively charged ions) are shown in figure 13 for shielding gases of N_2, O_2, synthetic air and for the eN_2 shield gas. The electron impact ionization source and electric field are shown in figure 14. The times of the images (20, 40, 60, and 80 ns) highlight the propagation of the guided negative streamer and the production of associated charged species. The 80 ns image is at the end of the maximum in applied voltage (-15 kV). The electron density inside the tube is basically independent of the composition of the gas curtain. The electrons separate from the powered pin electrode forming a cathode-fall-like sheath and have their highest density at the edge of the sheath. As the electrons drift from the pin electrode in the direction of the grounded ring, they charge the wall of the dielectric tube beneath the ring which produces parallel components of the
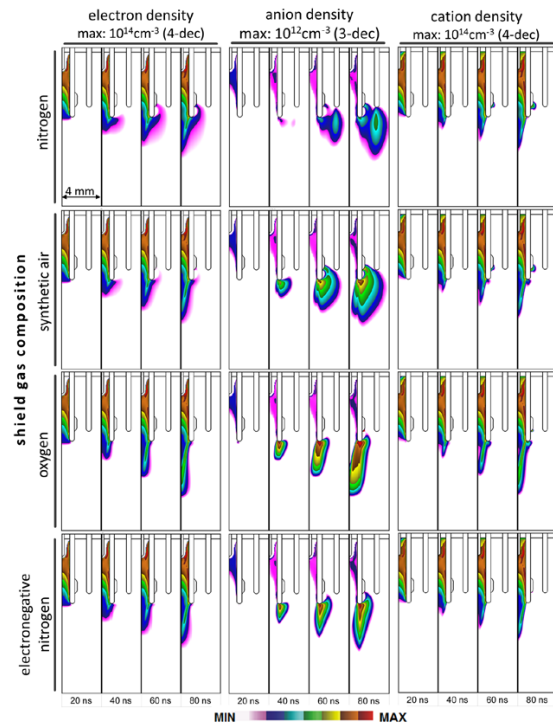
Figure 13. Electron, anion and cation density obtained from the numerical model for the indicated shielding gas compositions.

electric field. These parallel components of the electric field sustain a surface ionization wave along the interior wall. This annular plasma density is the source of the annular optical emission observed in previous investigations. The formation of the conducting channel inside the tube compresses the applied voltage into the non-conductive regions outside the plasma channel, and in part helps sustain that ionization wave shown as the source ionization term, S_e, in figure 14. As the plasma channel approaches the edge of the tube and passes by the grounded electrode outside the tube, the electric field is locally maximum at the end of the tube as shown at 20 ns in figure 14. Also independent of composition of the shielding gas, upon exiting the tube, the ionization wave and plasma density move towards the axis, approximately following the 0.1% contour line of the shielding gas mole fraction. However, the manner in which this transition occurs is sensitive to the shielding gas composition as shown by the propagation of the guided ionization wave into the shielding gas in figure 14.

With the pure N_2 shield gas, the plasma density (represented by the electron density in figure 13) forms a halo around the end of the tube that is absent (or at least greatly diminished) when O_2 is in the shield. The source of the halo is Penning ionization by He_m, photoionization and diffusion of electrons from the edge of the ionization waves which seeds electrons at larger radii. These electrons then avalanche in the intensified electric field at the edge of the tube. In gas shields containing O_2, these low energy electrons diffusing or produced by photoionization are quickly consumed to form O_2^- by 3-body attachment or O^- by dissociative attachment.
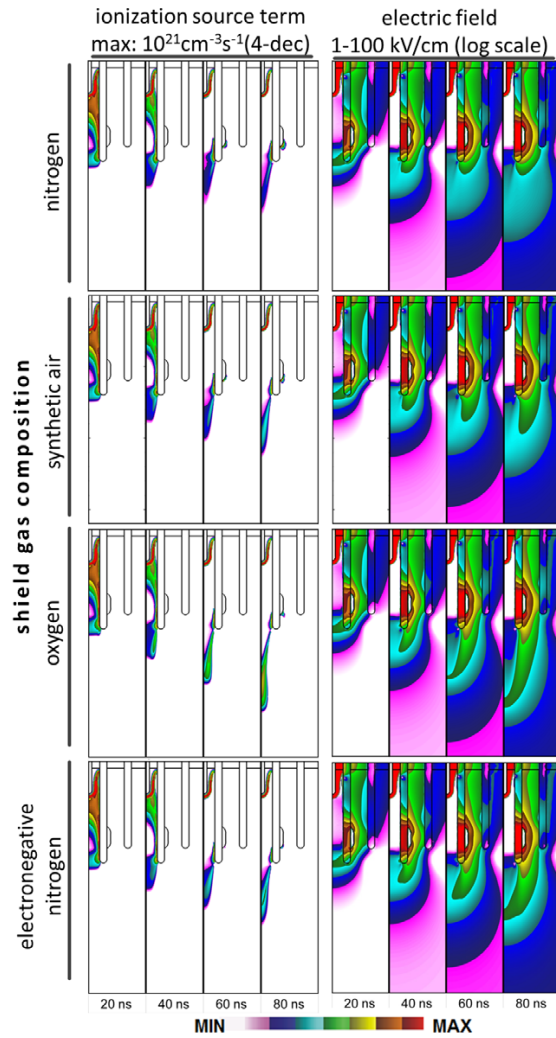
Figure 14. Ionization rates and electric field obtained from the model for the indicated shielding gas compositions.

This suppression of the halo is shown by the anion density at the interface between the shield gas and the He plume. This negative ion halo replaces the electron halo produced in the absence of O_2. Note that with the N_2 shield, there are low densities of anions at the interface between the N_2 shield and surrounding air. This small density of negative ions results from the same processes—dominantly photoionization that seeds electrons in the O_2 containing interface between the air and the N_2 shield.

The length of the electron plume with the O_2 shielding gas is twice as long as for the N_2 shielding gas, 4 mm compared to 2 mm after 80 ns. The on-axis electron density is about an order of magnitude larger for the O_2 shield. The dry air shield is intermediate between the pure gas shields. These densities result from the ionization wave propagating proportionately further with the O_2 shield as shown in figure 14. This further propagation of the ionization wave with the O_2 shield is enabled by an electric field that extends through the low

conductivity of the anion dominated interface between the He plume and the gas shield. The higher conductivity of the interface with the N_2 gas shield shorts out the electric field, and so reduces the magnitude of the ionization wave.

The density of anions is largest with the pure O_2 shield and decreases with the fraction of O_2 in the shield. The sharp demarcation of the anion density at the edge of the tube results from a number of causes. First, the electric field is fairly continuous across the intersection of the He plume and the gas shield while the composition changes over a distance of only a few hundred microns. This change in composition from impure He to O_2 containing molecular gas increases the self-sustaining E/N (electric field/gas number density) from tens of Td in the He plume to hundreds of Td in the molecular gas. (1 Td = 10^{-17} Vcm^2 or 250 Vcm^{-1} at atmospheric pressure). The self-sustaining E/N in the molecular gas exceeds that available. The transition between net-ionization and net-attachment across the interface occurs in only 80 μm. Any electrons that are produced at larger radii are quickly attached. With the N_2 shield, the local maximum in anion density at 80 ns below the inner tube results from the 1% O_2 in the N_2 gas shield and the maximum below the outer tube is where the electrons that have spread through the N_2 gas curtain attach to the O_2 in the humid ambient air.

For each composition, the cations follow the electron density with the exception of the lateral spread in the N_2 case. Here the plasma density is below the ambipolar limit in the intense electric fields between the tubes adjacent to the grounded electrons. This allows electrons to rapidly drift independent of the ions but not produce significant ionization.

The higher electric fields obtained for the O_2 containing gas shields are consistent with the proposed mechanisms based on experimental OES measurements. As discussed in section 3.1, the relative change of FNS and SPS emission and the increase in He emission with O_2 content in the shielding suggest higher electric fields in the plasma plume.

The electron plume with the fictitious electronegative eN_2 shield gas closely resembles that for the O_2 shields, having a near complete absence of the electron halo and having the extended electric field enabled by the low conductivity interfacial region. The ionization wave for the eN_2 shield does not extend as far as for the O_2 shield. The vibrational and electronic excitation of eN_2 diffusing into the He plume provides more non-ionizing energy losses for the electrons compared to the O_2 shield. The anion density is lower than in the O_2 shield case, as dissociative attachment is not included for eN_2.

3.5. Electrostatic focusing mechanism (negative half-cycle)

Without O_2 in the shielding gas electrons are transported in radial direction where they excite N_2 at the side of the jet nozzle (see figure 8 phase positions 20–24). The electrons are focused towards the axis when O_2 is present and are able to excite the high energy He and N_2 states. The results from the model (figures 13 and 14) for a negative pulse suggest that N_2 shielding leads to more transport of electrons in the radial direction whereas an electronegative shielding gas is more likely to confine and guide the streamer. As these dynamics
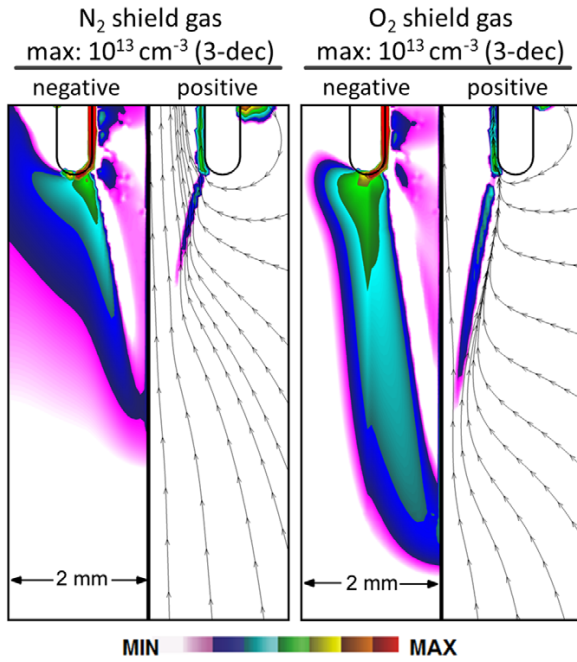
Figure 15. Total density of positive and negative charge for N_2 and O_2 shielding gas and electric field lines.

are similar for the O_2 and eN_2 shielded cases, it is likely that the focusing is associated with the electronegativity of the gas.

Based on these observations, an electrostatic focusing mechanism is proposed. The computed positive and negative charge densities in the plasma plume of the jet shielded with N_2 and O_2 are shown in figure 15. The resulting electric field lines (pointing in the opposite direction of electron drift) are also shown. If N_2 is the shield gas, electrons are the primary negative charge carriers. As the streamer head is negatively charged, electrons drift radially outward due to their high mobility. If O_2 shield gas is used, electrons that drift outward are attached to form negative ions that have comparably low mobility. The electric field produced by the anions focuses electrons towards the axis of the jet. In this sense, the negative ions produced by an electronegative shielding gas play a similar role to the charging of the dielectric by electrons for negative streamers propagating inside tubes. In these cases, the surface is charged in front of the streamer head and turns the electric field parallel to the axis of the tube which reinforces the streamer propagation [21]. The second effect of the electronegative gas is the attachment process itself, which prevents ionization waves from propagating outwards in radial direction. In the N_2 shielded case these two confining mechanisms are absent.

This mechanism is consistent with the measurements of OES for an N_2 shield with the additional pipet flow of O_2 and N_2 (see figures 10 and 11). Here the negative space charge with the O_2 injection only acts on one side of the plume. Instead of focusing the ionization wave with attachment on both sides of the channel, the ionization wave migrates towards the other side of the guiding He channel where propagation is less inhibited.

3.6. Backwards directed excitation wave (positive half-cycle)

While the mechanisms leading to the backwards directed excitation wave during the positive half-cycle are not yet fully understood, some conclusions can be drawn from the our experimental and numerical results. As shown in section 3.3, providing O_2 in the downstream region is not sufficient to produce the backwards directed excitation wave. Consequently, it is also unlikely that photoionization or Penning-ionization of O_2 at the starting point of the backwards directed excitation wave can explain this behavior [38, 39]. The situation is similar for Penning ionization by metastable He_m, which also has a minor effect on guided streamer propagation [15]. The rate coefficients k_i for the Penning ionization of N_2 and O_2 [23],

$$He_m + N_2 \rightarrow He + N_2^+ + e, \ k_1 = 8 \cdot 10^{-11} \, cm^{-3} \, s^{-1} \quad (4)$$

$$He_m + O_2 \rightarrow He + O_2^+ + e, \ k_2 = 17 \cdot 10^{-11} \, cm^{-3} \, s^{-1} \quad (5)$$

are likely too similar to explain the observed differences. (The same is true for Penning ionization in three-body processes [40]).

Our current hypothesis is that the backwards directed excitation wave depends on the dynamics of the previous negative half-cycle. Anions generated in the downstream region by attachment to O_2 could provide seed electrons through electron detachment reactions for the backwards directed excitation wave in the subsequent positive half-cycle. Electron detachment reactions through thermal reactions such as

$$O_2^- + He \rightarrow He + O_2 + e, \ k_3 = 3.9 \cdot 10^{-10}$$
$$\exp(-7400 \,/ T_g) \, cm^{-3} \, s^{-1} \quad (6)$$

are typically important only at temperatures higher than in the plume for our conditions, $T_g = 350 \, K$ [23], ($k_3 = 2.6 \cdot 10^{-19} \, cm^3 \, s^{-1}$). However, detachment by excited states proceeds with nearly gas kinetic rate coefficients,

$$O_2^- + He_m/He_2^* \rightarrow e + products, \ k_4 = 3 \cdot 10^{-10} \, cm^{-3} \, s^{-1} \quad (7)$$

In the previous work [23] Winter *et al* measured sufficient metastable densities of $10^{12} \, cm^{-3}$ at the starting point of the excitation wave before it starts propagating towards the inner pin electrode (1–1.5 mm from the nozzle). Associative attachment producing ozone (O_3) from O^- and O_2 can yield electrons in the plasma plume, as well as the formation of nitrogen oxides in reactions involving O^- or O_2^- with typical rate coefficients in the order of 10^{-10} cm^{-3} s^{-1} [41]. Further modelling and experimental studies using other electronegative shielding gases, would provide additional insights on the origin of the backwards directed excitation wave.

4. Concluding remarks

In this work the effects of the composition of the gas shield surrounding a cold atmospheric He plasma jet was investigated both experimentally and numerically. We found that the ratio of optical emission of the first negative system and second positive system of N_2 significantly change depending on whether the shielding gas contains O_2. Phase resolved
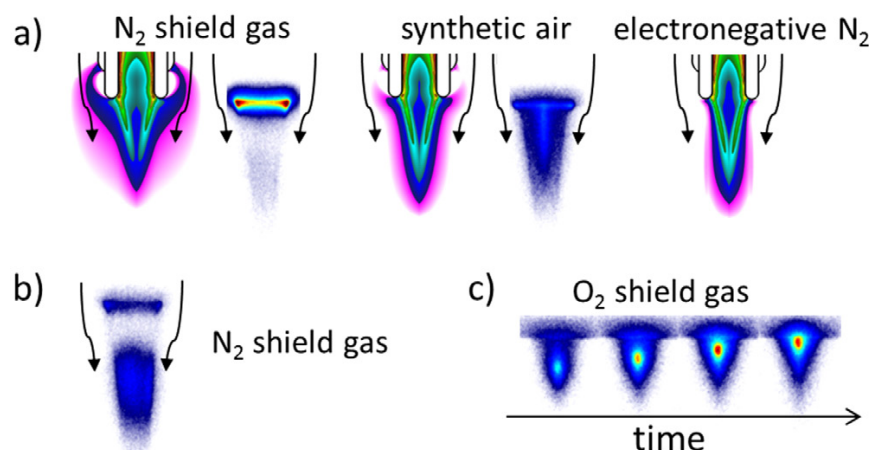
Figure 16. Summary illustrating our findings. In (a) the effects of various shielding gas compositions on the propagation of the ionization wave during the negative half-cycle are shown by the electron density obtained from the numerical model and PROES measurements (N_2 emission). If the shielding gas does not contain any O_2, the ionization wave tends to spread sideways when exiting the tube. The artificial electronegative eN_2 shielding case behaves similar to shielding with synthetic air. In (b) the dark space occurring in the N_2-shielded jet during the positive half-cycle is shown. In (c) the backwards directed excitation wave occurring during the positive half-cycle of the O_2-shielded jet is illustrated. (b) and (c) are experimental observations.

optical emission spectroscopy revealed three emission features that are summarized in figure 16: If pure N_2 is used as shielding gas, strong N_2 emission occurs at the side of the jet nozzle during the negative half-cycle. A dark space also occurs close to the exit of the nozzle. If the shielding gas contains O_2, emission propagates from the ambient towards the jet nozzle against the direction of the gas flow during the positive half-cycle of the jet. From results of modelling, it was found, that when a pure N_2 shielding gas is used, electrons spread radially outward at the edge of the nozzle. This spreading does not occur if the shielding gas contains O_2. In this case an anion sheath forms around the He channel in which the ionization wave propagates further and produces higher electric fields in the head of the guided streamer. This is due to the lower conductivity outside the core of the guided streamer that enables greater penetration of the electric field.

Based on these experimental and numerical findings, the following mechanism is proposed. The electric field generated by the anions contributes to a focusing of the electrons towards the center of the He channel, thereby promoting the propagation of the ionization wave during the negative half-cycle. In this way anions can be generated at distances of a few mm from the jet nozzle. These anions can then provide the seed electrons for the backwards directed excitation wave observed during the next positive half-cycle. This mechanism is consistent with the behavior of the jet when injecting O_2 with a pipette. The injected O_2 focuses the ionization wave to the opposite side of the He channel from where the gas is injected. Electrostatic forces due to negative space charge caused by anions can have a significant effect on the propagation of guided streamers in cold atmospheric pressure plasma jets operated with noble gases. The observed effects appear to arise from the interface of a non-electronegative and an electronegative gas. Through a variation of the shield gas composition fundamental plasma parameters (plasma density, mean electron energy) in the plasma plume of

CAPJ can be influenced. This can be exploited for the optimization of plasma processes for the typical fields of application of such devices, e.g. for the treatment of biotechnological surfaces or biological tissue.

Acknowledgments

References

[1] Ehlbeck J, Schnabel U, Polak M, Winter J, Von Woedtke T, Brandenburg R, Von dem Hagen T and Weltmann K 2011 Low temperature atmospheric pressure plasma sources for microbial decontamination *J. Phys. D: Appl. Phys.* **44** 013002

[2] Park G, Park S, Choi M, Koo I, Byun J, Hong J, Sim J, Collins G and Lee J 2012 Atmospheric-pressure plasma sources for biomedical applications *Plasma Sources Sci. Technol.* **21** 043001

[3] von Woedtke T, Reuter S, Masur K and Weltmann K-D 2013 Plasmas for medicine *Phys. Rep.* **530** 291–320

[4] Lu X, Laroussi M and Puech V 2012 On atmospheric-pressure non-equilibrium plasma jets and plasma bullets *Plasma Sources Sci. Technol.* **21** 034005

[5] Lu X, Naidis G, Laroussi M and Ostrikov K 2014 Guided ionization waves: theory and experiments *Phys. Rep.* **540** 123–66

[6] Reuter S, Winter J, Schmidt-Bleker A, Tresp H, Hammer M U and Weltmann K-D 2012 Controlling the ambient air affected reactive species composition in the effluent of an argon plasma jet *IEEE Trans. Plasma Sci.* **40** 2788–94

[7] Schmidt-Bleker A, Winter J, Iseni S, Dünnbier M, Weltmann K and Reuter S 2014 Reactive species output of a plasma jet with a shielding gas device—combination of FTIR absorption spectroscopy and gas phase modelling *J. Phys. D: Appl. Phys.* **47** 145201

[8] Reuter S, Winter J, Schmidt-Bleker A, Schroeder D, Lange H, Knake N, Gathen V S-v d and Weltmann K-D 2012 Atomic oxygen in a cold argon plasma jet: TALIF spectroscopy in ambient air with modelling and measurements of ambient species diffusion *Plasma Sources Sci. Technol.* **21** 024005

[9] Barton A 2014 Impact of non-thermal plasma on cell signaling in keratinocytes *PhD Thesis* Ernst-Moritz-Arndt-Universität Greifswald, Germany

[10] Zhu W-C, Li Q, Zhu X-M and Pu Y-K 2009 Characteristics of atmospheric pressure plasma jets emerging into ambient air and helium *J. Phys. D Appl. Phys.* **42** 202002

[11] Hofmann S, Sobota A and Bruggeman P 2012 Transitions between and control of guided and branching streamers in dc nanosecond pulsed excited plasma jets *IEEE Trans. Plasma Sci.* **40** 2888–99

[12] Breden D, Miki K and Raja L 2012 Self-consistent two-dimensional modeling of cold atmospheric-pressure plasma jets/bullets *Plasma Sources Sci. Technol.* **21** 034011

[13] Sakiyama Y and Graves D B 2009 Neutral gas flow and ring-shaped emission profile in non-thermal RF-excited plasma needle discharge at atmospheric pressure *Plasma Sources Sci. Technol.* **18** 025022

[14] Goree J, Liu B, Drake D and Stoffels E 2006 Killing of S. mutans bacteria using a plasma needle at atmospheric pressure *IEEE Trans. Plasma Sci.* **34** 1317–24

[15] Naidis G 2011 Modelling of plasma bullet propagation along a helium jet in ambient air *J. Phys. D Appl. Phys.* **44** 215203

[16] Naidis G 2010 Modelling of streamer propagation in atmospheric-pressure helium plasma jets *J. Phys. D Appl. Phys.* **43** 402001

[17] Boeuf J-P, Yang L L and Pitchford L C 2013 Dynamics of a guided streamer ('plasma bullet') in a helium jet in air at atmospheric pressure *J. Phys. D: Appl. Phys.* **46** 015201

[18] Babaeva N Y and Kushner M J 2014 Interaction of multiple atmospheric-pressure micro-plasma jets in small arrays: He/O$_2$ into humid air *Plasma Sources Sci. Technol.* **23** 015007

[19] Naidis G 2011 Simulation of streamers propagating along helium jets in ambient air: polarity-induced effects *Appl. Phys. Lett.* **98** 141501

[20] Jiang C, Chen M and Gundersen M 2009 Polarity-induced asymmetric effects of nanosecond pulsed plasma jets *J. Phys. D: Appl. Phys.* **42** 232002

[21] Xiong Z, Robert E, Sarron V, Pouvesle J-M and Kushner M J 2013 Atmospheric-pressure plasma transfer across dielectric channels and tubes *J. Phys. D: Appl. Phys.* **46** 155203

[22] Luque A, Ratushnaya V and Ebert U 2008 Positive and negative streamers in ambient air: modelling evolution and velocities *J. Phys. D: Appl. Phys.* **41** 234005

[23] Winter J, Sousa J S, Sadeghi N, Schmidt-Bleker A, Reuter S and Puech V 2015 The spatio-temporal distribution of He (2^3S_1) metastable atoms in a MHz-driven helium plasma jet is influenced by the oxygen/nitrogen ratio of the surrounding atmosphere *Plasma Sources Sci. Technol.* **24** 025015

[24] Dünnbier M, Schmidt-Bleker A, Winter J, Wolfram M, Hippler R, Weltmann K and Reuter S 2013 Ambient air particle transport into the effluent of a cold

atmospheric-pressure argon plasma jet investigated by molecular beam mass spectrometry *J. Phys. D: Appl. Phys.* **46** 435203

[25] Lay B, Moss R S, Rauf S and Kushner M J 2003 Breakdown processes in metal halide lamps *Plasma Sources Sci. Technol.* **12** 8

[26] Xiong Z and Kushner M J 2012 Atmospheric pressure ionization waves propagating through a flexible high aspect ratio capillary channel and impinging upon a target *Plasma Sources Sci. Technol.* **21** 034001

[27] Norberg S A, Johnsen E and Kushner M J 2015 Formation of reactive oxygen and nitrogen species by repetitive negatively pulsed helium atmospheric pressure plasma jets propagating into humid air *Plasma Sources Sci. Technol.* Accepted for publication

[28] Lofthus A and Krupenie P H 1977 The spectrum of molecular nitrogen *J. Phys. Chem. Ref. Data* **6** 113–307

[29] Brooks R and Hunt J 1988 Helium emission spectra from doped samples of solid hydrogen and deuterium *J. Chem. Phys.* **88** 7267–72

[30] Kramida A, Yu R and Reader J and NIST ASD Team 2014 *NIST Atomic Spectra Database (version 5.2)* (Gaithersburg, MD: National Institute of Standards and Technology)

[31] Winter J, Wende K, Masur K, Iseni S, Dünnbier M, Hammer M, Tresp H, Weltmann K and Reuter S 2013 Feed gas humidity: a vital parameter affecting a cold atmospheric-pressure plasma jet and plasma-treated human skin cells *J. Phys. D: Appl. Phys.* **46** 295401

[32] Gerling T, Nastuta A, Bussiahn R, Kindel E and Weltmann K 2012 Back and forth directed plasma bullets in a helium atmospheric pressure needle-to-plane discharge with oxygen admixtures *Plasma Sources Sci. Technol.* **21** 034012

[33] Iseni S, Schmidt-Bleker A, Winter J, Weltmann K and Reuter S 2014 Atmospheric pressure streamer follows the turbulent argon air boundary in a MHz argon plasma jet investigated by OH-tracer PLIF spectroscopy *J. Phys. D: Appl. Phys.* **47** 152001

[34] Schmidt-Bleker A, Reuter S and Weltmann K-D 2014 Non-dispersive path mapping approximation for the analysis of ambient species diffusion in laminar jets *Phys. Fluids* **26** 083603 *(*1994-*present)*

[35] Hagelaar G and Pitchford L 2005 Solving the Boltzmann equation to obtain electron transport coefficients and rate coefficients for fluid models *Plasma Sources Sci. Technol.* **14** 722

[36] Biagi-v7.1 database, www.lxcat.net, retrieved on October 1, 2014

[37] Phelps database, www.lxcat.net, retrieved on October 1, 2014

[38] Kurunczi P, Lopez J, Shah H and Becker K 2001 Excimer formation in high-pressure microhollow cathode discharge plasmas in helium initiated by low-energy electron collisions *Int. J. Mass Spec.* **205** 277–83

[39] Huebner W F and Mukherjee J 2014 Photoionization and photodissociation rates in solar and blackbody radiation fields *Planetary and Space Science* **106** 111–45

[40] Myers G and Cunningham A J 1977 Quenching reactions of He($2\,3S$) and He2($2\,3\Sigma$) metastables in the presence of N$_2$ and O$_2$ *J. Chem. Phys.* **67** 3352–9

[41] Murakami T, Niemi K, Gans T, O'Connell D and Graham W G 2013 Chemical kinetics and reactive species in atmospheric pressure helium–oxygen plasmas with humid-air impurities *Plasma Sources Sci. Technol.* **22** 015003

Article A6

Reactive species output of a plasma jet with a shielding gas device—combination of FTIR absorption spectroscopy and gas phase modelling

A Schmidt-Bleker[1,2]**, J Winter**[1,2]**, S Iseni**[1,2]**, M Dünnbier**[1,2]**,
K-D Weltmann**[2] **and S Reuter**[1,2]

[1] Centre for Innovation Competence plasmatis, 17489 Greifswald, Germany
[2] Leibniz Institute for Plasma Science and Technology (INP), 17489 Greifswald, Germany

E-mail: Ansgar.Schmidt-Bleker@inp-greifswald.de

Abstract

In this work, a simple modelling approach combined with absorption spectroscopy of long living species generated by a cold atmospheric plasma jet yields insight into relevant gas phase chemistry. The reactive species output of the plasma jet is controlled using a shielding gas device. The shielding gas is varied using mixtures of oxygen and nitrogen at various humidity levels. Through the combination of Fourier transform infrared (FTIR) spectroscopy, computational fluid dynamics (CFD) simulations and zero dimensional kinetic modelling of the gas phase chemistry, insight into the underlying reaction mechanisms is gained. While the FTIR measurements yield absolute densities of ozone and nitrogen dioxide in the far field of the jet, the kinetic simulations give additional information on reaction pathways. The simulation is fitted to the experimentally obtained data, using the CFD simulations of the experimental setup to estimate the correct evaluation time for the kinetic simulation. It is shown that the ozone production of the plasma jet continuously rises with the oxygen content in the shielding gas, while it significantly drops as humidity is increased. The production of nitrogen dioxide reaches its maximum at about 30% oxygen content in the shielding gas. The underlying mechanisms are discussed based on the simulation results.

Keywords: Fourier transform infrared spectroscopy, kinetic modelling, gas phase, plasma jet, fluid dynamics, neutral particles

(Some figures may appear in colour only in the online journal)

1. Introduction

Cold atmospheric plasma (CAP) jets are gaining attention as a tool for biomedical applications, such as wound healing or cancer therapy [1–5]. Atmospheric pressure plasma sources generate a great variety of different reactive oxygen species (ROSs) and reactive nitrogen species (RNSs), which are relevant for their biological effects [6]. Plasma medicine research therefore faces the problem of disentangling the mechanisms involved in both the plasma and the biological samples or models. One approach enabling a distinction between biological effects based on ROSs and RNSs is the application of gas shielding devices, which can be used to generate a defined atmosphere, a shielding gas curtain, around the effluent of CAP jets [7, 8]. The effect of different shielding gas compositions on nitrite, nitrate and hydrogen peroxide (H_2O_2) concentrations in plasma treated liquids, on the viability of skin cells and on the cytotoxicity for skin and immune cells has been investigated [7, 9, 10].

In order to understand the underlying mechanisms in plasma sources, zero dimensional (volume averaged) models involving hundreds to thousands of reactions [11–15] as well

as space resolved simulations with reduced reaction sets have been successfully applied [16–19]. While space resolved models yield insight into fundamental physical aspects such as the streamer propagation [17, 18] or the interaction with biological tissue [16], zero dimensional models are useful for their fast computation time, which allows both large reaction sets and parametric studies. Sakiyama and Graves [15] have combined Fourier transform infrared (FTIR) spectroscopy and zero dimensional modelling for the investigation of the reactive species output of a dielectric barrier discharge. The direct combination of experimental techniques and simulations is particularly interesting, as it yields not only validated quantitative information on the species output, but also insight into the underlying chemical mechanisms. For the setup of the zero dimensional model presented in the following, the study of Van Gaens and Bogaerts [11] was especially valuable, as a similar argon operated plasma jet was investigated and main reaction pathways were discussed. The ozone production predicted therein was validated by UV-absorption measurements, yielding insight into its production and destruction mechanisms [20].

Quantitative measurements of several species on the plasma jet kinpen 09 (neoplas tools, Germany) used in this study have previously been made using spectroscopic methods such as laser induced fluorescence measurements [21, 22], infrared [23, 24] and ultraviolet [22, 24, 25] absorption spectroscopy or mass spectrometry [26]. Depending on the species investigated, the studies were carried out using argon with molecular admixtures as feed gas: when atomic oxygen or ozone was measured oxygen was admixed with the feed gas [21, 24, 25], for the measurement of OH water was admixed [22], and for NO_2 air was admixed [23]. By using admixtures, the generation of the respective reactive species can be significantly increased. However, by adding molecular admixtures to the feed gas, not only one but presumably all reactive species generated by the jet are affected, as especially excited and ionized argon atoms and molecules are subject to significant quenching by molecular gases and the energy input and electron energy distribution in the core plasma zone inside of the jet is significantly altered. The theoretical description of the effects of feed gas admixture is therefore hard to achieve. In this work the kinpen 09 is operated with pure argon in combination with a shielding gas device. The shielding gas composition is varied from pure nitrogen to pure oxygen at different humidity levels. The goal of this approach is to leave the core plasma processes largely unaltered while the reactive species output is significantly regulated. The generation of reactive species is investigated by FTIR spectroscopy combined with computational fluid dynamics (CFD) simulations and zero dimensional kinetic modelling. FTIR spectroscopy yields the ozone (O_3) and nitrogen dioxide (NO_2) densities in the far field of the jet. In order to increase the absorption length in the FTIR measurements, a White-type multipass cell (MPC) is used. The time particles need to enter the MPC is determined by CFD simulations of the actual experimental setup. Through the combination of FTIR measurements and kinetic modelling, insight into the dynamics of reactive species upon shielding gas variations is gained.

The initial values of these simulations are fitted to the densities obtained from the FTIR measurements, while the evaluation time is determined from the CFD simulations. It is shown that not only can shielding gas variations be used as a tool for tailoring the reactive species output of a CAP jet, but also the variations of oxygen to nitrogen ratio and humidity level extend the experimental data set by two dimensions. This can be exploited to validate simulations and investigate reaction pathways.

As CAP sources are usually operated at ambient air and thus subject to varying ambient humidity, the influence of ambient humidity on some ROSs and RNSs relevant in the field of plasma medicine is discussed.

2. Methods

2.1. Plasma jet and shielding gas device

For the present study the cold atmospheric pressure plasma jet kinpen 09 is used. In the centre of a ceramics capillary a needle electrode driven at a frequency of 1.1 MHz is mounted [27]. As feed gas argon (ALPHAGAZ 1, Air Liquide, France) with a gas flow rate of 3 standard liters per minute (slm) is applied.

In order to control the environment of the plasma jet, a shielding gas device is applied as presented in [7, 8]. The shielding gas forms a curtain around the effluent of the plasma jet, shielding it from the ambient air and mixing the shielding gas into the reactive effluent. In the present work, different mixtures of oxygen and nitrogen (ALPHAGAZ 1, Air Liquide, France) with a constant total gas flow rate of 5 slm are used as shielding gas. Furthermore, the humidity of the shielding gas can be adjusted using a bubbler setup in order to investigate the effect of ambient humidity on the generation of reactive species. In figure 1 the geometry of the plasma jet and the mole fraction of the shielding gas are depicted. The mole fraction is obtained by a CFD simulation using COMSOL 4.3 as discussed in [8]. Three regions are distinguished in figure 1: first, the core plasma zone inside of the plasma jet, where, apart from impurities, only argon is present; second, the effluent region, where mixing of the argon jet with the shielding gas occurs, and third, the far field, starting at a distance of about 12 mm. While many reactive species may still be present in the far field, no visible emission takes place.

2.2. FTIR absorption spectroscopy

FTIR spectroscopy in the spectral range from 700 to 4000 cm^{-1} is used to both identify and quantify long living infrared active components produced by the argon plasma jet. As described above, the plasma jet is operated with dry argon as feed gas and mixtures of oxygen and nitrogen as shielding gas. The used experimental setup is schematically shown in figure 2. The ratio of oxygen and nitrogen in the shielding gas is precisely adjusted by two mass flow controllers (labelled MFC; MKS Instruments, USA). By leading a part of this shielding gas flow through a water reservoir and combining it afterwards with the remaining dry shielding gas fraction, the shielding gas humidity can be varied in a very defined
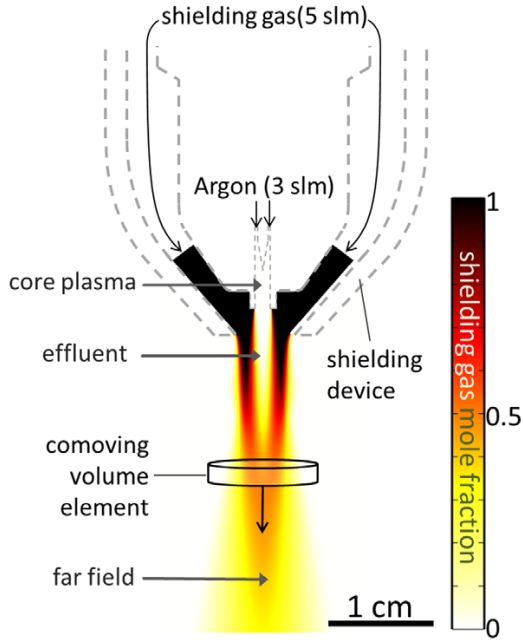
Figure 1. Sketch of the kinpen 09 geometry and visualization of the shielding gas curtain by CFD simulation. The zero dimensional reaction kinetics model can be interpreted as a volume average over a volume element comoving with the fluid (see section 2.3).

way. The humidity level was then measured by a hygrometer (DewMaster, EdgeTech, USA).

The jet and the shielding gas device are mounted on a cylindrical glass chamber with a diameter and length of 8 cm and 10 cm, respectively. In this chamber plasma produced species interact with the artificially set ambient conditions before a fraction of the resulting composition is sucked into a evacuable multipass cell (Bruker, USA) with an absorption length of 19.2 m. The pressure inside the multipass cell is monitored by a pressure gauge and set by an inlet and an outlet needle valve to 100 mbar. The gas flow rate from the mixing chamber into the multipass cell is 1.5 slm. The advantage of the lower pressure is the reduction of the particle collision rate, which results in a longer lifetime of the investigated species. Therefore, it is possible to detect species which tend to react and diminish quickly at ambient conditions. Additionally, the pressure broadening of the absorption signal is decreased, thus a differentiation of the measured signal and attribution to the respective molecules is easier to achieve. For the absorption measurements an FTIR spectrometer (Vertex 70v, Bruker, USA) was used.

In order to identify and quantify infrared active species from the measured absorption spectrum, a simulated spectrum is computed using spectroscopic data from the HITRAN database and the IR simulation software QMACSoft (neoplas control, Germany) [28, 29] By means of the Levenberg–Marquardt algorithm, the simulation is fitted to the measured absorption spectrum, yielding the species concentration [30].
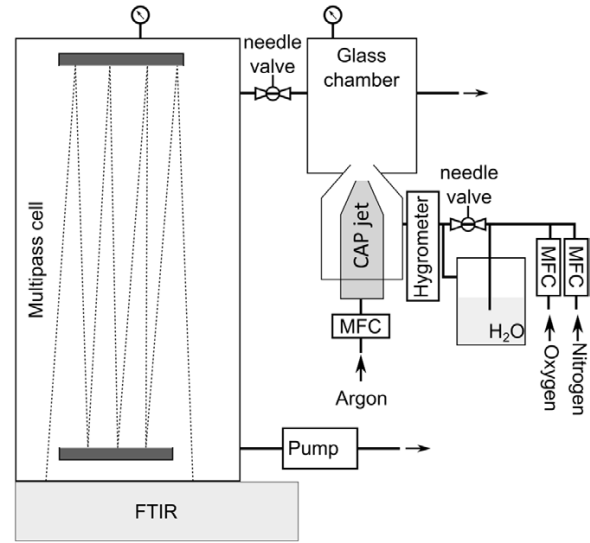
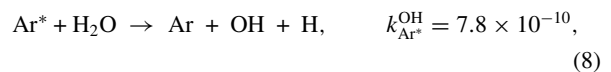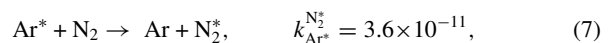**Figure 2.** Schematic diagram of FTIR setup.

2.3. Gas phase chemistry model

In the core plasma of the CAP jet excited and ionized argon species are formed via electron impact reactions, e.g.

$$e + Ar \rightarrow e + Ar^*, \tag{1}$$

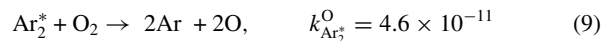$$e + Ar \rightarrow 2e + Ar^+ \tag{2}$$
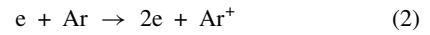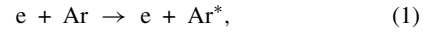
In the following Ar^* denotes the metastable 4s states of argon. As discussed in [11], it is very likely at atmospheric pressure that these argon species undergo three body collisions with an arbitrary collision partner M forming the argon excimer and the molecular argon ion via the reactions

$$Ar^* + Ar + M \rightarrow Ar_2^* + M \tag{3}$$
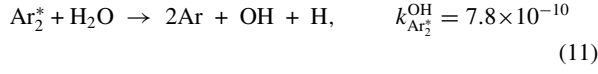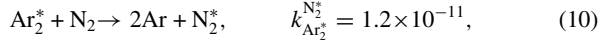
$$Ar^+ + Ar + M \rightarrow Ar_2^+ + M \tag{4}$$
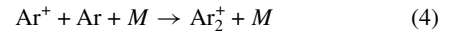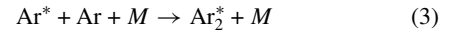
The VUV emission from the argon excimer Ar_2^* has been detected in end-on measurements with the jet used in this study and was applied for the measurement of oxygen diffusion into the effluent of the jet [21]. In the effluent, electrons and reactive argon species may then dissociate, excite or ionize nitrogen, oxygen and water from the ambient, forming ROSs and RNSs. As discussed by van Gaens and Bogaerts [11], the most important loss reactions for the argon metastables and excimers are

$$Ar^* + O_2 \rightarrow Ar + 2O, \qquad k_{Ar^*}^O = 2.1 \times 10^{-10}, \tag{5}$$

$$Ar^* + N_2 \rightarrow Ar + 2N, \qquad k_{Ar^*}^N = 3.6 \times 10^{-11}, \tag{6}$$

$$Ar^* + N_2 \rightarrow Ar + N_2^*, \qquad k_{Ar^*}^{N_2^*} = 3.6 \times 10^{-11}, \tag{7}$$

$$Ar^* + H_2O \rightarrow Ar + OH + H, \qquad k_{Ar^*}^{OH} = 7.8 \times 10^{-10}, \tag{8}$$

while the argon excimers are mostly lost through

$$Ar_2^* + O_2 \rightarrow 2Ar + 2O, \qquad k_{Ar_2^*}^O = 4.6 \times 10^{-11} \tag{9}$$

108

J. Phys. D: Appl. Phys. 47 (2014) 145201　　　　　　　　　　　　　　　　　　　　　　　　　　　A Schmidt-Bleker *et al*

$$\text{Ar}_2^* + \text{N}_2 \rightarrow 2\text{Ar} + \text{N}_2^*, \qquad k_{\text{Ar}_2^*}^{\text{N}_2^*} = 1.2 \times 10^{-11}, \qquad (10)$$

$$\text{Ar}_2^* + \text{H}_2\text{O} \rightarrow 2\text{Ar} + \text{OH} + \text{H}, \qquad k_{\text{Ar}_2^*}^{\text{OH}} = 7.8 \times 10^{-10} \qquad (11)$$

Here k_j^i denote the rate constants for the reaction of the argon species j yielding the excited or dissociated species i from the respective air species. The rate constants were taken from [11], apart from the dissociation of water by Ar^*, which is based on the studies presented in [31, 32]. The rate for the dissociation of water to hydroxide (OH) and hydrogen (11) is estimated based on (8). From the secondary species atomic oxygen, atomic nitrogen, nitrogen metastables (N_2^* denotes the $\text{N}_2(A)$ state) various ROSs and RNSs can be formed. Similarly, ions can be formed from air species via charge transfer from Ar^+ and Ar_2^+, Penning ionization or electronic processes. However, the quantity of the most abundant charged species is expected to be at least two orders of magnitude lower than those of the neutral species with highest abundance, as previous studies of argon operated atmospheric pressure plasma sources suggest [11, 33–35].

The gas phase simulations presented in the present work are based on two assumptions:

(i) The initial concentrations of O, N, N_2^*, OH and H mainly determine the dynamics of the most abundant ROSs and RNSs upon variation of the shielding gas composition.

(ii) The total amount of energy deposited in the plasma is independent of the shielding gas composition.

Assumption (i) is based on previous studies [11, 33–35]. Excited oxygen states such as $\text{O}_2(^1\Delta_g)$ and $\text{O}(1\text{D})$ (in the following denoted as O_2^* and O^*) were not accounted for as discussed in section 3.2. Assumption (ii) is fulfilled by initializing each simulation, regardless of the shielding gas composition, with the same numbers of argon metastables and argon excimers. These argon species can then create O, N, N_2^*, OH and H via reactions (5)–(11). While electrons also contribute to the generation of these species, they are not taken into account in the present simulation, as no information on the electron energy is available. This leaves the initial argon metastable and initial argon excimer density as free parameters, which can be used to fit the simulations to the FTIR measurements.

The simulations are carried out as follows. First, the branching ratios of the argon metastables and excimers are calculated based on reactions (5)–(11), yielding the initial densities for the secondary species i, n_i, as a function of the air species densities n_{O_2}, n_{N_2} and $n_{\text{H}_2\text{O}}$ in the shielding gas and initial excited argon species densities n_{Ar^*} and $n_{\text{Ar}_2^*}$:

$$n_\text{O} = 2n_{\text{O}_2} \left(n_{\text{Ar}^*} k_{\text{Ar}^*}^\text{O} \tau_{\text{Ar}^*} + n_{\text{Ar}_2^*} k_{\text{Ar}_2^*}^\text{O} \tau_{\text{Ar}_2^*} \right) \qquad (12)$$

$$n_\text{N} = 2n_{\text{N}_2} \left(n_{\text{Ar}^*} k_{\text{Ar}^*}^\text{N} \tau_{\text{Ar}^*} \right), \qquad (13)$$

$$n_{\text{N}_2^*} = n_{\text{N}_2} \left(n_{\text{Ar}^*} k_{\text{Ar}^*}^{\text{N}_2^*} \tau_{\text{Ar}^*} + n_{\text{Ar}_2^*} k_{\text{Ar}_2^*}^{\text{N}_2^*} \tau_{\text{Ar}_2^*} \right), \qquad (14)$$

$$n_{\text{OH/H}} = n_{\text{H}_2\text{O}} \left(n_{\text{Ar}^*} k_{\text{Ar}^*}^{\text{OH}} \tau_{\text{Ar}^*} + n_{\text{Ar}_2^*} k_{\text{Ar}_2^*}^{\text{OH}} \tau_{\text{Ar}_2^*} \right). \qquad (15)$$

Here $\tau_{\text{Ar}^*} = \left(\sum_i n_i n_{\text{Ar}^*} k_{\text{Ar}^*}^i \right)^{-1}$ and $\tau_{\text{Ar}_2^*} = \left(\sum_i n_i n_{\text{Ar}_2^*} k_{\text{Ar}_2^*}^i \right)^{-1}$ denote the lifetimes of the argon metastables and excimers due to the loss reactions (5)–(11). Two dimensional maps of the initial densities n_i of the secondary species are plotted in figure 3 in dependence on the oxygen to nitrogen ratio and ambient humidity in the shielding gas. For the plots argon metastable and excimer densities of $n_{\text{Ar}^*} = 0.5 \times 10^{14}\,\text{cm}^{-3}$ and $n_{\text{Ar}_2^*} = 1 \times 10^{14}\,\text{cm}^{-3}$ were assumed, which are the values obtained from the fit of the simulations to the FTIR data on ozone and nitrogen dioxide as described in section 3.2. The kinetic simulations for the gas phase are then carried out solving the ordinary differential equations $\frac{\text{d}n_i}{\text{d}t} = \sum \text{generation} - \sum \text{destruction}$ for all species, where the generation and destruction processes for each species are the reactions (R1)–(R42) given in the appendix. Additional wall loss reactions in the glass chamber or the MPC are not considered, but are assumed to be negligible, as the surface to volume ratio is large. The number of reactions considered in the model is purposely kept minimal, as the model is intended as an advanced fitting routine rather than a self-consistent model. In this zero dimensional plug flow approach, time corresponds to the time of flight of a given volume element and is therefore equivalent to the distance $d = \int_0^t v(t)\text{d}t$ of a volume element moving at a speed $v(t)$. The volume element can be thought of as a cylinder comoving with the fluid as depicted in figure 1, in which all species densities are spatially averaged. The correct time t/distance d after which the model should be evaluated are discussed in the next section. Mixing of the shielding gas with the reactive argon jet is assumed to occur instantaneously, with the ambient species density rising to $\frac{5}{8} \times 2.49 \times 10^{19}\,\text{cm}^{-3}$, accounting for the composition in the mixing cell (5 slm shielding gas plus 3 slm argon). The abrupt increase of the ambient species density resembles the situation at the edge of the plasma jet nozzle. More detailed models should include the gradual diffusion of ambient species and the sub-microsecond excitation and dissociation process in the plasma jet. The current model is however designed to keep the number of free parameters minimal in order to function as a fitting routine.

2.4. Estimation of timescales by CFD simulation

In order to estimate the time of flight of a volume element that is transported from the plasma jet to the FTIR cell, a CFD simulation of the impulse response of the glass chamber was performed. That is, the mass flow of a tracer species through the inlet of the FTIR cell is computed when a short pulse of this tracer species at the inlet of the glass chamber is applied:

In a first step, the Navier–Stokes equations with the standard k–ε model for turbulent flows were solved using COMSOL 4.3, yielding the steady state velocity field $\boldsymbol{v}$ within the cell and the turbulent diffusion coefficient $D = \nu/Sc$. Here ν is the turbulent kinematic viscosity obtained from the k–ε model, and for the turbulent Schmidt number the value $Sc = 0.7$ recommended for turbulent jet flows is used [36]. In a second step, the time dependent convection–diffusion equation $\partial_t c + \boldsymbol{v} \cdot \nabla c + \nabla \cdot (D\nabla) c = 0$ for a tracer species c is solved using

Original Publications

J. Phys. D: Appl. Phys. **47** (2014) 145201   A Schmidt-Bleker *et al*
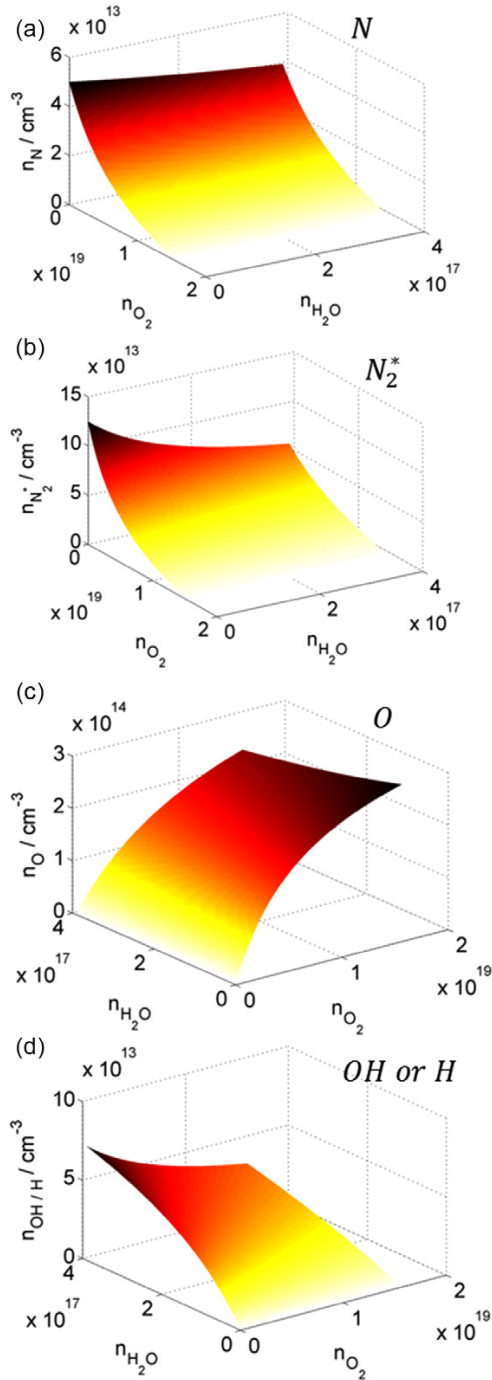
Figure 3. Initial densities of N, N_2^*, O and OH/H due to the reaction of Ar_2^* and Ar^* with air species according to equations (12)–(15). The densities serve as initial values for the presented gas phase simulations. Note that (c) and (d) are turned in the $x−y$ plane for better readability.

the velocity field and diffusion coefficient from the previous calculation.

At the inlet of the mixing cell a short Gaussian pulse $c_{In}(t) \sim \exp(−(t/t_0)^2)$ with duration of $t_0 = 10$ ms is applied.
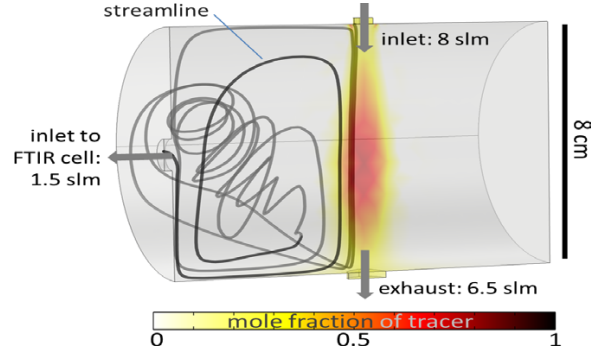
Figure 4. CFD simulation of the distribution of a tracer species inserted in the glass chamber, the stage before the FTIR MPC. The streamline indicates a typical recycling that particles entering the mixing cell undergo, which prolongs their residence time in this cell.

The impulse response is determined by evaluating the mass flow of the tracer species through the inlet of the mixing cell. The symmetry of the mixing cell can be exploited in order to halve the simulation domain and reduce the computation time, as can be seen in figure 4.

3. Results and discussion

3.1. Timescales derived from CFD simulation of the mixing cell

In figure 4 a snapshot of the tracer distribution in the mixing cell after 0.1 s is shown. In the simulation, the detailed geometry of the kinpen 09 and the shielding gas device was not resolved as in the simulation shown previously in figure 1, but simplified by a circular inlet through which a mass flow of 8 slm air enters the mixing cell. The differences in viscosity and mass of the different mixtures are assumed to be negligible for this study and thus the respective values for air are applied.

The streamline drawn in figure 4 shows that particles originating from the inlet may recirculate in the glass chamber several times before entering the FTIR cell, thus prolonging the period before they are actually measured. This explains the observed impulse response at the inlet of the FTIR MPC: as can be seen in the inset of figure 5, a first sharp pulse after 0.1 s the particles remaining in the mixing cell may recirculate and enter the FTIR after 0.4 s. Most particles however, more than 95%, stay in the mixing cell for a few seconds. While the tracer pulse diffuses and disperses in the mixing cell, the tracer concentration and the pulse response assume an exponential decay, which is fully developed after 2 s.

The impulse response $w(t)$ shown in figure 5 is normalized to unity and used as a weighting function for the evaluation of the gas phase simulation. The densities $n_i(t)$ of species i obtained from the simulation are weighted according to $n_i = \int \mathrm{d}t\, w(t) n_i(t)$.

The time the particles spend in the MPC is assumed to be negligible. In spite of its larger volume of 15 l, the typical timescale during which it is expected to be flushed at a flux of 1.5 slm and a pressure of 100 mbar is one minute. However, due to the reduced pressure, two body collisions are slowed
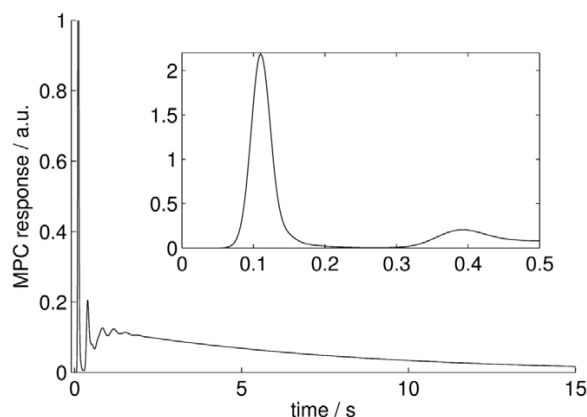
Figure 5. Impulse response at the MPC inlet; recirculation manifested in pulses at 0.1 and 0.4 s. The full frame shows the exponential decay of the impulse response for $t > 2$ s while the inset resolves the full height of the first pulse.

down by a factor of 100 and three body collisions by a factor of 1000. Therefore, a further effect of the residence time in the MPC is not expected.

3.2. FTIR densities and simulation

In figure 6 the transmission signals of two infrared spectral regions are depicted. The clear absorptions occurring in these regions are attributed to ozone and nitrogen dioxide. Other species such as nitric acid (HNO_3) or H_2O_2 are also identified, but owing to their weak absorption signal a serious quantitative evaluation is not feasible [30].

The absorption profiles of O_3 and NO_2 in figure 6 are both influenced by the shielding gas composition. For both species, no absorption is found when the shielding gas consists of nitrogen only. However, when increasing the oxygen concentration a different behaviour evolves. While the O_3 absorption steadily increases with increasing oxygen content in the shielding gas, an indifferent behaviour is found for NO_2. The NO_2 absorption increases with increasing oxygen concentration but only up to a certain level. When the oxygen concentration exceeds this level the absorption signal decreases again. Besides the impact of different oxygen/nitrogen ratios, shielding gas humidity also affects the absorption signals (not shown in figure 6). In order to explain the behaviour of O_3 and NO_2 for these varying conditions the concentration of both species is calculated from the measured absorption profiles and compared with the results of the gas phase simulation. In figure 7 the ozone and nitrogen dioxide concentration obtained by FTIR spectroscopy and computed with the gas phase simulation is shown for different shielding gas compositions. Figure 7(*a*) shows a shielding gas variation from 100% O_2 and 0% N_2 to 0% O_2 and 100% N_2 in dry conditions. As indicated by the absorption profiles, the ozone density continuously rises with the amount of oxygen in the shielding gas, while the nitrogen dioxide densities are minimal at 0% oxygen or 0% nitrogen and have a maximum at around 30% oxygen. The remaining NO_2 density measured at 0% nitrogen presumably originates from impurities in the

employed gas. The simulated curves of the O_3 and NO_2 densities were fitted against the experimentally obtained values using the initial argon metastable and argon excimer densities as fitting parameters. The obtained initial densities $n_{Ar^*} = 0.5 \times 10^{14}$ cm^{-3} and $n_{Ar_2^*} = 1 \times 10^{14}$ cm^{-3} are certainly overestimated, as in the model the argon metastables and excimers are produced instantaneously. The fitted initial values therefore correspond to the total number of produced argon metastables and excimers produced by several pulses and not to actual densities that can be expected in the effluent. Also, electronic dissociation and excitation processes are likely to contribute to the generation of secondary species. In a simulation of a similar jet, argon metastable and excimer densities do not exceed $n_{Ar^*} = 10^{12}$ cm^{-3} and $n_{Ar^*} = 10^{13}$ cm^{-3} [11]. Figures 7(*b*) and (*c*) again show shielding gas variations from pure oxygen to pure nitrogen, but at a relative humidity of 18% (*b*) and 36% (*c*). The agreement between the experimental data and the simulation is best at a relative humidity of 36%. While the amount of ozone produced drops with rising humidity, the nitrogen dioxide production remains constant. In both experimental data and simulation the maximum of NO_2 production shifts towards lower oxygen concentrations at higher humidity. In dry conditions, the NO_2 production is overestimated by the model, and both the simulated O_3 and NO_2 curves deviate from the measured data. The cause for this could be either water impurities in the feed gas, which may amount to 3 ppm (according to the manufacturer [37]) and are not considered in the model, or that in the absence of water other reaction pathways that are not considered in the current model become important. The NO_2 density obtained in this work agrees very well with the far-field density of 8×10^{12} cm^{-3} obtained by Iseni *et al* by the infrared absorption technique using a quantum cascade laser for the kinpen 09. In the simulation shown in figure 7(*d*) the mixing ratio of oxygen to nitrogen is set to 20/80 (artificial air), while the humidity of the shielding gas is varied. The drop in the net ozone production observed in the experimental data agrees remarkably well with the simulation. Note that for all simulations presented in this work the same initial argon metastable and excimer densities are used, and only the shielding gas composition is varied. In figure 7(*d*) an additional numerical study is shown, in which the role of oxygen metastables O_2^* and the excited atomic oxygen state O^* is investigated for stability analysis. The density of O_2^* was initialized using an excitation degree of 0.1% of the oxygen density based on the simulation study [11], while for the atomic oxygen 50% of the atoms were initialized as ground state O and 50% as O^*. The respective branching ratio for dissociation of O_2 by Ar^* can be expected to be 27% O^*, 73% O based on the rate coefficients found in [38]; however, a higher O^* was assumed, as further excitation processes are neglected. Note that in all previous studies O_2^* and O^* were initialized with density zero. From figure 7(*d*) it is clear that the addition of both species does not significantly affect the dynamics of ozone and nitrogen dioxide upon shielding gas variation, which is the reason why they were excluded from the base cases as they would yield bad fitting parameters. Although O_2^* does destroy a significant amount of ozone via reaction (R3), this
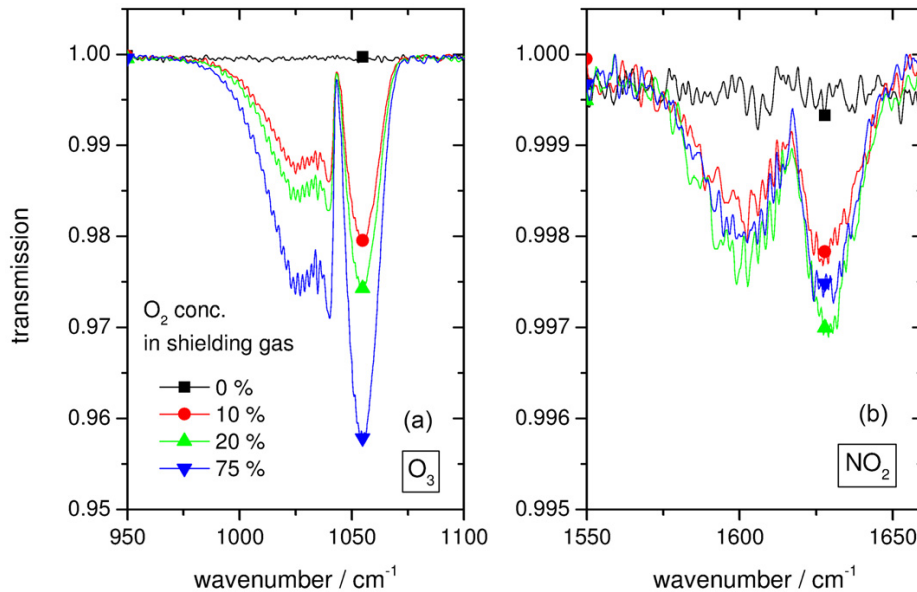
Figure 6. FTIR absorption spectra for O_3 and NO_2 at different oxygen concentrations in the shielding gas.

reaction produces atomic oxygen, most of which is recycled to ozone via reaction (R8). O^* was considered in the study, as it may play a role in the destruction of ozone via reactions (R37) and (R38); however, in the model, quenching of O^* to ground state atomic oxygen was more effective.

In figure 8 the temporal development of atomic oxygen, ozone, atomic nitrogen, nitrogen metastable, nitric oxide (NO), nitrogen dioxide, hydroxide, hydrogen peroxide, nitric acid and nitrous acid (HNO_2) is shown. As discussed in the previous section, due to the mixing cell the species reach the FTIR MPC after 0.1 s or more. From the kinetic simulations ozone and nitrogen dioxide can be expected to have reached a fairly stable level by this time, which is advantageous for the interpretation of the experimental data, as the conversion from short living species to O_3 and NO_2 is almost completed. The temporal evolution also shows that in the active effluent other neutral species than O_3 and NO_2 can be present in significant amounts: large fractions of O_3, NO_2 or H_2O_2 have not been generated yet and the respective preceding species (e.g. O, NO and OH or HO_2) can be expected in significant amounts. The concentration of nitrogen dioxide and ozone measured in the far field may therefore be significantly higher than the one present in the effluent. It is noted that the temporal evolution of species shown should not directly be converted to a spatial distribution in the effluent region, as the initial generation and destruction processes are modelled to occur instantaneously. The instantaneous initialization mimics the fast dissociation and excitation processes caused by a single plasma bullet hitting a given volume element. More detailed models should, however, include multiple pulses, which is not feasible in the current zero dimensional model. While atomic oxygen is known to be stable for milliseconds and reach distances of several centimetres in the effluent of plasma jets [39], in the current model it is consumed after approximately 0.2 ms by the

reaction with O_2, forming O_3 via reaction (R8). This occurs as the shielding gas density rises instantaneously in the current model. Especially in the centre of the stream where shielding gas densities are low (see figure 1), the lifetime of oxygen can be expected to be significantly longer.

From figure 8 it is evident that only the two long living species with the highest densities were detected. From the model, the stable species with the third highest density is hydrogen peroxide. The H_2O_2 density in the far field of a kinpen 09 has recently been detected via FTIR spectroscopy at higher pressure to be in the range of about 5×10^{12} cm^3 and the HNO_3 density was found to be in the range of 3×10^{12} cm^3, which is in perfect agreement with the current model [30]. Verreyken *et al* have obtained an OH density of the order of 10^{14} cm^{-3} in the effluent of a kinpen 09 by LIF measurements with admixture of 400 ppm water in the feed gas [22]. The lower OH values obtained in our simulation (of the order of 10^{13} cm^{-3}) are expected, as the feed gas humidity in our experimental setup was measured to be lower than 20 ppm [40].

Pipa *et al* have measured the NO and NO_2 density produced by a kinpen operated at a higher frequency (1.4 MHz) and higher gas flow rates with air admixture in the feed gas [41]. The density was measured in a multipass cell with 100 m absorption length using tunable diode laser absorption spectroscopy in the infrared. They obtained both NO and NO_2 densities in the range of some 10^{13} cm^{-3}. Again, the maximum NO and NO_2 densities predicted by the current model are lower, as can be expected as no molecular admixtures are used. NO is not stable enough to be measured directly with the current experimental setup. However, it can be measured directly in the effluent of plasma jets using laser induced fluorescence as presented by van Gessel *et al* who found NO densities in the range of 10^{14} cm^{-3} in an argon operated plasma jet [39].
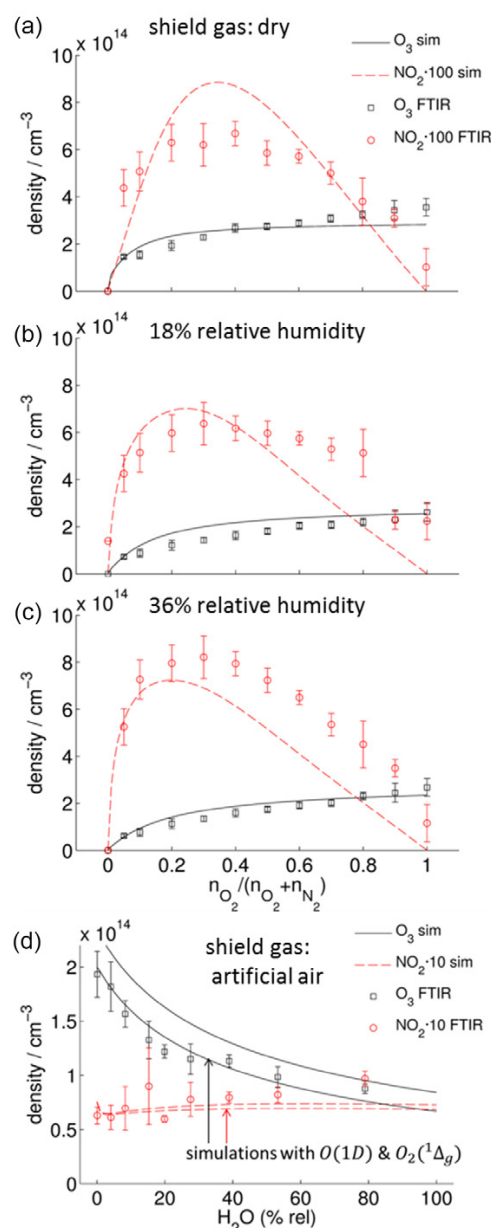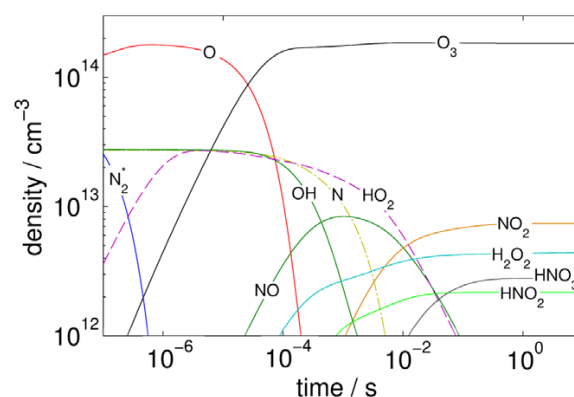
Figure 8. Temporal development of several species. The shielding gas in the simulation is artificial air with a relative humidity of 18%.

of the dynamics of reactive species production upon shielding gas variation.

3.3.1. Generation/destruction of NO$_2$. In figure 9(*a*) the main generation and destruction mechanisms for NO$_2$ upon oxygen to nitrogen shielding gas variation at a relative humidity of 18% are shown. Pointwise summation of the three plotted curves yields the NO$_2$ dynamics simulated and measured in figure 7(*a*). NO$_2$ is mainly produced via reactions (R22) and (R24) from NO reacting with O$_3$ or HO$_2$. The contribution of HO$_2$ explains why the maximum of net NO$_2$ production shifts towards lower oxygen content in the shielding gas when the humidity is increased (see figure 7(*a*)–(*c*)): HO$_2$ is mainly formed via the three body reaction (R16) of H and O$_2$. The production of hydrogen is in turn assumed to be dominated by the dissociation of water by reactions (8) and (11). While the absolute concentration of NO$_2$ remains almost unchanged upon humidity variation (see figure 7(*d*), the underlying generation and destruction mechanisms may well involve a dynamic behaviour as shown in figure 9(*b*). The most important loss reaction (R15) for NO$_2$ via OH is a main source for HNO$_3$.

It is noted that the production of NO$_2$ from NO and O (R21) may be underestimated in the current model, as atomic oxygen is already consumed before NO reaches its maximum density.

3.3.2. Generation/destruction of NO. As NO$_2$ is mainly produced via NO, we also briefly discuss the mechanisms for the NO generation and destruction shown in figure 10. It is noted that for the generation of NO atomic nitrogen is the key species in the model. Two pairs of generation and destruction mechanisms revealing the same dynamics can be distinguished: on the one hand generation of NO via N with OH (R5) and destruction by N (R6), both depending on the atomic nitrogen density; on the other hand NO can be generated via reaction of N with O$_2$ (R7) and destroyed by HO$_2$ (R24). Here both mechanisms require the presence of O$_2$ (as HO$_2$ is generated from H and HO$_2$; see (R16)).

Figure 7. Density of ozone and nitrogen dioxide upon oxygen to nitrogen shielding gas variation (*a*)–(*c*) at different humidity levels and humidity variation at O$_2$/N$_2$ = 20/80 (*d*). (*d*) includes an additional study of the influence of O* and O$_2^*$.

3.3. Evaluation of reaction dynamics: variation of shielding gas composition

Figures 9–11 show the dynamics of the most important generation and destruction processes for NO$_2$, NO and atomic oxygen as computed by the model. The plotted densities are the total densities of the respective species produced (positive values) or destroyed (negative values) by the given reaction. While the data shown in this section cannot be verified experimentally, they serve to gain insight into the cause
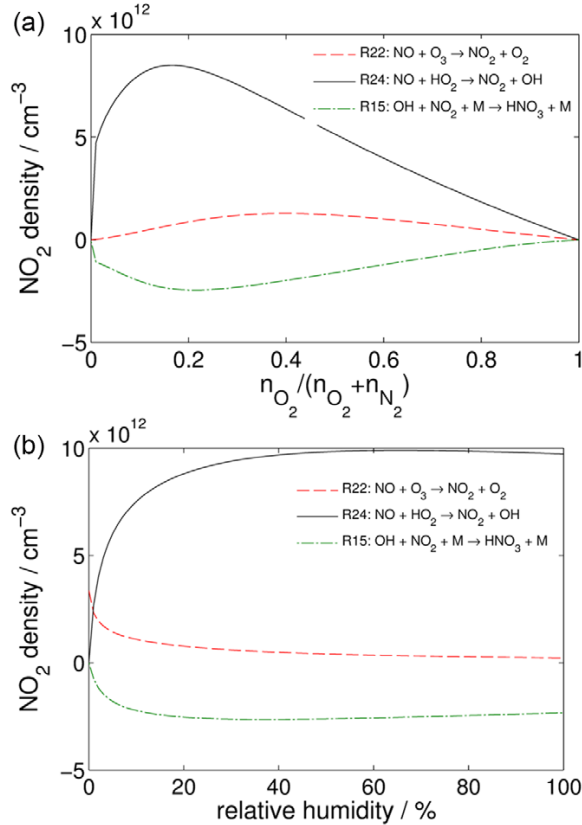
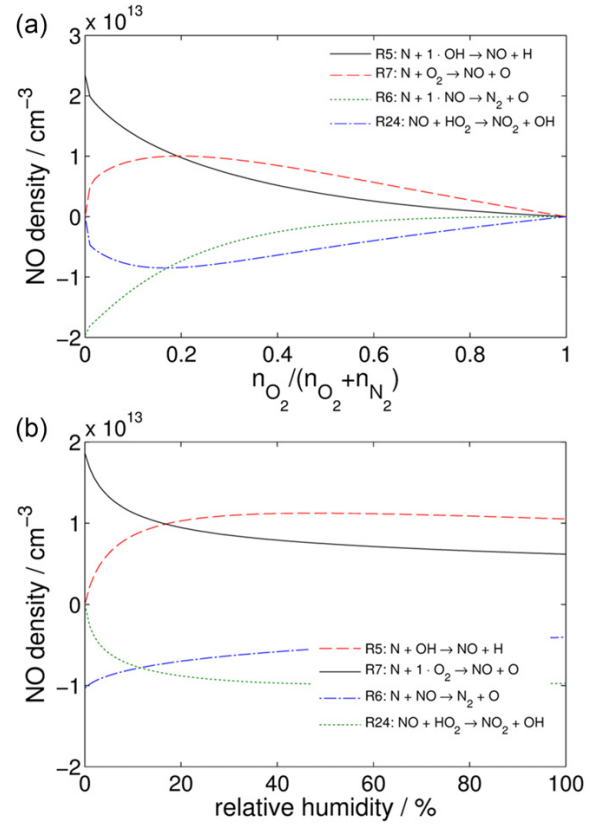**Figure 9.** Most important generation and destruction mechanisms for NO_2.

Figure 10. Most important generation and destruction mechanisms for NO.

3.3.3. Generation/destruction of O and O_3. The generation and destruction dynamics for atomic oxygen are shown in figure 11. In the current model two generation processes are important: first, the initial density due to dissociation of O_2 by excited argon species according to (12); second, the very effective dissociation of O_2 by N_2^*, which is the reason why high ozone concentrations can be observed at low oxygen shield gas concentrations. The most important destruction mechanism for atomic oxygen is the three body reaction with O_2 and another arbitrary reaction partner (R8). This reaction also directly determines the density of ozone obtained. If O_2^* is included in the model, an additional destruction of O_3 via reaction (R3) is observed. However, as the destruction of ozone by O_2^* recycles atomic oxygen, the net ozone production observed in figure 7(*d*) is not significantly affected by the addition of O_2^* in the model.

3.4. Influence of ambient humidity on water related species

As atmospheric pressure plasma sources for biomedical applications are usually operated in open air, the effect of the ambient humidity on various species produced by the plasma is investigated numerically. In figure 12 the relative density of various water related species is evaluated upon humidity variation of the shielding gas after a simulation time of 1 ms,

while the O_2/N_2 ratio is kept at 20/80. The relative densities (normalized to the respective maximum value) are evaluated after a simulation time of 10^{-3} s. The species evaluated in figure 12 have already been detected experimentally in liquid medium (Dulbecco's phosphate buffered saline) after plasma treatment with an identical plasma jet, and are of special relevance for their biological effects. The OH radical and superoxide anion O_2^- (which may be produced by dissolution of HO_2) were detected by electron paramagnetic resonance spectroscopy [10], nitrite and nitrate (which may be produced by dissolution of HNO_2 and HNO_3) by colorimetric assays and H_2O_2 using test stripes [30, 40]. Although the data shown in figure 12 are only of qualitative nature, as the current study mainly focuses on the far field production of O_3 and NO_2, it indicates that the relative humidity, which often varies between 20 and 100% within a day in most locations, may have a significant impact on the plasma chemistry of CAP jets.

4. Summary and conclusion

The effect of shielding gas variations on the reactive species generation of a CAP jet has been investigated by the combination of FTIR measurements and zero dimensional kinetic simulations.
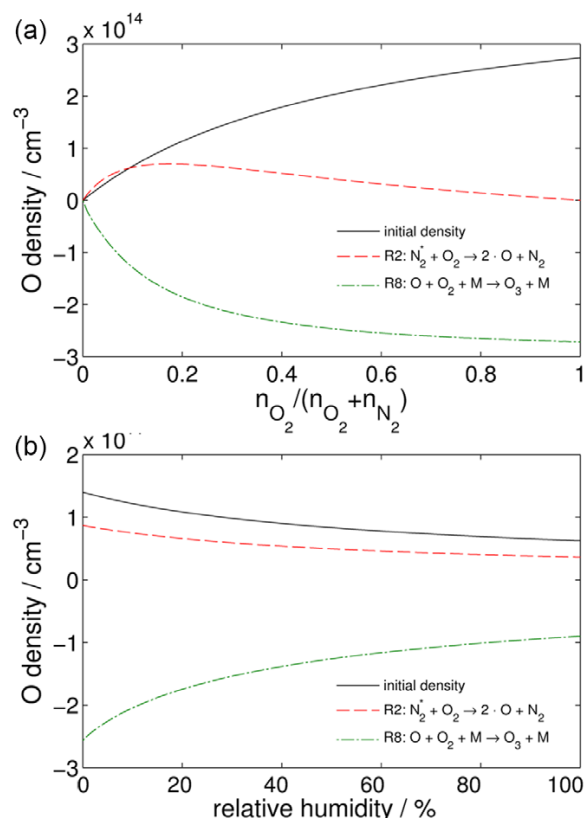
A Schmidt-Bleker *et al*

Figure 11. Most important generation and destruction mechanisms for O.
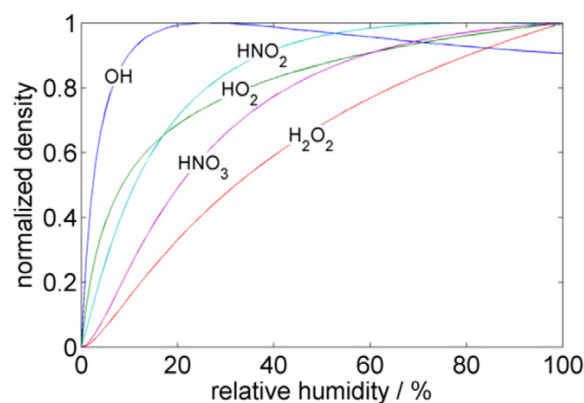

Figure 12. Relative densities of water-related species upon humidity variation in the shielding gas according to the simulation.

As both the oxygen to nitrogen ratio and the humidity concentration of the shielding gas were varied, the FTIR measurements yielded two dimensional datasets for the ozone and nitrogen dioxide densities.

The kinetic model was designed to have only two free fitting parameters: the initial densities of argon metastables and argon excimers. These were used to fit the ozone and

nitrogen dioxide densities obtained from the simulations to the experimental data. Shielding gas variations have proven to be a valuable tool for the validation of the kinetic simulations, which in turn give insight into the relevant reaction pathways.

The gas flow from the CAP jet to the FTIR MPC was modelled by CFD simulations in order to determine the correct evaluation time of the kinetic simulations. It was shown that particles travel for at least 0.1 s before they enter the MPC.

In the FTIR experiments and kinetic simulation maximum ozone densities of about $3 \times 10^{14}\,\text{cm}^{-3}$ were obtained. Ozone continuously increases with the amount of oxygen in the shielding gas. However, even at low oxygen admixture significant amounts of ozone are produced, as nitrogen metastables effectively contribute to the ozone production. With rising humidity, the amount of ozone produced by the jet is halved. The simulations suggest that this is mainly due to the fact that chemical energy is spent on the dissociation of water molecules, and thus less energy is available for the dissociation of oxygen and excitation of nitrogen (which in turn contribute to the creation of ozone). The maximum nitrogen dioxide production amounts to $6 \times 10^{12}\,\text{cm}^{-3}$. The lowest amount of nitrogen dioxide is produced at zero percent oxygen and zero percent nitrogen, as the formation of nitrogen dioxide naturally requires both molecules to be present. The maximum production occurs at around 40% oxygen in dry conditions. The maximum shifts towards lower oxygen concentrations as the humidity in the shielding gas increases. Simulations suggest that this occurs as HO_2 is involved in the creation of nitrogen dioxide. HO_2 in turn requires water and oxygen to be present.

Various species, namely OH, H_2O_2, HNO_2, HNO_3 and HO_2, which may be relevant for biomedical applications of plasmas, were evaluated for their dependence on the humidity in the shielding gas. The ambient humidity has a significant impact on the densities of these species. Controlling the environment of atmospheric pressure plasma sources may therefore help improve the reproducibility of experimental studies. This may especially be relevant for experimental studies in the field of plasma medicine, where biological deviations add up to deviations in the reactive species output in the applied sources. Also, varying the ratio of oxygen and nitrogen in the shielding gas, the cocktail of reactive oxygen and nitrogen species can not only be tuned to an optimal value for the given application, but also be altered continuously in order to perform parametric studies in experiments in the field of plasma medicine.

Acknowledgment

Appendix. Chemical reactions

Table 1. List of rate coefficients used in the gas phase kinetic simulation, evaluated for a temperature of 300 K. The rate coefficients are given in units of s^{-1}, $cm^3\,s^{-1}$ and $cm^6\,s^{-1}$ for first, second and third order reactions.

ID	Reaction	Rate Coeff.	Ref.
(R1)	$N_2^* + N_2 \rightarrow 2N_2$	1.9×10^{-13}	[42]
(R2)	$N_2^* + O_2 \rightarrow 2O + N_2$	1.5×10^{-12}	[42]
(R3)	$O_2^* + O_3 \rightarrow O + 2O_2$	3.8×10^{-15}	[43]
(R4)	$O_2^* + N_2 \rightarrow O_2 + N_2$	1.5×10^{-18}	[42]
(R5)	$N + OH \rightarrow NO + H$	4.7×10^{-11}	[44]
(R6)	$N + NO \rightarrow N_2 + O$	2.9×10^{-11}	[43]
(R7)	$N + O_2 \rightarrow NO + O$	8.5×10^{-17}	[43]
(R8)	$O + O_2 + M \rightarrow O_3 + M$	3.4×10^{-10}	[42]
(R9)	$O + OH \rightarrow H + O_2$	3.5×10^{-11}	[45]
(R10)	$O + O_3 \rightarrow 2O_2$	8×10^{-15}	[45]
(R11)	$H + O_3 \rightarrow OH + O_2$	2.9×10^{-11}	[43]
(R12)	$O + HO_2 \rightarrow OH + O_2$	5.8×10^{-11}	[45]
(R13)	$OH + HO_2 \rightarrow H_2O + O_2$	1.1×10^{-10}	[45]
(R14)	$OH + O_3 \rightarrow HO_2 + O_2$	7.3×10^{-14}	[45]
(R15)	$OH + NO_2 + M \rightarrow HNO_3 + M$	1.9×10^{-30}	[42]
(R16)	$H + O_2 + M \rightarrow HO_2 + M$	5.7×10^{-32}	[43]
(R17)	$2\,HO_2 + M \rightarrow H_2O_2 + O_2 + M$	4.9×10^{-32}	[43]
(R18)	$2OH + M \rightarrow H_2O_2 + M$	6.2×10^{-31}	[43]
(R19)	$H_2O_2 + OH \rightarrow H_2O + HO_2$	1.7×10^{-12}	[45]
(R20)	$O + NO_2 \rightarrow NO + O_2$	9.7×10^{-12}	[43]
(R21)	$NO + O + M \rightarrow NO_2 + M$	9×10^{-32}	[43]
(R22)	$NO + O_3 \rightarrow NO_2 + O_2$	1.7×10^{-14}	[45]
(R23)	$NO + OH + M \rightarrow HNO_2 + M$	7×10^{-31}	[43]
(R24)	$NO + HO_2 \rightarrow NO_2 + OH$	8.8×10^{-12}	[45]
(R25)	$OH + HNO_2 \rightarrow NO_2 + H_2O$	6×10^{-12}	[45]
(R26)	$NO_2 + N \rightarrow N_2O + O$	1.2×10^{-11}	[43]
(R27)	$NO_2 + O + M \rightarrow NO_3 + M$	9×10^{-32}	[43]
(R28)	$OH + HNO_3 \rightarrow NO_3 + H_2O$	1.5×10^{-13}	[46]
(R29)	$NO_3 + NO_2 + M \rightarrow N_2O_5 + M$	2.7×10^{-30}	[47]
(R30)	$N_2O_5 \rightarrow NO_3 + NO_2$	0.07	[45]
(R31)	$2\,H + M \rightarrow H_2 + M$	8.9×10^{-33}	[48]
(R32)	$N_2^* + O \rightarrow O^* + N_2$	2.3×10^{-11}	[15]
(R33)	$O^* + O_2 \rightarrow O + O_2$	8×10^{-12}	[15]
(R34)	$O^* + O \rightarrow 2O$	8×10^{-12}	[15]
(R35)	$O^* + O_2^* \rightarrow O + O_2$	10^{-11}	[49]
(R36)	$O^* + O_2 \rightarrow O + O_2^*$	10^{-12}	[15]
(R37)	$O^* + O_3 \rightarrow 2O + O_2$	1.2×10^{-10}	[43]
(R38)	$O^* + O_3 \rightarrow 2 \cdot O_2$	1.2×10^{-10}	[43]
(R39)	$O^* + N_2 \rightarrow O + N_2$	2.7×10^{-11}	[15]
(R40)	$O^* + NO \rightarrow O + NO$	4×10^{-11}	[49]
(R41)	$O^* + NO_2 \rightarrow O_2 + NO$	1.3×10^{-10}	[50]
(R42)	$O^* + H_2O \rightarrow 2OH$	2.2×10^{-10}	[51]

References

[1] Fridman G, Friedman G, Gutsol A, Shekhter A B, Vasilets V N and Fridman A 2008 Applied plasma medicine *Plasma Process. Polym.* **5** 503–33

[2] Heinlin J, Morfill G, Landthaler M, Stolz W, Isbary G, Zimmermann J L, Shimizu T and Karrer S 2010 Plasma medicine: possible applications in dermatology *J. Dtsch. Dermatol. Ges.* **8** 968–76

[3] Laroussi M, Kong M, Morfill G and Stolz W 2012 *Plasma Medicine: Applications of Low-temperature Gas Plasmas in Medicine and Biology* (Cambridge: Cambridge University Press)

[4] von Woedtke T, Reuter S, Masur K and Weltmann K D 2013 Plasmas for medicine *Phys. Rep.* **530** 291–320

[5] Weltmann K-D, Polak M, Masur K, Woedtke T v, Winter J and Reuter S 2012 Plasma processes and plasma sources in medicine *Contrib. Plasma Phys.* **52** 644–54

[6] Graves D B 2012 The emerging role of reactive oxygen and nitrogen species in redox biology and some implications for plasma applications to medicine and biology *J. Phys. D: Appl. Phys.* **45** 263001

[7] Reuter S, Tresp H, Wende K, Hammer M U, Winter J, Masur K, Schmidt-Bleker A and Weltmann K-D 2012 From RONS to ROS: tailoring plasma jet treatment of skin cells *IEEE Trans. Plasma Sci* **40** 2986–93

[8] Reuter S, Winter J, Schmidt-Bleker A, Tresp H, Hammer M U and Weltmann K-D 2012 Controlling the ambient air affected reactive species composition in the effluent of an argon plasma jet *IEEE Trans. Plasma Sci* **40** 2788–94

[9] Barton A, Wende K, Bundscherer L, Weltmann K-D, Lindequist U and Masur K 2013 Non-thermal atmospheric pressure plasma treatment of human cells: the effect of ambient conditions *Proc ISPC 21 (Cairns, Queensland, Australia)*

[10] Tresp H, Hammer M U, Winter J, Weltmann K-D and Reuter S 2013 Quantitative detection of plasma-generated radicals in liquids by electron paramagnetic resonance spectroscopy *J. Phys. D: Appl. Phys.* **46** 435401

[11] Gaens W V and Bogaerts A 2013 Kinetic modelling for an atmospheric pressure argon plasma jet in humid air *J. Phys. D: Appl. Phys.* **46** 275201

[12] Gentile A C and Kushner M J 1995 Reaction chemistry and optimization of plasma remediation of N_xO_y from gas streams *J. Appl. Phys.* **78** 2074–85

[13] Liu D X, Bruggeman P, Iza F, Rong M Z and Kong M G 2010 Global model of low-temperature atmospheric-pressure He + H_2O plasmas *Plasma Sources Sci. Technol.* **19** 025018

[14] Murakami T, Niemi K, Gans T, O'Connell D and Graham W G 2013 Chemical kinetics and reactive species in atmospheric pressure helium–oxygen plasmas with humid-air impurities *Plasma Sources Sci. Technol.* **22** 015003

[15] Sakiyama Y, Graves D B, Chang H-W, Shimizu T and Morfill G E 2012 Plasma chemistry model of surface microdischarge in humid air and dynamics of reactive neutral species *J. Phys. D: Appl. Phys.* **45** 425201

[16] Babaeva N Y and Kushner M J 2013 Reactive fluxes delivered by dielectric barrier discharge filaments to slightly wounded skin *J. Phys. D: Appl. Phys.* **46** 025401

[17] Boeuf J-P, Yang L L and Pitchford L C 2013 Dynamics of a guided streamer ('plasma bullet') in a helium jet in air at atmospheric pressure *J. Phys. D: Appl. Phys.* **46** 015201

[18] Naidis G V 2011 Modelling of plasma bullet propagation along a helium jet in ambient air *J. Phys. D: Appl. Phys.* **44** 215203

[19] Sakiyama Y and Graves D B 2009 Neutral gas flow and ring-shaped emission profile in non-thermal RF-excited plasma needle discharge at atmospheric pressure *Plasma Sources Sci. Technol.* **18** 025022

[20] Zhang S, Gaens W v, Gessel B v, Hofmann S, Veldhuizen E v, Bogaerts A and Bruggeman P 2013 Spatially resolved ozone densities and gas temperatures in a time modulated RF driven atmospheric pressure plasma jet: an analysis of the production and destruction mechanisms *J. Phys. D: Appl. Phys.* **46** 205202

[21] Reuter S, Winter J, Schmidt-Bleker A, Schroeder D, Lange H, Knake N, Gathen V S-v d and Weltmann K-D 2012 Atomic oxygen in a cold argon plasma jet: TALIF spectroscopy in ambient air with modelling and measurements of ambient species diffusion *Plasma Sources Sci. Technol.* **21** 024005

[22] Verreycken T, Mensink R, van der Horst R, Sadeghi N and Bruggeman P J 2013 Absolute OH density measurements in the effluent of a cold atmospheric-pressure Ar–H$_2$O RF plasma jet in air *Plasma Sources Sci Technol.* **22** 055014

[23] Iséni S, Reuter S and Weltmann K-D 2014 NO$_2$ dynamics of an Ar/Air plasma jet investigated by *in situ* quantum cascade laser spectroscopy at atmospheric pressure *J. Phys. D: Appl. Phys.* **47** 075203

[24] Reuter S, Winter J, Iseni S, Peters S, Schmidt-Bleker A, Dünnbier M, Schäfer J, Foest R and Weltmann K-D 2012 Detection of ozone in a MHz argon plasma bullet jet *Plasma Sources Sci Technol.* **21** 034015

[25] Winter J, Dünnbier M, Schmidt-Bleker A, Meshchanov A, Reuter S and Weltmann K 2012 Aspects of UV-absorption spectroscopy on ozone in effluents of plasma jets operated in air *J. Phys. D: Appl. Phys.* **45** 385201

[26] Dünnbier M, Schmidt-Bleker A, Winter J, Wolfram M, Hippler R, Weltmann K-D and Reuter S 2013 Ambient air particle transport into the effluent of a cold atmospheric-pressure argon plasma jet investigated by molecular beam mass spectrometry *J. Phys. D: Appl. Phys.* **46** 435203

[27] Weltmann K D, Kindel E, Brandenburg R, Meyer C, Bussiahn R, Wilke C and von Woedtke T 2009 Atmospheric pressure plasma jet for medical therapy: plasma parameters and risk estimation *Contrib. Plasma Phys.* **49** 631–40

[28] Rothman L S *et al* 2005 The HITRAN 2004 molecular spectroscopic database *J. Quant. Spectrosc. Radiat.* **96** 139–204

[29] neoplas control 2010 Q-MACSoft (IR simulation software)

[30] Winter J, Wende K, Masur K, Iseni S, Dunnbier M, Hammer M U, Tresp H, Weltmann K-D and Reuter S 2013 Feed gas humidity: a vital parameter affecting a cold atmospheric-pressure plasma jet and plasma-treated human skin cells *J. Phys. D: Appl. Phys.* **46** 295401

[31] Novicki S and Krenos J 1988 Absolute quenching cross section for collisions between Ar(3P0,2) and H$_2$O *J. Chem. Phys.* **89** 7031–3

[32] Sheldon J W and Muschlitz E Jr 1978 Quenching cross sections for Ar (P) and Kr (P) by HO and DO *J. Chem. Phys.* **68** 5288

[33] Kutasi K, Guerra V and Sá P 2010 Theoretical insight into Ar–O$_2$ surface-wave microwave discharges *J. Phys. D: Appl. Phys.* **43** 175201

[34] Moravej M, Yang X, Barankin M, Penelon J, Babayan S and Hicks R 2006 Properties of an atmospheric pressure radio-frequency argon and nitrogen plasma *Plasma Sources Sci. Technol.* **15** 204

[35] Moravej M, Yang X, Hicks R F, Penelon J and Babayan S E 2006 A radio-frequency nonequilibrium atmospheric pressure plasma operating with argon and oxygen *J. Appl. Phys.* **99** 093305

[36] Yimer I, Campbell I and Jiang L-Y 2002 Estimation of the turbulent Schmidt number from experimental profiles of axial velocity and concentration for high-Reynolds-number jet flows *Can. Aeronaut. Space J.* **48** 195–200

[37] AirLiquide 2014 http://www.airliquide.com/en/alphagaz-specifications.html

[38] Gudmundsson J T and Thorsteinsson E G 2007 Oxygen discharges diluted with argon: dissociation processes *Plasma Sources Sci Technol.* **16** 399

[39] Waskoenig J, Niemi K, Knake N, Graham L M, Reuter S, Schulz-von der Gathen V and Gans T 2010 Diagnostic-based modeling on a micro-scale atmospheric-pressure plasma jet *Pure Appl. Chem.* **82** 1209–22

[40] Winter J, Wende K, Masur K, Iseni S, Dünnbier M, Hammer M U, Tresp H, Weltmann K-D and Reuter S 2013 Feed gas humidity: a vital parameter affecting a cold atmospheric-pressure plasma jet and plasma-treated human skin cells *J. Phys. D: Appl. Phys.* **46** 295401

[41] Pipa A V, Reuter S, Foest R and Weltmann K-D 2012 Controlling the NO production of an atmospheric pressure plasma jet *J. Phys. D: Appl. Phys.* **45** 085201

[42] Dorai R and Kushner M J 2003 A model for plasma modification of polypropylene using atmospheric pressure discharges *J. Phys. D: Appl. Phys.* **36** 666

[43] DeMore W, Sander S, Golden D, Hampson R, Kurylo M, Howard C, Ravishankara A, Kolb C and Molina M 1997 JPL Publication 97-4 *Jet Propulsion Laboratory* 12

[44] Baulch D, Cobos C, Cox R, Frank P, Hayman G, Just T, Kerr J, Murrells T, Pilling M and Troe J 1994 Evaluated kinetic data for combustion modeling: supplement I *J. Phys. Chem. Ref. Data* **23** 847

[45] Atkinson R, Baulch D, Cox R, Crowley J, Hampson R, Hynes R, Jenkin M, Rossi M and Troe J 2004 Evaluated kinetic and photochemical data for atmospheric chemistry: Volume I-gas phase reactions of O$_x$, HO$_x$, NO$_x$ and SO$_x$ species *Atmos. Chem. Phys.* **4** 1461–738

[46] Atkinson R, Baulch D, Cox R, Hampson R Jr, Kerr J, Rossi M and Troe J 1997 Evaluated kinetic and photochemical data for atmospheric chemistry suppl VI. IUPAC subcommittee on gas kinetic data evaluation for atmospheric chemistry *J. Phys. Chem. Ref. Data* **26** 1329

[47] Atkinson R, Baulch D, Cox R, Hampson R Jr, Kerr J and Troe J 1992 Evaluated kinetic and photochemical data for atmospheric chemistry: Supplement IV. IUPAC subcommittee on gas kinetic data evaluation for atmospheric chemistry *Atmos. Environ. A—Gen.* **26** 1187–230

[48] Baulch D, Cobos C, Cox R, Esser C, Frank P, Just T, Kerr J, Pilling M, Troe J and Walker R 1992 Evaluated kinetic data for combustion modelling *J. Phys. Chem. Ref. Data* **21** 411–734

[49] Doroshenko V, Kudryavtsev N and Smetanin V 1992 Quenching mechanisms for electronically excited species in partially dissociated air *High Energy Chem.* **26** 227

[50] Gauthier M J and Snelling D R 1975 La photolyse de l'ozone a 253.7 nm: Desactivation de O (1D) et de O2($^1\Sigma$) par les gaz de l'atmosphere *J. Photochem.* **4** 27–50

[51] Dunlea E J and Ravishankara A 2004 Measurement of the rate coefficient for the reaction of O (1D) with H$_2$O and re-evaluation of the atmospheric OH production rate *Phys. Chem. Chem. Phys.* **6** 3333–40

Article A7

On the plasma chemistry of a cold atmospheric argon plasma jet with shielding gas device

Ansgar Schmidt-Bleker[1,2]**, Jörn Winter**[1,2]**, André Bösel**[2]**, Stephan Reuter**[1,2]
and Klaus-Dieter Weltmann[1]

[1] ZIK plasmatis, Felix-Hausdorff Str. 2, 17489 Greifswald, Germany
[2] INP Greifswald e.V., Felix-Hausdorff Str. 2, 17489 Greifswald, Germany

E-mail: ansgar.schmidt-bleker@inp-greifswald.de and stephan.reuter@inp-greifswald.de

CrossMark

Abstract

A novel approach combining experimental and numerical methods for the study of reaction mechanisms in a cold atmospheric Ar plasma jet is introduced. The jet is operated with a shielding gas device that produces a gas curtain of defined composition around the plasma plume. The shielding gas composition is varied from pure N_2 to pure O_2.

The density of metastable argon $Ar(4s, {}^3P_2)$ in the plasma plume was quantified using laser atom absorption spectroscopy. The density of long-living reactive oxygen and nitrogen species (RONS), namely O_3, NO_2, NO, N_2O, N_2O_5 and H_2O_2, was quantified in the downstream region of the jet in a multipass cell using Fourier-transform infrared spectroscopy (FTIR).

The jet produces a turbulent flow field and features guided streamers propagating at several $\mathrm{km\,s^{-1}}$ that follow the chaotic argon flow pattern, yielding a plasma plume with steep spatial gradients and a time dependence on the ns scale while the downstream chemistry unfolds within several seconds. The fast and highly localized electron impact reactions in the guided streamer head and the slower gas phase reactions of neutrals occurring in the plasma plume and experimental apparatus are therefore represented in two separate kinetic models. The first electron impact reaction kinetics model is correlated to the LAAS measurements and shows that in the guided streamer head primary reactive oxygen and nitrogen species are dominantly generated from $Ar(4s, {}^3P_2)$. The second neutral species plug-flow model hence uses an $Ar(4s, {}^3P_2)$ source term as sole energy input and yields good agreement with the RONS measured by FTIR spectroscopy.

Keywords: plasma jet, plasma chemistry, Fourier-transform infrared spectroscopy, kinetic modeling, laser atom absorption spectroscopy, atmospheric pressure plasma

(Some figures may appear in colour only in the online journal)

1. Introduction

Cold atmospheric plasma (CAP) sources are of interest for their applicability in the field of plasma medicine. Several reviews on biomedical applications of CAP [1–4], the various

kinds of CAP sources available [5–8] and the role of plasma generated reactive oxygen and nitrogen species (RONS) [9] can be found in the literature. An important goal in plasma medical research is to assign specific plasma-generated RONS (or specific RONS mixtures) to a given biological response. For this purpose shielding gas devices have previously been applied in order to control the environment of plasma jets and hence influence the RONS generated by the plasma [10, 11]. Continuously varying the shielding gas composition from pure

N_2 to pure O_2 then allows for the correlation of plasma generated species [12, 13] to biological effects such as viability [10], cytotoxicity and gene response of eukaryotes [14, 15] or antimicrobial effects [16]. Another approach is to use different operating modes of CAP sources to influence the species chemistry: Pavlovich *et al* have recently shown that nitrogen oxides-dominated plasma chemistry was more successful in bacterial inactivation than a plasma chemistry dominated by reactive oxygen species using different operating modes of a DBD [17], which is consistent with the findings of Jablonowski and Hänsch *et al* [16] obtained with the jet and shielding gas device employed in the present study.

The goal of this study is to investigate the reaction pathways that lead to the generation of RONS in an argon-operated CAP jet operated with a shielding gas device. Therefore, time-resolved measurements of the metastable state $Ar(4s, ^3P_2)$ (in the following also denoted Ar^*) are performed in the plasma plume via laser atom absorption spectroscopy (LAAS) and the RONS O_3, NO_2, N_2O_5, N_2O, HNO_3 and H_2O_2 are monitored in the far-field of the jet using Fourier-transform infrared (FTIR) spectroscopy. While for biomedical applications, the long-living RONS in the far-field are merely of interest where safety issues are concerned (e.g. ensuring that RONS densities comply with threshold limit values), the RONS composition in the plasma plume of CAP jets differs significantly. In order to gain insight into the near-field RONS composition, two zero-dimensional reaction kinetics models are developed that describe the fast electron processes and the long-term kinetics of RONS separately. A parametric study is performed using shielding gas mixtures with varying composition and the models are correlated to data obtained from LAAS and FTIR measurements.

The approaches for numerical investigation of plasma processes in CAP jets operated with noble gases range from zero-dimensional kinetic models (also termed volume averaged) [18–21] to two dimensional self-consistent approaches [22–27]. While zero-dimensional models come with the advantage of short computation times, the resulting possibility of including thousands of chemical reactions and easy implementation, they naturally cannot be self-consistent and therefore require close correlation to experimental measurements and/or verification by space-resolved models. A major challenge in plasma chemistry modeling in CAP jets that feature guided streamers is that the relevant timescales range from nanoseconds (fast electron dynamics and propagation of guided streamers) to several milliseconds (gas phase reactions in the plasma plume of CAP jets) or in case of non-flow driven CAP sources (typically dielectric barrier discharges) even several seconds [19]. To overcome this problem, Naidis has developed a hybrid model [28, 29]: In a first step, the propagation of a single guided streamer is calculated, yielding the production rates of primary reactive species (such that are generated directly from electron impact reactions). The production rates are then used as input values for a zero-dimensional reaction kinetics model. A similar approach has recently been presented by Tian and Kushner [30], who have developed a 2D model that first computes the generation of primary species using the complete set of electron-impact reactions for one

pulse. For the calculation of hundreds of subsequent pulses, the model reuses the previously computed generation rates, hence yielding much faster computation times than would be required for including the detailed electron model for every pulse.

In this work the argon-operated CAP jet kinpen is investigated by means of LAAS on the $Ar(4s, ^3P_2)$ metastable state, FTIR spectroscopy and kinetic modeling. The CAP jet is operated at a frequency of $\sim$1 MHz with 3 slm pure argon as feed gas and a shielding gas device is employed with composition ranging from pure N_2 to pure O_2 at a flow rate of 5 slm. The quantification of RONS is experimentally challenging for two reasons: First, as no molecular admixtures are used, the RONS densities are comparably low. Second, at the given flow rate the Reynold number is $Re \approx 3000$ ($Re = v_0 d\nu^{-1}$, with kinematic viscosity $\nu = 1.5 \times 10^{-5}\,m^2\,s^{-1}$, average velocity $v_0 = 25\,m\,s^{-1}$ at nozzle outlet and nozzle diameter $d = 1.6$ mm) and hence the flow is fully turbulent. However, these operating parameters are of interest as they have been applied in several biological and medical studies using the kinpen 09 and the similar kinpen Med [14, 31–35]. The turbulence has also been verified experimentally by planar laser induced fluorescence (LIF) measurements on OH as tracer molecule [36] and Schlieren imaging [37]. Diagnostics on turbulent CAP jets is challenging as experimental techniques that rely on averaging procedures may give misleading results. An illustrative example is given in [38], where instantaneous snapshots of guided streamer emission are compared to phase resolved measurements (in which images with same phase respect to the voltage signal are averaged).

In a previous work it was found that in a similar argon-operated CAP jet (kinpen Sci), the guided streamer is following the argon channel in a turbulent jet flow. In helium-operated jets, it was recently found, that besides the lower required self-sustaining electric field in the helium channel, also an electrostatic focusing mechanism is responsible for the guidance of the streamer within the helium gas channel [37]. Phase resolved optical emission spectroscopy measurements suggest that the same mechanism may also be relevant for argon-operated jets [39]. Since the instantaneous densities of ambient species can be expected to be much lower than the averaged quantities obtained by molecular beam mass spectrometry and Reynolds-averaged computational fluid dynamics (CFD) simulations [40], the respective densities at the position of the guided streamer can be estimated to be between the value obtained for the laminar case [11] and the Reynolds-averaged values.

The kinetic model presented in this study is similar to the plug-flow models developed for argon-operated CAP jets by van Gaens and Bogaerts [21, 27, 41], in which the system of ordinary differential equations describing the reaction kinetics is solved together with an electron energy balance equation in a volume element co-moving with the flow and which has recently also been applied to study the kinpen operated with argon and molecular admixtures [27]. This work is an extension of our previous work where CFD simulations, kinetic modeling of gas phase reactions and FTIR spectroscopy was combined to investigate the RONS chemistry [12]. A highlight in the current work and an extension to previous

approaches is, that the different time- and length-scales are accounted for in this model using a novel approach involving two separate kinetic models: The first model accounts for the electron impact reactions that occur in a stationary volume element of 100 μm diameter in the streamer head. The Ar* densities obtained in the model are fitted to experimental data using the time-dependent input power as a fitting parameter in the model. The model suggests, that Ar* is the major reactive species, in the sense that other RONS are mainly generated from reactions of Ar* with N_2, O_2 and H_2O. The second model hence uses an Ar* source term as time-dependent energy input in a larger volume element of diameter 1 mm (corresponding to the diameter of the visible plasma plume). This model only accounts for neutral reactive species. The second model itself consists of three simulation steps accounting for (1) the reactions in the visible plasma plume, (2) the reactions in the far-field of the jet, where RONS are diluted due to diffusion and (3) reactions occurring in the multipass cell of the FTIR setup at reduced pressure. The RONS densities obtained from the second model are fitted to the densities obtained from FTIR spectroscopy using the magnitude of the Ar* source term as fitting parameter. Compared to the models employed by Naidis [28, 29] and Tian and Kushner [30], which also treat fast electron impact processes and slower gas phase chemistry reactions in separate models, this approach comes with the advantage of fast computation times since here both models are zero-dimensional, allowing for vast parametric studies. The downside of this approach is, that it is not self-consistent and therefore requires close correlation to experimental data, here realized through LAAS and FTIR measurements.

2. Methods

2.1. Plasma jet and shielding gas device

In this study the cold atmospheric plasma jet kinpen 09 (neoplas tools, Germany) was used, which operates at a frequency of ∼1 MHz [42]. The jet was operated with a shielding gas device producing an annular flow of a defined gas around the effluent of the plasma jet as described in [43]. As feed gas a flux of 3 slm argon corresponding to an average velocity of 25 m s^{-1} (ALPHAGAZ 1, Air Liquide, France), as shielding gas a mixture of nitrogen and oxygen (ibid.) at a flux of 5 slm (average velocity of 7 m s^{-1}) was applied. The visible effluent has a length of approximately 1 cm.

2.2. Laser absorption spectroscopy

Laser absorption spectroscopy was performed on the Ar(1s$_5$ − 2p$_9$) optical transition at a wavelength of 811.53 nm using a novel acousto-optic laser system (EasyLAAS, neoplas control GmbH, Germany). The basic scheme of the laser system is similar to an external cavity diode laser in Littrow configuration. However, the frequency tuning is not realized by turning the grating but by altering the acoustic signal applied to the two included acousto-optic modulators (AOMs) [44, 45]. In consequence, fast single mode frequency tuning with a repetition frequency of 10 kHz at a tuning range

of 30 GHz is achieved due to the lack of mechanically actuated elements. The maximum repetition rate is 50 kHz with 4.5 GHz tuning range. The here-presented measurements were performed at 1 kHz repetition rate and 30 GHz tuning range. By means of a single mode optical fiber, the laser radiation is transferred to the absorption setup. The collimated laser beam is reflected by an adjustable mirror and focused subsequently in the absorbing region of the plasma jet by an achromatic lens (focal length of 45 mm). A second achromatic lens collimates the beam before it enters an argon low pressure discharge lamp that acts as reference. Behind the reference lamp a band pass filter with a central wavelength of 810 nm and a full width at half maximum (FWHM) of 10 nm is utilized to block unwanted spectral components of the light emitted by the plasma jet. The intensity of the light is detected by a fast photodetector (HCA-S, Femto, Germany) providing a bandwidth of 200 MHz. In order to be able to conduct axially resolved measurements (*z*-direction), the plasma jet is precisely positioned by a motorized linear stage.

For temporally resolved measurements, the laser wavelength is kept at a constant value, which is adjusted to the maximum of the reference discharge absorption signal. The spectral absorption profile is determined by tuning the laser wavelength over the optical transition and averaging the transient signal. The respective frequency scaling is obtained by a Michelson interferometer included into the EasyLAAS AOM Laser system.

According to Lambert–Beers law the temporal optical density $\rho(\lambda, z, t)$ in axial direction is calculated from the absorption signal $I(\lambda, z, t)$ and the plasma-off signal I_0 by

$$\rho(\lambda, z, t) = -\ln \frac{I(\lambda, z, t)}{I_0(\lambda)} = \int_0^L k(\lambda, x, z, t)\mathrm{d}x \qquad (1)$$

where L is the absorption length, k is the absorption coefficient and x is the position in laser beam direction. The absorber density n is calculated by

$$n(x, z, t) = \frac{4\epsilon_0 mc^2}{e^2 \lambda_0 f P(\lambda)} \cdot k(\lambda, x, z, t), \qquad (2)$$

where ϵ_0 is the vacuum permitivity, m the electron mass, c the vacuum speed of light, e the elementary charge, λ_0 the center wavelength and f the oscillator strength of the transition. For the investigated Ar(1s$_5$ − 2p$_9$) transition λ_0 and f are 811.5 nm and 0.457, respectively. Furthermore, the spectral absorber distribution is described by the normalized profile function $P(\lambda)$, where $\int_0^\infty P(\lambda)\mathrm{d}\lambda = 1$. The measured profile function is shown in figure 1 together with the best-fit Voigt profile. Due to the low gas temperature of the jet of about 330 K [37] and the operation at atmospheric pressure, Doppler broadening is small against the dominant pressure broadening. The Gaussian width of the Voigt profile is thus only 0.76 GHz, whereas the measured Lorentzian width is 12.8 GHz. The latter value is in good agreement with values determined by other groups in atmospheric pressure argon plasmas. In a filamentary argon discharge within a capillary, Schröter *et al* measured a Lorentzian width of 8.6 GHz [46]. Niermann *et al* found a Lorentzian width of 12.7 GHz
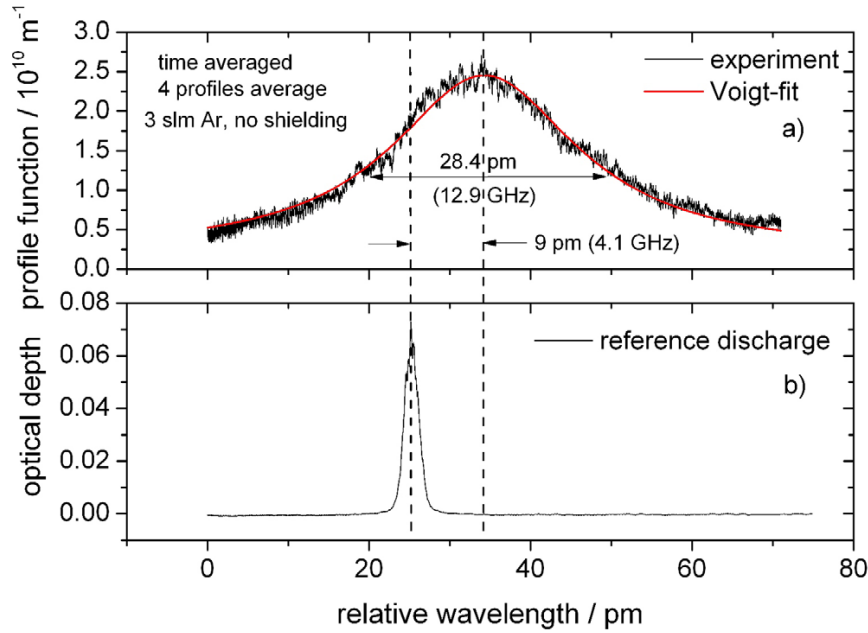
Figure 1. (a) absorption profile function measured on the plasma jet in the radial center and at the nozzle exit. The jet was operated with 3 slm Ar and no shielding gas. (b) absorption signal of the low pressure reference discharge.

from measurements on a parallel plate radio frequency driven μ-plasma jet operated in a mixture of He and Ar [47]. Besides the pressure broadening also a shift between the absorption maxima of the low pressure discharge and the plasma jet of about 9 pm (4.1 GHz) is observed.

Owing to the transient behavior of the filamentary plasma jet on a μs time scale, it is rather statistical whether a filament crosses the laser beam and generates a peak in the optical depth signal [47]. A straight forward evaluation and comparison of the temporal absorption signals at different axial positions and shielding gas settings is thus difficult. However, by recording the optical depth signal over a sufficient long time (4 ms in this work), a statistical analysis becomes possible. In this analysis, the 20 highest peaks of the optical depth are detected as exemplary shown in figure 2 for an axial position of $z = 2$ mm and a shielding gas composition of 1 slm O_2 + 4 slm N_2. In the further evaluation of different shielding gas compositions and axial positions, the average of those 20 peak values is used instead of a single absorption event.

The correct absorption length and argon metastable distribution within a single filament is unknown and therefore either an absorption length of the filament is assumed to estimate the argon metastable density (e.g. from emission measurements, as done in [48]) or just the line-of-sight density $\tilde{n}$ is given, which is calculated by

$$\tilde{n}(z,t) = \int_0^L n(x,z,t)\mathrm{d}x \frac{4\epsilon_0 mc^2}{e^2 \lambda_0 f P(\lambda)} \cdot \rho(\lambda,z,t) \qquad (3)$$

From single shot emission measurements on a similar kinpen-type plasma jet over a single excitation period [38], the streamer width and therefore the absorption length is estimated to a value of about 100 μm. This value and the assumption of a homogeneous absorber distribution are used when comparing the simulated temporal argon metastable densities with the measurement.

2.3. FTIR absorption spectroscopy

In order to quantify RONS in the far field of the jet, FTIR absorption spectroscopy in the spectral range from 800 to 4000 cm^{-1} is used. A schematic of the experimental setup is shown in figure 3. The plasma jet with the shielding gas device is mounted to a glass chamber with a volume of 0.5 l. Both feed gas and shielding gas flux of the plasma jet are controlled using mass flow controllers (MFC, MKS Instruments, USA). In the acquired measurements the shielding gas composition was varied from pure nitrogen to pure oxygen. From the glass chamber, 4 slm of jet and shielding gas flow is sucked into a multipass cell (Bruker, USA) using a vacuum pump, while the rest of the gas exits the glass chamber through an exhaust pipe. The relative flux through the exhaust pipe was monitored using a ball flow meter. The MPC has a volume of around 15 l and provides an absorption length of $L = 32$ m. For the absorption measurements an FTIR spectrometer (Vertex 80v, Bruker, USA) was used. The pressure in the MPC was adjusted to 600 mbar. Prior to the experiments, the system was flushed with 3 slm Ar and 5 slm N_2 for 8 h in order to remove residual humidity from the system.

The identification and quantification of the reactive species was achieved using spectroscopic data from the HITRAN database and PNNL quantitative infrared database [49, 50]. The IR simulation software QMACSoft (neoplas control, Germany) was used to calculate cross sections from the molecular line data provided in the HITRAN database.
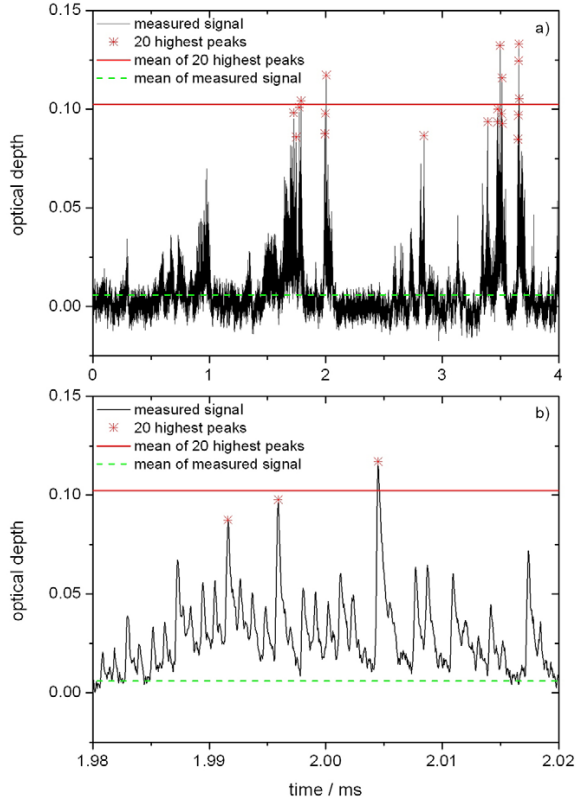
Figure 2. Temporal optical depth signal for a shielding gas setting of 1 slmO$_2$ + 4 slmN$_2$ at $z = 2$ mm. The symbols represent the 20 highest peaks and the solid horizontal line is the mean of those values. The mean value of the entire optical depth signal is represented by the dashed line. (b) is a closeup of (a).
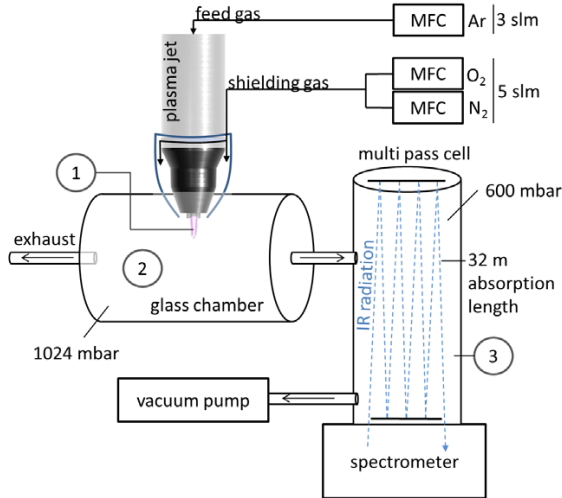

Figure 3. Schematics of the setup used in the FTIR measurements. The encircled labels 1–3 correspond to the simulation steps of the kinetic model as explained in the following section 2.4.

The densities n_i of the species $\{i\}$ were then used as a fitting parameter when fitting the absorbance function

$$A = -\ln \frac{I(\nu)}{I_0(\nu)} = \sum_i n_i \sigma_i(\nu) L \qquad (4)$$

to the experimental data. Here I_0 is the background intensity measured when the plasma jet is turned off, ν is the wavenumber and σ_i are the respective cross sections. The intensity I_0 was acquired before the plasma jet was turned on with a shielding gas mixture of $n_{O_2}/n_{N_2} = 1$. In figure 4 the absorbance obtained from the experimental data and the respective fit is illustrated. The species O$_3$, NO$_2$, HNO$_3$, N$_2$O$_5$, N$_2$O, CO, and CO$_2$ could clearly be identified. An absorbance signal due to H$_2$O$_2$ was also fitted to the data, however as the signal is low and superposed by the N$_2$O$_5$ and HNO$_3$ signal, a clear identification is not possible as discussed in section 3.2.

In the previous work [12] a similar setup was used, however using an absorption length of 19.2 m and a MPC pressure of 100 mbar. These changes result in a tenfold higher sensitivity of the current system. However, using larger pressures in the MPC results in higher reaction rates, leading to the generation and destruction of reactive species in the MPC itself.

2.4. Numerical models

In the plasma plume, the energy is deposited through guided streamers, which typically feature high electric fields in the streamer head (single shot images of the streamer can be found in [38]). In the downstream region of the jet, the highly reactive species generated in these processes successively react to more stable compounds such as can be detected by FTIR spectroscopy. Two zero-dimensional kinetic models are developed in order to investigate both the fast electron impact reactions occurring locally in the head of the guided streamer and the slower reactive species chemistry occurring in the broader plasma plume and the measurement apparatus itself.

2.4.1. Electron impact plasma reaction kinetics model. The first kinetic model aims at investigating the generation of primary reactive species (such species that are generated directly from dissociation, electron attachment, ionization or excitation of N$_2$, O$_2$ or H$_2$O) through electron impact reactions in the streamer head at a fixed spatial position. Therefore, the system of ordinary differential equations describing the reaction kinetics,

$$\partial_t n_s = \sum_j \phi_{s,j} f_{s,j} R_j, \quad \text{with} \quad R_j = k_j \prod_i n_i^{f_{s,j} \delta_{i,j}} \qquad (5)$$

is solved together with the electron energy balance equation

$$\partial_t \left(\frac{3}{2} n_e k_B T_e \right) = P_{in}(t) + \sum_j R_j \Delta \epsilon_j - \sum_j \frac{3}{2} R_j \left(\frac{2 m_e}{M_j} k_B (T_e - T_g) \right). \qquad (6)$$
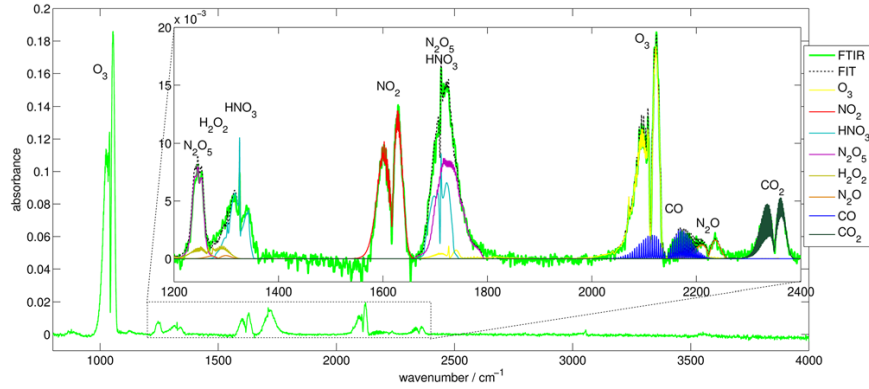
Figure 4. Absorbance as measured by FTIR spectroscopy and as obtained from the fitting procedure for individual species densities for a shielding gas composition of $O_2/N_2 = 0.2$.
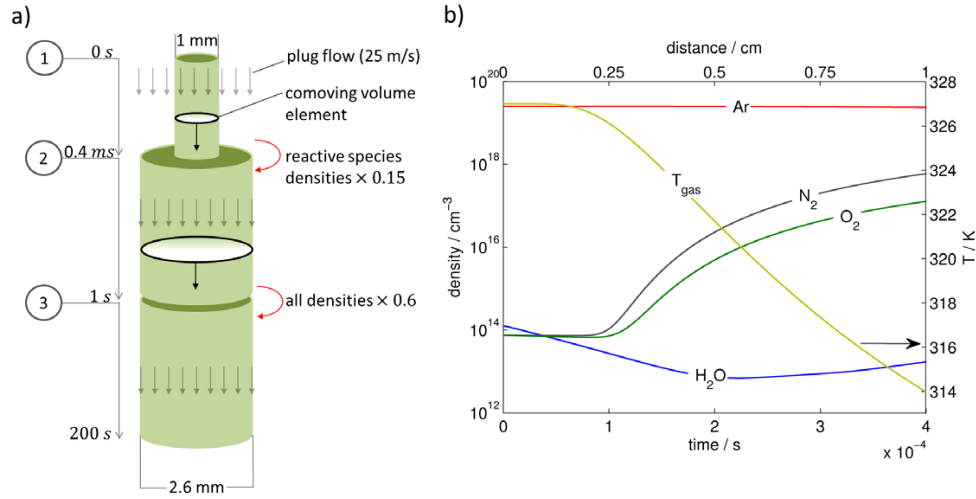

Figure 5. Illustration of the plug-flow approach used in the model (a) and densities of ambient species (shown for synthetic air shielding gas case), water impurities and gas temperature as assumed in the effluent model (b). The encircled labels 1–3 denote the simulation steps and can be identified with the corresponding labels in the experimental setup (figure 3).

Here R_j is the reaction rate of reaction j with the rate coefficient k_j, $\phi_{s,j}$ is 1 if species s is a product in reaction j and -1 if it is a reactant, $f_{s,j}$ is the stoichiometric number of species s in reaction j and $\delta_{i,j}$ is 1 if species i is a reactant in reaction j and 0 otherwise. In the energy balance equation T_e denotes the electron temperature (defined as $2/3\,k_B$ of the mean electron energy), k_B is the Boltzmann constant, $P_{in}(t)$ is the power transferred to the electrons, $\Delta\epsilon_j$ is the energy lost or gained in reaction j and M_j is the mass of the heavy species in reaction j. The last term is only evaluated for elastic collisions. The input power is defined as T-periodic Gaussian pulses

$$P_{in}(t) = \sum_m A\exp(-(t - (m + 1/2)T)^2/\tau^2) \quad (7)$$

with $m \in \mathbb{N}$. The amplitude A and pulse width τ are chosen to match the excitation of $Ar(4s,^3P_2)$ measured in the absorption measurements. The list of reactions E1 to E48 used in the electron impact model is given in table A1 in the appendix. Besides to electron impact reactions further quenching and radiative

processes for the argon states are considered (reactions E9 to E23). Additionally, quenching of argon states by O_2, N_2 and H_2O as listed in table A2 (reactions R4-7 and R14-17) is considered.

2.4.2. Neutral reactive species reaction kinetics model. The electron impact plasma reaction kinetics model introduced in the previous section is designed for describing the fast and highly localized processes in the guided streamer head with an estimated width of 100 μm. For the investigation of reaction pathways of neutral RONS produced in the broader (diameter approximately 1 mm) plasma plume, a zero-dimensional (volume-averaged) plug-flow model is developed. As detailed in the below section 3.1, the Ar* density measurements and the electron impact model show that metastable argon is mainly responsible for the generation of primary reactive species. The neutral chemistry model hence uses an argon metastable source term as its sole energy input. The principle of the model is illustrated in figure 5 and will be described in the following. Only the reaction kinetics equations

$$\partial_t n_s = \sum_j \sigma_{s,j} f_{s,j} R_j + G_s(t), \quad \text{with} \quad R_j = k_j \prod_i n_i^{f_{s,j}} \delta_{i,j} \quad (8)$$

are solved for all reactive species in a volume element co-moving with the flow. Comparing to the balance equation for the electron impact model, the source term $G_s(t)$ is added. For N_2 and O_2 the source term

$$G_s(t) = n_s^{\max} \partial_t \exp(-r_0^2 v_0/(4Dz(t))) \quad (9)$$

describes the diffusion of shielding gas species into the active plasma. Equation (9) describes a typical on-axis density profile for ambient species diffusing into laminar jets [11]. Here $n_s^{\max}$ is the maximum density that species s reaches, r_0 the jet radius and D is the diffusion coefficient. However, it needs to be accounted for that the jet is operated in a turbulent flow regime. The temporally averaged diffusion of ambient species in this turbulent jet has been quantified in [40] using mass spectrometry measurements and Reynolds averaged CFD simulations. As the guided streamer follows the turbulent argon-air boundary [36], which is static on the timescale of streamer propagation (less than 0.5 μs), the local and instantaneous shielding gas density that the guided streamer sees is expected to be lower than the previously obtained average quantities. In the kinetic model the estimated value $D = 1\,\text{cm}^2\,\text{s}^{-1}$ is chosen, which is five times higher than the standard value expected for molecular diffusion of air in argon, accounting for the increased mixing in the turbulent flow, but is still approximately only half of the value obtained in Reynolds averaged CFD models and mass spectrometry measurements. The influence of the diffusion coefficient on the generation of RONS is discussed in the appendix B. The volume element is assumed to move with a constant velocity of $v_0 = 25\,\text{m s}^{-1}$, corresponding to the average gas velocity at the nozzle of the plasma jet. $z(t) = v_0 t$ is the position of the volume element. The reactive species accounted for in the model are Ar^*, $Ar_2^*(Ar_2(a^3\Sigma_u^+))$, O, $O^*(O(^1D))$, $O_2^*(O_2(^1\Delta_g))$, O_3, N, $N_2^*(N_2(A^3\Sigma_u^+))$, NO, NO_2, N_2O, NO_3, N_2O_5, H, H_2, OH, H_2O, H_2O_2, HO_2, HNO, HNO_2, HNO_3. The set of reactions used in the model is given in table A2 in the appendix A.

The simulation is subdivided into three steps corresponding to the conditions in the experimental setup. The simulation steps successively model the reaction kinetics in the effluent, the glass chamber and the MPC as illustrated in figure 5(a):

Step 1: Plasma plume (0–0.4 ms). The diameter of the co-moving volume element is chosen as 1 mm in the plasma plume, which roughly corresponds to the diameter of the visible plume. This value is larger than the diameter of the guided streamer (estimated around 100 μm). The model can hence only yield densities averaged over the volume element, while the actual local densities may be higher or lower (due to diffusion). In the plasma plume region the T-periodic Ar^* source term

$$G_{Ar^*} = \sum_m G_{\max} \exp(-(t - (m + 1/2)T)^2/\tau^2) \quad (10)$$

is added, where $G_{\max}$ is the maximum production rate. For Ar^* no further generation processes are included as it is the

species carrying the highest energy in the model and hence an back-transfer of energy from other excited species is not expected. In figure 5(b) the density of N_2 and O_2 diffusing into the effluent of the jet, the feed gas Ar and H_2O originating from impurities in the gas bottles and/or tubing is shown. Also the temperature profile used in the model is given. The H_2O impurity density is not constant as H_2O is partially consumed. The temperature profile was chosen to agree with measurements obtained using a quantitative Schlieren technique as described in [51].

Step 2: Glass chamber (0.4 ms–1 s). In the second step the reaction kinetics in the glass chamber is modeled. As the argon jet will rapidly mix with the shielding gas in the turbulent flow, an instant dilution of all reactive species is assumed. In a plug flow this corresponds to an expansion of the volume element from 1 mm to 2.6 mm diameter (which at an average velocity of 25 m s^{-1} yields the total mass flow of 8 slm) and a dilution of the species by a factor 0.15. Based on previous computational fluid dynamics simulations of the flow field in the glass chamber, an average residence time of 1 s is assumed [12].

Step 3: Multi pass cell (1–200 s). In the MPC the pressure is reduced to 600 mbar and hence all species are diluted by a factor 0.6. The simulation is run up to a time of 200 s. However, as the reactive species are continuously measured while residing in the MPC, the densities computed by the model are averaged over the interval from $t = 1$ s to $t_{\max} = 120$ s. The maximum evaluation time $t_{\max}$ is chosen to give best agreement with the experimental values. Estimating $t_{\max}$ based on the flow rate of 4 slm through the MPC with a volume of 15 l at 600 mbar gives a residence time of 135 s which agrees reasonably well.

The average computation time for the all model steps and post processing routines on an Intel Xeon X5680 is 3.7 s enabling its application in vast parametric sweeps and in fitting routines.

3. Results and discussion

3.1. Density of Ar^*

In figure 6 the average line-of-sight Ar^* density of the 20 largest absorption peaks is shown at different axial positions and for shielding gas compositions ranging from pure N_2 to pure O_2. The general trend is that the average density is not substantially affected by the shielding gas composition. As the excitation of Ar^* by the guided streamer occurs much faster than the quenching by molecular species, this implies that the local electric field provided in a single guided streamer head is not significantly affected by the shielding gas composition. However, at a distance of $z = 2$ mm the measured Ar^* density is significantly lower for pure N_2 shielding gas, than when O_2 is present. For the kinpen operated with He feed gas it was found that O_2 in the shielding gas significantly promotes the propagation of the guided streamer through an electrostatic focusing mechanism caused by anions (e.g. O_2^-, O^-) in the He-shielding gas interface [51], which results in a significant
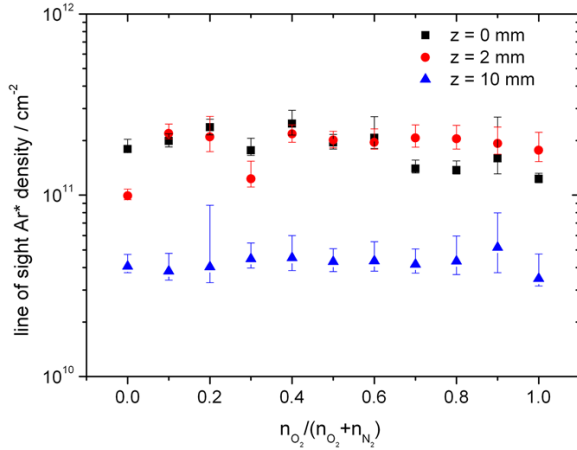
Figure 6. Line-of-sight Ar* density in dependence on the oxygen/nitrogen ratio in the shielding gas for three different axial positions.
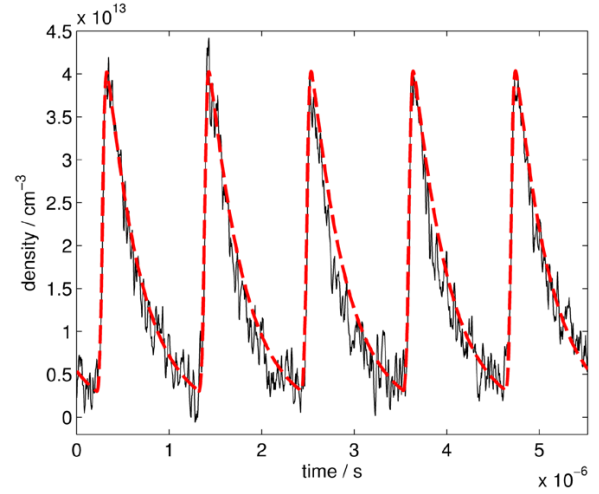

Figure 7. Ar*-density obtained from LAAS measurements (black line) and from the electron impact plasma reaction kinetics model (red dashed line).
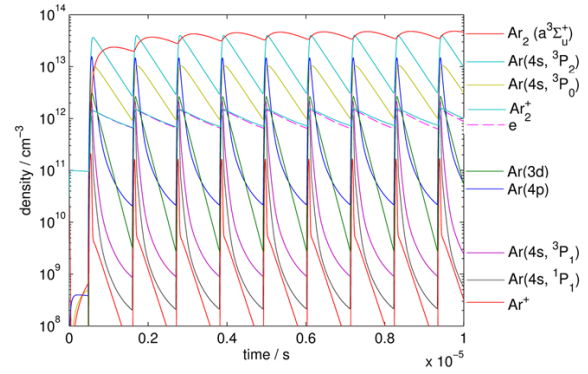

Figure 8. Denities of argon species considered in the electron impact model.

drop of metastable He concentration [52]. A similar mechanism may exist for Ar-operated jets, however this requires further investigation and cannot be stated based on the present statistical evaluation. Assuming an homogeneous absorber distribution within a filament of 100 μm, the peak Ar* density drops from 2×10^{13} cm^{-3} to 4×10^{12} cm^{-3} for an increase of the axial position from $z = 0$ to $z = 10$ mm, respectively.

Figure 7 shows a closeup of the Ar* density obtained from an LAAS measurement assuming 100 μm absorption length at a distance of 2 mm from the nozzle. As shown in figure 2 the Ar* absorption signal is subject to strong temporal fluctuations due to the turbulent flow and filamentary nature of the discharge. In order to receive a clean excitation pattern over several periods, the oscilloscope was triggered to a high absorption signal. The magnitude $A = 4614$ W cm^{-3} and pulse width $\tau = 3 \times 10^{-8}$ s of the power input (7) of the electron impact model was fitted to match the Ar* densities obtained experimentally. A good agreement of the decay of the Ar* was obtained assuming an air mole fraction of 5×10^{-4}.

In figure 8 all argon species included in the model are shown for several periods. The model reaches a steady state after a few periods. The argon excimer Ar$_2^*$ is the most abundant argon species. It is entirely generated from the excited Ar states in three body reactions E19-E21. The measured state Ar(4s,^{3}P$_2$) is the dominant excited Ar state and also the major source of Ar$_2^*$. The Ar(4s,^{3}P$_0$) metastable state reaches approximately 25% of the Ar(4s,^{3}P$_2$) density. The densities of other states are comparably low. The sum of Ar(4p) states also reach similar densities, however they quickly radiate forming 4s states and hence can hardly contribute to the production of RONS. The dominant ion is Ar$_2^+$ with densities of Ar$_2^+ \approx n_e \approx 10^{12}$ cm^{-3}.

In figure 9 the electron density, electron temperature and input power obtained from the model are shown for different mole fractions of synthetic air. Note, that while the maximum power density in the model reaches more than 4500 Wcm^{-3} and is much higher than in previous kinetic studies, the average power density of 222 Wcm^{-3} is comparable to the values found in the literature for similar CAP devices: Van Gaens *et al* used a continuous power input of around 250 Wcm^{-3} in the plasma plume of argon CAP jets [21], Moravej *et al* used up to 150 Wcm^{-3} [53]. The electron density of 10^{12} cm^{-3} is in reasonable agreement with previous experimental studies: Taghizadeh *et al* measured electron densities of around 10^{12}–10^{13} cm^{-3} in the plume of an argon CAP jet by measuring its continuum radiation. Van Gessel *et al* measured higher electron densities of around 10^{13}–10^{14} cm^{-3} in the plume of an argon-operated CAP jet by Thomson scattering [54]. In that study also the electron temperature was measured by Thomson scattering and values between $T_e = 1$ eV to 1.5 eV were obtained. However, due to the duration of the laser pulse employed in the measurement, the authors state that mainly bulk electrons in the low electric field region behind the ionization front contribute to the Thomson scattering signal. Taghizadeh also determined the electron temperature in the plume of an argon CAP jet [55] and received similar values of around 1 eV combining spectroscopic measurements with a collisional radiative model.
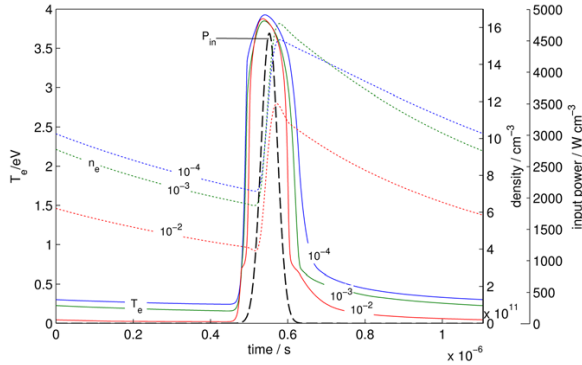
Figure 9. Electron temperature (left *y*-axis) and electron density (first *y*-axis on the right) obtained for the specified input power (second *y*-axis on the right) and three different mole fractions of synthetic air ($x_{air} = 10^{-4}, 10^{-3}, 10^{-2}$).

Schäfer *et al* reported electron densities in the range of some 10^{14} cm^{-3} and temperatures of 2–3 eV in a RF argon plasma jet operated at 27 MHz [56]. A space resolved numerical model of a single filament of the plasma source yielded comparable values of $n_e = 7 \times 10^{13}$ cm^{-3} and $T_e = 1.9$ eV [56, 57]. Balcon *et al* investigated α to γ mode switching in a capacitive plane-to-plane micro discharge operated at 13.56 MHz using a 1D numerical model and obtained values of $n_e = 10^{12}$ cm^{-3} and $T_e = 2.5$–4 eV [58].

The recent numerical study for the argon-operated kinpen by van Gaens *et al* yielded an electron temperature of 3.2 eV and densities of 2×10^{11} cm^{-3} in the plasma plume. In our study we receive much higher temperatures of 3.9 eV. The difference arises from the short pulses we apply in our model: Running our model with a continuous power input of 220 Wcm^{-3} (same as for our pulsed study), we receive similar values of $T_e = 3.4$ eV and $n_e = 5 \times 10^{11}$ cm^{-3}. Comparing the effect of the different air concentrations in figure 9, it is observed that the maximum electron temperature during the short pulse is not significantly affected. With higher air concentration, the electron density decreases and the electron temperature drops faster after the pulse. This is associated to electron attachment to O$_2$ and rotational and vibrational energy losses. However, these studies were performed with the same power input. Whether the power input does actually reach similar values at positions where the air concentration is high, cannot be answered by a zero-dimensional model.

The main goal of the electron impact model is to determine how primary reactive species are generated from O$_2$, N$_2$ and H$_2$O. For this purpose the number of the most abundant primary RONS generated by a single pulse were evaluated for different mole fractions of air as shown in figure 10. Furthermore, the contributions from Ar*-reactions such as

$$X^* + O_2 \rightarrow 2 \cdot O + \text{products}, \qquad (R4/14)$$
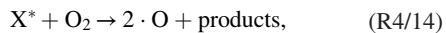
where X* denotes Ar* (R4), Ar$_2^*$ (R14) and electron impact reactions, e.g.

$$e + O_2 \rightarrow e + O + O(^lD), \qquad (E43)$$
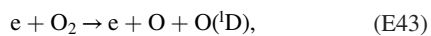
are distinguished. Note that here the states O and O(^{l}D) as well as O$_2$(a) and O$_2$(b) are grouped. Additionally, fast radiative
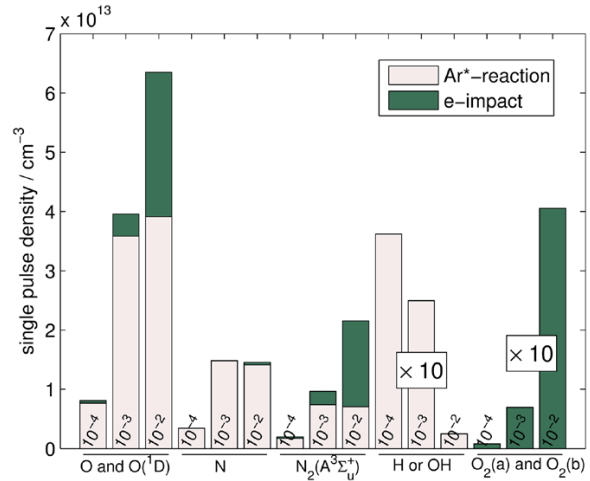
Figure 10. Density of various primary RONS generated by a single guided streamer at dry synthetic air mole fractions 10^{-4}, 10^{-3} and 10^{-2}. Contributions from direct electron impact reactions and reactions involving excited argon species are distinguished.

decay from N$_2$(B/C) to N$_2$(A) is assumed. In the dissociative electron attachment reactions of H$_2$O (E50 and E51) where H$^-$ and OH or OH$^-$ and H are formed a fast recombination of the anions to neutrals is assumed as found by van Gaens and Bogaerts [21]. It is observed, that for the given power input, most primary RONS are generated from reactions involving Ar* rather than from direct electron impact reactions. This does not apply for the low-energy (0.98 eV / 1.63 eV) O$_2$(a/b) states. It is assumed that due to their low energy these states do not dominantly contribute to the formation of RONS in the plasma plume of CAP jets. Therefore, merely using an Ar* source term to model the energy input in the plume of this CAP jet is a valid simplification to describe the resulting RONS chemistry. Figure 10 also shows that a significant amount of primary RONS is generated even when the mole fraction of air is 10^{-3} and lower, highlighting the importance of molecular impurities for the plasma chemistry in such CAP sources.

3.2. Reactive species output in the far field

The densities obtained by FTIR spectroscopy and from the neutral reactive species model are shown in figure 11 for shielding gas compositions ranging from pure N$_2$ to pure O$_2$. The magnitude of the Ar* source term (10) was varied until quantitative agreement of the computed and measured O$_3$ densities was obtained. Very good agreement was obtained for O$_3$, NO$_2$ and N$_2$O$_5$. For N$_2$O the dynamics was predicted correctly by the model, however the measured N$_2$O density is lower by a factor of 0.4. HNO$_2$ was predicted to be generated in measurable amounts by the model but was not detected. It was found that the sum of the computed HNO$_2$ and HNO$_3$ densities give the correct amount of HNO$_3$ as measured. The reaction mechanisms leading to the production of these RONS and possible reasons for the observed deviation of model and measurements are discussed in the following. Also CO$_2$ and CO
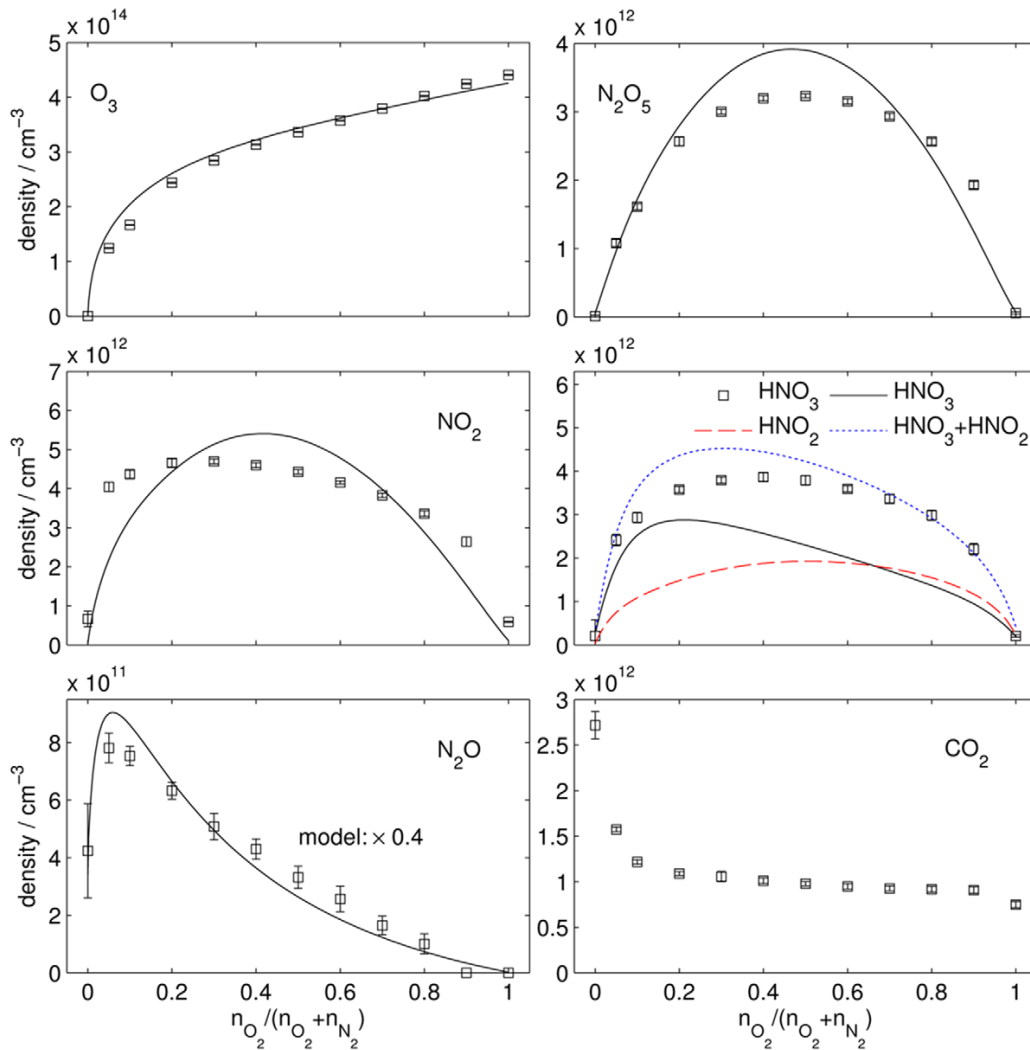
Figure 11. Reactive species densities obtained from FTIR spectroscopy and numerical model versus shielding gas composition. All densities were multiplied by 10/6 in order to be comparable to measurements obtained at standard pressure.

were detected. According to manufacturer specifications the argon feed gas contains up to 0.2 ppm hydrocarbons which is probably the main source for the measured CO_2. The increase of CO_2 at 0% O_2 content in the shielding gas is significant and was confirmed in several measurements. The cause for this increase is unclear. One assumption is that N_2^* exists longer if O_2 (being a major quencher of N_2^* through reactions R23 and R26) is absent and hence N_2^* may provide the energy necessary for cracking the hydrocarbons. Also CO impurities in the N_2 shield gas were detected at a density of 8×10^{12} cm^{-3}. However, CO is not expected to influence the further RONS chemistry as the density at the position of the guided streamer is negligible and it is unlikely to significantly influence the downstream reaction chemistry due to its large bond energy of 11.2 eV. Accordingly no significant consumption of CO was observed.

In figure 12(a) the absorbance between $\nu = 1220$ cm^{-1} and 1320 cm^{-1} is shown as measured using synthetic air as

shielding gas ($O_2/N_2 = 0.2$). As the absorption profile of H_2O_2 is superposed by N_2O_5 and HNO_3, H_2O_2 could not be clearly identified in the FTIR measurements. However, as the model suggests that it should be present, its cross section was included in the fitting routine. The respective densities obtained are shown in figure 12(b). While the quantitative agreement of kinetic model and FTIR results is acceptable, it is unclear if the differences upon shielding gas variation arise from shortcomings of the kinetic model or correlations of the H_2O_2 absorption profile with the N_2O_5 and HNO_3 profiles in the fitting process. Note that model and FTIR data agree well for pure O_2 and pure N_2, when no HNO_3 and N_2O_5 are generated.

The magnitude of the local Ar* source term obtained in this model is seven times lower than the source term obtained in the electron impact reaction kinetics model, while the total (volume integrated) production rate is 14 times higher as in the electron impact model due to the different radii of volume
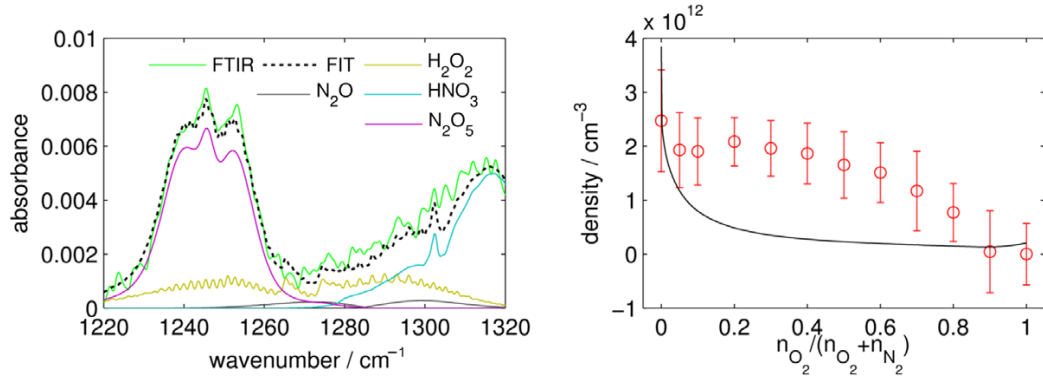
Figure 12. Measured and fitted absorbance of H_2O_2 (a) and respective densities obtained from the fit and the numerical model (b).

elements considered. A perfect agreement of both the production rates can be achieved by choosing the estimated diameters of the guided streamer (for the electron impact model) and the diffusive RONS channel (for the neutral reaction chemistry model) accordingly. However, this was not done as the total RONS output is affected by several parameters, e.g. the detailed shielding gas density at the position of the streamer (see figure 10), the assumed length of the discharge and the flow velocity.

3.3. Reaction pathways

In figure 13 the densities of reactive species are shown as computed for the plasma plume (a), glass chamber (b) and MPC (c). From the simulation it is obvious that the species composition measured in the far field of plasma sources by FTIR spectroscopy is very different from the species that can be expected in the plasma plume.

3.3.1. Reaction mechanisms: O and O_3. The generation of O_3 is determined by the three-body reaction

$$O + O_2 + M \rightarrow O_3 + M, \quad \text{(R43)}$$
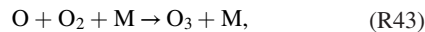
where M is an arbitrary reaction partner. The relevant generation and destruction mechanisms for O are illustrated in figure 14. In this and the following figures, the densities of the respective species generated through the indicated reactions is shown as positive values, the densities consumed when the species is a reactant is given as negative values. Only the reactions significantly contributing to the generation and destruction processes are shown. In the plasma plume, O is generated from the dissociation of O_2 from excited species in the reactions

$$X^* + O_2 \rightarrow 2 \cdot O + \text{products}, \quad \text{(R4/14/23)}$$

where X^* denotes Ar^* (R4), Ar_2^* (R44) and N_2^* (R46). Besides the formation of O_3, O can also be lost via reactions with OH and HO_2 (reactions R44 and R46). In the glass chamber additional O is generated (to a lesser extent) from reactions of N with NO (R42) and O_2.

3.3.2. Reaction mechanisms: NO. The relevant generation and destruction mechanisms for NO are illustrated in

figure 15. The main reaction leading to the generation of NO in the plasma plume and glass chamber is

$$N + OH \rightarrow NO + H \quad \text{(R64)}$$
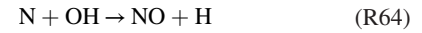
which is one of the reactions of the extended Zeldovich mechanism e.g. relevant for NO generation in combustion processes [59]. To a lesser extent, NO is also generated via the reaction of N_2^* and O (R86) and in the three body reaction of O with N (R38). Note that in the work of van Gaens and Bogaerts [21] R86 is the main reaction contributing to NO generation. The pathways differ as in [21] N_2^* reaches densities of $2 \times 10^{14} cm^{-3}$ which is 5 times higher than in our model, while in our model the Ar^* density is more than ten times higher than in [21]. The high Ar^* density yields significant amounts of N and consequently promotes reaction R64. N also leads to loss of NO by reacting to N_2 and O (R42). Further NO destruction mechanisms lead to the production of NO_2 and are discussed in the following.

3.3.3. Reaction mechanisms: NO_2. As illustrated in figure 16, many reactions contribute to the generation and destruction of NO_2 in the plasma plume and glass chamber. However, most NO_2 is generated through the oxidation of NO in reactions of the form

$$NO + Y \rightarrow NO_2 + \text{products}, \quad \text{(R49/R74/R72)}$$

where Y denotes O (R49, involving a third body), O_3 (R72) or HO_2 (R74). Further important mechanisms for the NO_2 generation and destruction involve HNO_x and N_2O_5 and are discussed below.

3.3.4. Reaction mechanisms: N_2O. For N_2O only two processes were found to be important on the relevant timescale as illustrated in figure 17: In the plasma plume the reaction

$$N_2^* + O_2 \rightarrow N_2O + O \quad \text{(R26)}$$
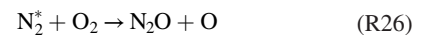
dominates, while in the glass chamber further N_2O is generated from the reaction of NO_2 and N (R35). The model predicts more than twice the amount of N_2O than what is measured via FTIR spectroscopy. A possible explanation is that R26 is exclusively responsible for the generation of N_2O, yielding the right quantity and dynamics under shielding gas variation. The reason for an overestimation of R35 could be, that mixing
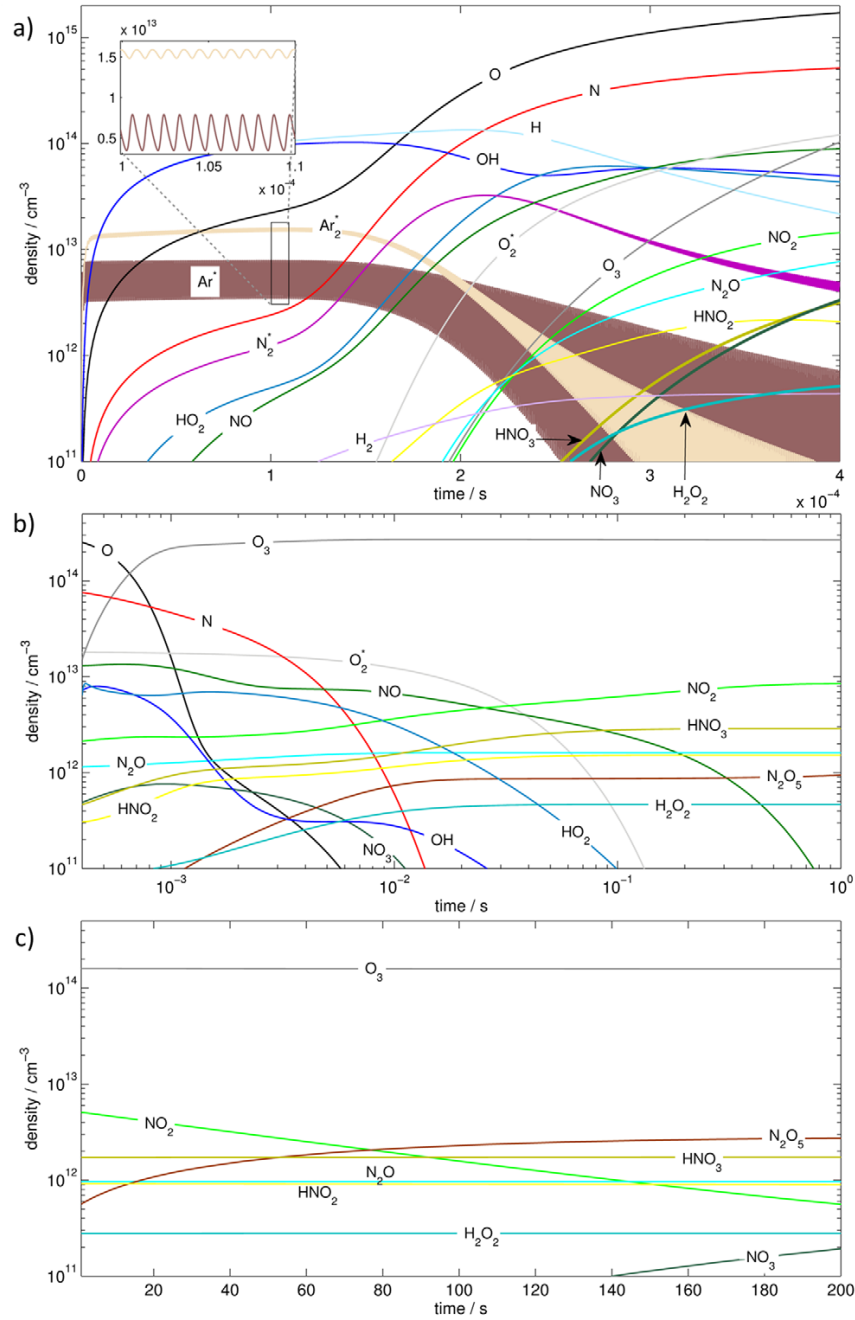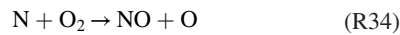
Figure 13. Computed temporal development of reactive species in the plasma plume (a), glass chamber (b) and MPC (c) using synthetic air as shielding gas.

in the glass chamber occurs faster than described by the diffusion source term (9), promoting the reaction
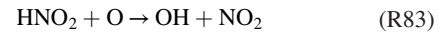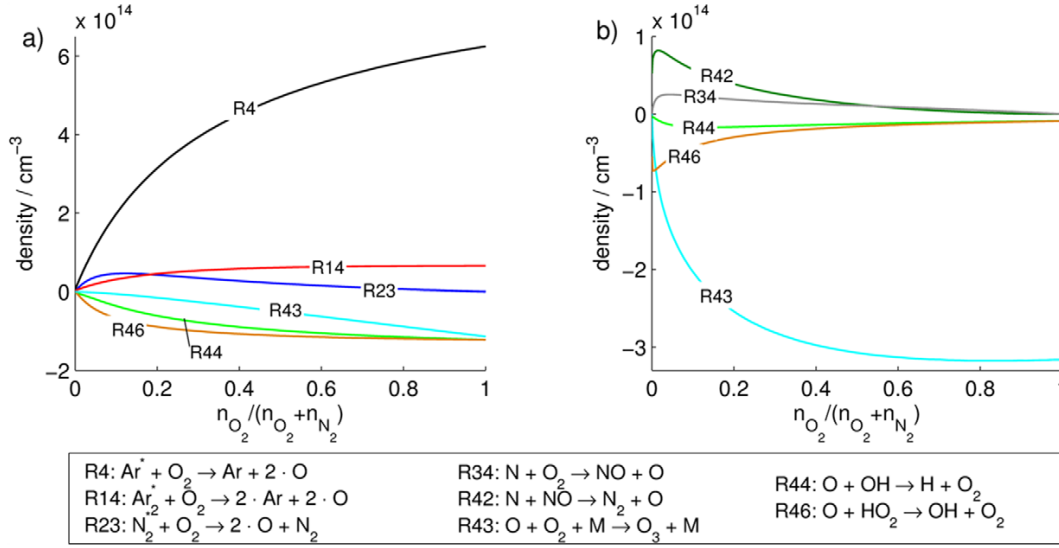
$$N + O_2 \rightarrow NO + O \quad (R34)$$

which effectively removes N, inhibiting reaction R35. Omitting R35 would also give better agreement of NO_2 model and experimental results, yielding higher NO_2 densities for low oxygen content in the shielding gas (see figure 4).

3.3.5. Reaction mechanisms: HNO_2 *and* HNO_3. In figure 18 the relevant reaction mechanisms for both HNO_2 and HNO_3 are shown. HNO_2 and HNO_3 are generated via the processes

$$NO_x + OH + M \rightarrow HNO_{x+1} + M. \quad (R73/67)$$

HNO_2 can be converted to HNO_3 in a two-step process, where

$$HNO_2 + O \rightarrow OH + NO_2 \quad (R83)$$

R4: $Ar^* + O_2 \rightarrow Ar + 2 \cdot O$
R14: $Ar_2^* + O_2 \rightarrow 2 \cdot Ar + 2 \cdot O$
R23: $N_2^* + O_2 \rightarrow 2 \cdot O + N_2$

R34: $N + O_2 \rightarrow NO + O$
R42: $N + NO \rightarrow N_2 + O$
R43: $O + O_2 + M \rightarrow O_3 + M$
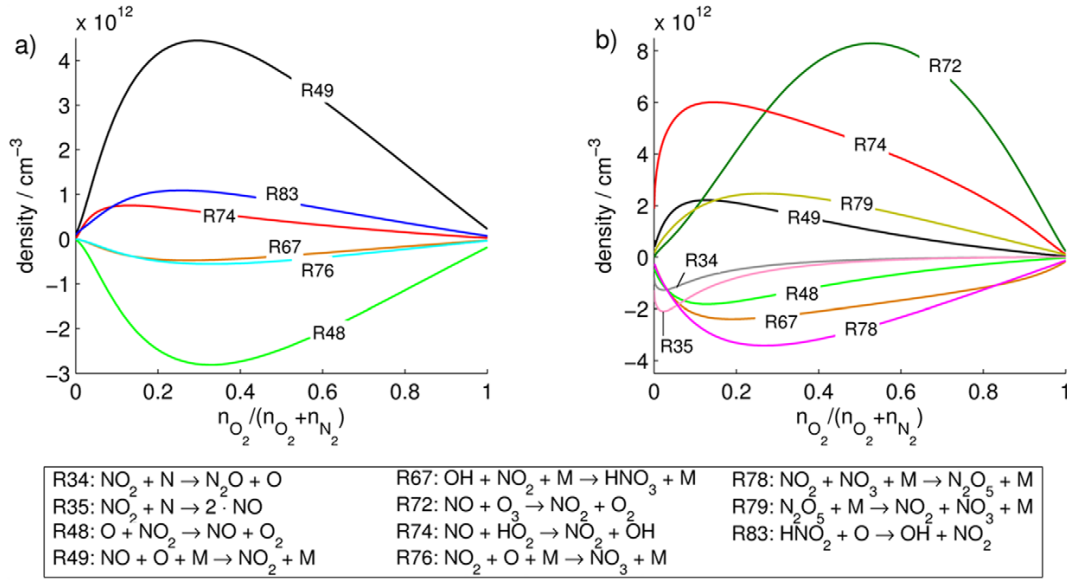
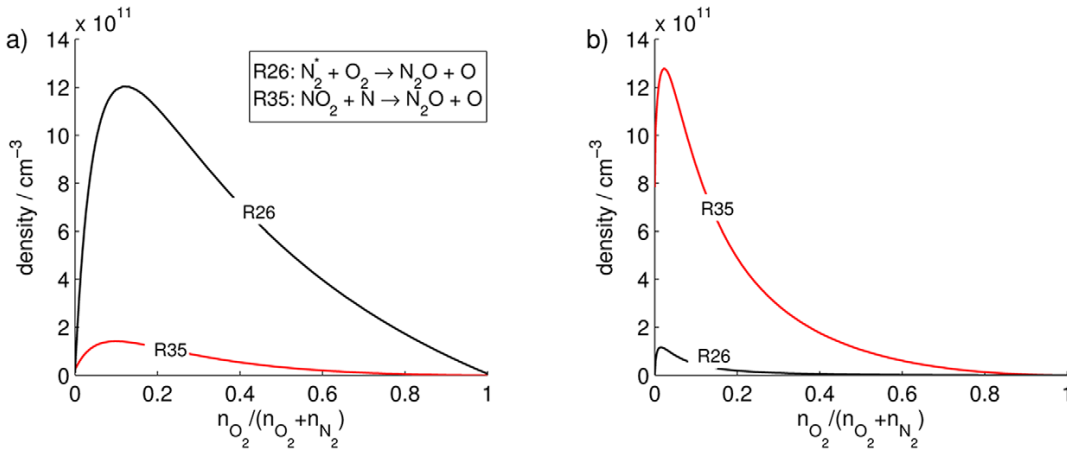R44: $O + OH \rightarrow H + O_2$
R46: $O + HO_2 \rightarrow OH + O_2$

Figure 14. Main reactions contributing to generation and destruction of O in the plasma plume (a) and glass chamber (b).

R34: $N + O_2 \rightarrow NO + O$
R38: $O + N + M \rightarrow NO + M$
R42: $N + NO \rightarrow N_2 + O$

R49: $NO + O + M \rightarrow NO_2 + M$
R64: $N + OH \rightarrow NO + H$
R74: $NO + HO_2 \rightarrow NO_2 + OH$

R86: $N_2^* + O \rightarrow NO + N$
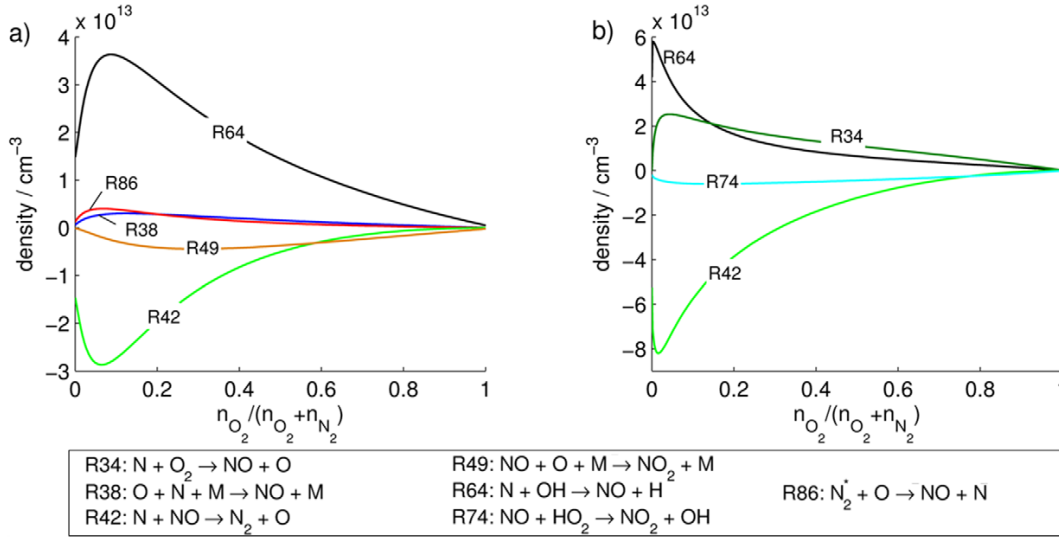
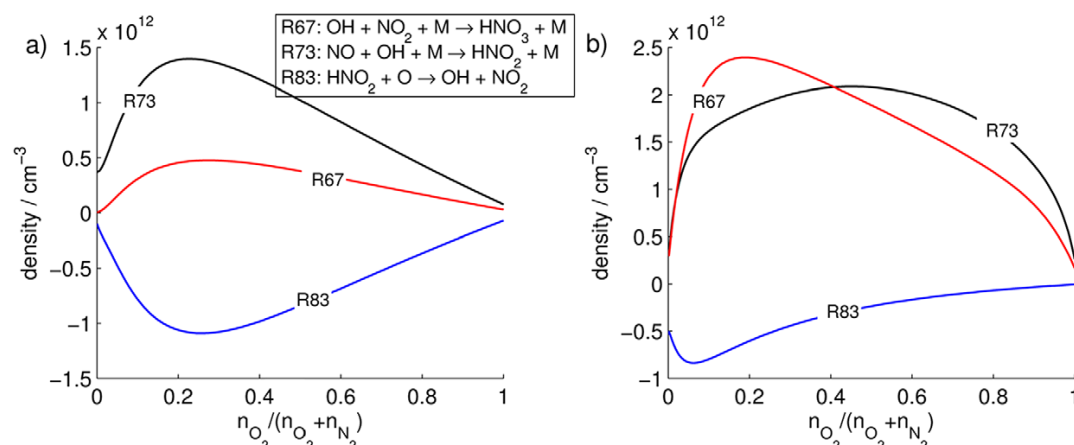**Figure 15.** Main reactions contributing to generation and destruction of NO in the plasma plume (a) and glass chamber (b).

yields the reactants for R67. Since the sum of the densities of HNO$_2$ and HNO$_3$ computed in the kinetic model add up to the correct value of HNO$_3$ measured via FTIR spectroscopy, we assumed that the conversion process R83 is underestimated in the model. The reason for this was assumed to be that O_2^* is underestimated in the model, which can be generated directly in electron impact reactions. It is well-known, that O_2^* can recycle a fraction of O$_3$ to O (R55), which could then initiate the conversion process of HNO$_2$ R83 and R67. For this reason a simulation was run with an additional O_2^* source term producing 10^{12} cm^{-3} O_2^* every period in the plasma plume (compare results of electron-impact study shown in figure 10), but the far-field species obtained were hardly affected. Another possibility is, that NO is converted to NO$_2$ faster than predicted by the model and hence HNO$_3$ is generated rather than HNO$_2$.

3.3.6. Reaction mechanisms: N$_2$O$_5$. In the MPC the only relevant reaction mechanism on this timescale is the generation of N$_2$O$_5$ from NO$_2$ in a two-step process as shown in figure 19: First NO$_3$ is formed from NO$_2$ and O$_3$ which is available in abundance in the reaction

$$NO_2 + O_3 \rightarrow NO_3 + O_2, \tag{R81}$$
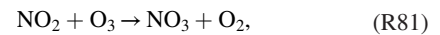
which then reacts to N$_2$O$_5$:

$$NO_2 + NO_3 + M \leftrightarrow N_2O_5 + M \tag{R78/79}$$
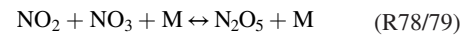
For longer timescales reactions R78 and R79 result in an equilibrium which can yield significant amounts of NO$_3$, a process relevant in dielectric barrier discharges that are not flow-driven [19].

R34: $NO_2 + N \rightarrow N_2O + O$	R67: $OH + NO_2 + M \rightarrow HNO_3 + M$	R78: $NO_2 + NO_3 + M \rightarrow N_2O_5 + M$
R35: $NO_2 + N \rightarrow 2 \cdot NO$	R72: $NO + O_3 \rightarrow NO_2 + O_2$	R79: $N_2O_5 + M \rightarrow NO_2 + NO_3 + M$
R48: $O + NO_2 \rightarrow NO + O_2$	R74: $NO + HO_2 \rightarrow NO_2 + OH$	R83: $HNO_2 + O \rightarrow OH + NO_2$
R49: $NO + O + M \rightarrow NO_2 + M$	R76: $NO_2 + O + M \rightarrow NO_3 + M$	

Figure 16. Main reactions contributing to generation and destruction of NO_2 in the plasma plume (a) and glass chamber (b).

Figure 17. Main reactions contributing to generation and destruction of N_2O in the plasma plume (a) and glass chamber (b).

4. Conclusion

In this work the reaction kinetics leading to the generation or RONS in an argon-operated CAP jet operated with shielding gas device were investigated. Experimental data of RONS densities obtained by FTIR spectroscopy in the far-field and Ar^* densities measured by LAAS in the plasma plume is combined with zero-dimensional modeling of the reaction kinetics using two separate models. The fast and localized generation of primary reactive species in the guided streamer head is evaluated using a first electron impact reaction kinetics model, while the further plasma chemical processes in the visible plasma plume and the downstream region (e.g. inside

the measurement apparatus) is considered in a second neutral reaction kinetics model. A parametric study is performed varying the shielding gas composition from pure N_2 to pure O_2.

The Ar^* densities obtained by the first electron impact model were fitted to the densities obtained by LAAS. It was found, that Ar^* is the main source of primary RONS in the plasma plume. The model yields a maximum electron temperature of 3.9 eV during the pulse and an electron density in the order of 10^{12} cm^{-3}.

The O_3 density computed by the second neutral reaction chemistry model was fitted to the density obtained from FTIR measurements using the magnitude of an Ar^* source term as

Figure 18. Main reactions contributing to generation and destruction of HNO_2 and HNO_3 in the plasma plume (a) and glass chamber (b).
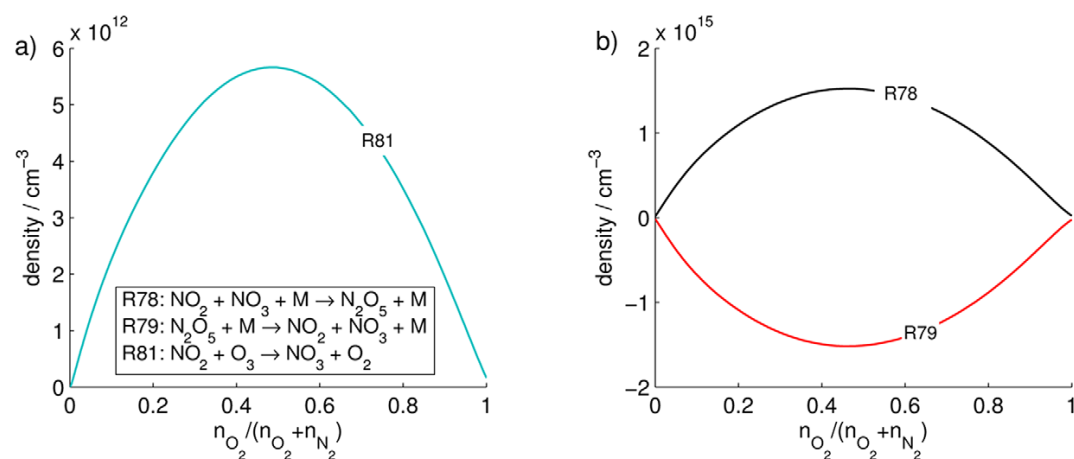
Figure 19. Main reactions contributing to generation and destruction of NO_3 (a) and N_2O_5 (b) in the MPC.

free parameter. The influence of this and further parameters is discussed in the appendix B. The densities of other RONS predicted by the model (NO_2, N_2O_5, N_2O, HNO_3 and H_2O_2) are in good agreement with the FTIR measurements.

For the here-investigated CAP jet operating with pure Ar as feed gas, it was found that it is sufficient to use Ar* as sole input species for the neutral reaction kinetics model. However, the approach can be extended to suit for a broader class of devices, also when using molecular admixtures, by considering the complete set of primary reactive species (also including ions if necessary) generated in quantities as predicted by the electron impact reaction kinetics model. The approach is especially suitable for performing large parametric studies and can hence be used to optimize the reactive species generation of CAP jets for the respective field of application, such as plasma medicine or surface modification.

Acknowledgments

Appendix A. Reactions considered in the model

Table A1. List of reactions used in the electron impact model.

ID	Reaction	Rate coefficient	Reference
E1	$e + Ar \rightarrow e + Ar$	$\sigma(\epsilon)$	[61]
E2	$e + Ar \rightarrow 2 \cdot e + Ar^+$	$\sigma(\epsilon)$	[61]
E3	$e + Ar \rightarrow e + Ar(4s, {}^3P_2)$	$\sigma(\epsilon)$	[61]
E4	$e + Ar \rightarrow e + Ar(4s, {}^3P_1)$	$\sigma(\epsilon)$	[61]
E5	$e + Ar \rightarrow e + Ar(4s, {}^3P_0)$	$\sigma(\epsilon)$	[61]
E6	$e + Ar \rightarrow e + Ar(4s, {}^1P_1)$	$\sigma(\epsilon)$	[61]
E7	$e + Ar \rightarrow e + Ar(4p)$	$\sigma(\epsilon)$	[62]
E8	$e + Ar \rightarrow e + Ar(3d)$	$\sigma(\epsilon)$	[62]
E9	$Ar(4s, {}^3P_1) \rightarrow Ar$	$1.19 \ 10^8$	[63]
E10	$Ar(4s, {}^1P_1) \rightarrow Ar$	$5.1 \ 10^8$	[63]
E11	$Ar(4p) \rightarrow Ar(4s, {}^3P_2)$	$5 \ 10^6$	[63][a]
E12	$Ar(4p) \rightarrow Ar(4s, {}^3P_1)$	$5 \ 10^6$	[63][a]
E13	$Ar(4p) \rightarrow Ar(4s, {}^3P_0)$	$5 \ 10^6$	[63][a]
E14	$Ar(4p) \rightarrow Ar(4s, {}^1P_1)$	$5 \ 10^6$	[63][a]
E15	$Ar(3d) \rightarrow Ar(4p)$	$5 \ 10^6$	[63][a]
E16	$Ar_2^+ + e \rightarrow Ar + Ar(4p)$	$8 \ 10^{-7}(300/T_e)^{2/3}$	[64]
E17	$Ar^+ + Ar + M \rightarrow Ar_2^+ + M$	$2.5 \ 10^{-31}$	[21]
E18	$2 \cdot Ar(4s, {}^3P_2) \rightarrow Ar^+ + Ar + e$	$5 \ 10^{-10}$	[53]
E19	$Ar(4p) + Ar + M \rightarrow Ar_2(a^3\Sigma_u^+) + M$	$1 \ 10^{-31}$	[21]
E20	$Ar(3d) + Ar + M \rightarrow Ar_2(a^3\Sigma_u^+) + M$	$1 \ 10^{-31}$	[21]
E21	$Ar(4s) + Ar + M \rightarrow Ar_2(a^3\Sigma_u^+) + M$	$2.8 \ 10^{-33}$	[65][b]
E22	$Ar_2(a^3\Sigma_u^+) + Ar \rightarrow 3 \cdot Ar$	10^{-14}	[66][c]
E23	$Ar_2(a^3\Sigma_u^+) \rightarrow 2 \cdot Ar$	$3.5 \ 10^5$	[65, 67]
E24	$e + N_2 \rightarrow e + N_2$	$\sigma(\epsilon)$	[68]
E25	$e + N_2 \rightarrow e + N_2(vib/rot)$	$\sigma(\epsilon)$	[68][d]
E26	$e + N_2 \rightarrow e + N_2(B^3\Pi_g)$	$\sigma(\epsilon)$	[68]
E27	$e + N_2 \rightarrow e + N_2(W^3\Delta_u)$	$\sigma(\epsilon)$	[68]
E28	$e + N_2 \rightarrow e + N_2(A^3\Sigma_u^+)$	$\sigma(\epsilon)$	[68]
E29	$e + N_2 \rightarrow e + N_2(B'^3\Sigma_u^-)$	$\sigma(\epsilon)$	[68]
E30	$e + N_2 \rightarrow e + N_2(a'^1\Sigma_u^-)$	$\sigma(\epsilon)$	[68]
E31	$e + N_2 \rightarrow e + N_2(a^1\Pi_g)$	$\sigma(\epsilon)$	[68]
E32	$e + N_2 \rightarrow e + N_2(w^1\Delta_u)$	$\sigma(\epsilon)$	[68]
E33	$e + N_2 \rightarrow e + N_2(C^3\Pi_u)$	$\sigma(\epsilon)$	[68]
E34	$e + N_2 \rightarrow e + 2 \cdot N$	$\sigma(\epsilon)$	[68]
E35	$e + N_2 \rightarrow 2 \cdot e + N_2^+$	$\sigma(\epsilon)$	[68]
E36	$e + O_2 \rightarrow O + O^-$	$\sigma(\epsilon)$	[69]
E37	$e + O_2 \rightarrow e + O_2$	$\sigma(\epsilon)$	[69]
E38	$e + O_2 \rightarrow e + O_2(vib/rot)$	$\sigma(\epsilon)$	[69]
E39	$e + O_2 \rightarrow e + O_2(a^1\Delta_g)$	$\sigma(\epsilon)$	[69]
E40	$e + O_2 \rightarrow e + O_2(b^1\Sigma_g^+)$	$\sigma(\epsilon)$	[69]
E41	$e + O_2 \rightarrow e + O(c^1, C^3, A^3)$	$\sigma(\epsilon)$	[69]
E42	$e + O_2 \rightarrow e + 2 \cdot O$	$\sigma(\epsilon)$	[69]
E43	$e + O_2 \rightarrow e + O + O(^1D)$	$\sigma(\epsilon)$	[69]
E44	$e + O_2 \rightarrow 2 \cdot e + O_2^+$	$\sigma(\epsilon)$	[69]
E45	$e + O_2 \rightarrow e + O + O^+$	$\sigma(\epsilon)$	[69]
E46	$e + H_2O \rightarrow e + H + OH$	$\sigma(\epsilon)$	[70]
E47	$e + H_2O \rightarrow e + O(^1D) + H_2$	$\sigma(\epsilon)$	[70]
E48	$e + H_2O \rightarrow e + H_2O^+$	$\sigma(\epsilon)$	[70]

(Continued)

A Schmidt-Bleker *et al*

Table A1. (Continued)

ID	Reaction	Rate coefficient	Reference
E49	$e + H_2O \rightarrow H_2 + O^-$	$\sigma(\epsilon)$	[70]
E50	$e + H_2O \rightarrow H^- + OH$	$\sigma(\epsilon)$	[70]
E51	$e + H_2O \rightarrow OH^- + H$	$\sigma(\epsilon)$	[70]

Note: The rate coefficients are given in units of s^{-1}, $cm^3\,s^{-1}$ or $cm^6\,s^{-1}$ for first, second or third order reactions. Rate coefficients for electron impact reactions were computed using BOLSIG + [60] with the cross section from the given reference.

[a] Estimated based on typical lifetimes of 4s and 3d states [63].

[b] Rate applied for all Ar(4s)-levels.

[c] Reaction yields $Ar_2^*(^1\Sigma_u^+)$, which dissociates quickly (lifetime 4.2ns [65]).

[d] All levels found in [68] were taken into account, but grouped into one level.

Table A2. List of reactions used in the electron impact model.

ID	Reaction	Rate coefficient	Reference
R1	$Ar^* + Ar + M \rightarrow Ar_2^* + M$	$2.8\ 10^{-33}$	[65]
R2	$Ar_2^* + Ar \rightarrow 3 \cdot Ar$	10^{-14}	[66][a]
R3	$Ar_2^* \rightarrow 2 \cdot Ar$	$3.5\ 10^5$	[65, 67]
R4	$Ar^* + O_2 \rightarrow Ar + 2 \cdot O$	$2.1\ 10^{-10}$	[71]
R5	$Ar^* + N_2 \rightarrow Ar + N_2^*$	$1.8\ 10^{-11}$	[71][b]
R6	$Ar^* + N_2 \rightarrow Ar + 2 \cdot N$	$1.8\ 10^{-11}$	[71][b]
R7	$Ar^* + H_2O \rightarrow Ar + OH + H$	$7.8\ 10^{-10}$	[72, 73]
R8	$Ar^* + O_3 \rightarrow Ar + O_2 + O^*$	$2.1\ 10^{-10}$	[21]
R9	$Ar^* + N_2^* \rightarrow Ar + 2 \cdot N$	$3.6\ 10^{-11}$	[21]
R10	$Ar^* + NO \rightarrow Ar + N + O$	$2.39\ 10^{-10}$	[21]
R11	$Ar^* + NO_2 \rightarrow Ar + NO + O$	$6.49\ 10^{-10}$	[21]
R12	$Ar^* + N_2O \rightarrow Ar + NO + N$	$4.4\ 10^{-10}$	[21]
R13	$Ar^* + N_2O \rightarrow Ar + N_2^* + O$	$4.4\ 10^{-10}$	[21]
R14	$Ar_2^* + O_2 \rightarrow 2 \cdot Ar + 2 \cdot O$	$4.6\ 10^{-11}$	[64]
R15	$Ar_2^* + N_2 \rightarrow 2 \cdot Ar + N_2^*$	$6\ 10^{-12}$	[66][c]
R16	$Ar_2^* + N_2 \rightarrow 2 \cdot Ar + 2 \cdot N$	$6\ 10^{-12}$	[66][c]
R17	$Ar_2^* + H_2O \rightarrow 2 \cdot Ar + OH + H$	$7.8\ 10^{-10}$	[72, 73][d]
R18	$Ar_2^* + O_3 \rightarrow 2 \cdot Ar + O_2 + O$	$2.1\ 10^{-12}$	[21]
R19	$Ar_2^* + NO \rightarrow 2 \cdot Ar + N + O$	$3.1\ 10^{-10}$	[21]
R20	$Ar_2^* + NO_2 \rightarrow 2 \cdot Ar + NO + O$	$8.44\ 10^{-10}$	[21]
R21	$Ar_2^* + N_2O \rightarrow 2 \cdot Ar + N_2 + O$	$5.5\ 10^{-10}$	[21]
R22	$2 \cdot N_2^* \rightarrow N_2^* + N_2$	$3.9\ 10^{-10}$	[74, 75][e]
R23	$N_2^* + O_2 \rightarrow 2 \cdot O + N_2$	$1.5\ 10^{-12}$	[76]
R24	$O_2^* + O_3 \rightarrow O + 2 \cdot O_2$	$5.2 \exp(-2840/T_g)10^{-11}$	[77][f]
R25	$N_2^* + N \rightarrow N_2 + N$	$4\ 10^{-11}$	[78]
R26	$N_2^* + O_2 \rightarrow N_2O + O$	$7.8\ 10^{-14}$	[21]
R27	$N_2^* + N_2O \rightarrow 2 \cdot N_2 + O$	$9.3 \exp(-120/T_g)10^{-12}$	[79][f]
R28	$N_2^* + N_2O \rightarrow NO + N + N_2$	10^{-11}	[21]
R29	$N_2^* + O \rightarrow O^* + N_2$	10^{-12}	[19]
R30	$N_2^* + Ar \rightarrow N_2 + Ar$	$4\ 10^{-17}$	[21]
R31	$N_2^* + N_2 \rightarrow 2 \cdot N_2$	$3.7\ 10^{-16}$	[21]
R32	$N_2^* + O_2 \rightarrow N_2 + O_2^*$	$1.29\ 10^{-12}$	[21]
R33	$O_2^* + N_2^* \rightarrow 2 \cdot O + N_2$	$2\ 10^{-11}$	[21]
R34	$N + O_2 \rightarrow NO + O$	$1.5 \exp(-3600/T_g)10^{-11}$	[77][f]
R35	$NO_2 + N \rightarrow N_2O + O$	$1.4\ 10^{-12}$	[80][f]
R36	$NO_2 + N \rightarrow 2 \cdot NO$	$2.3\ 10^{-12}$	[20]
R37	$O + N + N_2 \rightarrow N_2 + NO$	$1.76\ T_g^{-0.5}10^{-31}$	[20]
R38	$O + N + M \rightarrow NO + M$	$5.46 \exp(156/T_g)10^{-33}$	[81][f]
R39	$3 \cdot N \rightarrow N + N_2$	$3.31\ T_g^{-1.5}10^{-27}$	[20]

(Continued)

Table A2. (Continued)

ID	Reaction	Rate coefficient	Reference
R40	$2 \cdot N + Ar \rightarrow N_2 + Ar$	$1.25 \; 10^{-32}$	[82][f]
R41	$HNO + O \rightarrow OH + NO$	$5.99 \; 10^{-11}$	[83][f]
R42	$N + NO \rightarrow N_2 + O$	$2.1 \exp(96/T_g) 10^{-11}$	[77][f]
R43	$O + O_2 + M \rightarrow O_3 + M$	$3.4(T_g/298) 10^{-34}$	[76, 84]
R44	$O + OH \rightarrow H + O_2$	$2.4 \exp(108.2/T_g) 10^{-11}$	[85][f]
R45	$O + O_3 \rightarrow 2 \cdot O_2$	$8.00 \exp(-2060/T_g) 10^{-12}$	[85][f]
R46	$O + HO_2 \rightarrow OH + O_2$	$2.7 \exp(228.5/T_g) 10^{-11}$	[85][f]
R47	$2 \cdot O + M \rightarrow O_2^* + M$	$6.93(T_g/300)^{-0.63} \; 10^{-35}$	[21]
R48	$O + NO_2 \rightarrow NO + O_2$	$5.5 \exp(192.4/T_g) 10^{-12}$	[85][f]
R49	$NO + O + M \rightarrow NO_2 + M$	$9.02(T_g/298)^{-1.5} 10^{-32}$	[77][f]
R50	$O^* + O_2 \rightarrow O + O_2$	$6.4 \exp(67/T_g) 10^{-12}$	[19]
R51	$O^* + O \rightarrow 2 \cdot O$	$8 \; 10^{-12}$	[19]
R52	$O^* + O_2^* \rightarrow O + O_2$	10^{-11}	[19]
R53	$O^* + O_2 \rightarrow O + O_2^*$	10^{-12}	[19]
R54	$O^* + O_3 \rightarrow 2 \cdot O + O_2$	$1.2 \; 10^{-10}$	[19]
R55	$O^* + O_3 \rightarrow 2 \cdot O_2$	$1.2 \; 10^{-10}$	[19]
R56	$O^* + N_2 \rightarrow O + N_2$	$1.8 \exp(107/T_g) 10^{-11}$	[19]
R57	$O^* + N_2 + M \rightarrow N_2O + M$	$3.5 \; 10^{-37}(T_g/298)^{-0.6}$	[86][f]
R58	$O^* + N_2O \rightarrow N_2 + O_2$	$4.4 \; 10^{-11}$	[19]
R59	$O^* + N_2O \rightarrow 2 \cdot NO$	$7.2 \; 10^{-11}$	[19]
R60	$O^* + NO \rightarrow O + NO$	$4 \; 10^{-11}$	[19]
R61	$O^* + NO_2 \rightarrow O_2 + NO$	$1.4 \; 10^{-10}$	[19]
R62	$O^* + H_2O \rightarrow 2 \cdot OH$	$2.2 \; 10^{-10}$	[19]
R63	$O^* + M \rightarrow O + M$	$5 \; 10^{-12}$	[21]
R64	$N + OH \rightarrow NO + H$	$3.8 \exp(85/T_g) 10^{-11}$	[87][f]
R65	$OH + HO_2 \rightarrow O_2 + H_2O$	$4.8 \exp(252.6/T_g) 10^{-11}$	[85][f]
R66	$OH + O_3 \rightarrow HO_2 + O_2$	$1.7 \exp(-938.1/T_g) 10^{-12}$	[85][f]
R67	$OH + NO_2 + M \rightarrow HNO_3 + M$	$2.2(T_g/298)^{-2.9} 10^{-30}$	[87][f]
R68	$H + O_2 + M \rightarrow HO_2 + M$	$5.71(298/T_g)^{-1.6} 10^{-32}$	[77][f]
R69	$2 \cdot HO_2 + M \rightarrow H_2O_2 + O_2 + M$	$1.7 \exp(999.5/T_g) 10^{-33}$	[77][f]
R70	$2 \cdot OH + M \rightarrow H_2O_2 + M$	$6.2(T_g/298)^{-1} 10^{-31}$	[77][f]
R71	$H_2O_2 + OH \rightarrow H_2O + HO_2$	$2.9 \exp(-156/T_g) 10^{-12}$	[85][f]
R72	$NO + O_3 \rightarrow NO_2 + O_2$	$1.4 \exp(-1306/T_g) 10^{-12}$	[85][f]
R73	$NO + OH + M \rightarrow HNO_2 + M$	$7(T_g/298)^{-2.6} 10^{-31}$	[77][f]
R74	$NO + HO_2 \rightarrow NO_2 + OH$	$3.6 \exp(268/T_g) 10^{-12}$	[85][f]
R75	$OH + HNO_2 \rightarrow NO_2 + H_2O$	$2.5 \exp(259/T_g) 10^{-12}$	[85][f]
R76	$NO_2 + O + M \rightarrow NO_3 + M$	$9.0(T_g/298)^{-2} 10^{-32}$	[77][f]
R77	$OH + HNO_3 \rightarrow NO_3 + H_2O$	$1.5 \exp(650./T_g) 10^{-14}$	[86][f]
R78	$NO_2 + NO_3 + M \rightarrow N_2O_5 + M$	$2.81(T_g/298)^{-3.5} 10^{-30}$	[86][f]
R79	$N_2O_5 + M \rightarrow NO_2 + NO_3 + M$	$3.7 e^{-10039/T_g} 10^{-5}$	[86][f]
R80	$2 \cdot H + M \rightarrow H_2 + M$	$6.04(T_g/298)^{-1} 10^{-33}$	[88][f]
R81	$NO_2 + O_3 \rightarrow NO_3 + O_2$	$1.4 \exp(-2465/T_g) 10^{-13}$	[85][f]
R82	$H + NO + M \rightarrow HNO + M$	$1.3(T_g/298)^{-1.32} e^{-370/T_g} 10^{-31}$	[83][f]
R83	$HNO_2 + O \rightarrow OH + NO_2$	$2.01 \; 10^{-11}$	[83][f]
R84	$HNO_2 + O_3 \rightarrow HNO_3 + O_2$	$5 \; 10^{-19}$	[77][f]
R85	$HO_2 + NO + M \rightarrow HNO_3 + M$	$1.4 \; 10^{-33}$	[89][f]
R86	$N_2^* + O \rightarrow NO + N$	$7 \; 10^{-12}$	[21]
R87	$O_2 + O_2^* \rightarrow O_3 + O$	$3 \; 10^{-21}$	[21]
R88	$2 \cdot O_2^* \rightarrow 2 \cdot O_2$	$9 \exp(-560/T_g) 10^{-17}$	[21]
R89	$O_2^* + M \rightarrow O_2 + M$	$3 \exp(-200/T_g) 10^{-30}$	[21]

(Continued)

Table A2. (Continued)

ID	Reaction	Rate coefficient	Reference
R90	$H + O_3 \rightarrow OH + O_2$	$1.4 \exp(-470/T_g)10^{-10}$	[77][f]

Note: The rate coefficients are given in units of s^{-1}, $cm^3\,s^{-1}$ or $cm^6\,s^{-1}$ for first, second or third order reactions.

[a] Reaction yields $Ar_2^*(^1\Sigma_u^+)$, which dissociates quickly (lifetime 4.2ns [65]).

[b] Quenching rate of Ar^* by N_2 ($3.6 \cdot 10^{-11}\,cm^3\,s^{-1}$) is branched for creation of N_2^* and 2N.

[c] Quenching rate of Ar_2^* by N_2 ($1.2 \cdot 10^{-11}\,cm^3\,s^{-1}$) is branched to N_2^* and 2N.

[d] Estimation based on quenching rate for $Ar^* + H_2O$.

[e] These rates describe the energy pooling reactions for the formation of $N_2(B)$ and $N_2(C)$. Fast radiative relaxation to $N_2(A)$ from these levels is assumed.

[f] Rate obtained from NIST database [90]. The rate coefficient originates from the cited publication.

Appendix B. Sensitivity analysis of the gas phase reaction kinetics model

Even though the agreement of experimental data and the reaction kinetics model is good, this does not necessarily mean that all mechanisms presented here are correct. In the following the sensitivity of the model outcome is investigated by means of examples.

B.1. Different pathways can lead to similar far-field results

For the nitrogen oxides various reaction pathways can eventually lead to the same far-field species. This can for example be seen in figures 15 and 16, where the main reactions contributing to NO and NO_2 production and destruction are shown. In figure B1 the respective reactions leading to the generation of NO and NO_2 are summarized.

Even excluding the dominant reaction pathways for NO generation in the plasma plume via N (R38 and R64) and for NO_2 generation from NO (reactions R11 and R49) hardly affects the far-field species as shown in figure B2. In this case the generation proceeds mainly along the alternative pathways R86 and R83. Also, the oxidation of N to NO or of NO to NO_2 can occur via slower processes in the downstream region via alternative pathways: E.g. instead of oxidation of NO by O R49), in the plasma plume, the oxidation can also occur by reaction with O_3, which is available in high amounts in the downstream region (compare figure 15(b)).

B.2. The influence of free model parameters

Another issue is, that the model involves fitting parameters. The most obvious parameter is the magnitude of the Ar^* source term. However, this parameter mainly affects the magnitude of the RONS generated in the far-field, not the dynamic behavior upon shielding gas variation. The result for four parameters is given in the following: First, the influence of the Ar^* source term magnitude is discussed. Second, the influence of stronger and weaker shielding gas diffusion is studied. Third, the influence of feed gas humidity is discussed. Fourth, the influence of the branching ratio in the reactions

$$Ar^* + N_2 \rightarrow 2 \cdot N \text{ or } N_2^*, \quad \text{(R5/6)}$$
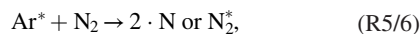
as well as reactions

$$Ar_2^* + N_2 \rightarrow 2 \cdot Ar + 2 \cdot N \text{ or } N_2^*, \quad \text{(R15/16)}$$
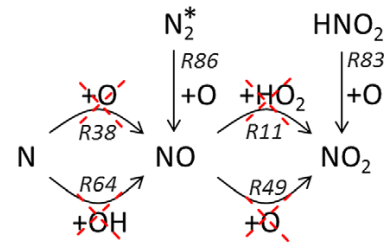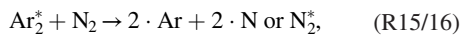

Figure B1. Main reaction pathways leading to the generation of NO and NO_2 in the plasma plume.

is studied (in the original work only the quenching ratio of Ar^*/Ar_2^* was given [66, 71]).

It is found, that general trends always agree with the experimental data, hence the validity of the presented model does not depend too strictly on the choice of open parameters: It is not possible to obtain any desired result by varying these parameters. The downside of this behavior is, that it is not possible to derive an exact value of the fitting parameters from the model results. E.g. the branching ratio of reactions R5/R6 does not influence the results enough to use the agreement of model and FTIR values as an indicator. Only significant changes and unexpected behavior compared to the basic study presented in section 3 are discussed below.

B.3. Influence of the Ar^* source term magnitude

The densities obtained are shown in figure B3.

- Generally behaves as expected: The higher the Ar^* source term magnitude, the more RONS are generated.
- Exception: The NO_2 density does not change significantly. This occurs, as NO_2 is converted to N_2O_5, which is also present in higher quantities. Also, the destruction of NO with N (R42) damps the increased production of NO_2.

B.4. Influence of the shielding gas diffusion

The densities obtained are shown in figure B4.

- The more O_2 is present, the faster the conversion of O to O_3 (reaction R43).
- The formation of O from dissociation of O_2 by N_2^* is promoted, effecting the strong production of O_3 at low O_2 content in the shielding gas.
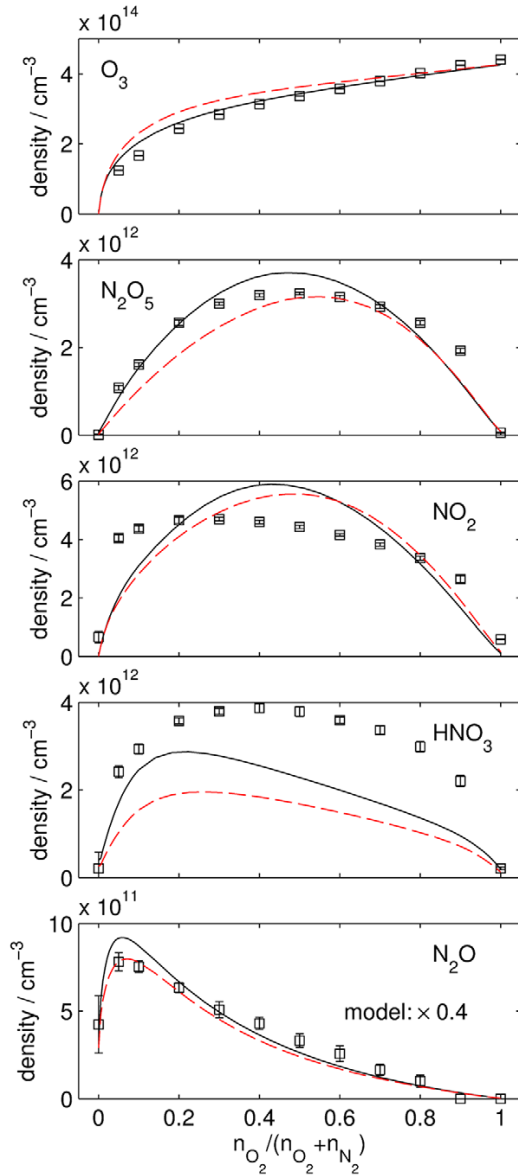
Figure B2. The black line reproduces the results shown in figure 11. The model results shown as red dashed line were obtained by setting reaction coefficients of reactions R11, R38, R49 and R64 to zero.

- As more O_3 is produced, NO_2 is converted to N_2O_5 faster than in the basic study.
- For the production of NO the reaction of N with O_2 (R34) becomes more important.
- With rising shielding gas content, the generation of N_2O from N_2^* and O_2 (R26) increases.

B.5. Influence of the feed gas humidity

The densities obtained are shown in figure B5.

- With increasing humidity, less O is available as O is consumed in reactions with HO_2 (R46) and OH (R44).
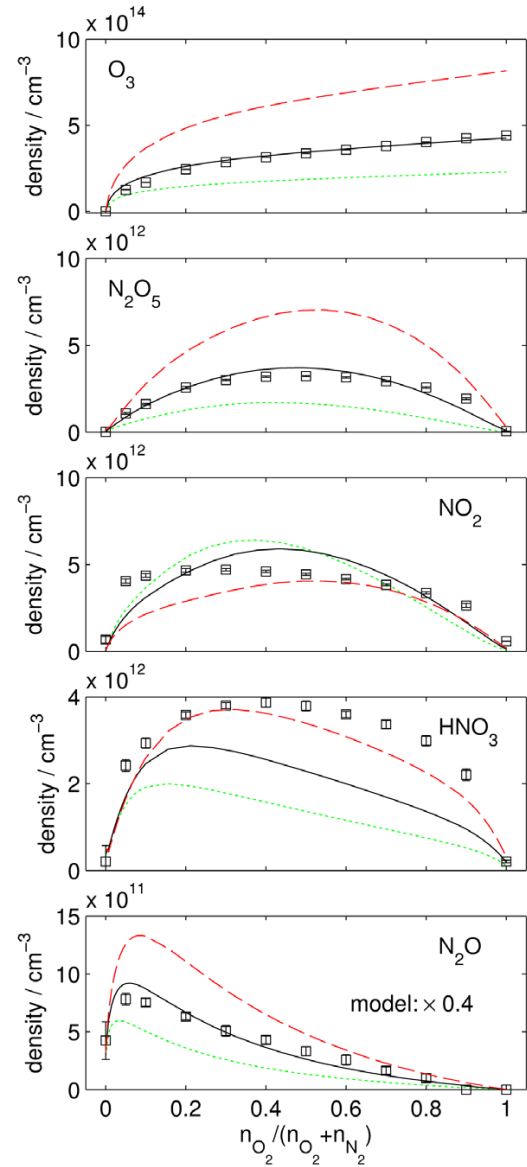
Figure B3. Sensitivity analysis of Ar* source term magnitude: The black line reproduces the results shown in figure 11. Green dotted line: The magnitude of the argon source term is multiplied by 0.5. Red dashed line: The magnitude of the argon source term is multiplied by 2.

- If no humidity is available, NO cannot be generated via the main pathway (from N and OH, R64) in the effluent and is generated in the reaction of N and O with a third body (R37), from N_2^* and O with a third body (R86) and from the reaction of N with O_2 (R32).
- If much humidity is available, large amounts of NO_2 and HNO_3 can be expected even when no oxygen is present. It is noted that NO_2, HNO_3 and HNO_2 in the range of some 10^{12} cm^{-3} were indeed detected with pure nitrogen shielding while the system tubes were flushed. However, the humidity was not quantified during this drying phase and therefore the data is not shown.
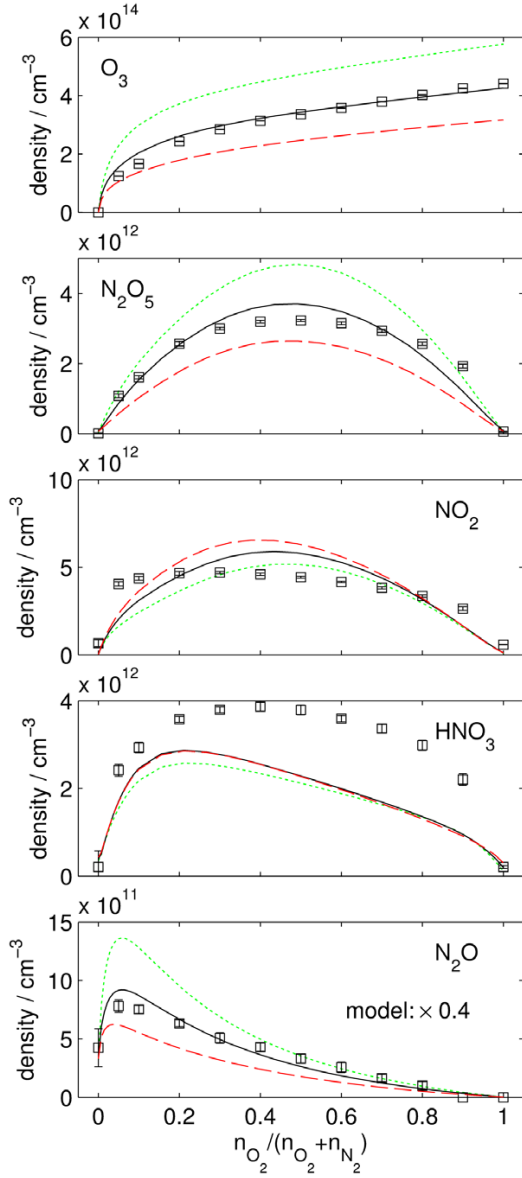
Figure B4. Sensitivity analysis of shielding gas diffusion: The black line reproduces the results shown in figure 11 (maximum shiedling gas density in the plasma plume: 2.4%). Green dotted line: 0.9%. Red dashed line: 6.5%.
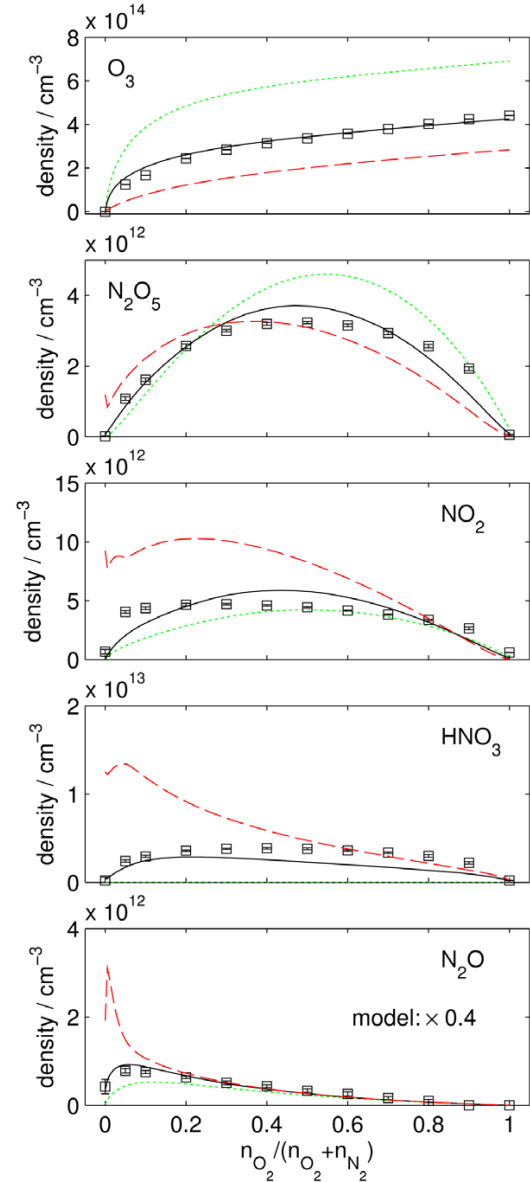
Figure B5. Sensitivity analysis of feed gas humidity: The black line reproduces the results shown in figure 11 (H_2O density: 5 ppm). Green dotted line: 0 ppm. Red dashed line: 50 ppm.

B.6. Influence of the $Ar^*/Ar_2^* + N_2$ branching ratio

The densities obtained are shown in figure B6. The same branching rates for quenching of Ar^* and Ar_2^* were assumed.

- The RONS densities are not heavily affected by the branching ratio.

- The underlying mechanisms for the NO generation change: While the generation of NO from N and OH (R64) still produces most, the generation from N_2^* and O_2 (R86) becomes almost as important. This also effects the changes observed in the NO_2, HNO_3 and N_2O_5 density.

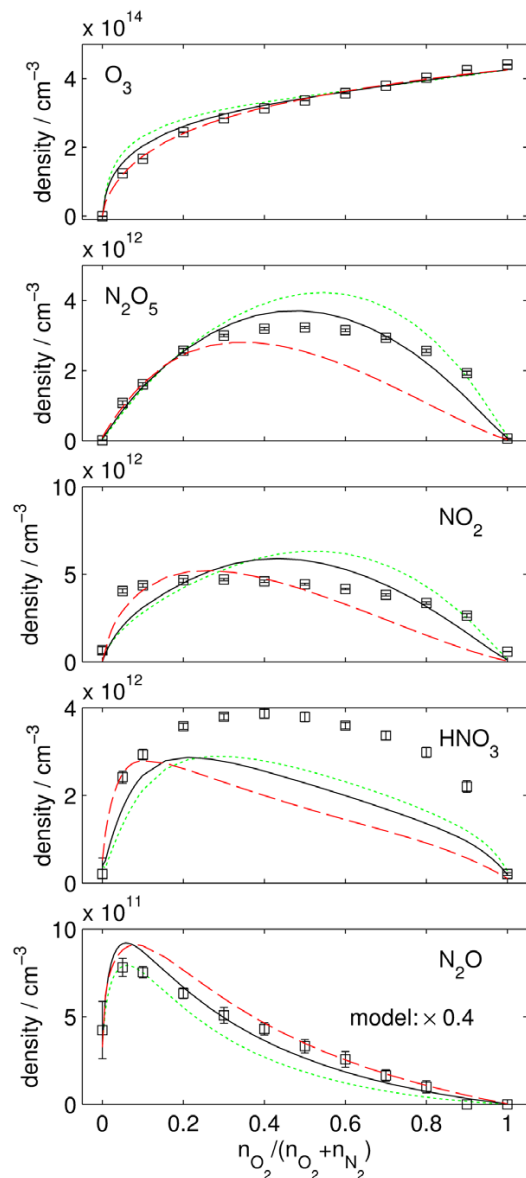- The N_2O density increases with the amount of N_2^* produced as can be expected from reaction R26.

Figure B6. Sensitivity analysis of $Ar^*/Ar_2^* + N_2$ branching ratio: The black line reproduces the results shown in figure 11 (branching ratio 0.5). Green dotted line: Branching ratio 0.2 (more N). Red dashed line: Branching ratio 0.8 (more N_2^*).

References

[1] Kong M G *et al* 2009 Plasma medicine: an introductory review *New J. Phys.* **11** 115012

[2] Fridman A and Friedman G 2012 *Plasma Medicine* (New York: Wiley)

[3] Von Woedtke T, Reuter S, Masur K and Weltmann K D 2013 Plasmas for medicine *Phys. Rep.* **530** 291–320

[4] Graves D B 2014 Low temperature plasma biomedicine: a tutorial review *Phys. Plasmas* **21** 080901–2100

[5] Iza F *et al* 2008 Microplasmas: sources, particle kinetics, and biomedical applications *Plasma Process. Polym.* **5** 322–44

[6] Park G *et al* 2012 Atmospheric-pressure plasma sources for biomedical applications *Plasma Sources Sci. Technol.* **21** 043001

[7] Lu X, Laroussi M and Puech V 2012 On atmospheric-pressure non-equilibrium plasma jets and plasma bullets *Plasma Sources Sci. Technol.* **21** 034005

[8] Ehlbeck J *et al* 2011 Low temperature atmospheric pressure plasma sources for microbial decontamination *J. Phys. D: Appl. Phys.* **44** 013002

[9] Graves D B 2012 The emerging role of reactive oxygen and nitrogen species in redox biology and some implications for plasma applications to medicine and biology *J. Phys. D: Appl. Phys.* **45** 263001

[10] Reuter S *et al* 2012 From RONS to ROS: tailoring plasma jet treatment of skin cells *IEEE Trans. Plasma Sci.* **40** 2986–93

[11] Schmidt-Bleker A, Reuter S and Weltmann K D 2014 Non-dispersive path mapping approximation for the analysis of ambient species diffusion in laminar jets *Phys. Fluids* **26** 083603

[12] Schmidt-Bleker A, Winter J, Iseni S, Dünnbier M, Weltmann K and Reuter S 2014 Reactive species output of a plasma jet with a shielding gas device-combination of FTIR absorption spectroscopy and gas phase modelling *J. Phys. D: Appl. Phys.* **47** 145201

[13] Tresp H, Hammer M U, Weltmann K D and Reuter S 2013 Effects of atmosphere composition and liquid type on plasma-generated reactive species in biologically relevant solutions *Plasma Med.* **3** 45–55

[14] Barton A 2014 *Impact of Non-Thermal Plasma on Cell Signaling in Keratinocytes* (Greifswald: Ernst-Moritz-Arndt-Universität)

[15] Bekeschus S, Iseni S, Reuter S, Masur K and Weltmann K D 2015 Nitrogen shielding of an argon plasma jet and its effects on human immune cells *IEEE Trans. Plasma Sci.* **43** 776–81

[16] Jablonowski H *et al* 2015 Plasma jet's shielding gas impact on bacterial inactivation *Biointerphases* **10** 029506

[17] Pavlovich M J, Clark D S and Graves D B 2014 Quantification of air plasma chemistry for surface disinfection *Plasma Sources Sci. Technol.* **23** 065036

[18] Liu D X, Bruggeman P, Iza F, Rong M Z and Kong M G 2010 Global model of low-temperature atmospheric-pressure $He^+ H_2O$ plasmas *Plasma Sources Sci. Technol.* **19** 025018

[19] Sakiyama Y, Graves D B, Chang H W, Shimizu T and Morfill G E 2012 Plasma chemistry model of surface microdischarge in humid air and dynamics of reactive neutral species *J. Phys. D: Appl. Phys.* **45** 425201

[20] Murakami T, Niemi K, Gans T, O'Connell D and Graham W G 2013 Chemical kinetics and reactive species in atmospheric pressure helium–oxygen plasmas with humid-air impurities *Plasma Sources Sci. Technol.* **22** 015003

[21] Van Gaens W and Bogaerts A 2013 Kinetic modelling for an atmospheric pressure argon plasma jet in humid air *J. Phys. D: Appl. Phys.* **46** 275201

[22] Sakiyama Y and Graves D B 2009 Neutral gas flow and ring-shaped emission profile in non-thermal RF-excited plasma needle discharge at atmospheric pressure *Plasma Sources Sci. Technol.* **18** 025022

[23] Naidis G 2011 Modelling of plasma bullet propagation along a helium jet in ambient air *J. Phys. D: Appl. Phys.* **44** 215203

[24] Breden D, Miki K and Raja L 2012 Self-consistent two-dimensional modeling of cold atmospheric-pressure plasma jets/bullets *Plasma Sources Sci. Technol.* **21** 034011

[25] Boeuf J, Yang L and Pitchford L 2013 Dynamics of a guided streamer ('plasma bullet') in a helium jet in air at atmospheric pressure *J. Phys. D: Appl. Phys.* **46** 015201

[26] Babaeva N Y and Kushner M J 2014 Interaction of multiple atmospheric-pressure micro-plasma jets in small arrays: He/O$_2$ into humid air *Plasma Sources Sci. Technol.* **23** 015007

[27] Van Gaens W, Iseni S, Schmidt-Bleker A, Weltmann K D, Reuter S and Bogaerts A 2015 Numerical analysis of the effect of nitrogen and oxygen admixtures on the chemistry of an argon plasma jet operating at atmospheric pressure *New J. Phys.* **17** 033003

[28] Naidis G V 2013 Modelling of OH production in cold atmospheric-pressure He–H$_2$O plasma jets *Plasma Sources Sci. Technol.* **22** 035015

[29] Naidis G 2014 Production of active species in cold helium–air plasma jets *Plasma Sources Sci. Technol.* **23** 065014

[30] Tian W and Kushner M J 2014 Long term effects of multiple DBD pulses on thin liquid layers over tissue: reactive fluences and electric fields *Bulletin of the American Physical Society* vol 59

[31] Lademann J *et al* 2011 Comparison of the antiseptic efficacy of tissue-tolerable plasma and an octenidine hydrochloride-based wound antiseptic on human skin *Skin Pharmacol. Physiol.* **25** 100–6

[32] Metelmann H R *et al* 2012 Experimental recovery of CO$_2$-laser skin lesions by plasma stimulation *Am. J. Cosmetic Surg.* **29** 52–6

[33] Schmidt A *et al* 2015 Non-thermal plasma activates human keratinocytes by stimulation of antioxidant and phase II pathways *J. Biol. Chem.* **290** 6731–50

[34] Bekeschus S *et al* 2014 Hydrogen peroxide: a central player in physical plasma-induced oxidative stress in human blood cells *Free Radical Res.* **48** 542–9

[35] Daeschlein G *et al* 2014 In vitro susceptibility of multidrug resistant skin and wound pathogens against low temperature atmospheric pressure plasma jet (APPJ) and dielectric barrier discharge plasma (DBD) *Plasma Process. Polym.* **11** 175–83

[36] Iseni S, Schmidt-Bleker A, Winter J, Weltmann K D and Reuter S 2014 Atmospheric pressure streamer follows the turbulent argon air boundary in a MHz argon plasma jet investigated by OH-tracer PLIF spectroscopy *J. Phys. D: Appl. Phys.* **47** 152001

[37] Schmidt-Bleker A, Reuter S and Weltmann K 2015 Quantitative schlieren diagnostics for the determination of ambient species density, gas temperature and calorimetric power of cold atmospheric plasma jets *J. Phys. D: Appl. Phys.* **48** 175202

[38] Reuter S, Schmidt-Bleker A, Iseni S, Winter J and Weltmann K D 2014 On the bullet-streamer dualism *IEEE Trans. Plasma Sci.* **42** 2428–9

[39] Schmidt-Bleker A *et al* 2013 Controlling the effluent chemistry of a CAP jet for biomedical applications: FTIR diagnostics and gas phase modeling *Bulletin of the American Physical Society* vol 58

[40] Dünnbier M *et al* 2013 Ambient air particle transport into the effluent of a cold atmospheric-pressure argon plasma jet investigated by molecular beam mass spectrometry *J. Phys. D: Appl. Phys.* **46** 435203

[41] Van Gaens W, Bruggeman P and Bogaerts A 2014 Numerical analysis of the NO and O generation mechanism in a needle-type plasma jet *New J. Phys.* **16** 063054

[42] Weltmann K D *et al* 2009 Atmospheric pressure plasma jet for medical therapy: plasma parameters and risk estimation *Contrib. Plasma Phys.* **49** 631–40

[43] Reuter S, Winter J, Schmidt-Bleker A, Tresp H, Hammer M U and Weltmann K D 2012 Controlling the ambient air affected reactive species composition in the effluent of an argon plasma jet *IEEE Trans. Plasma Sci.* **40** 2788–94

[44] Bösel A, Ehlbeck J, König N, Salewski K D and Röpcke J 2012 On enhanced tuning capabilities of external cavity lasers using acousto-optic modulators *Opt. Rev.* **19** 332–6

[45] Bösel A and Salewski K D 2009 Fast mode-hop-free acousto-optically tuned laser: theoretical and experimental investigations *Appl. Opt.* **48** 818–26

[46] Schröter S *et al* 2013 Time-resolved characterization of a filamentary argon discharge at atmospheric pressure in a capillary using emission and absorption spectroscopy *J. Phys. D: Appl. Phys.* **46** 464009

[47] Niermann B, Böke M, Sadeghi N and Winter J 2010 Space resolved density measurements of argon and helium metastable atoms in radio-frequency generated He–Ar micro-plasmas *Eur. Phys. J. D: At. Mol. Opt. Plasma Phys.* **60** 489–95

[48] Niermann B, Reuter R, Kuschel T, Benedikt J, Böke M and Winter J 2012 Argon metastable dynamics in a filamentary jet micro-discharge at atmospheric pressure *Plasma Sources Sci. Technol.* **21** 034002

[49] Johnson T J, Sams R L and Sharpe S W 2004 The PNNL quantitative infrared database for gas-phase sensing: a spectral library for environmental, hazmat, and public safety standoff detection *Optical Technologies for Industrial, Environmental, and Biological Sensing. Int. Society for Optics and Photonics* 159–67

[50] Rothman L S *et al* 2004 The HITRAN 2004 molecular spectroscopic database *J. Quant. Spectrosc. Radiat. Transfer* **96** 139–204

[51] Schmidt-Bleker A *et al* 2015 Propagation mechanisms of guided streamers in plasma jets: the influence of electronegativity of the surrounding gas *Plasma Sources Sci. Technol.* **24** 035022

[52] Winter J, Sousa J S, Sadeghi N, Schmidt-Bleker A, Reuter S and Puech V 2015 The spatio-temporal distribution of He (23S1) metastable atoms in a MHz-driven helium plasma jet is influenced by the oxygen/nitrogen ratio of the surrounding atmosphere *Plasma Sources Sci. Technol.* **24** 25015–25

[53] Moravej M, Yang X, Barankin M, Penelon J, Babayan S and Hicks R 2006 Properties of an atmospheric pressure radio-frequency argon and nitrogen plasma *Plasma Sources Sci. Technol.* **15** 204

[54] Van Gessel B, Brandenburg R and Bruggeman P 2013 Electron properties and air mixing in radio frequency driven argon plasma jets at atmospheric pressure *Appl. Phys. Lett.* **103** 064103

[55] Taghizadeh L, Nikiforov A, Morent R, van der Mullen J and Leys C 2014 Determination of the electron temperature of atmospheric pressure argon plasmas by absolute line intensities and a collisional radiative model *Plasma Process. Polym.* **11** 777–86

[56] Schäfer J, Sigeneger F, Foest R, Loffhagen D and Weltmann K D 2010 On plasma parameters of a self-organized plasma jet at atmospheric pressure *Eur. Phys. J. D: At. Mol. Opt. Plasma Phys.* **60** 531–8

[57] Sigeneger F and Loffhagen D 2014 Modeling of striated filaments occurring in a nonthermal RF plasma jet at atmospheric pressure *IEEE Trans. Plasma Sci.* **42** 2498–9

[58] Balcon N, Hagelaar G and Boeuf J 2008 Numerical model of an argon atmospheric pressure RF discharge *IEEE Trans. Plasma Sci.* **36** 2782–7

[59] Lavoie G A, Heywood J B and Keck J C 1970 Experimental and theoretical study of nitric oxide formation in internal combustion engines *Combust. Sci. Technol.* **1** 313–26

[60] Hagelaar G and Pitchford L 2005 Solving the Boltzmann equation to obtain electron transport coefficients and rate coefficients for fluid models *Plasma Sources Sci. Technol.* **14** 722

[61] Puech database 2015 retrieved on January 27, 2015 available from: www.lxcat.net

[62] Biagi-v7 1 database 2015 retrieved on January 27, 2015 available from: www.lxcat.net

A Schmidt-Bleker *et al*

[63] Kramida A, Yu R, Reader J and NIST ASD Team 2014 NIST Atomic Spectra Database (version 5.2); available from: http://physics.nist.gov/asd

[64] Keto J W, Hart C F and Kuo C 1981 Electron beam excited mixtures of O_2 in argon. III. Energy transfer to O_2 and O_3 *J. Chem. Phys.* **74** 4450–4

[65] Keto J, Gleason R Jr and Walters G 1974 Production mechanisms and radiative lifetimes of argon and xenon molecules emitting in the ultraviolet *Phys. Rev. Lett.* **33** 1365

[66] Mehnert R, Brede O and Hermann R 1986 Quenching of the argon (4s) levels and of the excimer $Ar_2(^3\Sigma_u^+)$ by N_2,N_2O, SF_6 and CF_3H—a pulse radiolysis study *Int. J. Radiat. Appl. Instrum.: Part C Radiat. Phys. Chem.* **28** 455–60

[67] Millet P, Birot A, Brunet H, Dijolis H, Galy J and Salamero Y 1982 Spectroscopic and kinetic analysis of the VUV emissions of argon and argon-xenon mixtures. I. Study of pure argon *J. Phys. B: At. Mol. Phys.* **15** 2935

[68] PHELPS database 2015 available from: www.lxcat.net

[69] TRINITI database 2015 available from: www.lxcat.net

[70] Morgan database 2015 available from: www.lxcat.net

[71] Piper L G, Velazco J E and Setser D W 1973 Quenching cross sections for electronic energy transfer reactions between metastable argon atoms and noble gases and small molecules *J. Chem. Phys.* **59** 3323–40

[72] Sheldon J W and Muschlitz E E 1978 Quenching cross sections for Ar(3P0, 2) and Kr(3P0, 2) by H_2O and D_2O *J. Chem. Phys.* **68** 5288–9

[73] Novicki S and Krenos J 1988 Absolute quenching cross section for collisions between Ar (3P0, 2) and H_2O *J. Chem. Phys.* **89** 7031–3

[74] Piper L G 1988 State-to-state $N_2(A^3\Sigma_u^+)$ energy-pooling reactions. I. The formation of $N_2(C^3\Pi_u)$ and the Herman infrared system *J. Chem. Phys.* **88** 231–9

[75] Piper L G 1988 $^3\Sigma$-state $N_2(A^3\Sigma_u^+)$ energy pooling reactions. II. The formation and quenching of $N_2(B^3\Pi_g, v' = 1 - 12)$ *J. Chem. Phys.* **88** 6911–21

[76] Dorai R and Kushner M J 2003 A model for plasma modification of polypropylene using atmospheric pressure discharges *J. Phys. D: Appl. Phys.* **36** 666

[77] DeMore W *et al* 1997 JPL publication 97-4 *Evaluation* **12** 1–266

[78] Piper L G 1989 The excitation of $N(^2P)$ by $N_2(A^3\Sigma_u^+, v' = 0, 1)$ *J. Chem. Phys.* **90** 7087–95

[79] Herron J T 1999 Evaluated chemical kinetics data for reactions of N (2D), N (2P), and N2($A3\Sigma_u^+$) in the gas phase *J. Phys. Chem. Ref. Data* **28** 1453–83

[80] Clyne M A and McDermid I S 1975 Mass spectrometric determinations of the rates of elementary reactions of NO and of NO_2 with ground state $N(^4S)$ atoms *J. Chem. Soc. Faraday Trans. 1: Phys. Chem. Condens. Phases* **71** 2189–202

[81] Campbell I and Gray C 1973 Rate constants for O (^3P) recombination and association with N (^4S) *Chem. Phys. Lett.* **18** 607–9

[82] Knipovich O, Rubtsova E and Nekrsov L 1988 Volume recombination of nitrogen atoms in the afterglow of a condensed discharge *Russ. J. Phys. Chem.* **62** 867–70

[83] Tsang W and Herron J T 1991 Chemical kinetic data base for propellant combustion I. Reactions involving NO, NO_2, HNO, HNO_2, HCN and N_2O *J. Phys. Chem. Ref. Data* **20** 609–63

[84] Sehested J, Nielsen O J, Egsgaard H, Larsen N W, Andersen T S and Pedersen T 1998 Kinetic study of the formation of isotopically substituted ozone in argon *J. Geophys. Res.: Atmos.* **103** 3545–52

[85] Atkinson R *et al* 2004 Evaluated kinetic and photochemical data for atmospheric chemistry: volume I-gas phase reactions of O_x, HO_x, NO_x and SO_x species *Atmos. Chem. Phys.* **4** 1461–738

[86] Atkinson R *et al* 1997 Evaluated kinetic and photochemical data for atmospheric chemistry: supplement VI. IUPAC subcommittee on gas kinetic data evaluation for atmospheric chemistry *J. Phys. Chem. Ref. Data* **26** 1329–499

[87] Atkinson R, Baulch D, Cox R, Hampson R Jr, Kerr J and Troe J 1989 Evaluated kinetic and photochemical data for atmospheric chemistry: supplement III. IUPAC subcommittee on gas kinetic data evaluation for atmospheric chemistry *J. Phys. Chem. Ref. Data* **18** 881–1097

[88] Baulch D *et al* 1992 Evaluated kinetic data for combustion modelling *J. Phys. Chem. Ref. Data* **21** 411–734

[89] Cox R and Derwent R 1975 Kinetics of the reaction of HO_2 with nitric oxide and nitrogen dioxide *J. Photochem.* **4** 139–53

[90] National Institute of Standards and Technology 2014 NIST chemical kinetics database available from: http://kinetics.nist.gov/kinetics/index.jsp

Bibliography

[1] G. Fridman, G. Friedman, A. Gutsol, A. B. Shekhter, V. N. Vasilets, and A. Fridman. Applied plasma medicine. *Plasma Processes and Polymers*, 5(6): 503–533, 2008.

[2] M. G. Kong, G. Kroesen, G. Morfill, T. Nosenko, T. Shimizu, J. Van Dijk, and J. Zimmermann. Plasma medicine: an introductory review. *New Journal of Physics*, 11(11):115012, 2009.

[3] G. Morfill, M. G. Kong, and J. Zimmermann. Focus on plasma medicine. *New Journal of Physics*, 11(11):115011, 2009.

[4] J. Ehlbeck, U. Schnabel, M. Polak, J. Winter, T. von Woedtke, R. Brandenburg, T. von dem Hagen, and K.-D. Weltmann. Low temperature atmospheric pressure plasma sources for microbial decontamination. *Journal of Physics D: Applied Physics*, 44(1):013002, 2011.

[5] K.-D. Weltmann, M. Polak, K. Masur, T. von Woedtke, J. Winter, and S. Reuter. Plasma processes and plasma sources in medicine. *Contributions to Plasma Physics*, 52(7):644–654, 2012.

[6] M. Laroussi, M. Kong, and G. Morfill. *Plasma Medicine: Applications of Low-Temperature Gas Plasmas in Medicine and Biology*. Cambridge University Press, 2012.

[7] T. von Woedtke, S. Reuter, K. Masur, and K.-D. Weltmann. Plasmas for medicine. *Physics Reports*, 530(4):291–320, 2013.

[8] T. von Woedtke, H.-R. Metelmann, and K.-D. Weltmann. Clinical plasma medicine: state and perspectives of in vivo application of cold atmospheric plasma. *Contributions to Plasma Physics*, 54(2):104–117, 2014.

[9] D. B. Graves. Low temperature plasma biomedicine: A tutorial review. *Physics of Plasmas (1994-present)*, 21(8):080901, 2014.

[10] P. Favia and R. d'Agostino. Plasma treatments and plasma deposition of polymers for biomedical applications. *Surface and Coatings Technology*, 98(1-3):1102–1106, 1998. Papers presented at the Fifth International Conference on Plasma Surface Engineering.

[11] A. Ohl and K. Schröder. Plasma-induced chemical micropatterning for cell culturing applications: a brief review. *Surface and Coatings Technology*, 116-119(0):820 – 830, 1999.

[12] P. Chu, J. Chen, L. Wang, and N. Huang. Plasma-surface modification of biomaterials. *Materials Science and Engineering: R: Reports*, 36(5-6):143 – 206, 2002.

[13] R. Brandenburg, J. Ehlbeck, M. Stieber, T. v. Woedtke, J. Zeymer, O. Schlüter, and K.-D. Weltmann. Antimicrobial treatment of heat sensitive materials by means of atmospheric pressure rf-driven plasma jet. *Contributions to Plasma Physics*, 47(1-2):72–79, 2007.

[14] M. Moreau, N. Orange, and M. Feuilloley. Non-thermal plasma technologies: New tools for bio-decontamination. *Biotechnology Advances*, 26(6):610 – 617, 2008.

[15] G. E. Morfill and J. L. Zimmermann. Plasma health care - old problems, new solutions. *Contributions to Plasma Physics*, 52(7):655–663, 2012.

[16] J. Robotis, P. Sechopoulos, and T. Rokkas. Argon plasma coagulation: clinical applications in gastroenterology. *Annals of Gastroenterology*, 16:131–137, 2003.

[17] J. Raiser and M. Zenker. Argon plasma coagulation for open surgical and endoscopic applications: state of the art. *Journal of Physics D: Applied Physics*, 39(16):3520, 2006.

[18] K. Stalder and J. Woloszko. Some physics and chemistry of electrosurgical plasma discharges. *Contributions to Plasma Physics*, 47(1-2):64–71, 2007.

[19] S. Kalghatgi, C. M. Kelly, E. Cerchar, B. Torabi, O. Alekseev, A. Fridman, G. Friedman, and J. Azizkhan-Clifford. Effects of non-thermal plasma on mammalian cells. *PloS one*, 6(1):e16270, 2011.

[20] A. Barton. *Impact of non-thermal plasma on cell signaling in keratinocytes.* PhD thesis, Ernst-Moritz-Arndt-University of Greifswald, Germany, 2014.

[21] S. Bekeschus. *Effects of cold physical plasma on human leukocytes.* PhD thesis, Ernst-Moritz-Arndt-University of Greifswald, Germany, 2015.

[22] E. Stoffels, I. Kieft, and R. Sladek. Superficial treatment of mammalian cells using plasma needle. *Journal of Physics D: Applied Physics*, 36(23):2908, 2003.

[23] E. Stoffels, R. Sladek, and I. Kieft. Gas plasma effects on living cells. *Physica Scripta*, 2004(T107):79, 2004.

[24] G. Fridman, A. Shereshevsky, M. M. Jost, A. D. Brooks, A. Fridman, A. Gutsol, V. Vasilets, and G. Friedman. Floating electrode dielectric barrier discharge plasma in air promoting apoptotic behavior in melanoma skin cancer cell lines. *Plasma Chemistry and Plasma Processing*, 27(2):163–176, 2007.

[25] M. Keidar, R. Walk, A. Shashurin, P. Srinivasan, A. Sandler, S. Dasgupta, R. Ravi, R. Guerrero-Preston, and B. Trink. Cold plasma selectivity and the possibility of a paradigm shift in cancer therapy. *British journal of cancer*, 105(9):1295–1301, 2011.

[26] L. I. Partecke, K. Evert, J. Haugk, F. Doering, L. Normann, S. Diedrich, F.-U. Weiss, M. Evert, N. O. Huebner, C. Guenther, et al. Tissue tolerable plasma (ttp) induces apoptosis in pancreatic cancer cells in vitro and in vivo. *BMC cancer*, 12(1):473, 2012.

[27] J. L. Zimmermann, T. Shimizu, H.-U. Schmidt, Y.-F. Li, G. E. Morfill, and G. Isbary. Test for bacterial resistance build-up against plasma treatment. *New Journal of Physics*, 14(7):073037, 2012.

[28] G. Isbary, J. L. Zimmermann, T. Shimizu, G. E. Morfill, A. Mitra, H. M. Thomas, T. G. Klampfl, J. Koeritzer, V. Boxhammer, J. Schlegel, et al. Reasons why we need cold atmospheric plasmas in bacteria-related diseases in medicine. *Plasma Medicine*, 2(1-3), 2012.

[29] R. Tiede, J. Hirschberg, G. Daeschlein, T. von Woedtke, W. Vioel, and S. Emmert. Plasma applications: A dermatological view. *Contributions to Plasma Physics*, 54(2):118–130, 2014.

[30] R. Matthes, O. Assadian, and A. Kramer. Repeated applications of cold atmospheric pressure plasma does not induce resistance in staphylococcus aureus embedded in biofilms. *GMS hygiene and infection control*, 9(3), 2014.

[31] G. Isbary, G. Morfill, H. Schmidt, M. Georgi, K. Ramrath, J. Heinlin, S. Karrer, M. Landthaler, T. Shimizu, B. Steffes, W. Bunk, R. Monetti, J. Zimmermann, R. Pompl, and W. Stolz. A first prospective randomized controlled trial to decrease bacterial load using cold atmospheric argon plasma on chronic wounds in patients. *British Journal of Dermatology*, 163(1):78–82, 2010.

[32] G. Isbary, J. Heinlin, T. Shimizu, J. Zimmermann, G. Morfill, H.-U. Schmidt, R. Monetti, B. Steffes, W. Bunk, Y. Li, T. Klaempfl, S. Karrer, M. Landthaler, and W. Stolz. Successful and safe use of 2 min cold atmospheric argon plasma in chronic wounds: results of a randomized controlled trial. *British Journal of Dermatology*, 167(2):404–410, 2012.

[33] H.-R. Metelmann, T. T. Vu, H. T. Do, T. N. B. Le, T. H. A. Hoang, T. T. T. Phi, T. M. L. Luong, T. T. H. Nguyen, T. H. M. Nguyen, T. L. Nguyen, et al. Scar formation of laser skin lesions after cold atmospheric pressure plasma (cap) treatment: A clinical long term observation. *Clinical Plasma Medicine*, 1(1):30–35, 2013.

[34] F. Brehmer, H. Haenssle, G. Daeschlein, R. Ahmed, S. Pfeiffer, A. Görlitz, D. Simon, M. Schön, D. Wandke, and S. Emmert. Alleviation of chronic venous leg ulcers with a hand-held dielectric barrier discharge plasma generator

(plasmaderm vu-2010): results of a monocentric, two-armed, open, prospective, randomized and controlled trial (nct01415622). *Journal of the European Academy of Dermatology and Venereology*, 29(1):148–155, 2015.

[35] M. Klebes, C. Ulrich, F. Kluschke, A. Patzelt, S. Vandersee, H. Richter, A. Bob, J. von Hutten, J. T. Krediet, A. Kramer, J. Lademann, and B. Lange-Asschenfeld. Combined antibacterial effects of tissue-tolerable plasma and a modern conventional liquid antiseptic on chronic wound treatment. *Journal of Biophotonics*, 8(5):382–391, 2015.

[36] D. B. Graves. The emerging role of reactive oxygen and nitrogen species in redox biology and some implications for plasma applications to medicine and biology. *Journal of Physics D: Applied Physics*, 45(26):263001, 2012.

[37] K. Wende, P. Williams, J. Dalluge, W. Van Gaens, H. Aboubakr, J. Bischof, T. von Woedtke, S. M. Goyal, K.-D. Weltmann, A. Bogaerts, et al. Identification of the biologically active liquid chemistry induced by a nonthermal atmospheric pressure plasma jet. *Biointerphases*, 10(2):029518, 2015.

[38] S. Iseni, S. Zhang, A. van Gessel, S. Hofmann, B. van Ham, S. Reuter, K. Weltmann, and P. Bruggeman. Nitric oxide density distributions in the effluent of an rf argon appj: effect of gas flow rate and substrate. *New Journal of Physics*, 16(12):123011, 2014.

[39] W. Van Gaens and A. Bogaerts. Kinetic modelling for an atmospheric pressure argon plasma jet in humid air. *Journal of Physics D: Applied Physics*, 46(27):275201, 2013.

[40] W. Van Gaens, P. Bruggeman, and A. Bogaerts. Numerical analysis of the no and o generation mechanism in a needle-type plasma jet. *New Journal of Physics*, 16(6):063054, 2014.

[41] T. Murakami, K. Niemi, T. Gans, D. O'Connell, and W. Graham. Chemical kinetics and reactive species in atmospheric pressure helium-oxygen plasmas with humid-air impurities. *Plasma Sources Science and Technology*, 22(1):1–29, 2013.

[42] J. Waskoenig, K. Niemi, N. Knake, L. Graham, S. Reuter, V. Schulz-Von Der Gathen, and T. Gans. Atomic oxygen formation in a radio-frequency driven micro-atmospheric pressure plasma jet. *Plasma Sources Science and Technology*, 19(4):045018, 2010.

[43] T. Shimizu, B. Steffes, R. Pompl, F. Jamitzky, W. Bunk, K. Ramrath, M. Georgi, W. Stolz, H.-U. Schmidt, T. Urayama, et al. Characterization of microwave plasma torch for decontamination. *Plasma Processes and Polymers*, 5(6):577–582, 2008.

[44] G. Morfill and W. Stolz. Forschungs-Projekt "Plasma-Medizin" Phase II Niedertemperatur-Argon-Plasma zur in-vivo-Sterilisation chronischer Wunden (Abschlussbericht). Technical report, Max-Planck Institut für extraterrestrische Physik, 2013.

[45] G. A. Lavoie, J. B. Heywood, and J. C. Keck. Experimental and theoretical study of nitric oxide formation in internal combustion engines. *Combustion science and technology*, 1(4):313–326, 1970.

[46] G. Ni, Q. Lin, L. Li, C. Cheng, L. Chen, J. Shen, Y. Lan, and Y. Meng. Alternating current-driven non-thermal arc plasma torch working with air medium at atmospheric pressure. *Journal of Physics D: Applied Physics*, 46 (45):455204, 2013.

[47] A. B. Shekhter, V. A. Serezhenkov, T. G. Rudenko, A. V. Pekshev, and A. F. Vanin. Beneficial effect of gaseous nitric oxide on the healing of skin wounds. *Nitric oxide*, 12(4):210–219, 2005.

[48] X. Hao, A. M. Mattson, C. M. Edelblute, M. A. Malik, L. C. Heller, and J. F. Kolb. Nitric oxide generation with an air operated non-thermal plasma jet and associated microbial inactivation mechanisms. *Plasma Processes and Polymers*, 11(11):1044–1056, 2014.

[49] Y. Sakiyama, D. B. Graves, H.-W. Chang, T. Shimizu, and G. E. Morfill. Plasma chemistry model of surface microdischarge in humid air and dynamics of reactive neutral species. *Journal of Physics D: Applied Physics*, 45(42): 425201, 2012.

[50] W. Tian and M. J. Kushner. Atmospheric pressure dielectric barrier discharges interacting with liquid covered tissue. *Journal of Physics D: Applied Physics*, 47(16):165201, 2014.

[51] A. Helmke, M. Franck, D. Wandke, and W. Vioel. Tempo-spatially resolved ozone characteristics during single-electrode dielectric barrier discharge (se-dbd) operation against metal and porcine skin surfaces. *Plasma Medicine*, 4 (1-4), 2014.

[52] T. Shimizu, Y. Sakiyama, D. B. Graves, J. L. Zimmermann, and G. E. Morfill. The dynamics of ozone generation and mode transition in air surface micro-discharge plasma at atmospheric pressure. *New Journal of Physics*, 14(10): 103028, 2012.

[53] C. Van Gils, S. Hofmann, B. Boekema, R. Brandenburg, and P. Bruggeman. Mechanisms of bacterial inactivation in the liquid phase induced by a remote rf cold atmospheric pressure plasma jet. *Journal of Physics D: Applied Physics*, 46(17):175203, 2013.

[54] M. J. Pavlovich, H.-W. Chang, Y. Sakiyama, D. S. Clark, and D. B. Graves. Ozone correlates with antibacterial effects from indirect air dielectric barrier discharge treatment of water. *Journal of Physics D: Applied Physics*, 46(14): 145202, 2013.

[55] M. J. Pavlovich, Z. Chen, Y. Sakiyama, D. S. Clark, and D. B. Graves. Effect of discharge parameters and surface characteristics on ambient-gas plasma disinfection. *Plasma Processes and Polymers*, 10(1):69–76, 2013.

[56] H. Jablonowski, M. A. C. Hänsch, M. Dünnbier, K. Wende, M. U. Hammer, K.-D. Weltmann, S. Reuter, and T. von Woedtke. Plasma jet's shielding gas impact on bacterial inactivation. *Biointerphases*, 10(2):029506, 2015.

[57] I. Yimer, I. Campbell, and L.-Y. Jiang. Estimation of the turbulent schmidt number from experimental profiles of axial velocity and concentration for high-reynolds-number jet flows. *Canadian Aeronautics and Space Journal*, 48(3): 195–200, 2002.

[58] L. Prandtl. Über Flüssigkeitsbewegung bei sehr kleiner Reibung. *Verhandlungen des Dritten Internationalen Mathematiker-Kongresses*, pages 484–491, 1904.

[59] H. Schlichting. Laminare Strahlenausbreitung. *Zeitschrift für Angewandte Mathematik und Mechanik*, 13:260–263, 1933.

[60] W. Bickley. The plane jet. *The London, Edinburgh, and Dublin Philosophical Magazine and Journal of Science*, 23:727–731, 1937.

[61] A. Revuelta, A. L. Sánchez, and A. Liñán, A. The virtual origin as a first-order correction for the far-field description of laminar jets. *Physics of Fluids*, 14(6):1821–1824, 2002.

[62] L. J. Crane and D. C. Pack. The mixing of a jet of gas with an atmosphere of a different gas at large distances from the orifice: Part i. the plane jet. *Quarterly Journal of Mathematics*, 14(4):385–391, 1961.

[63] L. J. Crane. The mixing of a jet of gas with an atmosphere of a different gas at large distances from the orifice: Part ii. the round jet. *Quarterly Journal of Mathematics*, 14(4):393–402, 1961.

[64] R. Günther and H. Wilhelmi. *Verbrennung Und Feuerungen*. Springer, 1984.

[65] A. L. Sánchez, M. Vera, and A. Liñán. Exact solutions for transient mixing of two gases of different densities. *Physics of Fluids*, 18(7):078102, 2006.

[66] S. Reuter, H. Tresp, K. Wende, M. U. Hammer, J. Winter, K. Masur, A. Schmidt-Bleker, and K.-D. Weltmann. From RONS to ROS: Tailoring Plasma Jet Treatment of Skin Cells. *IEEE Transactions on Plasma Science*, 40(11):2986–2993, 2012.

[67] J. Winter, J. S. Sousa, N. Sadeghi, A. Schmidt-Bleker, S. Reuter, and V. Puech. The spatio-temporal distribution of He (23S1) metastable atoms in a MHz-driven helium plasma jet is influenced by the oxygen/nitrogen ratio of the surrounding atmosphere. *Plasma Sources Science and Technology*, 24(2): 25015–25025, 2015.

[68] S. Kanazawa, H. Tanaka, A. Kajiwara, T. Ohkubo, Y. Nomoto, M. Kocik, J. Mizeraczyk, and J.-S. Chang. LIF imaging of OH radicals in DC positive streamer coronas. *Thin Solid Films*, 515(9):4266–4271, 2007.

[69] X. Pei, Y. Lu, S. Wu, Q. Xiong, and X. Lu. A study on the temporally and spatially resolved oh radical distribution of a room-temperature atmospheric-pressure plasma jet by laser-induced fluorescence imaging. *Plasma Sources Science and Technology*, 22(2):025023, 2013.

[70] R. Goldstein. *Fluid mechanics measurements*. CRC Press, Boca Raton, 1996.

[71] W. Merzkirch. *Flow visualization*. Academic Press Inc., Orlando, 1987.

[72] G. Settles. *Schlieren and Shadowgraph Techniques,(2001)*. Springer-Verlag, Berlin, 2001.

[73] P. K. Panigrahi and K. Muralidhar. *Schlieren and shadowgraph methods in heat and mass transfer*, volume 2. Springer, Berlin, 2012.

[74] N. Jiang, J. Yang, F. He, and Z. Cao. Interplay of discharge and gas flow in atmospheric pressure plasma jets. *Journal of Applied Physics*, 109(9):093305, 2011.

[75] J.-S. Oh, O. T. Olabanji, C. Hale, R. Mariani, K. Kontis, and J. W. Bradley. Imaging gas and plasma interactions in the surface-chemical modification of polymers using micro-plasma jets. *Journal of Physics D: Applied Physics*, 44 (15):155206, 2011.

[76] M. Ghasemi, P. Olszewski, J. Bradley, and J. Walsh. Interaction of multiple plasma plumes in an atmospheric pressure plasma jet array. *Journal of Physics D: Applied Physics*, 46(5):052001, 2013.

[77] E. Robert, V. Sarron, T. Darny, D. Riès, S. Dozias, J. Fontane, L. Joly, and J.-M. Pouvesle. Rare gas flow structuration in plasma jet experiments. *Plasma Sources Science and Technology*, 23(1):012003, 2014.

[78] M. Boselli, V. Colombo, E. Ghedini, M. Gherardi, R. Laurita, A. Liguori, P. Sanibondi, and A. Stancampiano. Schlieren high-speed imaging of a nanosecond pulsed atmospheric pressure non-equilibrium plasma jet. *Plasma Chemistry and Plasma Processing*, pages 1–17, 2014.

[79] Y. Sutton, J. Moore, D. Sharp, and N. S. J. Braithwaite. Looking into a plasma loudspeaker. *IEEE Transactions on Plasma Science*, 39(11):2146–2147, 2011.

[80] S. Bekeschus, S. Iseni, S. Reuter, K. Masur, and K.-D. Weltmann. Nitrogen shielding of an argon plasma jet and its effects on human immune cells. *IEEE Transactions on Plasma Science*, 43(3):776–781, 2015.

[81] S. Reuter, J. Winter, S. Iseni, S. Peters, A. Schmidt-Bleker, M. Dünnbier, J. Schäfer, R. Foest, and K. Weltmann. Detection of ozone in a MHz argon plasma bullet jet. *Plasma Sources Science and Technology*, 21(3):034015, 2012.

[82] M. Teschke, J. Kedzierski, E. Finantu-Dinu, D. Korzec, and J. Engemann. High-speed photographs of a dielectric barrier atmospheric pressure plasma jet. *IEEE Transactions on Plasma Science*, 33(2):310–311, 2005.

[83] X. Lu and M. Laroussi. Dynamics of an atmospheric pressure plasma plume generated by submicrosecond voltage pulses. *Journal of Applied Physics*, 100 (6):063302, 2006.

[84] R. Bussiahn, R. Brandenburg, T. Gerling, E. Kindel, H. Lange, N. Lembke, K.-D. Weltmann, T. von Woedtke, and T. Kocher. The hairline plasma: An intermittent negative dc-corona discharge at atmospheric pressure for plasma medical applications. *Applied Physics Letters*, 96(14):143701, 2010.

[85] M. Laroussi, W. Hynes, T. Akan, X. Lu, and C. Tendero. The plasma pencil: a source of hypersonic cold plasma bullets for biomedical applications. *IEEE Transactions on Plasma Science*, 36(4):1298–1299, 2008.

[86] X. Lu, M. Laroussi, and V. Puech. On atmospheric-pressure non-equilibrium plasma jets and plasma bullets. *Plasma Sources Science and Technology*, 21 (3):034005, 2012.

[87] D. Breden, K. Miki, and L. Raja. Self-consistent two-dimensional modeling of cold atmospheric-pressure plasma jets/bullets. *Plasma Sources Science and Technology*, 21(3):034011, 2012.

[88] G. Naidis. Modelling of plasma bullet propagation along a helium jet in ambient air. *Journal of Physics D: Applied Physics*, 44(21):215203, 2011.

[89] G. Naidis. Modelling of streamer propagation in atmospheric-pressure helium plasma jets. *Journal of Physics D: Applied Physics*, 43(40):402001, 2010.

[90] J. Boeuf, L. Yang, and L. Pitchford. Dynamics of a guided streamer ('plasma bullet') in a helium jet in air at atmospheric pressure. *Journal of Physics D: Applied Physics*, 46(1):015201, 2013.

[91] N. Y. Babaeva and M. J. Kushner. Interaction of multiple atmospheric-pressure micro-plasma jets in small arrays: He/O2 into humid air. *Plasma Sources Science and Technology*, 23(1):015007, 2014.

[92] Z. Xiong, E. Robert, V. Sarron, J.-M. Pouvesle, and M. J. Kushner. Atmospheric-pressure plasma transfer across dielectric channels and tubes. *Journal of Physics D: Applied Physics*, 46(15):155203, 2013.

[93] A. Luque, V. Ratushnaya, and U. Ebert. Positive and negative streamers in ambient air: modelling evolution and velocities. *Journal of Physics D: Applied Physics*, 41(23):234005, 2008.

[94] W.-C. Zhu, Q. Li, X.-M. Zhu, and Y.-K. Pu. Characteristics of atmospheric pressure plasma jets emerging into ambient air and helium. *Journal of Physics D: Applied Physics*, 42(20):202002, 2009.

[95] S. Hofmann, A. Sobota, and P. Bruggeman. Transitions between and control of guided and branching streamers in dc nanosecond pulsed excited plasma jets. *IEEE Transactions on Plasma Science*, 40(11):2888–2899, 2012.

[96] B. Lay, R. S. Moss, S. Rauf, and M. J. Kushner. Breakdown processes in metal halide lamps. *Plasma Sources Science and Technology*, 12(1):8, 2003.

[97] Z. Xiong and M. J. Kushner. Atmospheric pressure ionization waves propagating through a flexible high aspect ratio capillary channel and impinging upon a target. *Plasma Sources Science and Technology*, 21(3):034001, 2012.

[98] Y. Sakiyama and D. B. Graves. Neutral gas flow and ring-shaped emission profile in non-thermal rf-excited plasma needle discharge at atmospheric pressure. *Plasma Sources Science and Technology*, 18(2):025022, 2009.

[99] W. Van Gaens, S. Iseni, A. Schmidt-Bleker, K.-D. Weltmann, S. Reuter, and A. Bogaerts. Numerical analysis of the effect of nitrogen and oxygen admixtures on the chemistry of an argon plasma jet operating at atmospheric pressure. *New Journal of Physics*, 17(3):033003, 2015.

[100] D.-X. Liu, P. Bruggeman, F. Iza, M.-Z. Rong, and M. G. Kong. Global model of low-temperature atmospheric-pressure He+ H2O plasmas. *Plasma Sources Science and Technology*, 19(2):025018, 2010.

[101] G. V. Naidis. Modelling of oh production in cold atmospheric-pressure he–h 2 o plasma jets. *Plasma Sources Science and Technology*, 22(3):035015, 2013.

[102] G. Naidis. Production of active species in cold helium–air plasma jets. *Plasma Sources Science and Technology*, 23(6):065014, 2014.

[103] L. S. Rothman, D. Jacquemart, A. Barbe, D. Chris Benner, M. Birk, L. Brown, M. Carleer, C. Chackerian Jr, K. Chance, L. e. a. Coudert, et al. The hitran 2004 molecular spectroscopic database. *Journal of Quantitative Spectroscopy and Radiative Transfer*, 96(2):139–204, 2005.

[104] T. J. Johnson, R. L. Sams, and S. W. Sharpe. The pnnl quantitative infrared database for gas-phase sensing: a spectral library for environmental, hazmat, and public safety standoff detection. In *Optical Technologies for Industrial, Environmental, and Biological Sensing*, pages 159–167. International Society for Optics and Photonics, 2004.

[105] S. Iseni, S. Reuter, A. Schmidt-Bleker, and K.-D. Weltmann. Flow and Discharge Development in an Argon Atmospheric Pressure Plasma Jet Observed by ICCD and PLIF Imaging. *IEEE Transactions on Plasma Science*, 42(10): 2458–2459, 2014.

[106] Centers for Disease Control and Prevention - Department of Health and Human Services. *NIOSH Pocket Guide to Chemical Hazards*. National Institute for Occupational Safety and Health, 2007.

[107] S. Reuter, J. Winter, S. Iseni, A. Schmidt-Bleker, M. Dunnbier, K. Masur, K. Wende, and K.-D. Weltmann. The influence of feed gas humidity versus ambient humidity on atmospheric pressure plasma jet-effluent chemistry and skin cell viability. *IEEE Transactions on Plasma Science*, 2014.

[108] J. Winter, H. Tresp, M. Hammer, S. Iseni, S. Kupsch, A. Schmidt-Bleker, K. Wende, M. Dünnbier, K. Masur, K. Weltmann, et al. Tracking plasma generated H2O2 from gas into liquid phase and revealing its dominant impact on human skin cells. *Journal of Physics D: Applied Physics*, 47(28):285401, 2014.

[109] J. Winter, K. Wende, K. Masur, S. Iseni, M. Dünnbier, M. U. Hammer, H. Tresp, K.-D. Weltmann, and S. Reuter. Feed gas humidity: a vital parameter affecting a cold atmospheric-pressure plasma jet and plasma-treated human skin cells. *Journal of Physics D: Applied Physics*, 46(29):295401, 2013.

[110] S. Reuter, A. Schmidt-Bleker, H. Jablonowski, J. Winter, A. Bösel, M. Hammer, S. Iseni, and K. Weltmann. Fundamental aspects of filamentary jet discharges interacting with biologically relevant liquids and with cells. In *International Conference on Phenomenta in Ionized Gases in Iasi, Romania*, 2015.

[111] H. Tresp, M. U. Hammer, K.-D. Weltmann, and S. Reuter. Effects of atmosphere composition and liquid type on plasma-generated reactive species in biologically relevant solutions. *Plasma Medicine*, 3(1-2), 2013.

Eigenständigkeitserklärung

Hiermit erkläre ich, dass diese Arbeit bisher von mir weder an der Mathematisch-Naturwissenschaftlichen Fakultät der Ernst-Moritz-Arndt-Universität Greifswald noch einer anderen wissenschaftlichen Einrichtung zum Zwecke der Promotion eingereicht wurde.

Ferner erkläre ich, dass ich diese Arbeit selbstständig verfasst und keine anderen als die darin angegebenen Hilfsmittel und Hilfen benutzt und keine Textabschnitte eines Dritten ohne Kennzeichnung übernommen habe.

_____   _____
Datum   Ansgar Schmidt-Bleker

Curriculum Vitae

Ansgar Schmidt-Bleker

Feldstraße 79
17489 Greifswald, Germany
Phone: +49 3834 554 3939
email: ansgar.schmidt-bleker@inp-greifswald.de

Born: July 3, 1986 in Hamburg, Germany
Nationality: German

Professional Experience

since 4/2011	RESEARCH ASSISTANT, Leibniz-Institut für Plasmaforschung und Technologie e.V. Greifswald (INP Greifswald), Germany
8/2013	VISITING SCIENTIST, University of Michigan at Ann Arbor, USA
4/2012 - 7/2012	VISITING SCIENTIST, University of California at Berkeley, USA
6/2010-3/2011	RESEARCH ASSISTANT, Institute for Theory of Statistical Physics, RWTH Aachen University, Germany

Education

since 4/2011	PHD CANDIDATE, Ernst Moritz Arndt University of Greifswald, Germany
3/2010	DIPLOMA IN PHYSICS, RWTH Aachen University, Germany
2004	ABITUR, Bischöfliches Clara-Fey-Gymnasium Schleiden, Germany

Honors & Awards

2014	Poster Prize of the European Physical Society at the ESCAMPIG 2014 in Greifswald, Germany
2013	Best Interdisciplinary Talk at the 2$^{\text{nd}}$ Young Professional Workshop on Plasma-Medicine
2012	Best student paper award finalist at ICOPS 2012, Edinburgh, United Kingdom
2011	Publication selected for best of 2011 collection of European Physics Letters (A. Schmidt-Bleker, W. Gassen and H.J. Kull. Nonlinear plasma waves and wavebreaking in quantum plasmas. *EPL* 95(5): 55003, 2011.)

Teaching Assistance

2010 - 11	Theoretical Plasma Physics
2010	Computational Physics
2009 - 10	Computational Plasma Physics
2009	Theoretical Mechanics
2008 - 09	Theoretical Plasma Physics
2006 - 07	Physics Lab Courses

Patents

2014	A. SCHMIDT-BLEKER, S. REUTER, K.-D. WELTMANN (INP GREIFSWALD E.V.) Verfahren und Vorrichtung zum Erzeugen eines kalten Plasmas mit einer ersten und einer zweiten Kammer (pending)

_____
Date

_____
Ansgar Schmidt-Bleker

List of Publications and Conference Contributions

Publications in Peer Reviewed Journals

- <u>A. Schmidt-Bleker</u>, W. Gassen, and H.-J. Kull. Nonlinear plasma waves and wavebreaking in quantum plasmas. *EPL (Europhysics Letters)*, 95(5):55003, 2011.

- S. Reuter, H. Tresp, K. Wende, M. U. Hammer, J. Winter, K. Masur, <u>A. Schmidt-Bleker</u>, and K.-D. Weltmann. From RONS to ROS: Tailoring plasma jet treatment of skin cells. *IEEE Transactions on Plasma Science*, 40(11): 2986–2993, 2012.

- S. Reuter, J. Winter, S. Iseni, S. Peters, <u>A. Schmidt-Bleker</u>, M. Dünnbier, J. Schäfer, R. Foest, and K. Weltmann. Detection of ozone in a MHz argon plasma bullet jet. *Plasma Sources Science and Technology*, 21(3):034015, 2012.

- S. Reuter, J. Winter, <u>A. Schmidt-Bleker</u>, D. Schroeder, H. Lange, N. Knake, V. S. von der Gathen, and K.-D. Weltmann. Atomic oxygen in a cold argon plasma jet: TALIF spectroscopy in ambient air with modelling and measurements of ambient species diffusion. *Plasma Sources Science and Technology*, 21(2):024005, 2012.

- S. Reuter, J. Winter, <u>A. Schmidt-Bleker</u>, H. Tresp, M. Hammer, and K.-D. Weltmann. Controlling the ambient air affected reactive species composition in the effluent of an argon plasma jet. *IEEE Transactions on Plasma Science*, 40(11):2788–2794, 2012.

- M. Dünnbier, <u>A. Schmidt-Bleker</u>, J. Winter, M. Wolfram, R. Hippler, K.-D. Weltmann, and S. Reuter. Ambient air particle transport into the effluent of a cold atmospheric-pressure argon plasma jet investigated by molecular beam mass spectrometry. *Journal of Physics D: Applied Physics*, 46(43):435203, 2013.

- <u>A. Schmidt-Bleker</u>, J. Winter, S. Iseni, M. Dünnbier, K. Weltmann and S. Reuter. Reactive species output of a plasma jet with a shielding gas de-

vice—combination of FTIR absorption spectroscopy and gas phase modelling. *Journal of Physics D: Applied Physics*, 47(14):145201, 2014.

- A. Schmidt-Bleker, S. Reuter, and K.-D. Weltmann. Non-dispersive path mapping approximation for the analysis of ambient species diffusion in laminar jets. *Physics of Fluids (1994-present)*, 26(8):083603, 2014.

- S. Iseni, S. Reuter, A. Schmidt-Bleker, and K.-D. Weltmann. Flow and discharge development in an argon atmospheric pressure plasma jet observed by ICCD and PLIF imaging. *IEEE Transactions on Plasma Science*, 42(10): 2458–2459, 2014.

- S. Iseni, A. Schmidt-Bleker, J. Winter, K.-D. Weltmann, and S. Reuter. Atmospheric pressure streamer follows the turbulent argon air boundary in a MHz argon plasma jet investigated by OH-tracer PLIF spectroscopy. *Journal of Physics D: Applied Physics*, 47(15):152001, 2014.

- S. Reuter, J. Winter, S. Iseni, A. Schmidt-Bleker, M. Dunnbier, K. Masur, K. Wende, and K.-D. Weltmann. The influence of feed gas humidity versus ambient humidity on atmospheric pressure plasma jet-effluent chemistry and skin cell viability. *IEEE Transactions on Plasma Science*, 2014.

- J. Winter, H. Tresp, M. Hammer, S. Iseni, S. Kupsch, A. Schmidt-Bleker, K. Wende, M. Dünnbier, K. Masur, K. Weltmann, et al. Tracking plasma generated H2O2 from gas into liquid phase and revealing its dominant impact on human skin cells. *Journal of Physics D: Applied Physics*, 47(28):285401, 2014.

- S. Reuter, A. Schmidt-Bleker, S. Iseni, J. Winter, and K.-D. Weltmann. On the bullet-streamer dualism. *IEEE Transactions on Plasma Science*, 42(10): 2428–2429, 2014.

- A. Schmidt-Bleker, S. Reuter, and K. Weltmann. Quantitative schlieren diagnostics for the determination of ambient species density, gas temperature and calorimetric power of cold atmospheric plasma jets. *Journal of Physics D: Applied Physics*, 48(17):175202, 2015.

- A. Schmidt-Bleker, S. A. Norberg, J. Winter, E. Johnsen, S. Reuter, K. Weltmann, and M. J. Kushner. Propagation mechanisms of guided streamers in plasma jets: the influence of electronegativity of the surrounding gas. *Plasma Sources Science and Technology*, 24(3):035022, 2015.

- W. Van Gaens, S. Iseni, A. Schmidt-Bleker, K.-D. Weltmann, S. Reuter, and A. Bogaerts. Numerical analysis of the effect of nitrogen and oxygen admixtures on the chemistry of an argon plasma jet operating at atmospheric pressure. *New Journal of Physics*, 17(3):033003, 2015.

- J. Winter, J. S. Sousa, N. Sadeghi, A. Schmidt-Bleker, S. Reuter, and V. Puech. The spatio-temporal distribution of He metastable atoms in a MHz-driven helium plasma jet is influenced by the oxygen/nitrogen ratio of the surrounding

atmosphere. *Plasma Sources Science and Technology*, 24(2):25015–25025, 2015.

- A. Schmidt-Bleker, J. Winter, A. Bösel, S. Reuter, and K.-D. Weltmann. On the plasma chemistry of a cold atmospheric argon plasma jet with shielding gas device. *Plasma Sources Science and Technology*, 25(1):015005, 2016.

Contributions to Workshops and Conferences

Oral Presentations

- A. Schmidt-Bleker, S. Reuter, J. Winter, H. Lange, and K.-D. Weltmann. Investigation of ambient air species diffusion into the effluent of an atmospheric pressure plasma jet by measurements and modeling. At *64th Annual Gaseous Electronics Conference at Salt Lake City, Utah, USA*, volume 1, page 2010, 2011.

- A. Schmidt-Bleker, M. Dünnbier, J. Winter, K.-D. Weltmann, and S. Reuter. Convection-diffusion model for atmospheric pressure plasma jets: Obtaining off-axis data from on-axis measurements. At *65th Annual Gaseous Electronics Conference at Austin, Texas, USA*, volume 1, page 3007, 2012.

- A. Schmidt-Bleker, J. Winter, K.-D. Weltmann, and S. Reuter. Diagnostics of ambient air species diffusion into the effluent of an atmospheric pressure plasma jet assisted by analytical and numerical modeling. At *39th IEEE International Conference on Plasma Science (ICOPS) at Edinburgh, UK*, 2012.

- A. Schmidt-Bleker, J. Winter, S. Iseni, M. Dünnbier, S. Reuter, and K.-D. Weltmann. Diffusion and atmospheric pressure plasma jets: How ambient air species and heat are transported. At *1st Young Professional Workshop on Plasma Medicine at Boltenhagen, Germany*, 2012.

- A. Schmidt-Bleker, J. Winter, S. Iseni, M. Duennbier, A. Barton, L. Bundscherer, K. Wende, K. Masur, K.-D. Weltmann, and S. Reuter. Controlling the effluent chemistry of a CAP jet for biomedical applications: FTIR diagnostics and gas phase modeling. At *66th Annual Gaseous Electronics Conference at Princeton, NJ, USA*, volume 58, 2013.

- A. Schmidt-Bleker, J. Winter, S. Reuter, and K.-D. Weltmann. Controlling the effluent chemistry of a cold atmospheric pressure plasma jet for biomedical applications: FTIR diagnostics and gas phase modeling. At *2nd Young Professional Workshop on Plasma Medicine at Kölpinsee, Germany*, 2013.

- A. Schmidt-Bleker, J. Winter, J. S. Sousa, V. Puech, K.-D. Weltmann, and S. Reuter. On the role of metastable argon At cold atmospheric pressure plasma jets with shielding gas device. At *67th Annual Gaseous Electronics Conference at Princeton, Raleigh, NC, USA*, volume 1, page 3005, 2014.

- <u>A. Schmidt-Bleker</u>, J. Winter, K.-D. Weltmann, and S. Reuter. On the role of metastable argon At cold atmospheric pressure plasma jets with shielding gas device. At *3rd Young Professional Workshop on Plasma Medicine at Zinnowitz, Germany*, 2014.

- <u>A. Schmidt-Bleker</u>, J. Winter, K.-D. Weltmann, and S. Reuter. On the plasma chemistry of a cold atmospheric argon plasma jet with shielding gas device. At *4th Young Professional Workshop on Plasma Medicine at Rostock, Germany*, 2015.

Poster Presentations

- <u>A. Schmidt-Bleker</u>, J. Winter, H. Lange, S. Reuter, and K.-D. Weltmann. Investigation of ambient air species diffusion into the effluent of an atmospheric pressure plasma jet by measurements and modeling. At *Workshop „Plasmamedizin" des Anwenderkreises Atmosphärendruckplasma in Erfurt*, 2011.

- <u>A. Schmidt-Bleker</u>, J. Winter, S. Iseni, M. Dünnbier, K.-D. Weltmann, and S. Reuter. The influence of shielding gas composition on the dynamics, temperature and reactive species generated by a cold atmospheric pressure plasma jet with gas shielding device. At *The XXII Europhysics Conference on Atomic and Molecular Physics of Ionized Gases (ESCAMPIG)*, 2014.

Acknowledgment